APPLICATION OF SMA FIBER COMPOSITE AS SEISMIC REINFORCEMENT FOR CONCRETE MOMENT RESISTING FRAMES

BY

ADEEL ZAFAR

DISSERTATION

Submitted in partial fulfillment of the requirements
for the degree of Doctor of Philosophy in Civil Engineering
in the Graduate College of the
University of Illinois at Urbana-Champaign, 2013

Urbana, Illinois

Doctoral Committee:

Assistant Professor Bassem Andrawes, Chair and Director of Research
Professor David A. Lange
Associate Professor James M. LaFave
Associate Professor Junho Song

Abstract

For many years, steel has been used as the primary reinforcing material for concrete structures. Despite requisite stiffness, strength, ductility and desired deflection properties, steel reinforcing bars have tendency to incur permanent plastic deformations under excessive loading. Recently, fiber reinforced polymer (FRP) reinforcing bars have also been used in concrete structures to address corrosion issues typically associated with conventional steel bars. However, due to their linear elastic behavior, they are not considered in structures which require ductility and damping characteristics. The use of shape memory alloys (SMAs) with their nonlinear-elastic behavior in the composite could potentially provide solution for this problem. Small diameter super-elastic Nickel-Titanium (NiTi) SMA wires, coupled with polymer matrix is sought in this research as reinforcing bars in reinforced concrete (RC) moment resisting frames (MRFs) to improve the performance of the frames in terms of reducing residual inter-story drifts and damage under earthquake loading, while still maintaining the elastic characteristics associated with FRP. SMA fibers, conventional polymeric fibers and resin are infused together to manufacture the new composite under high pressure and temperature. Uni-axial cyclic tensile tests are carried out to characterize the mechanical hysteretic behavior of the new composite. Analytical constitutive models are developed for the SMA-based composite materials and calibrated based on experimental test results. These material models are then extended for use in structural models to capture the hysteretic behavior of the composite. The new SMA composite reinforcement is placed at the plastic hinge region of the MRFs, where most of the damage is expected. RC MRF prototype structures reinforced with steel, SMA-FRP and conventional glass-FRP (GFRP) composite reinforcement are designed using two different approaches involving equivalent static

force procedure and capacity spectrum method. Multiple non-linear time history analyses are conducted using incremental dynamic technique for assessing the performance of the MRFs under suite of ground motions. Main shock-aftershock ground motion sequences are utilized to examine the efficacy of using SMA-FRP composite in plastic hinge zones of MRFs. Damage assessment is performed based on residual inter-story drift and drift performance levels. Efficacy of proposed SMA-FRP composite reinforcement is further explored by embedding it in a small scale beam tested under 3-point bending.

Adeel Zafar

Department of Civil and Environmental Engineering

University of Illinois at Urbana-Champaign

April, 2013

Dedication

I dedicate this dissertation to my loving parents, Brig(r) Zafar Iqbal Chaudhry and Rukhsana Zafar who have always been a great source of inspiration; to my beautiful daughters Iman, Eshal and Aiza and to my wife Mominah who makes my life meaningful and enjoyable.

In memory of my father-in-law

Raja Muhammad Atta

Acknowledgement

Looking back over the years, I feel that the time has really flown by, but the persons around me have made this a very memorable journey. It is with great appreciation that I thank all of those people who have been part of it and have rendered their support along the way.

I am deeply grateful to my advisor, Dr Bassem Andrawes, for providing me the opportunity to pursue my goals in achieving a doctoral degree. Without his support, guidance and advice, this work would not have been possible. Special thanks go out to Dr David A. Lange, Dr James M. LaFave and Dr Junho Song for serving on my dissertation advisory committee. Throughout my time at University of Illinois at Urbana-Champaign, I have been very lucky to be surrounded by some of top and renowned faculty members in their fields who enlightened me with the needed knowledge and advice throughout my academic tenure. I want to express my thanks to Timothy J. Prunkard, Donald E. Marrow and Kevin Hart for their assistance during the experimental stage of my research work. I also want to thank my colleagues, Moochul Shin, Nicholas Wierschem, Qiwen Chen and Piyush Chausali for their help.

I have been extremely blessed to have parents, brother and sisters who always had confidence and belief in me. I cannot find words to express appreciation for my parents for their encouragement and guidance throughout my life. Without them I would not be where I am today. My lovely and caring wife Mominah, who accepted the challenges associated with my graduate studies while pursuing her own academic degree. I cannot thank her enough for support and comforting during the difficult times throughout my doctoral studies. I also want to mention my

adorable daughters, who patiently waited and energized me, once I returned home late from my office.

I am grateful to Pakistan Army for initially selecting me for the post-graduate studies and then for financial support during my stay in USA.

Most importantly, I thank Allah for steering my way through out my life.

TABLE OF CONTENT

List of Abbreviations and Symbols

Abbreviations

3S1B	Three Story-One Bay
6S2B	Six Story-Two Bay
AFRP	Aramid Fiber Reinforced Polymer
AI	Arias Intensity
A-D	Acceleration versus Displacement
Au-Cd	Gold Cadmium
B	Strain hardening Ratio
BSE	Back Scatter Electrons
C	Seismic Coefficient factor
CFRP	Carbon Fiber Reinforced Polymer
CMOD	Crack Mouth Opening Displacement
CP	Collapse Prevention
CSM	Capacity Spectrum Method
DC	Damage Control
EPP	Elastically Perfectly Plastic
FRC	Fully Reinforced Composite
FRP	Fiber Reinforced Polymer
FVF	Fiber Volume Fraction
GFRP	Glass Fiber Reinforced Polymer

I	Importance factor
ID	Inter-story Drifts
IDA	Incremental Dynamic Analysis
IDR	Inter-story Drift Ratio
IO	Immediate Occupancy
IRS	Inelastic Response Spectrum
LERS	Linear Elastic Response Spectrum
LS	Limit State
LVDT	Linear Variable Displacement Transducer
MRF	Moment Resisting Frame
NiTi	Nickle-Titanium
OPC	Ordinary Portland Cement
PGA	Peak Ground Acceleration
PRC	Partially Reinforced Composite
RC	Reinforced Concrete
R	Curvature transition parameter
Rft	Reinforcement
R_m	Force Reduction Factor
RT	Room Temperature
SCWB	Strong Column Weak Beam
SMA	Shape Memory Alloy
SE	Secondary Electrons

SEM	Scanning Electron Microscopy
S.F	Scaling Factor
SG	Strain Gauge
SME	Shape Memory Effect
TWSME	Two-Way Shape Memory Effect
V	Base shear
W	Weight of structure

Symbols

A_f	Austenite finish temperature
A_s	Austenite start temperature
a(t)	Acceleration time history
cP	centi-poise
E	Seismic load effect
E_c	Initial modulus of composite
$E_{conc.}$	Initial modulus of concrete
E_f	Initial modulus of glass fiber
E_m	Initial modulus of resin matrix
E_S	Initial modulus of steel
E_{SMA}	Initial modulus of SMA
Fa	Site coefficient
f1	Reduction factor for live load

f'c	Peak compressive strength of concrete
fc	Compressive strength of concrete
fy	Yield stress of steel
fyh	Yield stress of steel hoops
fym	Yield stress of resin matrix
h	Depth of cross section
h_b	Depth of beam
h_c	Depth of column
Hz	Hertz
K	Confinement factor
L	Length of SMA-FRP composite rebar
M_f	Martensite finish temperature
M_s	Martensite start temperature
Mw	Moment magnitude
M-ϕ	Moment-Curvature
pbw	Parts by weight
PF_1	Modal participation factor for 1st mode
Q_E	Effect of horizontal seismic forces
S_1	Mapped spectral acceleration for 1 second period
S_a	Spectral acceleration
S_d	Spectral displacement
S_{DS}	Design spectral response acceleration at short period

S_S	Maximum spectral response acceleration
T	Period of structure
Tg	Glass transition temperature
tr	Total duration of earthquake record
V_m	Volume fraction of resin matrix
V_f	Volume fraction of glass fiber
V_{SMA}	Volume fraction of SMA
σ*	Stress in steel material
σ_{AMf}	Austenite to Martensite finish stress
σ_{AMs}	Austenite to Martensite start stress
σ_{MAf}	Martensite to Austenite finish stress
σ_{MAs}	Martensite to Austenite start stress
α_1	Modal mass coefficient for 1st mode
Δ	Roof displacement
δ_s	Ratio of volume of hoop to volume of concrete core
ε*	Strain in steel material
ε_{cu}	Ultimate compressive strain in concrete
ε_c	Compressive strain in concrete
μ	Ductility
ρ	Reinforcement ratio
ρ_r	Redundancy coefficient

Nomenclature for manufactured specimen

1XW	Resin matrix with EPON-862, EPIKURE-W and Heloxy-48 in 60:38:40 proportions
2XW	Resin matrix with EPON-862, EPIKURE-W and Heloxy-48 in 85:41:15 proportions
1XE	Resin matrix with EPON-862, EPIKURE-3274 and Heloxy-48 in 60:38:40 proportions
2XE	Resin matrix with EPON-862, EPIKURE-3274 and Heloxy-48 in 85:41:15 proportions
1YW	Resin matrix with EPON-828, EPIKURE-W and Heloxy-48 in 60:38:40 proportions
2YW	Resin matrix with EPON-828, EPIKURE-W and Heloxy-48 in 85:41:15 proportions
1YE	Resin matrix with EPON-828, EPIKURE-3274 and Heloxy-48 in 60:38:40 proportions
2YE	Resin matrix with EPON-828, EPIKURE-3274 and Heloxy-48 in 85:41:15 proportions
A1	Single strand GFRP specimen-1

A2	Double strand GFRP specimen-1
B1	Single strand GFRP specimen-2
B2	Double strand GFRP specimen-2
FRC-3	Fully Reinforced Composite with 3 SMA wires
FRC-7	Fully Reinforced Composite with 7 SMA wires
FRC-13	Fully Reinforced Composite with 13 SMA wires
M10	Resin matrix with EPON-862, EPIKURE-3274 and Heloxy-48 in 100:40:5 proportions
M30	Resin matrix with EPON-862, EPIKURE-3274 and Heloxy-48 in 85:41:40 proportions
N10	Resin matrix with EPON-828, EPIKURE-3274 and Heloxy-48 in 100:40:5 proportions
N30	Resin matrix with EPON-828, EPIKURE-3274 and Heloxy-48 in 85:41:40 proportions
PRC-3	Partially Reinforced Composite with 3 SMA wires
PRC-5	Partially Reinforced Composite with 5 SMA wires
U	Resin matrix with EPON-815C and EPIKURE-3274 in 100:40 ratio

S-1 to S-9	Single strand GFRP composite specimen
S-A to S-F	Weighted GFRP composite specimen
SC-1	1st SMA-FRP composite rebar
SC-2	2nd SMA-FRP composite rebar

CHAPTER 1

Introduction

1.1 Problem description

One of the most critical drawbacks in currently used steel reinforcement in reinforced concrete (RC) structures is accumulation of plastic deformation under excessive loads. Under seismic loading, the energy is dissipated through the hysteretic action of material and structure, which results in permanent damage to the steel reinforcement and the structure. The ductility in the structure is thus achieved through permanent plastic deformation. This plasticity in steel leads to residual drifts in RC structures and makes them susceptible to collapse. Excessive steel deformation (beyond yielding) in RC moment resisting frames (MRFs) for example often results in permanent residual drifts, which not only cause overall capacity degradation but also pose safety issues for the occupants even under gravity loads. Thus post-earthquake functionality of ductile RC structures reinforced with steel reinforcement has started to be questioned.

To address the issue of damage accumulation associated with ductility; this research presents a new type of shape memory alloy (SMA)-based composite reinforcement with ability to withstand seismic forces without accumulation of permanent residual drifts. The study investigated the use of shape memory alloy (SMA) fibers as reinforcing material in the composite. Although SMAs have been known for decades, they have not been used much in the building industry until recently (Janke et al. 2005). Like other metals and alloys, SMAs have more than one crystal structure. This is called polymorphism. The prevailing crystal structure or

phase in polycrystalline metals depends both on temperature and external stresses (Callister 2003). Often referred to as smart materials, SMAs have shown highly non-linear behavior in terms of shape memory effect, super-elasticity and martensite damping, which encouraged researchers to study their use in structural seismic applications. Recently, Nehdi et al. (2009) and Saiidi et al. (2007) studied the use of large diameter superelastic SMA bars as reinforcement in plastic hinge zone of concrete beams. However, research results showed that increasing the diameter of the SMA rod, reduces the hysteretic flag shape behavior of the SMA (Saiidi et al. 2007). Thus using small diameter wire would give better hysteretic behavior for the reinforcement, which will be critical for dissipating energy through hysteresis. Moreover, manufacturing large diameter rods is quite expensive, making their use in real applications cost prohibitive. To overcome these problems, the SMA-FRP reinforcing bars studied in this research comprises small diameter superelastic NiTi SMA fibers bonded together using a polymeric resin matrix. The nonlinearity, pseudo-elasticity, and corrosion resistance of SMA-FRP composite makes it ideal replacement to steel and conventional FRP. The proposed SMA-based composite reinforcement has capability to dissipate energy while showing high ductility levels, which was of concern with the use of FRP bars. Also SMA shows pseudo-elastic behavior (also known as superelastic behavior) which allows it to undergo large strains up to 8% and when unloaded, experience negligible residual strain (Naito et al. 2001). In this study, Nickle-Titanium (NiTi) alloy has been used which is the most commercially available alloy. This nonlinear, yet pseudo-elastic behavior of SMA fibers will allow SMA-FRP composite reinforcement to exhibit ductile and energy dissipating behavior with minimal damage to reinforced concrete structure. This is not likely in steel reinforcement which exhibit ductility

through permanent damage to the material and some residual drifts. The proposed SMA-FRP composite reinforcement is sought as a mean to introduce the features of ductility and re-centering to RC structures.

1.2 Research objectives and scope

The following are the two main objectives of this research:

- Establishing and validating manufacturing procedure for the new SMA-FRP composite.
- Studying the seismic behavior of RC MRFs reinforced with proposed SMA-FRP composite bars and comparing it with that of steel and conventional FRP reinforced MRFs.

In order to achieve these objectives, several core issues were first addressed related to; selection of composite constituents (fibers and resin), manufacturing of the SMA based composite, assessment of bond characteristics of the composite at the micro-structural level, design of composite material to achieve desired mechanical properties, evaluating numerically the behavior of the composite on the structural level under sequential seismic events, and finally examining the experimental behavior of small-scale concrete element reinforced with SMA-FRP composite rebars.

An experimental investigation involving exploration of constituents of the proposed SMA-FRP composite reinforcement was first carried out. Selected constituents were mixed in certain proportions followed by curing regimes to fabricate SMA-FRP composite. These manufactured composites were then tested under quasi-static loading to get constitutive material

behavior. Scanning electron microscopic (SEM) images were utilized to validate the manufacturing technique. The experimental results were utilized to develop numerical material models which were then used in structural level models to assess the performance of RC structures under sequential seismic loading. MRFs reinforced with steel, SMA-FRP and GFRP reinforcement types were designed using force based approach and performance based design criteria. For analysis, both single seismic event with incremental dynamic analysis (IDA) technique and multiple seismic sequential events (main shock-aftershock sequences) were utilized. Focus was drawn to examine the effects of increased displacement demands on the MRF due to multiple seismic sequences. The seismic responses of these MRFs were analytically compared between use of steel, conventional GFRP and SMA-FRP reinforcement types. Performance of these frames in terms of IDR and residual displacement were then analytically compared along with other seismic responses. Efficacy of the SMA-FRP composite reinforcement was further explored by manufacturing square rebars to be embedded in concrete T-beam. Ductility, re-centering and crack closing capabilities of SMA-FRP composite were explored.

1.3 Dissertation Outline

This Ph.D. dissertation is divided into the following chapters:

1.3.1 Chapter 2 : Literature Review

This chapter will discuss the performance of reinforced concrete structures during recent earthquakes. Trend towards replacing steel material with fiber reinforced polymer due to

corrosion issue is highlighted. Limitation of both steel and fiber reinforced polymer as reinforcing material is discussed.

1.3.2 Chapter 3 : New Composite Reinforcement

The concept of using shape memory alloys (SMA) composite as reinforcement is introduced with its advantages over other reinforcing materials in seismic applications. A brief overview of shape memory alloys (SMA) is further presented and some mechanical properties are highlighted. Background on SMA composites is introduced along with their applications in other fields.

1.3.3 Chapter 4: Exploration and Manufacturing of Composite Material

Introduction to SMA-FRP composite manufacturing process is presented. Equipment setup and mechanical parameters related to manufacturing process are discussed. Constituents for SMA based composite are selected based on desired properties and their fabrication technique is established.

1.3.4 Chapter 5: Experimental Material Testing

This chapter provides an overview of testing conducted for various coupon specimens. Testing equipment and its setup are explained. Mechanical training of SMA wires followed by uniaxial testing of composite is investigated.

1.3.5 Chapter 6 : Numerical Modeling Technique

A description of constitutive material properties and its modeling along with modeling approach has been done. Comparison with experimental results is conducted to validate the material models. These models are then incorporated in 2D frame elements to perform the inelastic analyses on the moment resisting frame (MRF) structures.

1.3.6 Chapter 7 : Force Based Design and Seismic Analysis

Prototype reinforced concrete moment resisting frames reinforced with steel, SMA-FRP and GFRP reinforcement are first designed and then analyzed under suite of ground motion. Inter story drift ratio and other response parameters are evaluated and comparison is drawn between different reinforcement types.

1.3.7 Chapter 8 : Performance Based Design and Sequential Seismic Analysis

Three story one bay reinforced concrete moment resisting frame is first designed based on modern performance based criterions. The designed frames are reinforced with steel, SMA-FRP and GFRP reinforcement and are subjected to main and aftershock sequence. Response of all designed frames is analyzed under multiplicity seismic events.

1.3.8 Chapter 9 : Small Scale RC Beam with SMA-FRP Composite Reinforcement

Small scale T-beam reinforced with proposed SMA-FRP composite reinforcement is designed and then tested cyclically under 3-point bending test. Test results are evaluated based on crack closing and accumulation of residual displacements.

1.3.9 Chapter 10 : Summary, Conclusions and Recommendations

Results from manufacturing of SMA-FRP composite, testing and numerical modeling are summarized and conclusions are drawn. Based on results and conclusions, future work is suggested.

1.3.10 Chapter 11: References

List of all the references used for this research and dissertation is provided.

CHAPTER 2

Literature Review

2.1 Seismic performance of RC structures

Earthquakes continue to expose deficiencies in today's infrastructure and call for engineers to continue to explore new ways to create resilient structures. The 1994 Northridge earthquake exposed numerous vulnerabilities in the moment resisting structures and columns in bridges. Many of the structural failures that occurred during past earthquakes were due to the collapse of one or more of the reinforced concrete (RC) columns or piers. Many previous earthquakes have highlighted the problems in old structural seismic design provisions, which were developed based on the elastic seismic design concept. Research studies have shown that the main factors causing the failures of RC members are their insufficient flexural ductility and/or inadequate shear capacity (Chai et al. 1991; Priestley et al. 1994). Yielding and rupture of reinforcement in the plastic hinge region of the columns and beams has been identified as the main reasons for the poor flexural ductility observed in many of the collapsed structures (Priestley et al., 1994). Many structures also experience collapse due to poor construction and material quality. Collapse of the high-rise Margala Towers in Islamabad (See Figure 2-1), located within 80 km from the epicenter during Kashmir 2005 earthquake, was an example of collapse of a structure due to poor construction and material quality.

Figure 2-1: Collapsed RC building during Kashmir 2005 earthquake
(http://www.geolocation.ws)

Post-earthquake evaluations of many major earthquakes around the world have shown numerous deficiencies that have been found in structural systems. Some of the deficiencies exhibited by the structures include, but not limited to non-ductile behavior, yielding of reinforcement, cracking and crushing of confined concrete, material imperfections, material degradation over time etc. Earthquake damage to reinforced concrete and masonry structures as shown in figure 2-2, has motivated research related to novel structural designs and material exploration that exhibit more robust performance under seismic loads.

Figure 2-2: Collapse of reinforced concrete moment resisting frames in Muzaffarabad, Pakistan. (Ahsan and Saif 2008)

2.2 Investigation of fiber reinforced polymers as reinforcement

Fiber-reinforced polymers (FRPs) are composite materials that have been used in several engineering applications such as aero-space, auto-mobile industry, and construction industry. Fiber Reinforced Polymers (FRPs) are now increasingly gaining popularity in the field of civil engineering. Common applications for FRPs in civil engineering range from retrofitting structures with patches and wraps to structures made entirely with FRP members. Another increasingly common application is internal FRP reinforcing bars for concrete structures. FRP bars for this application consist of a polymer matrix material, typically epoxy, polyester, or vinylester, reinforced with conventional fibers. Various different conventional fibers have been used in FRP bars, including E-glass, S-Glass, carbon, and aramid. Table 2-1 lists some of the

typical mechanical properties of these conventional fibers. As one can see from this table, the reinforcing fibers have a wide range of modulus of elasticity and rupture strains; however, all these conventional fibers are similar in that their stress-strain behavior is linear elastic until rupture.

Table 2-1: Properties of conventional FRP (Bank 2006)

Fiber Type	Modulus of Elasticty (GPa)	Ultimate Strength (MPa)	Ultimate Strain (mm/mm)
E-Glass	68.9	1378	0.020
S-Glass	86.2	2586	0.030
Arimid	124.1	3723	0.030
Low Modulus Carbon	230.0	3790	0.016
High Modulus Carbon	370.0	3520	0.010

Pictures of rebars manufactured with the pultrusion process are seen in figure 2-3. The surface deformations and roughness seen on some of the rebars shown in this figure are designed to increase the bond between the rebar and concrete (Katz 1999).

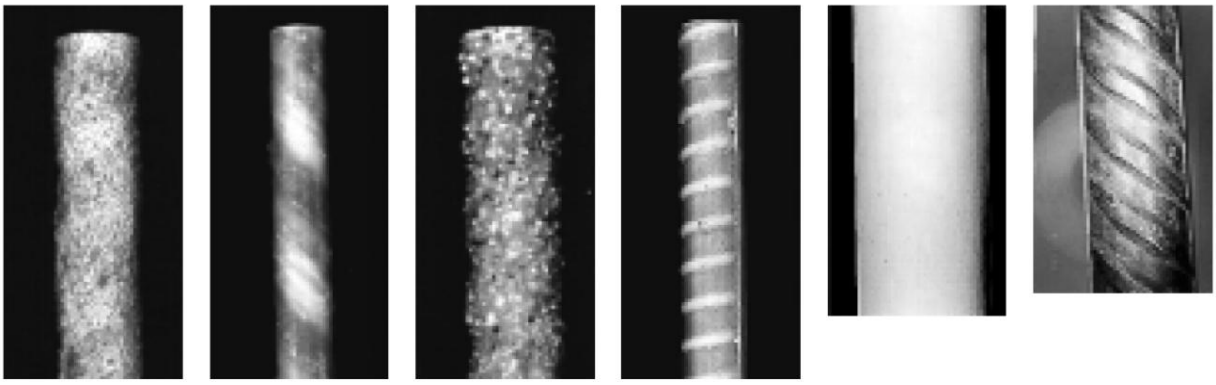

Figure 2-3: Manufactured FRP rebars through pultrusion process (Katz 1999)

When compared to traditional steel rebar, FRP rebars have numerous advantages. Some of the most prevalent of these advantages include high strength-to-weight ratio, magnetic invisibility, and high corrosion resistance (Bank 2006). Interest in exploiting the advantages of FRP rebar has lead to the implementation of FRP reinforcement in a multitude of different concrete structures, these including, diaphragm walls for tunnel boring (Weber et al. 2006) and slabs of parking structures (Benmokrane et al. 2004). However, today the most common use of FRP reinforcement is in bridge decks (Bank et al. 2006; Bradberry 2001). One reason for the relative popularity of FRP reinforcement of bridge decks is extreme environmental conditions some bridges are subjected to. Because of the environmental challenges, these bridges stand to benefit more from the corrosion resistance provided by the FRP reinforcement.

2.3 Limitations of current reinforcement techniques

As mentioned before, steel which has been used as reinforcement since last century in almost all reinforced concrete structures is prone to yielding which causes permanent damage to the structure. The most critical drawback in currently used steel reinforcement in reinforced concrete (RC) structures is susceptibility to accumulation of plastic deformation under seismic loading. Many concrete structures due to damaged (yielded) steel reinforcement have under gone costly repairs and replacements, which can result in huge repair cost. Because of these repairs the overall life cycle cost of the structure increase by many folds. Steel reinforced structure dissipates energy through the hysteretic action of material and structure during an earthquake event. This hysteretic action results in permanent damage to the steel reinforcement and the structure. Yielding of steel and development of cracks in concrete will cause permanent drift in

the structure, which is residual even after the seismic event has finished. The ductility in the structure is thus achieved through permanent plastic deformation. The damaged steel reinforced structure is now prone to any aftershock that may result after the main earthquake event. In several of the past earthquakes, aftershocks have caused failure of many structures which were damaged during the main seismic event. Civil engineering structures, like bridges and buildings are equally prone and vulnerable to such aftershocks due to yielding and permanent damage to steel reinforcement.

Similarly, FRP reinforcement has not yet been used in structures with the aim of mitigating their dynamic response under service or extreme dynamic loads such as vibration control or seismic design applications, respectively (Harris et al. 1998). The failure of FRP reinforcement to gain acceptance in such type of applications is attributed to their linear elastic behavior, which limits their ability to provide concrete structures with sufficient ductility or energy dissipation capability (Benmokrane et al. 1995). An example of this is found in a study that compared the behavior of FRP and steel reinforced beam-column joint sub-assemblages (Said and Nehdi 2004). In this study, beam-column joint sub-assemblages reinforced steel and FRP were subjected to a cyclic beam-column tip displacement loading. The resulting load deformation results from the steel reinforced and FRP reinforced specimens are found in Figure 2-4.

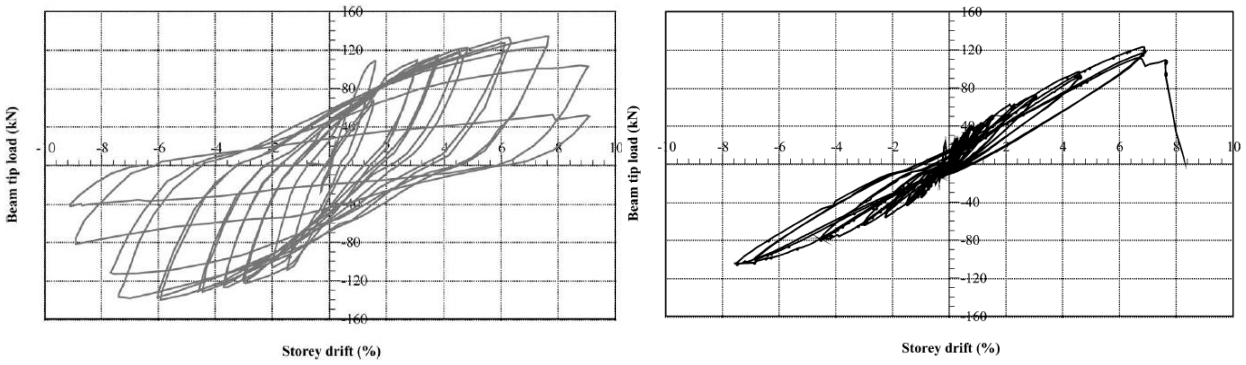

(a) (b)

Figure 2-4**:** Load-deformation results from a test of a beam-column joint specimen subjected to cyclic beam tip deflection (a) steel reinforced (b) FRP reinforced (Said and Nehdi 2004)

As discussed above, this figure shows that the FPR reinforced joint did not show the ductility or energy dissipation, denoted by wide hysteretic loops, that was seen in the steel reinforced specimen. This study suggested that the reason for this smaller hysteresis is the non-ductile nature of the FRP reinforcement.

Several researchers, (Harris et al. 1998; Somboonsong et al. 1998; Pastore et al. 1999), have attempted to address this concern by developing a ductile reinforcing material known as hybrid FRPs. The shortcoming of this reinforcement material is that the ductility is achieved through permanent damage to the reinforcement. Although a different damage mechanism is used, this is still similar to steel reinforcement, which achieves ductility also through permanent plastic deformations.

2.4 Trend towards use of composite reinforcement

2.4.1 Introduction

Composite materials are the most adaptive engineering material and are referred to as a combination of two or more distinct materials into one engineering material. History has shown that the more capable the material is, the greater the scope for ground breaking engineering achievement. This is true for all disciplines of engineering, especially civil engineering in which the structural performance is primarily dictated by material performance like steel and concrete. In the early 19^{th} century, steel played a remarkable role in developing understanding about building structures. However in 1960's this dominance was overshadowed by concrete which itself is a composite. Although natural composites, like wood is still being used in construction industry, man-made composites and smart materials which have mind boggling capabilities, open new and exciting possibilities / opportunities for civil engineering structures. Composites can be broadly categorized as particulate (asphalt and concrete) and fibrous. The latter being the epoxy / elastomeric matrix composite material, which can be embedded with other smart materials to produce even more superior performance material. Figure 2-5 shows evolution of material in mechanical and civil engineering applications.

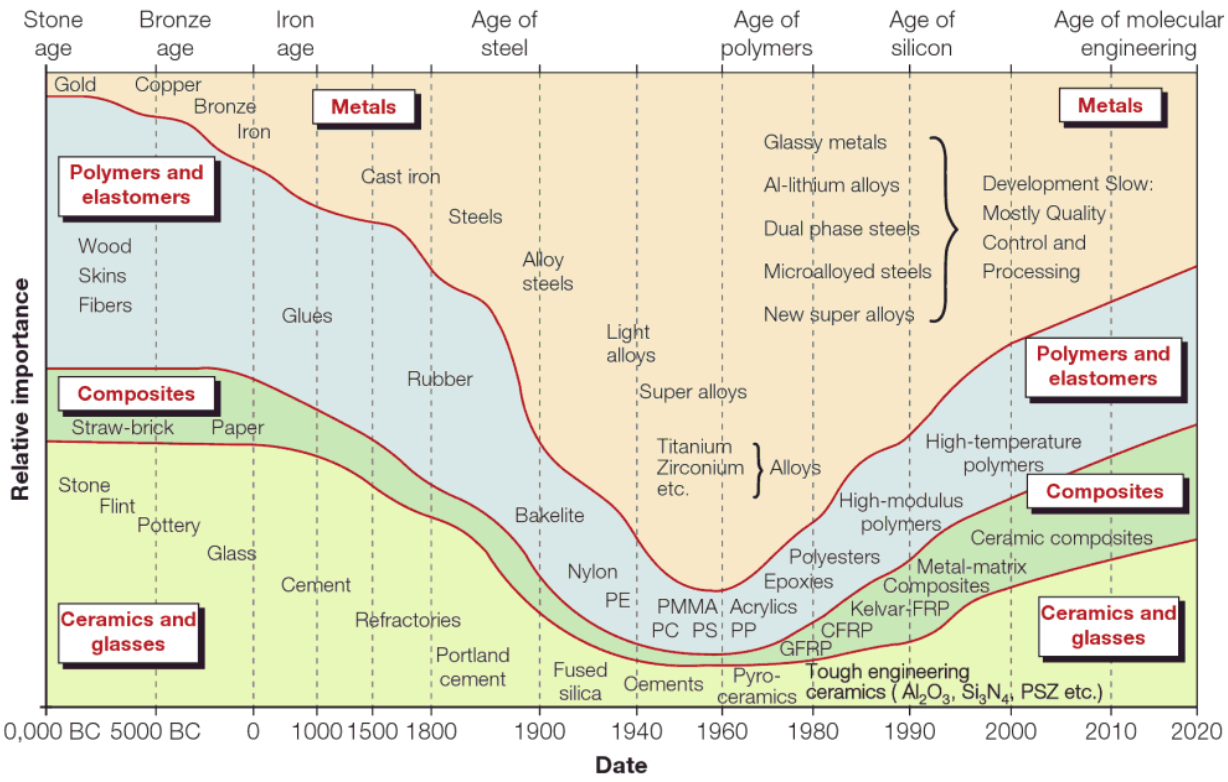

Figure 2-5**:** Evolution of materials used in mechanical and civil engineering applications (Ashby 2011)

As seen from the figure, dependence on metals especially steel is getting reduced at the start of the 21st century. Other materials like FRP composites and polymers are stepping up in terms of importance. This dissertation acknowledges the rise of composite materials to be the future material for all civil engineering structures, while using metal alloys to further enhance the performance.

2.4.2 *Composite concept*

As mentioned before, composite materials are typically made up of host polymer resin matrix and fiber reinforcement. The objective of the matrix is to integrally bind the reinforcement together so as to effectively introduce external loads to the reinforcement and to protect it from adverse effects of surrounding environment. Although, matrix resin is responsible to give shape, surface appearance and overall durability to the composite, the load bearing capability is primarily inherited by fibrous material. Thus most of the structural stiffness and strength of the composite is dictated by the fiber reinforcement.

There are two main type of polymer composites; thermoplastics and thermosets. Vast majority of current composite application utilizes thermoset, which solidify through chemical reaction called cross linking or curing. Thus curing time and temperature are very important for the final properties of a composite which would be later highlighted in Chapter 4. The composite reinforcement could be continuous (endless fibers) and discontinuous (short fibers). Figure 2-6 shows schematics of different reinforcement configurations. Since the reinforcement is the primary load-bearing constituent of a composite, its configuration and degree of orientation is critical to properties of composite. Composite embedded with continuous and aligned fibers give better mechanical properties as compared to randomly oriented and discontinuous fiber reinforced polymer.

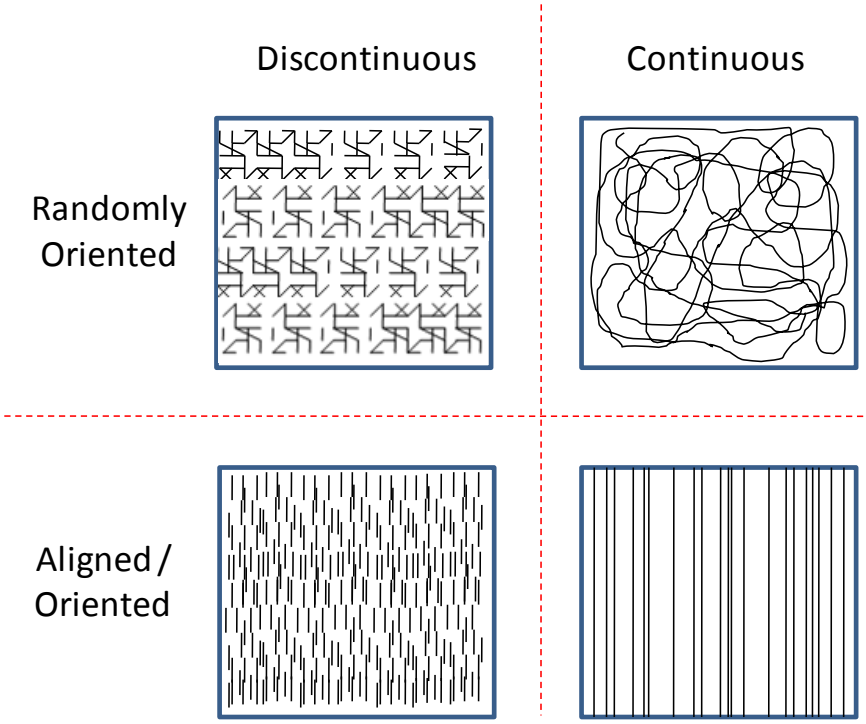

Figure 2-6**:** Schematics of different reinforcement configuration

2.4.3 *Composites in civil engineering applications*

Recently, fiber based polymer composites have been introduced in structural applications due to inherit advantages it offers over its competitor (steel). Some of these advantages like corrosion resistance, high stiffness and strength to weight ratio etc. have made them popular in the construction industry. Although in civil engineering, unlike other fields, for e.g. aerospace and motor manufacturing industry, weight is seldom sought, application of composites especially in bridge related area. As of now, primary application of FRP composites has been in the field of repair and rehabilitation for civil engineering structures, but advancements in terms of its use as primary longitudinal reinforcement is being sought. Figure 2-7 shows classification of composites in civil engineering infrastructures.

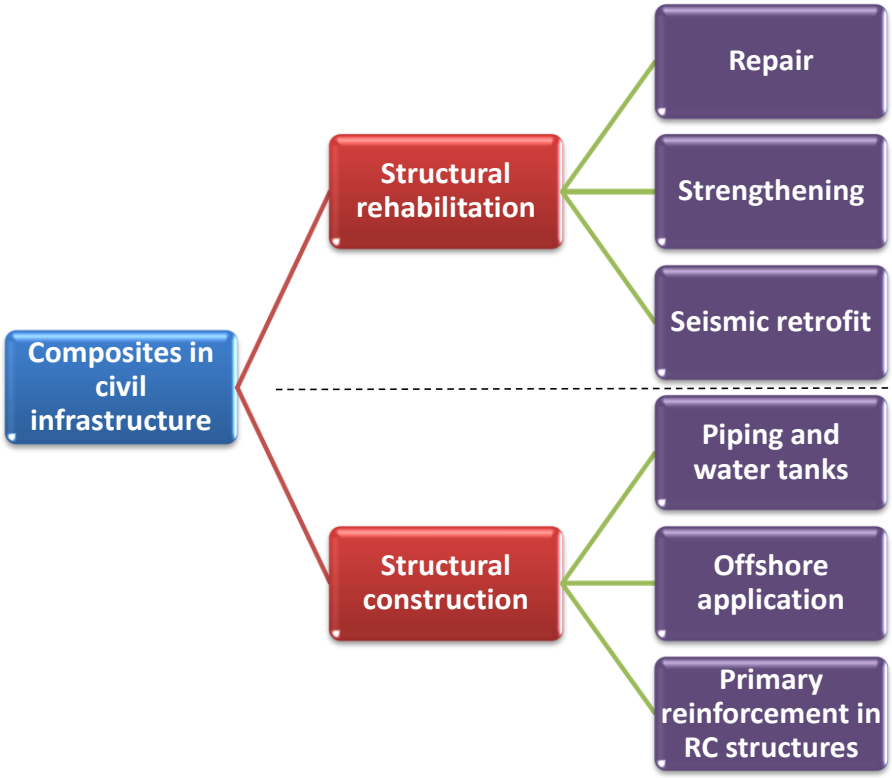

Figure 2-7**:** Classification of composites in civil infrastructures

For reasons explained in section 2.3, FRP composite alone has proved to provide unsatisfactory results in terms of prime player (main reinforcement) in a RC structural member. This dissertation addresses the shortcomings of steel reinforcing bar, in regards to permanent residual deformation and corrosion issues and also addresses shortfalls of FRP rebar, in regards to ductility and energy dissipation, with the introduction of shape memory alloy (SMA) composite referred to as SMA-FRP composite. SMA-FRP is an innovative composite material that consists of a polymer matrix reinforced with small diameter superelastic SMA wires with and without supplementary conventional fiber reinforcement. Accordingly, a thorough review of both SMAs and SMA composites is presented in next chapter.

CHAPTER 3

New Composite Reinforcement

3.1 New concept

A new category of hybrid composite, known as shape memory alloy-FRP (SMA-FRP) is sought in this research as reinforcement for RC structures. As shown in a schematic in figure 3-1(a), a SMA-FRP reinforcing bar comprises polymeric resin reinforced with small diameter superelastic SMA fibers with or without the supplementary conventional reinforcing fibers. The resin matrix acts as binding constituent of the reinforcement, keeping SMA and any supplementary glass fibers bonded together. The concept of using SMA-FRP composite as internal reinforcement in concrete structures was first proposed by Wierschem & Andrawes (2010) who conducted experimental testing on SMA-FRP hybrid coupons to develop numerical models for use at sectional and component levels. Their work showed promising preliminary results in terms of enhancing the damping and ductility of concrete members reinforced with SMA-FRP bars. This dissertation aims at advancing the knowledge in this novel concept through addressing several important issues related to selection of composite constituents (fibers and resin), manufacturing of the new composite, assessing the bond characteristics of the composite on the micro-structural level, designing of composite material to achieve desired mechanical properties, evaluating numerically the behavior of the composite on the structural level under sequential seismic events, and finally examining the experimental behavior of small-scale concrete element reinforced with SMA-FRP composite rebars.

The typical flag shape hysteresis of superelastic SMAs shown in figure 3-1(b) is a direct result of a reversible stress-induced phase transformation between austenite and martensite phases. Because of SMA's unique property of exhibiting re-centering even after experiencing 6-8% strains, makes it attractive choice for developing smart materials. The nonlinear, yet pseudo-elastic behavior typical of SMA fibers (Naito et al. 2001) will allow SMA-FRP composite reinforcement to exhibit hysteretic and ductile behavior with minimal damage to the RC structure. This is not likely in steel reinforcement which exhibit ductility through permanent damage to the steel and concrete which often yields significant residual (permanent) deformations in the structure. Thus, SMA composite reinforcement can both capture the non-corrosive properties typical of FRP reinforcement and at the same time exhibit the ductility similar to steel with negligible residual drifts as achieved in FRP. Thus the preliminary focus of this study was to explore the constituents of SMA-FRP composite and their while exploring their hysteretic behavior under tensile cyclic loading for use in developing numerical models for subsequent seismic analysis. With the aim to investigate the ductile behavior of SMA-FRP composite for large strains, while maintaining pseudo-elastic hysteresis, exploration of resin matrix with high elongation properties was also a unique component of this study.

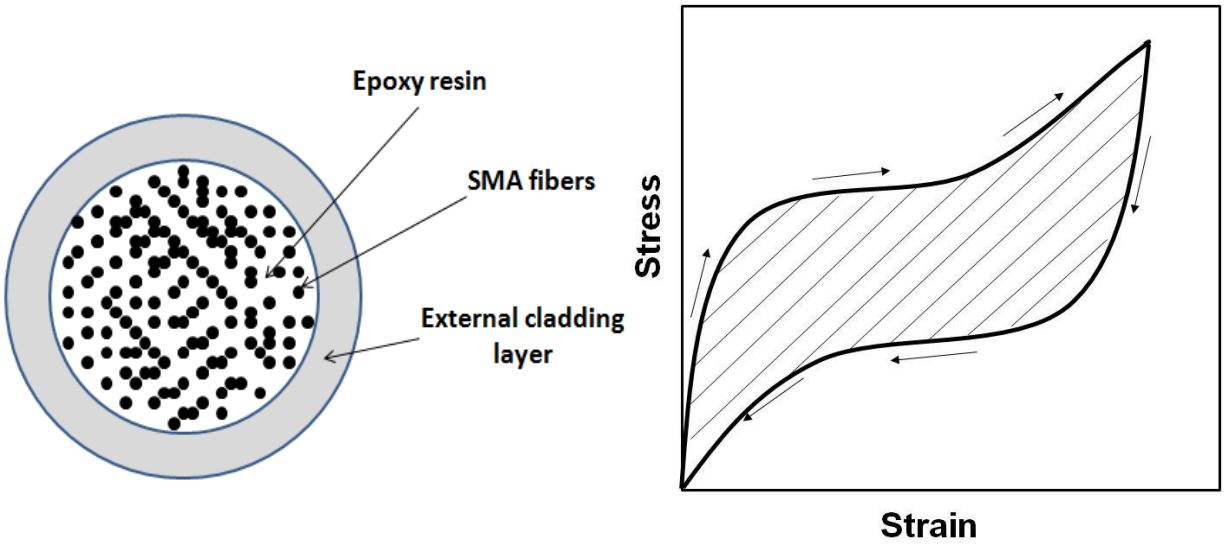

(a) (b)

Figure 3-1: Schematic drawing (a) 100% SMA composite rebar cross-section. (b) Stress-strain hysteresis of superelastic SMA.

Although SMAs have been known for decades, they have not been used much in the building industry until recently (Janke L. et al 2005). The superelasticity and shape memory phenomena typical of SMAs encouraged many researchers to study the application of SMAs in civil structures (e.g. DesRoches et al. 2004, Penar 2005, Nehdi et al. 2009, Shin and Andrawes 2010, among others). Among the researches that are relevant to this present study are the studies by Saiidi et al. (2007) and Nehdi et al. (2009), who investigated the use of SMAs in the plastic hinge zone of a RC beam as shown in figure 3-2. Unlike present study, these researchers used large diameter rods made of NiTi SMAs as reinforcement. The use of large diameter SMA bars reduces the hysteretic area of the SMA (Saiidi et al. 2007) and thus impacts its ability to dissipate energy compared to small diameter wires. This is due to the accumulation of more distorted martensite crystalline structure and inherent deficiencies which exist in larger diameter rods as compared to smaller diameter wires. Moreover, manufacturing large diameter SMA rods is

extremely expensive compared to small diameter wires, which makes use of large SMA bars in real applications cost-prohibitive. Non-availability of SMA rods commercially, is also a concern which restricts use of them in reinforcement application. From technical stand point, the larger the diameter of SMA rods, the more distortion and inconsistency observed at the microstructure level, which impacts the hysteretic behavior of the SMA. To overcome these problems, the SMA-FRP reinforcing bars studied in this research comprises small diameter super-elastic NiTi SMA fibers bonded together using a polymeric resin matrix. The primary focus of the study is to explore the use of SMA-FRP bars as reinforcement in RC moment resisting frame (MRF) structures subjected to earthquakes.

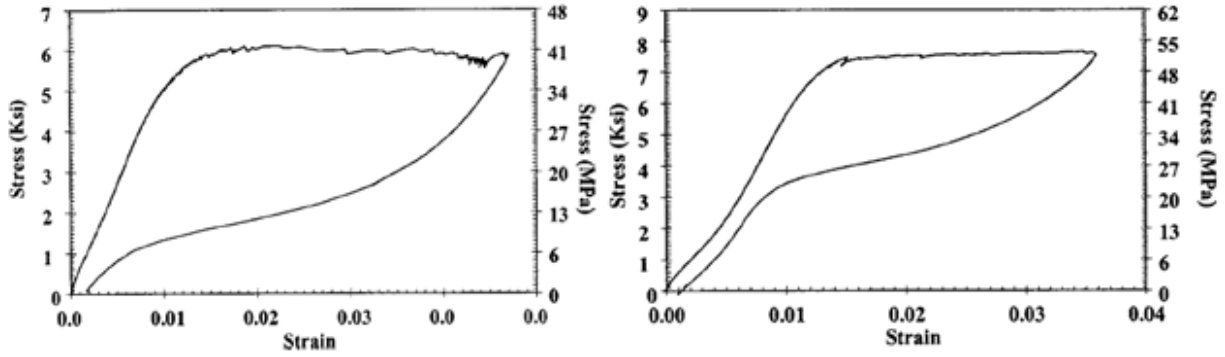

(a) (b)

Figure 3-2: Stress strain curve of SMA NiTi rod. (a) 9.52 mm (b) 12.7 mm. (Saiidi et al. 2007)

3.2 Overview of shape memory alloys (SMAs)

3.2.1 Introduction

Shape memory alloys are a group of metallic alloys which have the ability to undergo large deformations while falling back to their original un-deformed shape through either heating (shape memory effect) or removal of the load (superelastic effect). The ability of specific metallic materials to recover their shape was first discovered in the 1930's by Chang and Reid in Au-Cd alloys. Later further discoveries of the same recovery capabilities were observed in Ni-Ti alloy in 1963 (Otsuka and Wayman 1998). Although shape memory was discovered in the 1930's, it was not until the discovery of shape memory properties in near equiatomic NiTi (also known as Nitinol) by Buehler and Wiley at the Naval Ordnance Laboratory that research into the mechanics and applications of shape memory alloys began (Melton 1990). During the past three decades, several advances have been made in understanding the mechanisms associated with the shape memory and superelastic effects, their thermo-mechanical behavior, and the fabrication and production of SMAs leading to higher quality and more reliable materials at lower costs. These advances have prompted increased interest in the use of the material in a variety of engineering and commercial applications.

Shape memory alloys (SMAs) display two unique qualities, shape memory effect and superelasticity, both of which are related to the material phase of the SMA (Lagoudas 2008). The material phase of the alloy is dependent on temperature; consequently, the temperature of the SMA has a great effect on its mechanical properties. At relatively high temperatures, the alloy is

in an austenite phase while at relatively low temperatures, it is in a martensite phase (Brinson, 1993). The four transformation temperatures that define the SMA's transformation from one phase to the other are M_f , M_s , A_s , and A_f , which are the martensite finish temperature, martensite start temperature, austenite start temperature, and the austenite finish temperature, respectively. The relationship between these transformation temperatures can be seen in Figure 3-3. If a 100% martensite SMA was heated it would begin martensite to austenite phase transformation when the alloy reaches A_s and finish transformation to 100% austenite when the alloy reaches A_f. Additionally, if the alloy is cooled, reversed transformation would start at M_s and the transformation back to 100% martensite would be completed when the alloy reaches M_f. In addition to temperature induced phase changes, SMAs can undergo phase change due to changes in mechanical stress. For example, an increase in mechanical stress in an austenite SMA can lead to a phase change to martensite. Figure 3-2 also shows the generalized mechanical stress relationship for SMAs. In this figure, are the martensite to austenite finish stress, martensite to austenite start stress, austenite to martensite start stress, and the austenite to martensite finish stress. As one can see from this figure, these stresses are dependent on the temperature of the SMA.

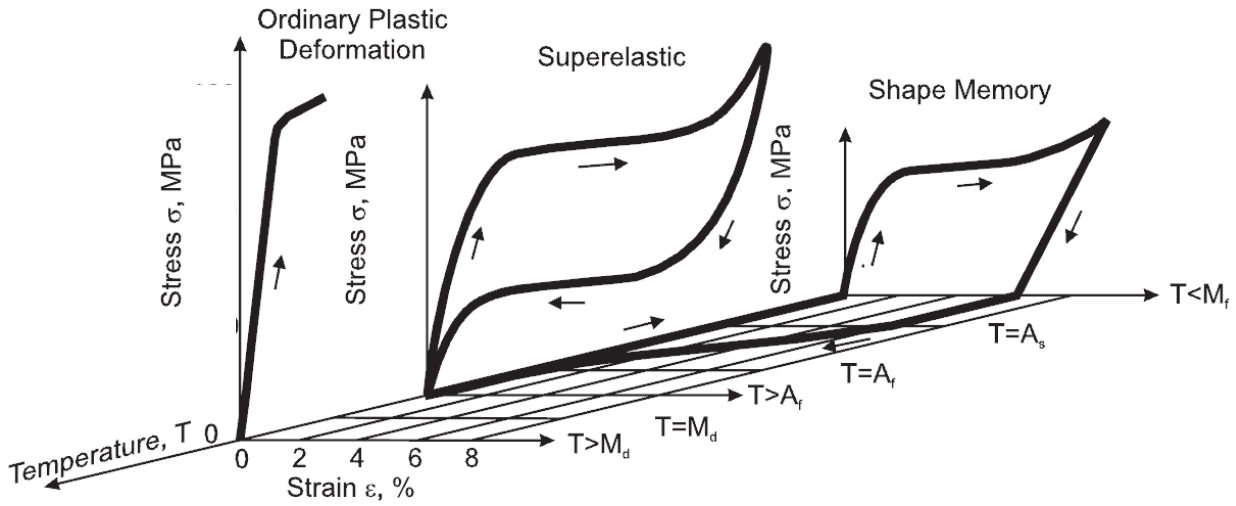

Figure 3-3: 3D stress-strain-temperature relationship for the mechanical behavior of SMA (DesRoches et al. 2004)

3.2.2 Basic microstructure of SMA

The crystalline structure of a material, in part, dictates the materials overall behavior. For this reason, it is important to have a basic understanding of the microscopic aspects of SMAs. Many authors (Perkins 1981, Otsuka and Shimizu 1986, Wayman and Duerig 1990, Otsuka and Wayman 1998) have provided detailed information on the crystallography of SMAs since their discovery. SMAs can typically be found in one of two stable phases, martensitic or austenitic. The parent phase, austenite occurs at high temperatures and its crystal structure has high order of symmetry. For NiTi (SMA used in this study), the crystal structure of the austenite phase is 'Body Centered Cubic', which means the phase is hard and rigid (Wayman and Duerig 1990). Conversely, the martensitic phase is stable, at low temperatures and under high stresses and has low symmetry crystal structure (NiTi has a monoclinic crystal structure). Martensitic phase is stable in either a multi-variant twinned form or a single variant detwinned form where the multi-

variants represent a change in the orientation of the crystalline structure. A three-dimensional atomic structure of the martensitic and austenitic phases can be seen in figure 3-4.

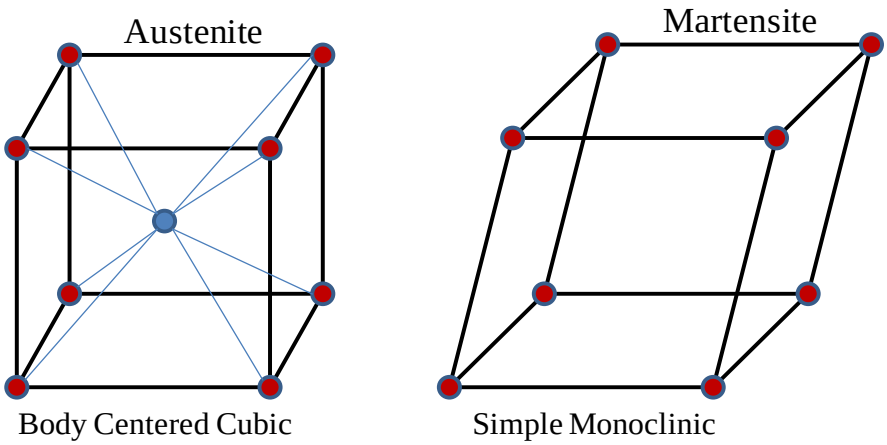

Figure 3-4: Body centered cubic and monoclinic lattice structure of Austenite and Martensite, respectively.

The unique ability of SMAs to recover their shape is in part due to the arranged crystalline structure between the austenitic and martensitic phases. The ordering of the atoms in the martensitic phase and austenitic phase does not change. This constant ordering allows the material to undergo a martensitic phase transformation either through a temperature change or the application of stress. This process consists only of a shape change (no volume change) with no permanent slip allowing the shape change to be reversible. This unique ability allows SMA to be able to undergo large deformations while returning to their original undeformed shape (Wayman and Duerig 1990). Schematic of this transformation is shown in figure 3-5.

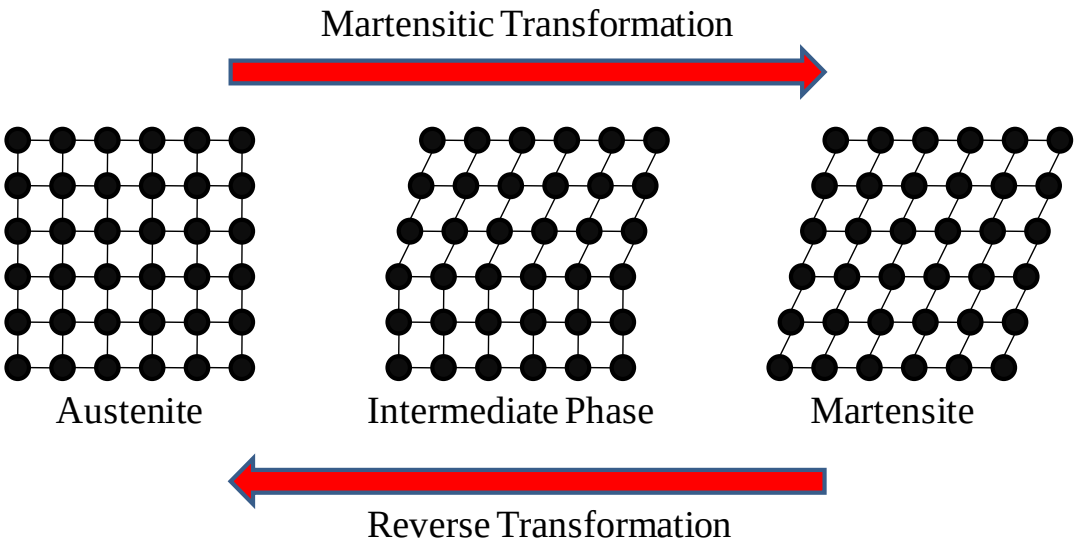

Figure 3-5: Schematic view of typical SMA microstructure.

There are two possible phases of martensite: a) twinned martensite and b) deformed or detwinned martensite. Since austenite is more symmetrical than martensite (Figure 3-3), the two different martensite phases are formed after the martensitic transformation. The two different shapes of martensite are depicted in figure 3-6.

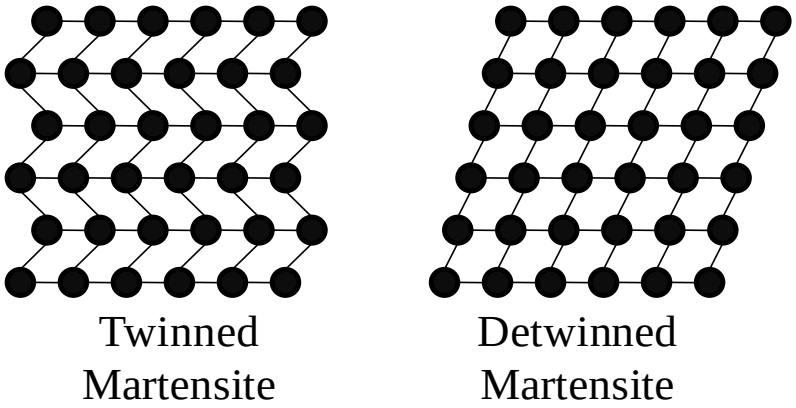

Figure 3-6: Twinned and detwinned martensite SMA.

3.2.3 Transformation temperatures of SMA

Like many other alloys and metals, SMAs also exhibit polymorphism, i.e. it possesses more than one crystal structure having the same chemical composition. The predominant crystal phase in a polycrystalline metal depends on both stress and temperature and is controlled by both chemical composition and thermomechanical processing (Dolce and Cardone 2001). At a relatively low temperature, SMA exists in the martensite phase. When heated, it undergoes a transformation to the austenite phase (crystalline change). In the stress-free state, SMA is characterized by four distinct transformation temperatures as shown in figure 3-7.

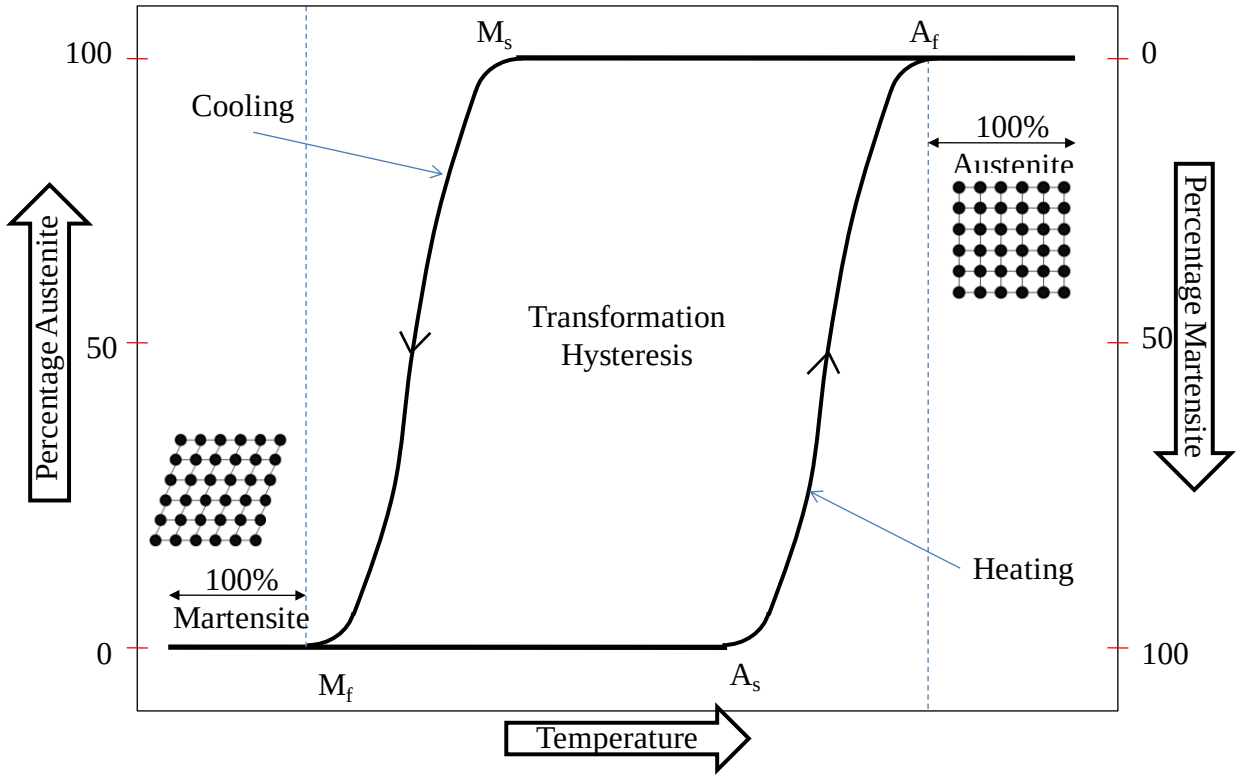

Figure 3-7: Phase transformation of SMA crystalline from martensite to austenite and vice versa as a function of temperature.

The martensite start temperature, M_s, martensite finish temperature, M_f, austenite start temperature, A_s, and austenite finish temperature, A_f, define the temperatures at which the phase transformations occur and result in hysteretic behavior during cooling and heating. SMA exists in a fully martensite state when its temperature T is less than M_f, and in a fully austenite state when T is greater than A_f. During the phase change from martensite to austenite and vice versa, both martensite and austenite phases coexist. When the material is heated to A_s, the phase of the material starts to change gradually from martensite to austenite. At a temperature of A_f, this transformation is complete. Cooling the material will result in a phase change from 100% austenite at a temperature greater than M_s to 100% martensite when temperature M_f is reached. If the temperature in the austenite phase increases above A_f, the superelasticity is lost.

3.2.4 Mechanical properties of SMA

Each SMA differs considerably in its mechanical properties with respect to each other. Such properties vary over a wider range, not only due to variation in chemical composition, but also due to the atomic arrangement in the martensite and austenite phase of the SMA that depends on the thermo-mechanical processing and heat treatment. Even a slight change in the relative proportion of the constitutive metals within the same alloy may significantly affect its mechanical properties (Strnadel et al. 1995). Various SMAs in the form of wires and bars with different diameters have been tested by a number of researchers under tensile and compressive forces. Because of the common availability and use, Nitinol (NiTi) was the prime focus of this research as part of exploring SMA alloy composite. A typical stress-strain curve of SMA (austenite or martensite) under tensile and compressive forces is presented in Figure 3-8. Liu et

al. (1998) tested NiTi SMA specimens under both tensile and compressive forces. In their test the length to diameter ratio was reduced in the case of specimens tested under compression compared to those in tension in order to avoid buckling.

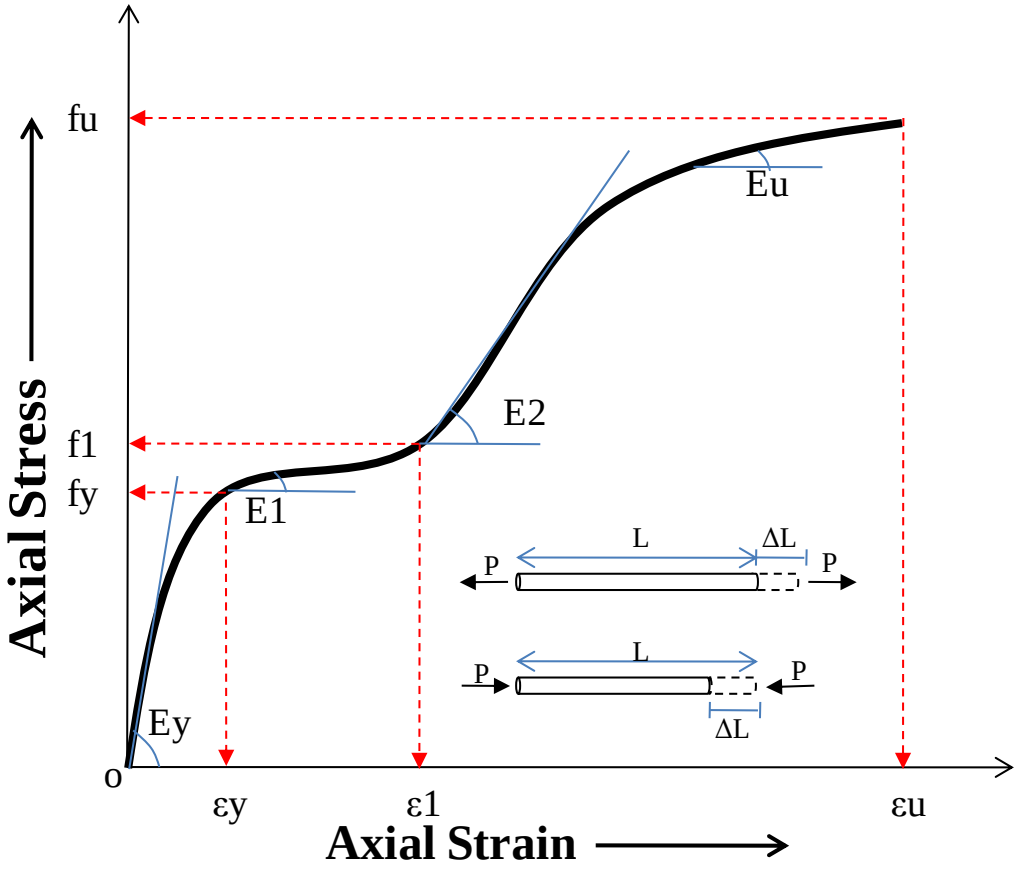

Figure 3-8: Typical stress-strain curve of SMA under tension and compression

NiTi SMA behaves elastically in the beginning with a modulus of elasticity E_y until it reaches the yield stress f_y (typically referred as forward transformation stress). As it crosses f_y, there is a significant reduction in stiffness, where the modulus of elasticity, E_1 reduces to about 3% to 8% of E_y. Such stiffness is maintained up to a stress of f_1 and strain of ε_1. As soon as it passes ε_1, the specimen becomes stiffer and its modulus of elasticity E_2 reaches about 50% to

60% of E_y. After reaching another plateau with a modulus of elasticity E_u (5% to 8% of E_y) the specimen fails with the ultimate stress, f_u at a strain of ε_u. The findings of some previous research / tests are summarized below in Table 3-1.

Table 3-1: Mechanical properties of steel and NiTi alloy

Property	**Unit**	**Steel**	**NiTi (Tension)**		**NiTi (Compression)**	
			Austenite	**Martensite**	**Austenite**	**Martensite**
Young' s modulus	GPa	200	30-83	21-41	56-69	20-80
Yield Strength	MPa	248-517	195-690	70-140	550-800	125-190
Ultimate strength	MPa	448-827	895-1900	800-2000	1500	1800-2120
Elongation at failure	%	20	15 to 20	15 to 20	-	17 to 24
Recoverable strain	%	0.2	6 to 8		3 to 6	
Density	g/cm^3	7.85	6.45	6.45	6.45	6.45
Reference			DesRoches et al. (2004), Janke et al. (2005)		Liu et al. (1998), Lim & McDowell (1999)	

3.2.5 Unique properties of SMA

As mentioned before, there are two mechanisms by which the deformation of SMAs can be recovered, the shape memory effect (SME) and the superelastic effect.

3.2.5.1 Shape memory effect

The shape memory effect occurs when the alloy is in the martensite phase. Upon loading, the twinned martensite undergoes typical elastic deformation until the “yield” stress / forward transformation stress is reached at which point twin boundary movement occurs and detwinning initiates. After the completion of the phase transformation, further elastic deformation of the

detwinned martensite occurs. Upon unloading, there remains residual strain which is recovered by heating the material above A_f causing a phase change to the high temperature austenite phase. This phenomenon is known as shape memory effect (SME) and can be used to recover strains up to 8%. Upon cooling, the structure returns to the original twinned martensite form with little or no residual strain (Wayman and Duerig 1990). Figure 3-9 provides the stress-strain curve associated with the shape memory effect.

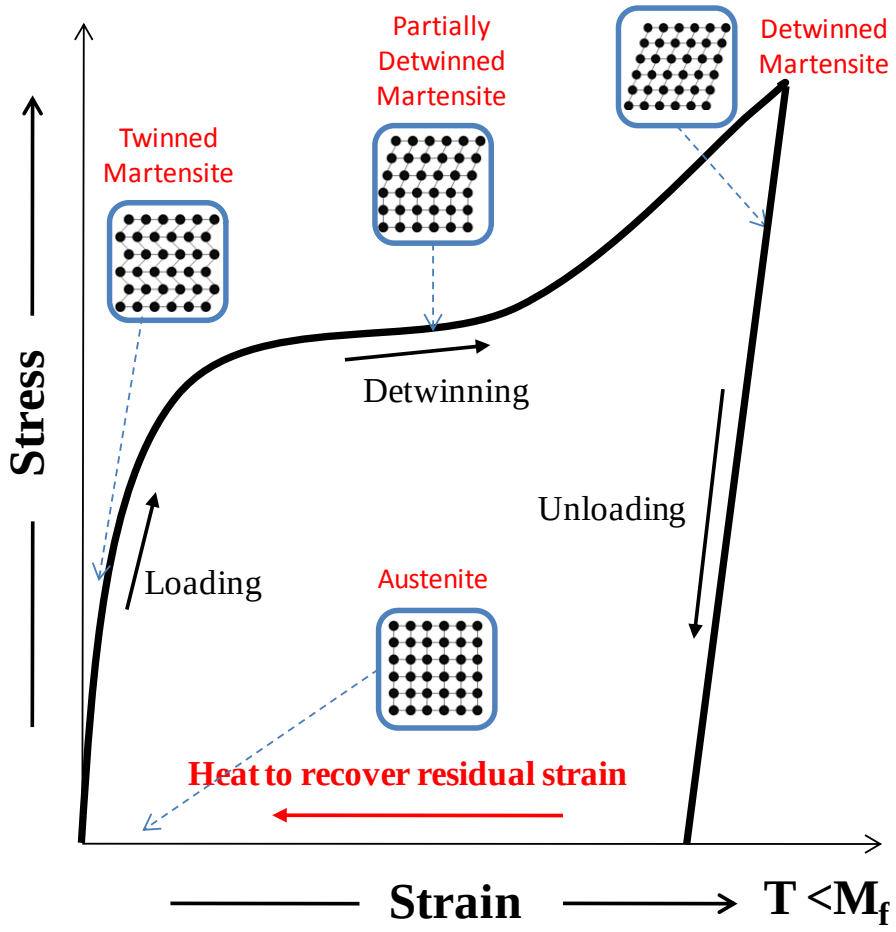

Figure 3-9: Schematics of stress-strain exhibiting shape memory effects of SMA.

3.2.5.2 Superelastic or pseudo-elastic behavior

The second means of shape recovery in SMAs is the superelastic effect. The superelastic effect occurs when SMA is deformed while being in the austenite phase. Upon loading, the austenite undergoes typical elastic deformation until the "phase transformation" stress is reached. At this point, the martensitic phase transformation initiates. Detwinning then occurs along the stress plateau until the NiTi is in its fully detwinned martensite phase. After completion of the phase transformation, further elastic deformation can occur. Upon removal of the load, the detwinned martensite is no longer stable and reverts back to its original austenite phase. The energy driving this reverse transformation is the chemical free energy between the austenite phase and martensite phase (Tadaki et al. 1988). Figure 3-10 provides a schematic of the stress-strain curve associated with the superelastic effect.

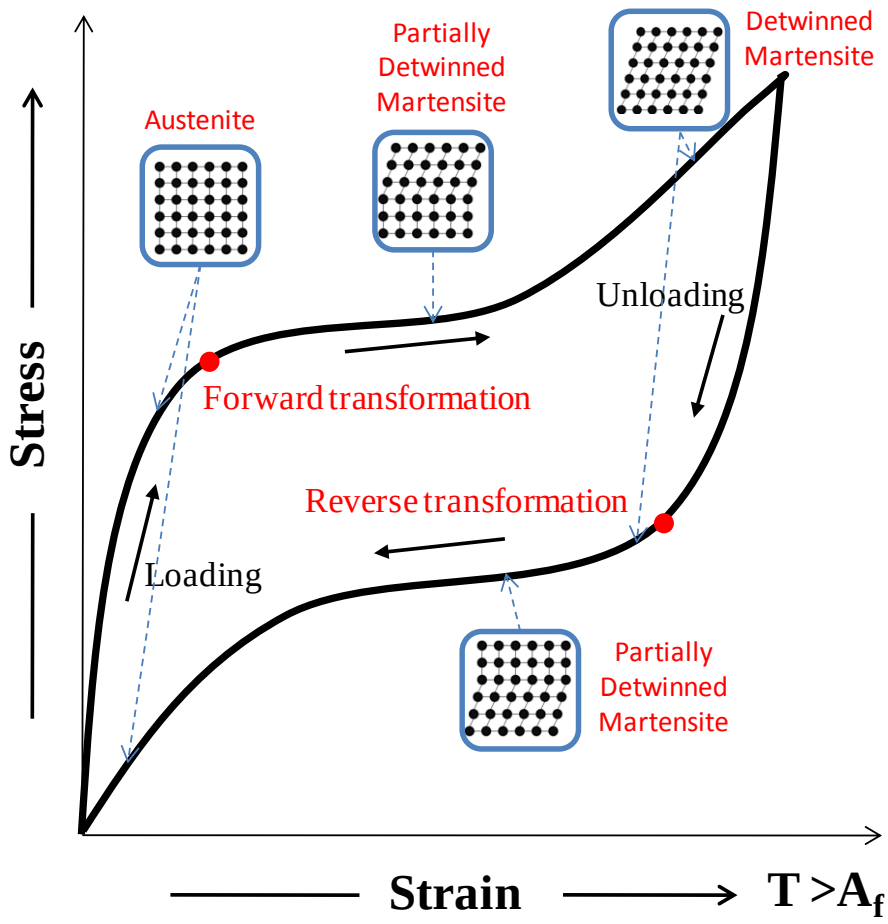

Figure 3-10: Stress-strain hysteresis of superelastic SMA with micro structure.

3.3 Overview of SMA-FRP composite

3.3.1 Introduction

SMA-FRP composite is a heterogeneous material type which is composed of polymeric matrix material reinforced with SMAs with or without supplementary conventional fibers. Figure 3-11 shows a schematic of a typical SMA-FRP composite.

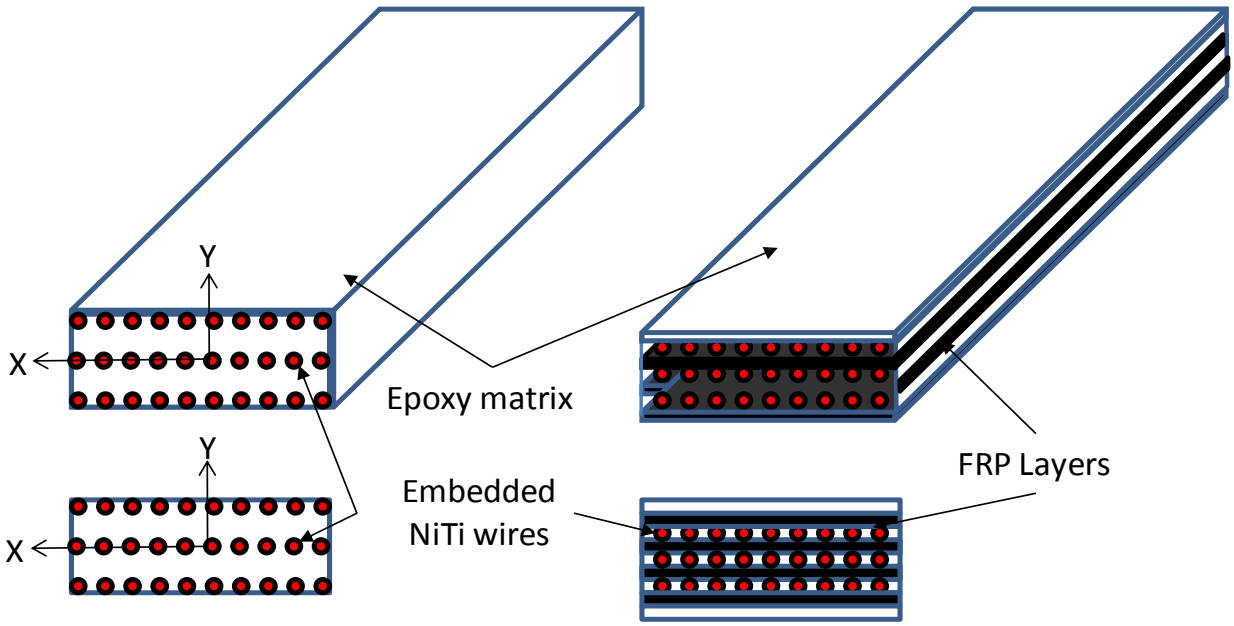

Figure 3-11: Schematics of SMA embedded FRP composite.

The polymer matrix materials that have been studied in previous research of SMA composites include epoxy, polyester, and vinylester. Some of the first research involving SMA composites was performed by Roger and others at Virgina Tech in the late 1980s and early 1990s (Rogers 1990, Rogers et al. 1991, Paine and Rogers 1994). Their research focused mainly on vibration control of a composite with embedded SMA wires. After this initial study, a wide variety of polymer matrix SMA composites have been studied, including a great deal of research on SMA composites that utilize SMA wires. Although wires are most prevalent reinforcement type, SMA ribbons, foils, fibers, and particles have also been studied as composite reinforcement (Jonnalagadda et al. 1998, Wei et al. 1998, Zhang and Ni 2007). There are multiple different reinforcing materials that have been studied to be used as reinforcement with SMAs in composites, most of which are conventional fibers, such as carbon, aramid, and glass fibers. The efficacy of the SMA based composite has been explored by Wierschem and Andrawes (2010)

who conducted basic experimental testing on SMA-FRP coupons and used the results to carry out analysis on the sectional and component levels. Although the percentage of SMA used in the composite was very small, the results showed that SMA-FRP reinforcement has the capability to dissipate energy while exhibiting high ductility, which was of concern with the use of FRP bars.

3.3.2 ***SMA wires based composite***

Some of the early research on SMA composites produced poor results, attributed to poor interfacial bonding of the SMA wires Xu et al. (2002), which is thought to occur because of air voids around SMA wires in the composite. This problem and, specifically, the void content of a SMA composite in relationship to the position of the SMA wires was studied by Hebda et al. (1995). The SMA composite in his study consisted of graphite / epoxy laminates with 0.2mm SMA wires. This composite was vacuum bagged and cured in an autoclave for a total of 5 hours with the maximum temperature of 177°C. Figure 3-12 shows the void content of the SMA composite in relation to the position of the SMA wires. From this figure it can be observed that near the SMA wires, the void content increases dramatically. In this composite the maximum void content near the wires was found to be 31%, while the void content for the whole composite was 7.3%.

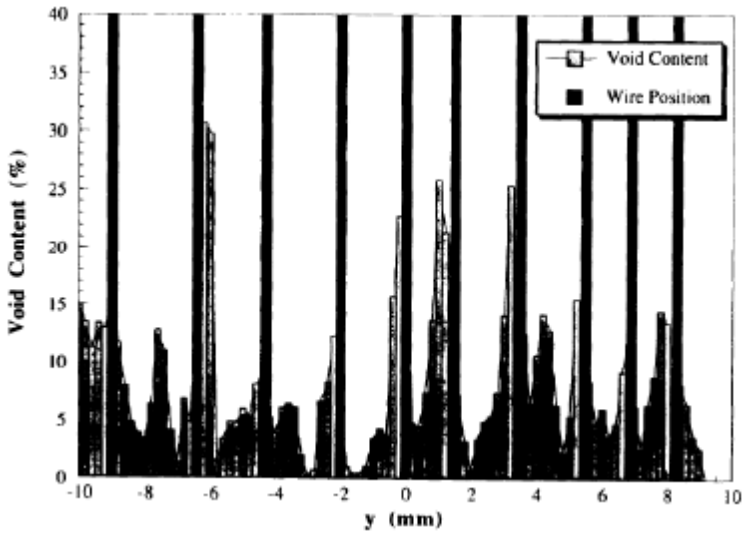

Figure 3-12: Void content of SMA composite relative to SMA wire position. (Hebda et al. 1995)

Other studies including one from Xu et al. (2002) investigated use of small diameter SMA wires to improve the interfacial bonding in SMA composites with the study of a composite reinforced with ultrathin, 50 μm diameter, SMA wires and carbon fibers. From this study it was found that the use of ultrathin SMA wires nearly eliminated voids near the SMA wires when conventional reinforcement in the composite ran parallel to the wires and greatly reduced voids when the reinforcement ran perpendicular to them. This is demonstrated in figure 3-13 which shows cross-sections from SMA composites with 50 μm diameter SMA wire reinforcement. In this figure the SMA composite with SMA wires and carbon fibers oriented in the same direction have little visible voids around SMA wires, while in rest of the composite the voids are virtually non-existent.

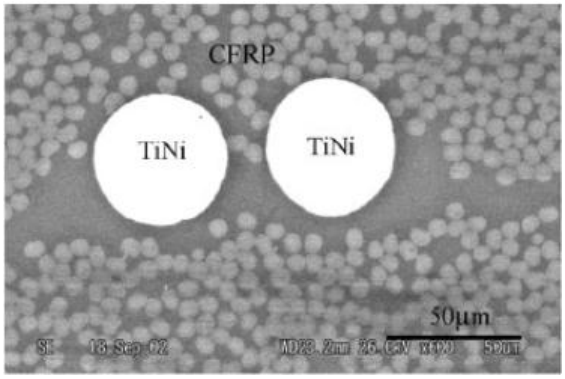

Figure 3-13: SMA-FRP composite cross-section (Xu et al. 2002)

3.3.3 ***SMA particles based composite***

The manufacturing techniques mentioned in last section are applicable for SMA composites with continuous pieces of SMA reinforcement, such as wires, but some SMA composites may utilize many discrete pieces of SMAs depending on application. Zhang and Ni (2007) detailed a process in which they manufactured a SMA composite that consisted of an epoxy matrix reinforced with either small SMA particles (diameter of 425 μm) or short SMA fibers (length of 1.5-2 mm). In this process the SMA reinforcing material combined with the epoxy resin and vacuum dried for 20 minutes. After drying, the mixture was then poured into molds and cured at room temperature for 24 hours. Finally, the composite was heated to 140°C over a period of 10 hours and the SMA composite layer was bonded to a bulk epoxy layer. The SMA content of the specimens varied from 1% to 27%, by weight. Figure 3-14 shows some of the small particle and short fiber SMA composites manufactured with this process.

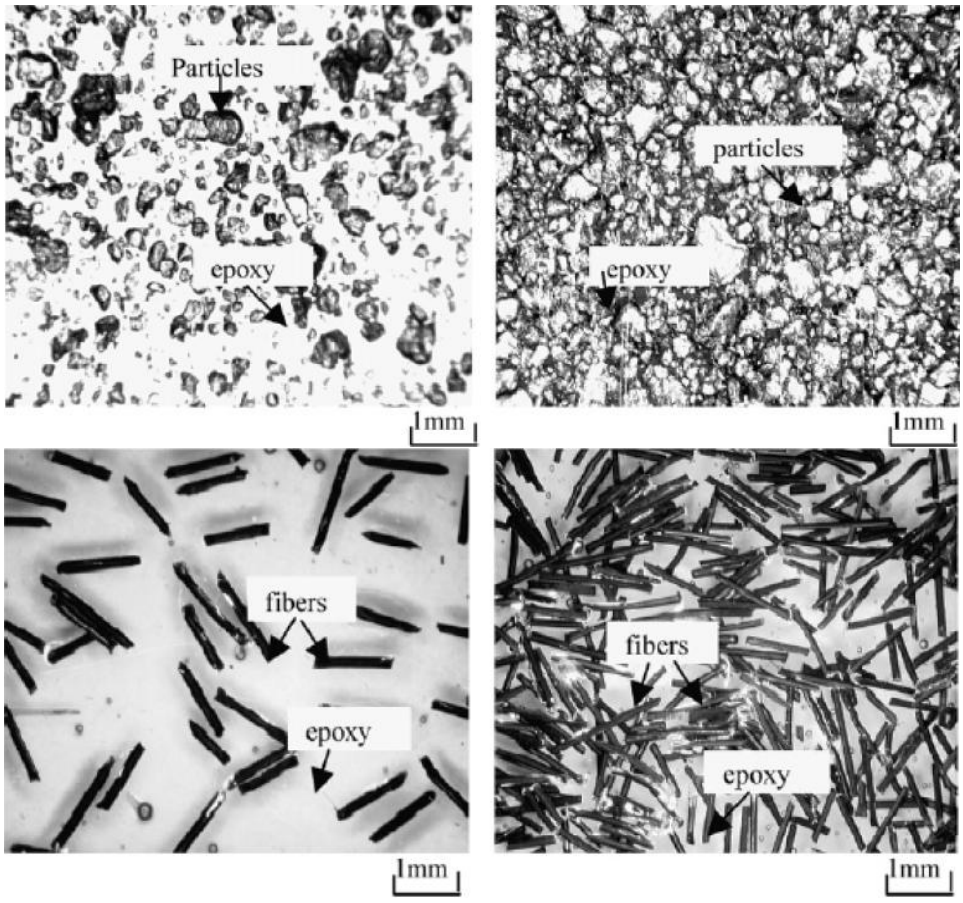

Figure 3-14: Use of SMA fibers and particles in composites matrix (Zhang and Ni. 2007)

3.3.4 ***SMA composite applications in other fields***

3.3.4.1 Impact damage resistance

Many researches, including Tsoi et al. (2002) and Pappada et al. (2008) have studied the effects of extreme loading on SMA composites. Their study focused on embedment of SMA wires along with FRP in the composite with better performance for mitigating the effect of an impact. Paine and Rodgers (1994) studied the impact damage resistance of SMA composites at both high and low velocities. The composite specimens used in their study were composed of

epoxy and layers of graphite reinforcement each with an outer layer of NiTi SMA wires and epoxy bonded to one face. Comparisons were made to the performance of graphite and epoxy reinforced composites with an outer layer of aluminum wires and epoxy on one face, as well as graphite or fiberglass composites that do not have an additional layer of wire and epoxy. From this study it was found that the energy required for an impact to cause perforation of the SMA composite was increased by up to 95% compared to conventionally reinforced specimens. This increase in energy related to perforation because of use of SMA wires. Similar results were observed under increased speed of the impact.

3.3.4.2 Actuation

The prime mechanical property of SMA to recover its residual strains through SME has transpired researches to investigate ways in utilizing SMA composites to produce actuators. There have been two main ways that have been followed to create SMA composites that actuate, the first is through the use of one-way SME, and the second utilizes two-way SME (TWSME). The reason for this is that the shape memory effect provides only one-way actuation; once the memorized shape is recovered the SMA cannot automatically assume any other shape. SMA composites, however, can be designed to be two-way actuators. One method for enabling an SMA composite to become a two-way actuator, is to design an elastic base matrix material such that its glass transition temperature (*Tg*), is between the SMA transformation temperatures *Ms* and *As*. In this process, the first shape is acquired when the SMA composite is heated up past *Af*. This corresponds to a temperature above, *Tg*; consequently, the epoxy decreases in stiffness and allows the SMA to recover a bent up shape. When cooled, the matrix stiffened in this shape, thus

helping to maintain it. The second shape is acquired when the SMA composite is heated past *Tg* but below *As*. When this occurs the SMA relaxes and the epoxy lets the composite acquire and keep a nearly flat shape when the temperature is lowered. Figure 3-15 shows an example of a two-way SMA composite actuator researched by Sterzla et al. (2003).

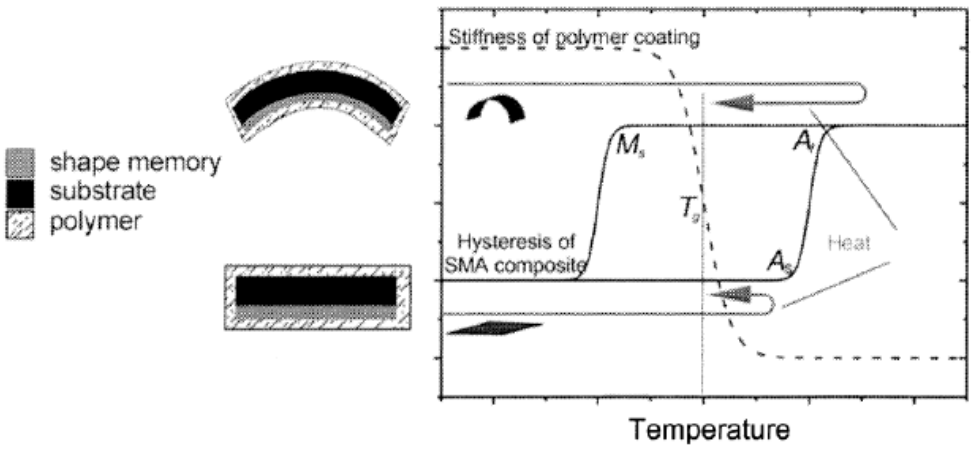

Figure 3-15: Two way actuation of SMA composite (Sterzla et al. 2003)

CHAPTER 4

Exploration and Manufacturing of SMA Composite Material

4.1 Introduction

This chapter focuses on developing an understanding of manufacturing process involved for SMA based composites. It also addresses the selection of right ingredients for a composite to withstand high ductility demand from seismic events. In this research, SMA wires were embedded in epoxy matrix with or without conventional fibers to develop a hybrid composite to overcome the ductility issues. As a preliminary research step, materials were selected and mechanical properties of each constituent of the hybrid composite were evaluated. Manufacturing process of the hybrid SMA composite took a design approach in which certain criteria's were established and then sought after. One of the fundamental criteria was high elongation ability of composite to strains of about 3.5% to 5% range. Stiffness and strength were also identified while achieving primary criteria.

4.2 Material selection and mechanical properties

4.2.1 Resin matrix

4.2.1.1 Epoxy

The host material selected for use in manufacturing of epoxy resin is EPON. EPON which is a liquid epoxy, when properly formulated with hardener and cured, provide an inert end

product acting as matrix for composite with unique combination of properties. Primary use of any resin base is to provide adhesive and bonding capabilities to the reinforcing constituents of the composite. They are also suitable for use in high performance applications such as coatings, adhesives, civil engineering, electronic and electrical insulation, composites and fiber sizing. For this research, three commonly available EPON epoxy {manufacturer: Momentive} namely, EPON 862, EPON 828 and EPON 815C were explored to get the desired mechanical properties. All these epoxy are product from the family of Bisphenol, which when combined with epoxide, gives desired EPON epoxy. Some of the advantages of using EPON are low viscosity, reacts with a full range of epoxy curatives, good balance of mechanical, adhesive, and electrical properties in addition to good chemical resistance. Some of its applications include but not limited to marine coatings, chemical resistant tank linings, floorings, and grouts, fiber reinforced pipes, tanks, composites, tooling, casting, and molding compounds, and use in construction, electrical, and aerospace adhesives.

EPON 828 is an undiluted clear difunctional Bisphenol-A / epichlorohydrin derived liquid epoxy. When cross-linked or hardened with appropriate curing agents, very good mechanical, adhesive, dielectric and chemical resistance properties are obtained. EPON 815C is a low viscosity liquid Bisphenol-A based epoxy containing a commercial grade of n-butyl glycidyl ether. It also has low viscosity and allows for easy application in many fields. In order to form EPON 862, an epoxide is combined with Bisphenol F as seen in figure 4-1. Typically the 'R' group in the epoxide is chlorine. Bisphenol F can be in three different forms ortho-ortho,

para-para, and paraortho. Out of these three para-para Bisephenol F molecular structure is shown in figure 4-1.

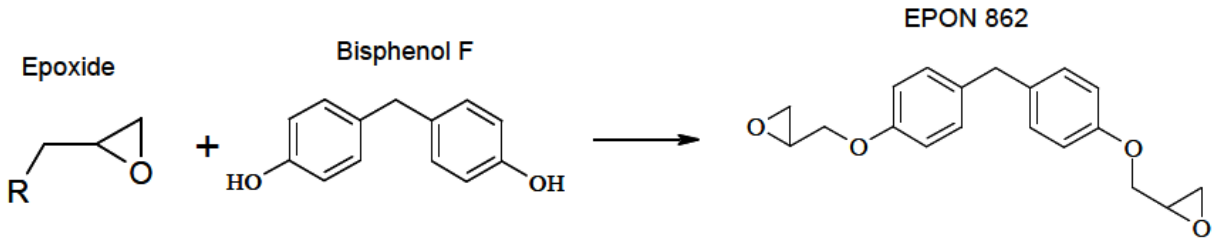

Figure 4-1: Formation of EPON 862 (Tack, 2006)

When EPON 862 is cross-linked with appropriate curing agents, superior mechanical, adhesive, electrical and chemical resistance properties can be obtained. Because of this versatility, EPON 862 has become a standard epoxy used in formulation, fabrication and fusion technology. EPON 862 may be used as the sole epoxy or combined with other epoxy such as EPON 828. These EPON epoxies can also be blended together to change some of the core properties like viscosity, solvent resistance and improved crystallization resistance when compared to individual epoxy types. Some of the properties of the above mentioned EPON epoxies obtained from manufacturer are given in Table 4-1.

Table 4-1: Typical properties of unmodified EPON epoxy

Epoxy	**Viscosity**	**Weight / epoxide**	**Color**	**Density**
	cP at 25^{o}C		Platinum Cobalt color scale	(lbs/gal)
EPON 862	25 to 45	165-173	200	9.8
EPON 828	110 to 150	185-192	250	9.7
EPON 815C	5 to 7	180-195	250	9.4

4.2.1.2 Curing agent

EPIKURE curing agents are used as hardeners and once combined with EPON epoxy system with certain ratio, produces cross-linking and curing process. The curing cycle and final properties of the resin matrix are dictated by type of epoxy (EPON) and curing agent (EPIKURE). Different combination of epoxy and curing agent (parts by weight, pbw) will also be crucial in determining the final desired mechanical properties. Two different type of curing agents were investigated in this study namely EPIKURE 3274 and EPIKURE W.

EPIKURE 3274 is a moderately reactive, low viscosity aliphatic amine. It is water insensitive and resists "blushing" and "sweat-out" in epoxy compositions cured in high humidity environments. Other features are light color, improved color retention as compared to conventional amine cured epoxy systems, and long pot life. Typical viscosity and density at 25^{o}C is 40-60 centipoise (cP) and 7.93 lbs/gal, respectively. EPIKURE 3274 is a low temperature curing agent when used with EPON epoxy to form a neat system. Possessing excellent compatibility with liquid epoxy resins, EPIKURE 3274 does not require an induction period to produce cured glossy surfaces even under adverse humidity conditions. Due to the great difference in viscosities between this curing agent and most liquid epoxy resins, thorough blending may take longer than usual to achieve. A mixing period of 2 or 3 minutes is usually adequate to ensure a homogeneous solution of resin and curing agent. Cure rate is proportional to temperature and just as an example for EPON resin 862/ EPIKURE 3274 systems, tack-free cure is obtained in approximately 24 hours at 25 °C.

EPIKURE curing agent W, is a modified polyamidoamine adduct which offers excellent hardness properties to composite once combined with suitable epoxy liquid. They are high temperature curing agent which when combined with EPON epoxy, produces a neat system having excellent adhesive and sealing properties. Typical viscosity and density of EPIKURE W at 25^{o} C is 63-148 cP and 8.77 lbs/gal, respectively.

4.2.1.3Modifiers / diluents

Incorporation of diluents such as HELOXY Modifiers 48 or mono-epoxide diluents generally extends the working life and modifies the curing period. HELOXY modifiers also help in further lowering the viscosity of the final resin system, thus allowing penetration through the fiber glass polymers. This seepage improves the dilution of the fiber polymer and filling of air voids during curing process. In addition, HELOXY modifiers have also proved to improve the tensile properties of the resin matrix, which is the primary property being achieved. As an example, a comparison is made between two neat systems, one with and the other without the addition of HELOXY modifier. The total weight of both the neat system was kept constant at 140 pbw and ratio of the three ingredients was changed. EPIKURE 3274 was combined with EPON epoxy 862 at ratios of 40 parts per 100 parts resin to produce a neat system A. Similar system was again developed but with addition of HELOXY modifier 48 with 15 pbw ratio. The viscosity of the neat system A was 1210 cP while for neat system B, it was 840 cP after a curing time of 2 weeks at 25 °C. The tensile strength and tensile strains are shown in Table 4-2 as reported by manufacturer. The curing time mentioned above can substantially be decreased with

increase in curing temperature. Some technical properties reported by the manufacturer are listed in table 4-2.

Table 4-2: Properties of neat systems

	Units	**A**	**B**
EPON 862	pbw	100	85
EPIKURE 3274	pbw	40	40
HELOXY Modifier 48	pbw	0	15
Viscosity	cP	1210	840
Tensile Strength	psi	9200	8800
Tensile Strain	%	4	6

As seen from above data, addition of HELOXY modifier may prove to be beneficial in order to achieve certain mechanical properties. Since EPON 862 and EPIKURE 3274 neat system only provides 4-6% strain before rupture, HELOXY modifiers were considered in this research to improve the elongation characteristics of the resin matrix.

4.2.2 Conventional fiber reinforced polymer (FRP)

4.2.2.1 Introduction

As mentioned before, fiber reinforcement is the main constituent of composite matrix, which carries the major structural loads. Composite reinforcement may be in the form of fibers or particles, as a polymer or a metal. In this section, focus will be concentrated on polymer fibers. All common fibers are manufactured in a drawing process, where liquid raw material is

used. Fiber reinforcement material is commercially available in three forms, namely glass, carbon and aramid based.

Several different glass compositions are available, with most common being E and S type. ‘E’ denotes electrical and ‘S’ for high strength. E glass offers excellent electrical properties and durability. S glass offers improved stiffness and elongation properties. They both have good tolerance to high temperatures and corrosion environments. Both are vulnerable to moisture and abrasiveness. Figure 4-2 shows some of fiber glass fabrics which are commercially available. Carbon fibers have much higher strength and stiffness properties as compared to glass fibers, but have low elongation properties, hence not suitable for this research. Kevlar fibers have outstanding toughness and damage tolerance which gives it a good contender for energy absorption application, such as bullet proof vests. The outstanding toughness property of Kevlar creates a problem of cutting and requires special cutting and machining tools. On top of this, Kevlar does not have good tensile elongation properties as compared to glass fiber and are prone to water absorption, making them unsuitable for marine application.

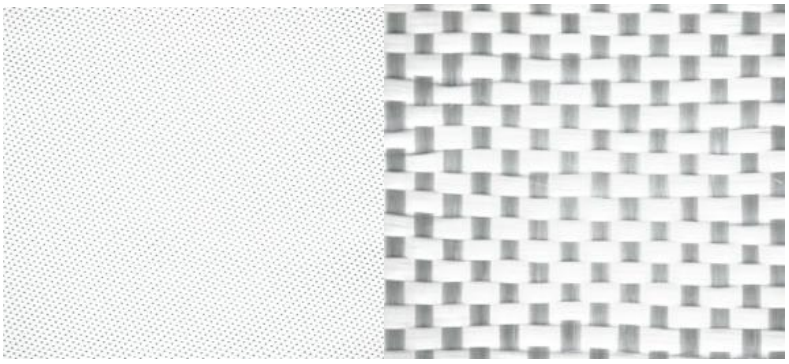

(a) (b)

Figure 4-2: Commercially available fiber glass. (a) Type S2 S-glass (b) Woven roving E-glass

4.2.2.2 Mechanical properties

Although the composite matrix is normally responsible for properties such as environmental tolerance and durability, fiber reinforcement is primarily responsible for the mechanical properties. Since it is difficult to get the measurements for fibers with diameters of order of 10μm, so most properties have been calculated through test on composite and properties of reinforcement have been calculated using micro-mechanics relationship. An overview of qualitative properties of fibers has been shown in table 4-3. Some literature also suggests hybrid composite made out of combination of various types of fibers, for e.g. layers of glass embedded with carbon fabric in a composite.

Table 4-3: Qualitative properties of fibers

Reinforcement Type	**Strength**	**Modulus**	**Abrasion resistance**	**Ease of Bonding**	**Ultimate Strain**	**Cost**
E-glass	**	**	***	***	**	*
S-glass	**	**	***	**	***	**
Carbon	***	***	*	***	*	**
Kevlar	***	**	*	*	**	***

Ratings: *** High ** Medium * Low. Abrasion resistance = resistance to wear

Some of the quantitative mechanical properties reported in previous research and literature are tabulated in table 4-4. Some of the advantages and disadvantages of various fibers as diagnosed during literature review have been highlighted in table 4-5.

Table 4-4: Quantitative mechanical properties of fibers (Bank 2006)

Fiber type	Young's Modulus	Ultimate Strength	Ultimate Strain
	(GPa)	(MPa)	(%)
E-glass	69	1378	1.5-2.5
S-glass	86	2586	3-3.5
Kevlar	124	3723	2.5
Carbon	370	3520	1-1.8

Table 4-5: Advantages and disadvantages of various conventional fibers

Fiber	Advantages	Disadvantages	Common Properties
E-glass	Reasonable elongation properties Excellent fabric-matrix compatibility Low cost	Low stiffness Low Strength Prone to water absorption	High Strength to Weight ratio (10-15 times of steel). Excellent corrosion resistance. Excellent fatigue characteristics. Low coefficient of thermal expansion. Magnetic invisibility. Radar transparency. Susceptible to creep.
S-glass	High ultimate strains Good fabric-matrix compatibility Low cost	Relatively low stiffness Relatively low strength Prone to water absorption	
Kevlar	High Toughness Damage tolerance Energy absorption	Prone to water absorption Poor fabric-matrix compatibility Difficult to machine	
Carbon	High Strength High stiffness Excellent fabric-matrix compatibility Moisture resistance	Low ultimate strains Low abrasion resistance	

4.2.3 Superelastic SMA wires

Shape memory alloys have already been discussed in detail in section 3.2. In this section the focus has been drawn in use of SMA wires in manufacturing of SMA-FRP composites. Most of the commercially available SMA wires have a presence of an oxide layer on them after

drawing and heat treatment. This layer is beneficial for the adhesion and bondage to the epoxy. The NiTi wires selected for this study had a diameter of 500µm (0.0197”). An important reason to select small size SMA wires for this study was to have flexibility and ease in the manufacturing of the hybrid composite during the embedment process of SMA.

4.3 Methodology and manufacturing process

4.3.1 Introduction

Manufacturing process of SMA composites varies considerably due to availability of different types of epoxy resin matrices, SMA reinforcement and supplementary fiber reinforcing materials. Differences also arise due to the fact that most SMA composites are now created in the research laboratories where standardized manufacturing techniques for particular SMA composite may not be adhered to. A review of SMA composite manufacturing processes can be used to identify common techniques and challenges that arise. One common manufacturing technique for SMA composites was discussed by Pappada et al. (2008), in which SMA composite was manufactured to study the impact resistance of the composite. The SMA composites consisted of a vinylester resin reinforced with superelastic SMA wires and glass or carbon fabric. Sheets of fabric reinforcement were then placed between the layers of SMA reinforcement and the process was repeated until the composite had a total of 4 layers of SMA wire reinforcement. To create a composite between these two reinforcing materials vinylester resin was added using vacuum assisted resin transfer molding, commonly known as VARTM. Another technique to manufacture SMA composites was presented by Michaud et al. (2009), in

which pre-strained SMA wires were embedded in epoxy resin matrix to study the effect of post cure schedules on composite mechanical properties. Pre-strained Ni-Ti-Cu SMA wires embedded with Kevlar reinforced fibers to manufacture SMA-FRP composite by Sittner and Stalmans in 2000. Clamping device was used to apply and hold the desired pre-staining in the SMA wires, throughout the manufacturing process. Once the pre-straining was applied to the SMA wires, epoxy Kevlar prepregs were then sandwiched between the SMA wires. The assemblage was then cured in an autoclave under vacuum, after which the SMA composite was removed from the frame and was ready for testing. Although the above mentioned manufacturing techniques were conducted in well-established laboratories with sophisticated equipment to control various parameters, the basic methodology remains the same. With this preface, an effort was made to develop a similar technique to first select the constituents and then manufacture, resin matrix, followed by fiber (Both SMA and FRP) composite and then finally an SMA hybrid composite.

4.3.2 Manufacturing of resin matrix

In order to manufacture SMA hybrid composite, first step was to investigate the type of resin matrix to be used, which will be compatible with SMA wires, so as to achieve high elongation composites. For this purpose different configurations of epoxy, curing agents and dilutes were used with at least two different curing regimes. The parameters which were varied in the initial manufacturing process were; type of epoxy, type of curing agent, use of diluents / modifier, curing temperature, curing time and the proportion of the constituents. Irrespective of how the above parameters varied, the general cross-linking process of epoxy and curing agent

results in an exothermic process, releasing internal heat and resulting in curing process. A typical temperature-time relationship for cross-linking process is shown in figure 4-3. The figure shows that once the epoxy (EPON) is mixed with the curing agents (EPIKURE) with or without diluents (Heloxy modifier), an exothermic reaction starts after initial inhibition time. Once the resin system reaches pot life, cross linking at molecular level really picks up, resulting in release of internal heat at higher rate. This cross-linking reaction is intimately related to internal temperature and continues at accelerated rate till the exothermic peak is achieved. After this, the curing process continues but with decrease in heat liberation, till the fully cured state is achieved. Figure 4-3 also shows the effect of external curing temperature. Higher the curing temperature, earlier the cross linking will start and hence higher exothermic peak with lesser full curing time and vice versa.

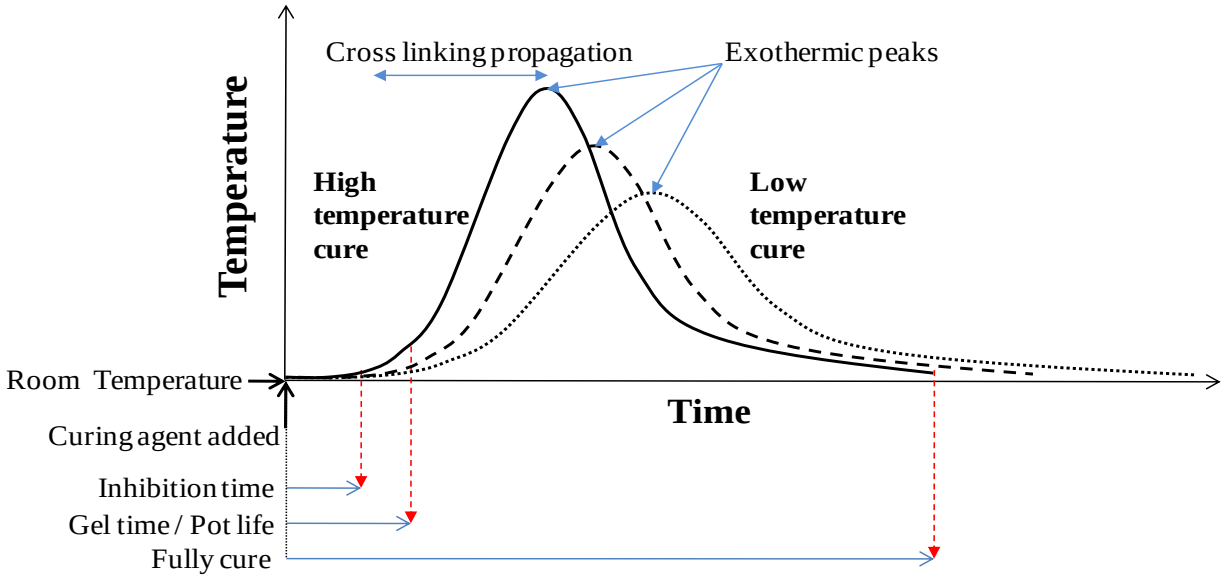

Figure 4-3: Temperature as a function of time for room temperature cured resin matrix

Methodology followed during the manufacturing of resin matrix, initiated with mixing of epoxy with curing agent in specific proportions which were measured by weight on a scale. After thorough mixing of the resin ingredients, the mixture was degassed to remove the air bubbles produced during the exothermic process. This process was done in a vacuum pump oven for 25 minutes. After degassing the resin matrix, the mixture which is still flow able, is poured into dog bone shaped moulds made out of silicone rubber. These moulds are then cured for specific time either at room temperature (RT=25^{o}C) or at 100^{o}C, depending on type of curing agent used for the resin matrix. EPIKURE 3274 which is a low temperature curing agent is generally cured at room temperature for 48 hours. This process can be accelerated by increasing the curing temperature up to 35^{o}C in which case the needed curing time is 24 hours. For EPIKURE W, which is high temperature curing agent, the curing temperature was kept at 100^{o}C for 24 hours. Schematics of the resin matrix manufacturing are shown in figure 4-4.

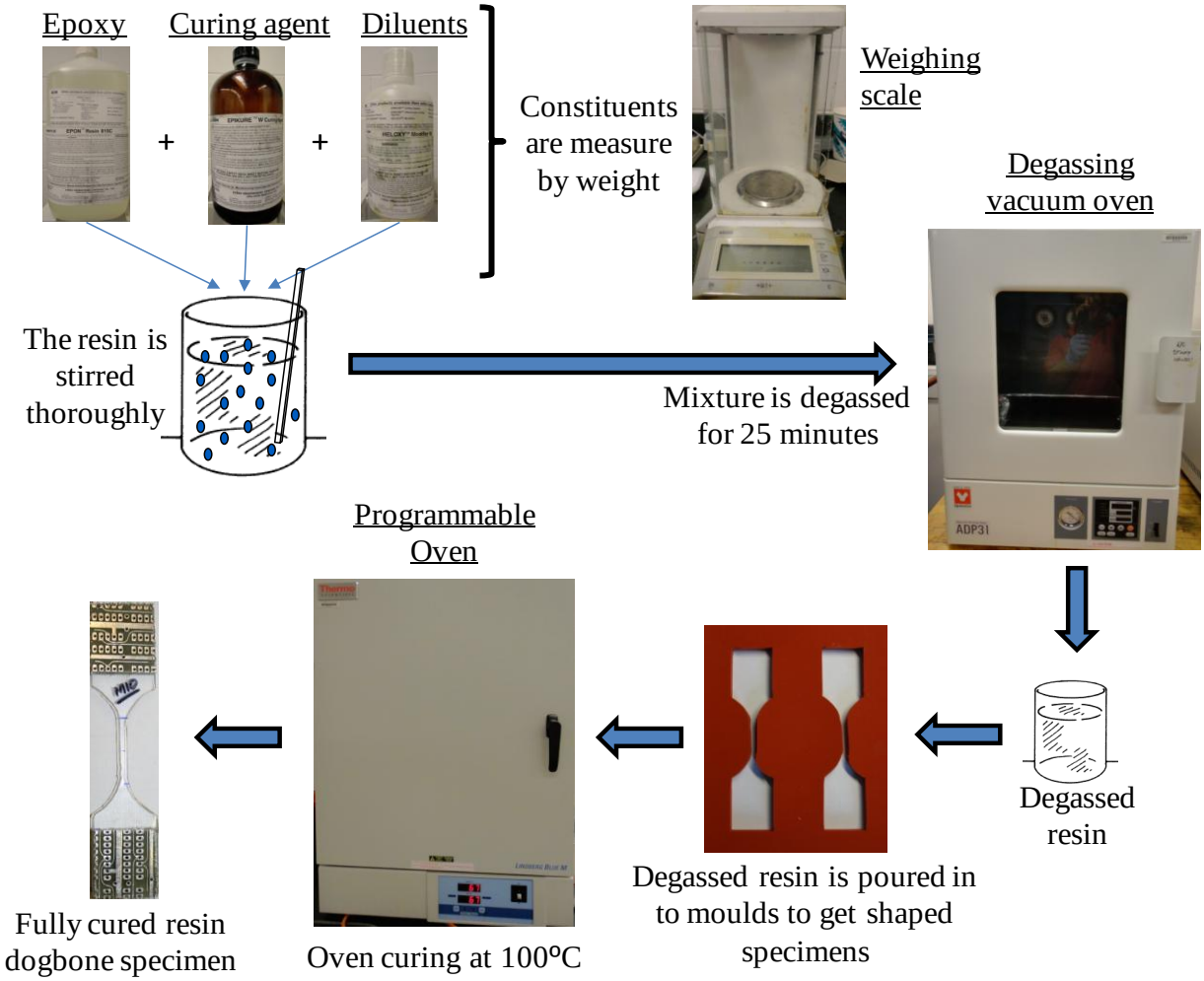

Figure 4-4: Methodology of manufacturing fully cured resin specimens

As mentioned before, various parameters were explored during the manufacturing process of resin in order to achieve desired elongation properties. For this purpose, an initial regime was developed to manufacture specimens with different configuration, as shown in table 4-6. This was the first batch of dog-bone resin specimen, manufactured and tested.

Table 4-6: Manufacturing regime for 1st batch of resin specimens

Resin System	Tag	Sub Tag	Epoxy (pbw)	EPIKURE W (pbw)	EPIKURE 3274 (pbw)	Heloxy 48 (pbw)	Curing
EPON 862	X	1XW	60	38	-	40	100°C for 24 hrs
		2XW	85	41	-	15	100°C for 24 hrs
		1XE	60	-	38	40	RT for 48 hrs
		2XE	85	-	41	15	RT for 48 hrs
EPON 828	Y	1YW	60	38	-	40	100°C for 24 hrs
		2YW	85	41	-	15	100°C for 24 hrs
		1YE	60	-	38	40	RT for 48 hrs
		2YE	85	-	41	15	RT for 48 hrs
EPON 815C	U	U	100	-	40	-	RT for 48 hrs

Table 4-6 shows nine configuration of resin matrix. The three different epoxy constituents were EPON 862, EPON 828 and EPON 815C. The two curing agents namely EPIKURE 3274 and W were used in combination of the epoxy and Heloxy modifier. Since EPIKURE W is a high temperature curing agent, the resin system made out of it, namely 1XW, 2XW, 1YW and 2YW were oven cured at 100°C for 24 hours. Other specimens made out of EPIKURE 3274 were cured at room temperature for 48 hours. Based off of tests done on above specimens (discussed in chapter 5), a second regime was developed in which epoxy EPON 815C and curing agent EPIKURE W was discarded for producing high strength but very brittle systems. Focus was then drawn on EPIKURE 3274 and its combination with EPON 862 and 828, with Heloxy diluents. The configuration used to manufacture resin specimen to achieve desired properties is as shown in table 4-7. In this regime, the curing temperature was increased from RT to be constant at 35°C, thus reducing the required curing time to 24 hours for fully cured specimens.

Table 4-7: Manufacturing regime for 2nd batch of resin specimens

Resin System	Tag	Sub tag	Resin (pbw)	Epikure 3274 (pbw)	Heloxy 48 (pbw)	Curing
EPON 862	M	M10	100	40	5	35°C for 24 hrs
		M30	85	41	40	35°C for 24 hrs
EPON 828	N	N10	100	40	5	35°C for 24 hrs
		N30	85	41	40	35°C for 24 hrs

Based off of results from this regime batch (discussed in chapter 5), M10 type resin matrix was selected for all future composite manufacturing due to its excellent elongation properties, while maintain reasonable stiffness and strength. This resin system had EPON 862 EPIKURE 3274 and Heloxy 48 in 100:40:5 pbw proportions, respectively.

4.3.3 Manufacturing of SMA-resin composite

This section explains the methodology followed to manufacture 100% SMA composite in which the reinforcing material is only SMA wires with no supplementary fibers. The selected resin system M10 (EPON-862, EPIKURE-3274 and Heloxy-48), was used to conduct this laboratory scale production of the composite, by embedding SMA wires which were 500µm (0.0197") in diameter. But before the SMA wires could be used in the composite, they needed to be trained (discussed in Section 5.3) in order to stabilize their properties and specifically to remove residual strains from them. Once the SMA wires were trained, they were ready to be embedded in the resin matrix. Silicone constraints were used to align the SMA wires along the principal direction of the sample. The geometry of the SMA embedded resin matrix is shown in figure 4-5 with dimensions.

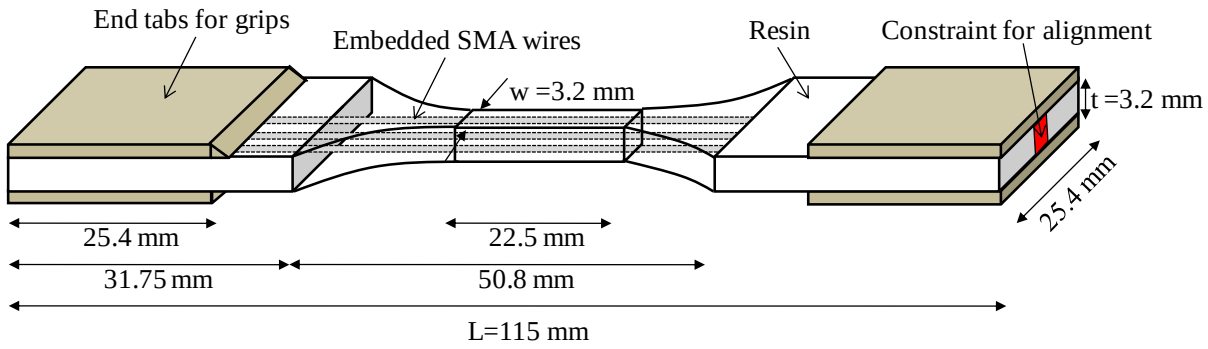

Figure 4-5: Geometry of SMA wires embedded composite specimen

In order to prepare SMA composite specimen as shown in figure 4-5, silicone rubber dam of 3.5mm thickness was first cut out to have a dog-bone shaped mould (Dimensions are shown in figure 4-8). This mould was then placed on a metal plate with impervious layer of Teflon sheet to avoid sticking of resin with metal plate. SMA wires were placed in layers with end constraints (to keep them aligned) inside the moulds. Layering of SMA wires in different horizontal planes helped in flow of resin between the SMA wires and saturation of all the void spaces. After this initial setup, resin system M10 was prepared and degassed, before pouring it in the mould. The whole mould setup was then covered with layer of permeable nylon and white bleeder cloth. Permeable nylon layer allows passage of excess resin through it, while the bleeder cloth collects this extra resin and protects from spillage. The whole assemblage was then covered by top metal plate. The schematics of above mentioned setup is shown in figure 4-6.

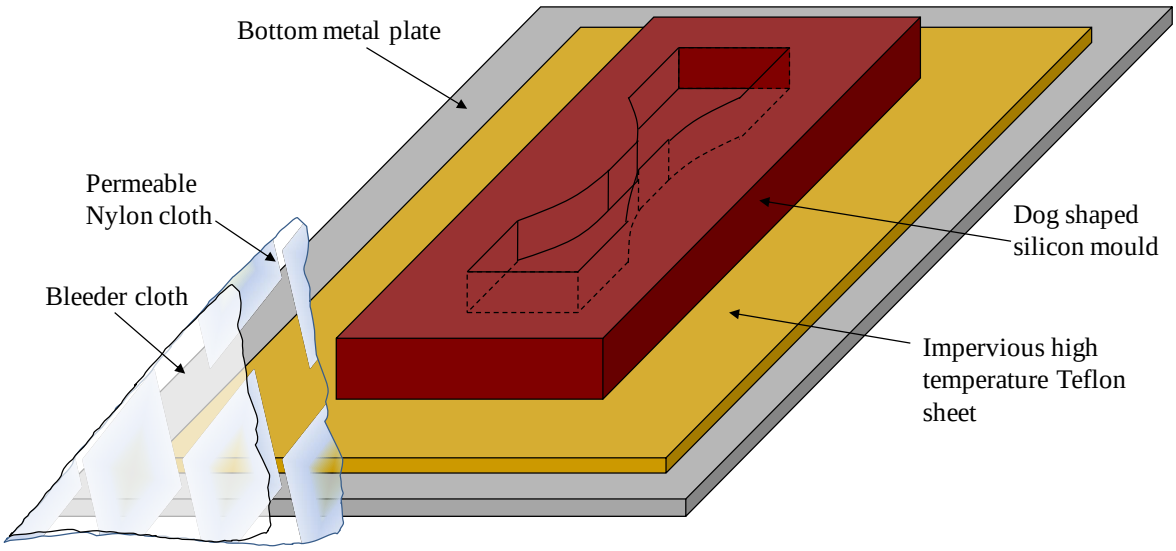

Figure 4-6: Schematics of specimen preparation setup

Once the assemblage with sandwiched specimen is prepared, it is placed in the hot-press / autoclave which allows controlling and monitoring of temperature and pressure during the curing process of the SMA composite specimen. The temperature was kept at 35^{o}C based on curing temperature of resin over 24 hours, while uniform pressure was maintained at 172.3 kPa. This pressure has been found to be ideal for resin percolations through conventional fiber layers (if present) and to shrink / get rid of any air bubbles if left out in the resin composite through positive pressure. Hot-press used to prepare SMA composite specimen is shown in figure 4-7. After 24 hours, the assemblage was removed from autoclave and the composite specimen was detached from the mould, while other items of sub-assemblage are discarded. Manufactured dog-bone SMA composite specimen with dimensions is shown in figure 4-8. During uni-axial testing, (discussed in chapter 5) premature failure of the specimen at the point of contact with load frame grips due to stress concentration is common. To avoid this, four end tabs (PCB, plastic) were attached at both the ends of the specimen for gripping during testing.

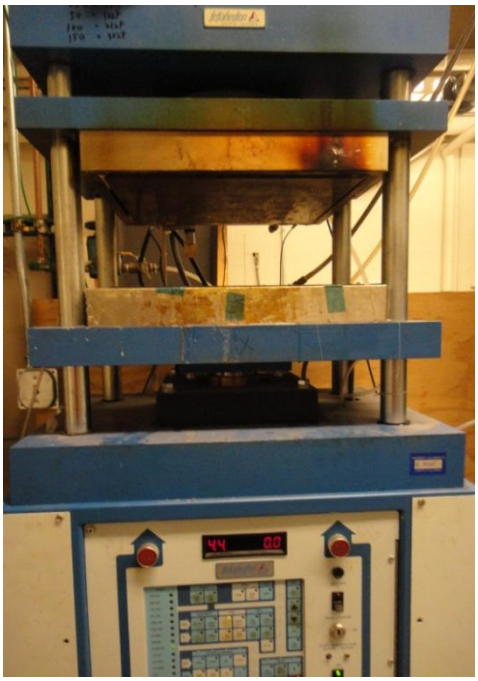

Figure 4-7: Hot-press setup for preparation of SMA composite

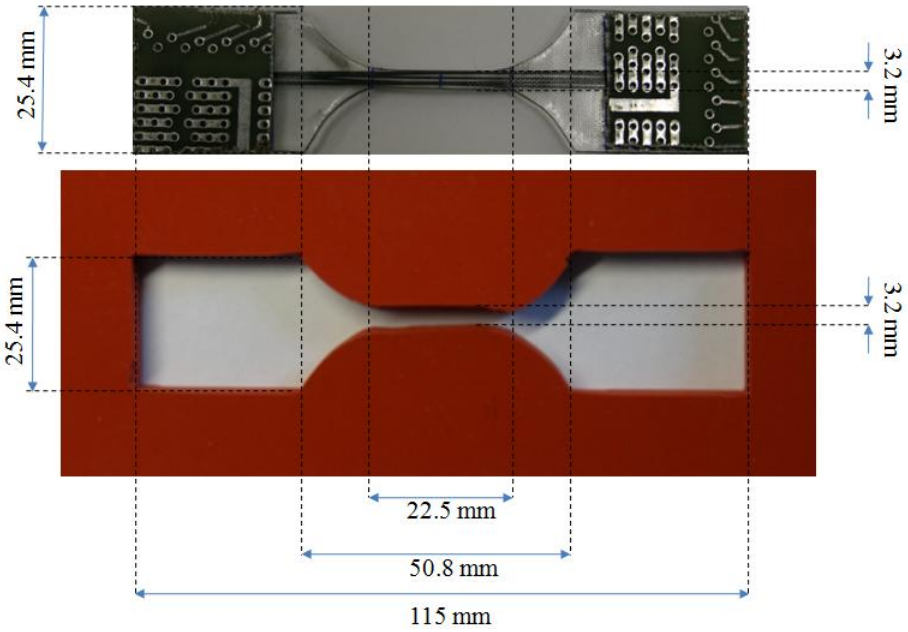

Figure 4-8: Manufactured dog-bone SMA composite specimen and its silicone mould

Three 100% SMA composite named hereafter as fully reinforced composite (FRC) samples namely FRC-3, FRC-7 and FRC-13 were prepared using above mentioned technique with 3, 7 and 13 numbers of SMA wires, impregnated in the resin matrix, respectively. The reinforcement volumetric fraction of FRC-3, FRC-7 and FRC-13 specimens was 8.46%, 20.3%, and 6.48% respectively. Table 4-8 shows details of these three specimens.

Table 4-8: Fully reinforced SMA composite (FRC) specimens

Specimen	**Tag**	**Resin Matrix M10**	**Area of Composite (mm^2)**	**Area of SMA wires (mm^2)**	**Reinforcement Volumetric ratio**
3 SMA wires	FRC-3	EPON-862, EPIKURE-3274, Heloxy-48	6.96	0.5895	8.46%
7 SMA wires	FRC-7		6.77	1.3755	20.30%
13 SMA wires	FRC-13		39.42	2.5545	6.48%
Area of 1 SMA wire = 0.1965 mm^2					

4.3.4 Manufacturing of conventional fiber-resin composite

The process of preparation of FRP-resin composite is similar to what has been described in section 4.3.3. Instead of embedding SMA wires into the resin matrix, FRP fibers are used as primary reinforcing material. The main aim of manufacturing and testing FRP-resin composite is to develop relationship between fiber volume fraction and weight of the fiber. Glass fiber strand used in this study has a density of 2.5 gm/cm^3 for S-glass and 2.2 gm/cm^3 for E-glass with continuous longitudinally aligned micro-fibers. The length of these FRP strands was kept at 112 mm, in order to fit into the mould (Shown in figure 4-8) without any bucking issues. Figure 4-9 shows glass fiber strand used as reinforcement in the FRP-resin composite specimens.

Figure 4-9: Glass fiber strand used as reinforcement in composite

The middle straight portion of the dog-bone silicone mould helps in aligning the fibers along the principal axis of the specimen, thus end constraints were not required. Dimensions of the specimen and manufacturing setup are the same as described in figure 4-5 and 4-4, respectively. Instead of having one mould, ten cutouts were made to have more number of samples with embedded glass fibers. Since the properties of FRP-resin composite can fluctuate more due to imperfections along the length of the fibers, during manufacturing process, more sample were manufactured and tested to have reliable results. Figure 4-10 shows the 10 cut outs in the silicone mould dam for preparation of FRP-resin composite.

(a) (b)

Figure 4-10: Manufacturing setup (a) Silicone moulds on metal plate with Teflon sheet (b) Permeable nylon and bleeder cloth

Once the assemblage was ready, it was placed in hot-press for a 24 hour cycle period at 35^{o}C. After this process, the specimens were de-molded and then tested under quasi-static loading. Unlike SMA composite specimen, the volumetric ratio of the fiber reinforcement cannot be calculated, hence the specimens after testing were required to undergo burn off test to find fiber volume fraction (FVF). The procedure to perform burn off test has been elaborated in figure 4-11. The procedure involves extracting undamaged segment from the specimen of certain length and dimension. Thereafter the specimen is weighted and placed in the furnace at 550^{o}C for 5 hours till all the epoxy is burned off and evaporated. The aim was to first find the weight of the extracted specimen with known dimensions (measured), and then to find the volume of glass fibers in the composite (FVF) using known density values. Table 4-9 shows the FVF of various specimens with single and double GFRP strands.

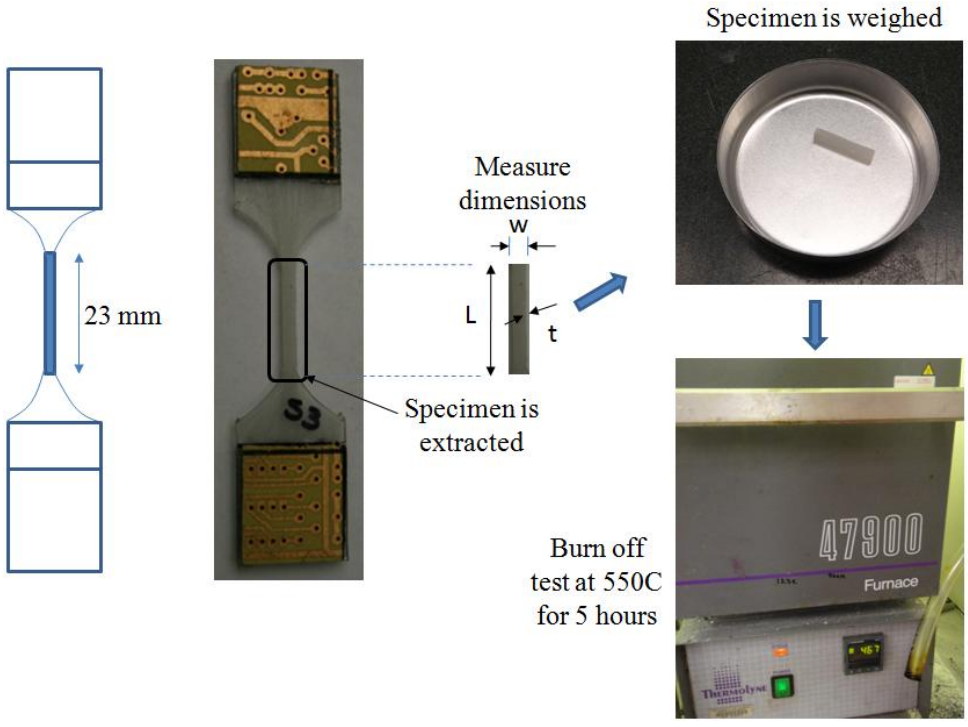

Figure 4-11: Burn off test procedure to find fiber volume fraction (FVF)

Table 4-9. Fiber volume fraction (FVF) of GFRP specimens

Sample	Weight of Container	GFRP Strands	Composite						GFRP			
			Length	Thickness	Width	Volume	Comp + container	Weight of Comp	GFRP + container	Weight of GFRP	Volume	FVF (%)
	W (gm)		L (mm)	T (mm)	W (mm)	V1 (cm^3)	W1 (gm)	W2 (gm) =W1-W	W3 (gm)	W4 (gm) = W3-W	V2 (cm^3) =W4/D*	V2/V1
A1	17.608	Single	22.85	2.33	3.07	0.163448	17.808	0.2	17.637	0.029	0.0116	**7.097**
B1	16.7153		23.48	2.85	3.18	0.212799	16.9673	0.252	16.7575	0.0422	0.01688	**7.932**
A2	16.1	Double	22.28	2.5	3.2	0.17824	16.3559	0.2559	16.188	0.088	0.0352	**15.64**
B2	17.6726		22.67	2.75	3.2	0.199496	17.9092	0.2366	17.7444	0.0718	0.02872	**14.4**
* Density of S-Glass fibers D = 2.5 gm/cm^3												

Specimen A1 and B1 specimens were made out of single glass fiber strand and after undergoing burn off test procedure rendered 7.09% and 7.93% FVF, respectively. On the other hand, A2 and B2 had double glass fiber strands, giving out 15.64% and 14.4% FVF, respectively. The fractions mentioned in table 4-9 were later helpful to develop relationship between weight of the glass fiber (volume) and FVF of the composite.

4.3.5 Manufacturing of SMA-FRP-resin hybrid composite

The process of manufacturing SMA-FRP composite was in line with the procedure explained in section 4.3.3 and 4.3.4. After knowing the FVF in relation to its weight, percentage of FRP in a SMA-FRP composite could be controlled. This allows achievement of exact ratio of SMA to FRP as part of reinforcement in the composite. Figure 4-12 shows schematics of SMA-FRP composite specimen with embedded SMA and FRP fibers in resin matrix. While manufacturing the composite, it was considered essential to sandwich the SMA wires and glass fiber with resin matrix to allow better flow of latter between the gaps and voids. The hybrid coupons were thus manufactured by first saturating the bottom half of the mould cut out and then laying SMA wires. The uni-directional glass fiber strands were then laid out on top of the SMA

wires in the mould and then saturating them with additional resin layer. Depending on required FVF of the whole composite and the percentage of each reinforcing material, this procedure of layering was altered to get a uniform distribution of reinforcing material along the cross section. This way both the reinforcing materials i.e. SMA wires and glass fibers were oriented along the same primary longitudinal direction of the composite with even distribution. For this study the coupon specimens made out of hybrid configuration were termed as 'partially reinforced composite' (PRC). The design technique to fabricate PRC specimens and their test results will be discussed in detail in section 5.4.4 and 5.4.5, respectively.

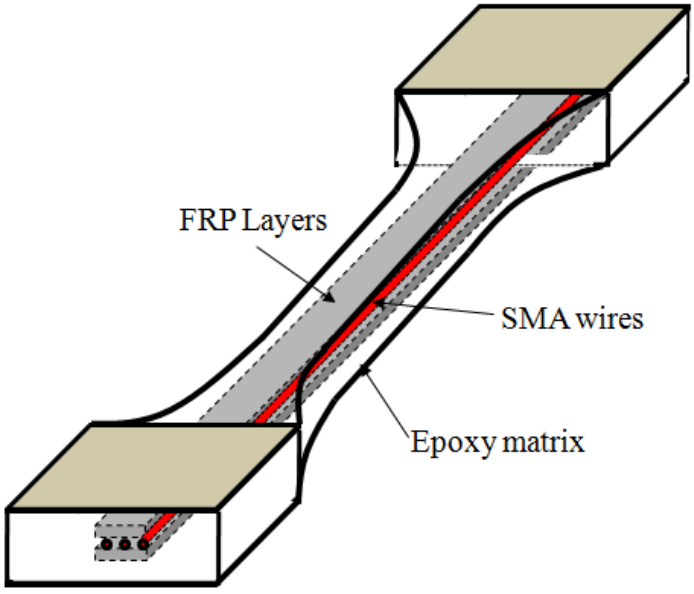

Figure 4-12: Schematic of SMA-FRP composite specimen

CHAPTER 5

Experimental Material Testing

5.1 Introduction

Based on the discussion in Chapter 3, superelastic NiTi shape memory alloys have shown potential for use in civil and structural applications by aiding in controlling structural response during a seismic event. The re-centering capability of SMA has provided a unique means to dissipate energy while limiting residual displacements in the structures. Although the cyclic properties of NiTi appear to be favorable for structural applications under the considered far-field type motion, there are other issues that need to be considered before NiTi material can be used to develop composite reinforcement for seismic resistant design. These issues include the degradation of the SMA properties with continued cycling, the low level of hysteretic damping, and the randomness in behavior of other constituents of the composite, namely epoxy matrix and the FRP. In part, these issues have limited widespread use of NiTi SMAs in civil and structural engineering. The problem lies in the fact that very few studies have focused on the use of SMA material in civil engineering application partly because of the cost and lack of in depth knowledge about seismic behavior of SMA material. Since this study proposes use of SMA wires embedded in resin with or without supplementary FRP matrix to form SMA hybrid composite, the focus of this chapter would be to find the mechanical properties of each of the components of the proposed composite and then evaluate the response of the complete matrix acting as a composite. This chapter addresses the gap in knowledge regarding mechanical

properties by performing a variety of experimental studies on NiTi wire specimens and SMA-FRP composites in order to determine their material level behavior for seismic applications. The first set of tests provides information in regards to mechanically training NiTi in order to obtain stable properties. The second set of tests which involves constituents of the SMA-FRP composite is conducted on the specimen prepared and discussed in chapter 4, to determine the material response of each constituent and the composite matrix as a whole. Work discussed in this chapter including manufacturing process has been presented in Zafar and Andrawes (2013).

5.2 Test setup

For the purpose of testing all the dog bone specimens and for training of SMA wire, a 97 kN uniaxial servo-controlled hydraulic frame was used. The frame is attached with hydraulic pump, actuator, load cell and mechanical grips. The test setup is shown in figure 5-1. A uniaxial tensile loading and unloading protocol was developed in order to find the tensile properties of all the constituents and the composite. For this, a protocol was developed using interface based MTS software. In the protocol program, both loading and unloading was governed by strain control, based off of values of elongation being read by extensometer. Since these tests were quasi-static based, strain rate was kept constant at 0.254 mm/min (0.0083 Hz). The cyclic tensile loading and unloading dictates that the specimen should not undergo compression. In order to ensure this, a limit detection was placed in the program, so as to stop unloading once the force reaches zero with tolerance of ±0.001 kN. After every cycle, the program was automated to start the next cycle with same strain rate until it reaches target strain values. The program developed for tensile loading and unloading is shown in figure 5-2.

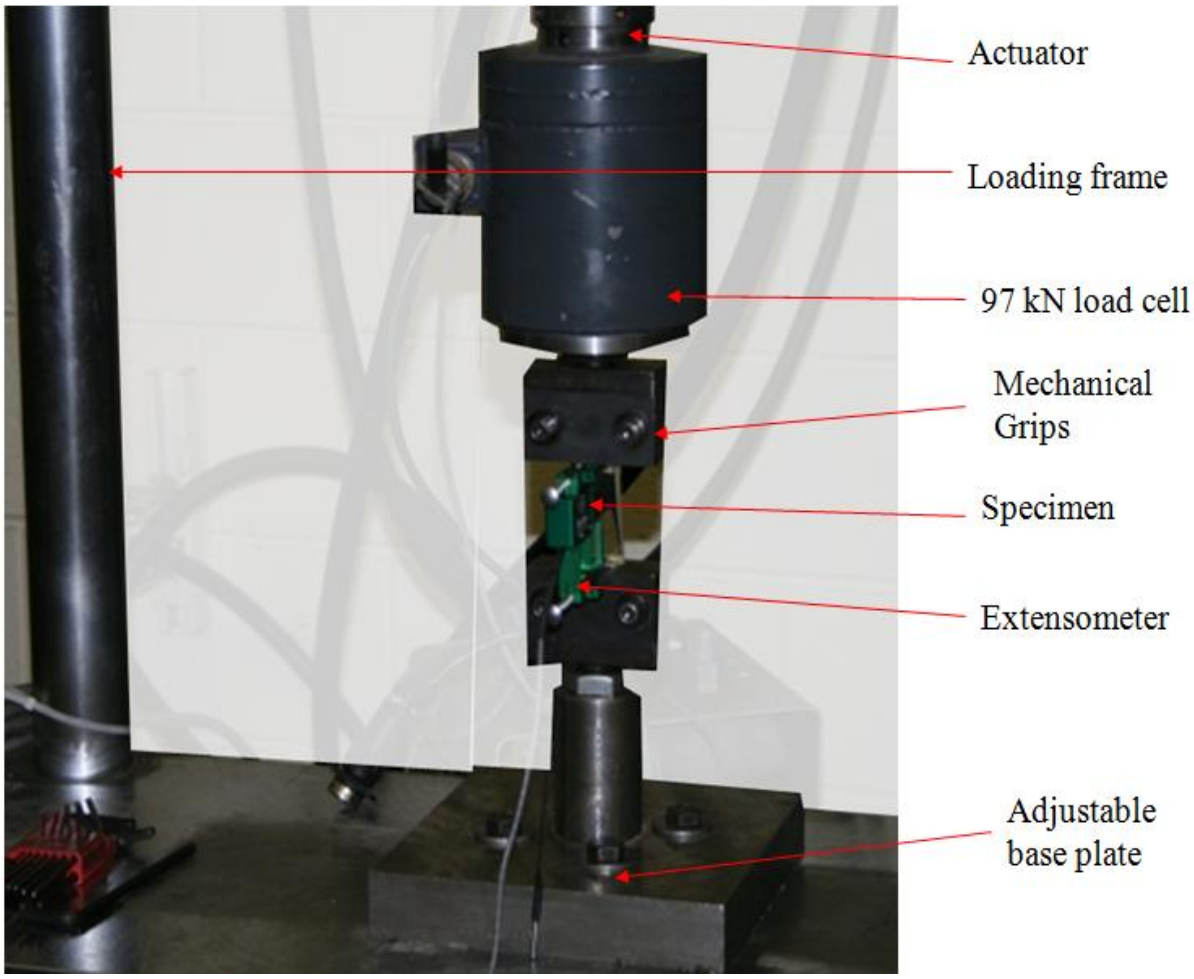

Figure 5-1: Uniaxial tensile test setup of SMA-FRP composite

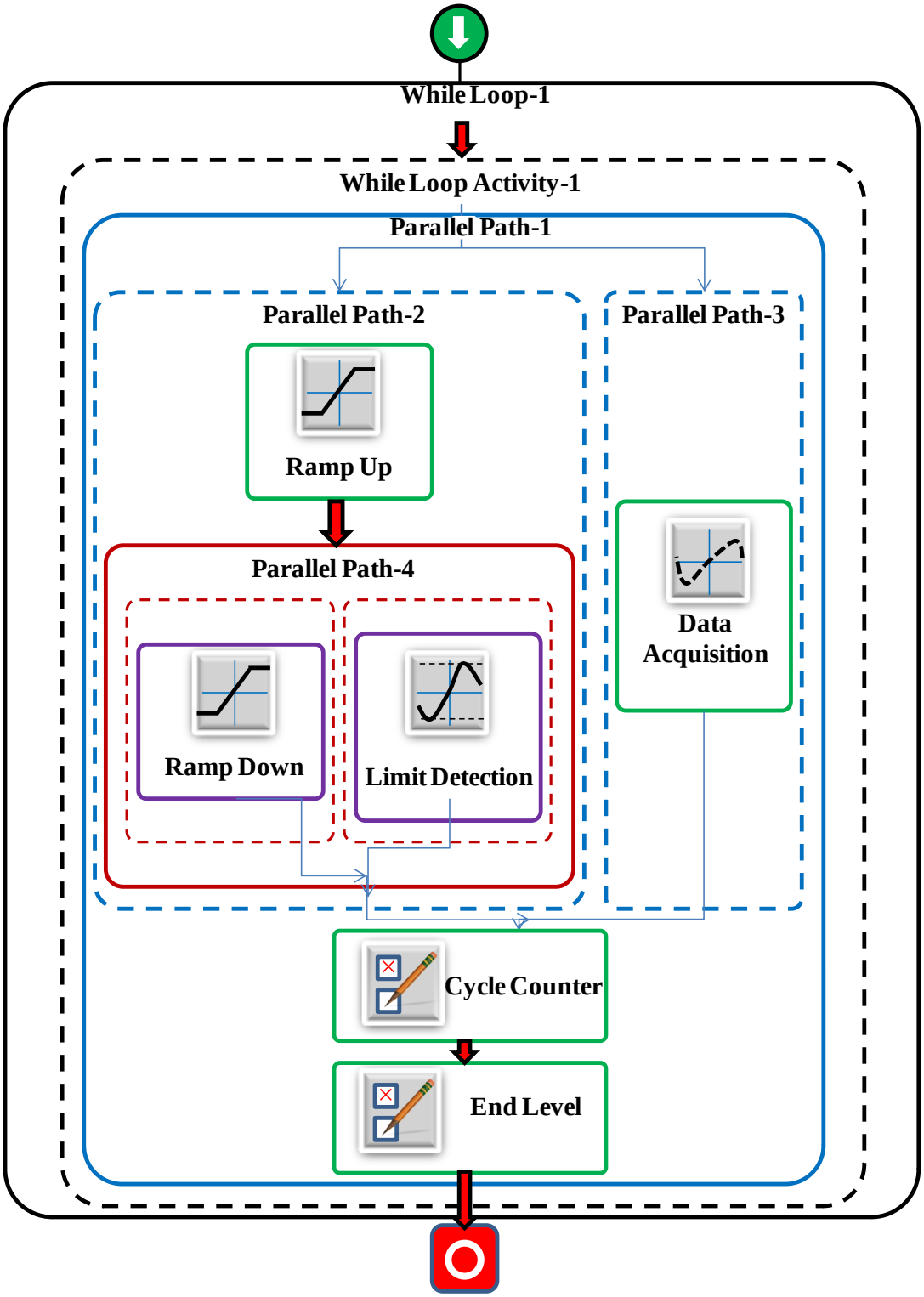

Figure 5-2: Protocol for tensile loading and unloading cycles

5.3 Mechanical training of NiTi wires

5.3.1 Introduction

During cyclic testing, many of the properties of superelastic NiTi SMAs such as forward and reverse transformation stress, residual strain, and energy dissipation capacity degrade with continued cycling as is shown in Figure 5-3 (Tobushi et al. 1998). Since stabilization occurs after continued cycling, researchers have suggested to first doing the training of NiTi SMA before using them in composite applications. Many studies have looked at thermal cycles in order to stabilize superelastic properties but very few have looked at the effect of mechanical training. Since mechanical constitutive behavior is the focus of this chapter, hereafter, cyclic testing of SMA will refer to mechanical uniaxial tests which are consistent with the typical deformation mode for SMAs in seismic applications. Typical tests on superelastic specimens consist of loading the specimens in tension up to strains between 4 to 8%. Several studies have found consistent results showing major decreases in the forward transformation stress (loading plateau), slight decreases in the reverse transformation stress (unloading plateau), and decrease in the residual strain (increase in residual elongation / displacement) with continued cycling until stabilization is reached (Dolce and Cardone 2001, Gong et al. 2002, Tobushi et al. 1998). Gong et al. (2002) attributed the decrease in this forward transformation stress to accumulation of dislocations which assist the martensite transformation. During repeated stress induced phase transformation on untrained SMA, residual martensite is formed which results in residual strains. As number of cycles is increased, formation of residual martensite continues to grow, but at reduced rate, until a stable behavior is reached with negligible residual strains. Due to the greater

decrease in the forward transformation stress as compared to the reverse transformation stress, the hysteretic area decreases with cycling resulting in a decrease in the energy dissipation capacity. As mentioned earlier, the reduction in Young's modulus is due to the appearance and accumulation of residual Martensite. Because of continuous phase transformation (change in molecular configuration) between Austenite and Martensite due to repeated cycles, molecular layout is modified at the beginning of every subsequent cycle. Martensite phase inherently exhibit lower modulus as compared to Austenite phase (Table 3-1); thus presences of this trapped residual Martensite tend to reduce the modulus of SMA wires at the start of every subsequent cycle. As number of cycle's increase, the number of these dislocated residual Martensite also increase but at reduced rate, thus stabilizing Young's modulus along with other properties. Tobushi et al. (1998) trained NiTi wire by applying 20 loading and unloading cycles to NiTi wire. These effects can be seen in figure 5-3.

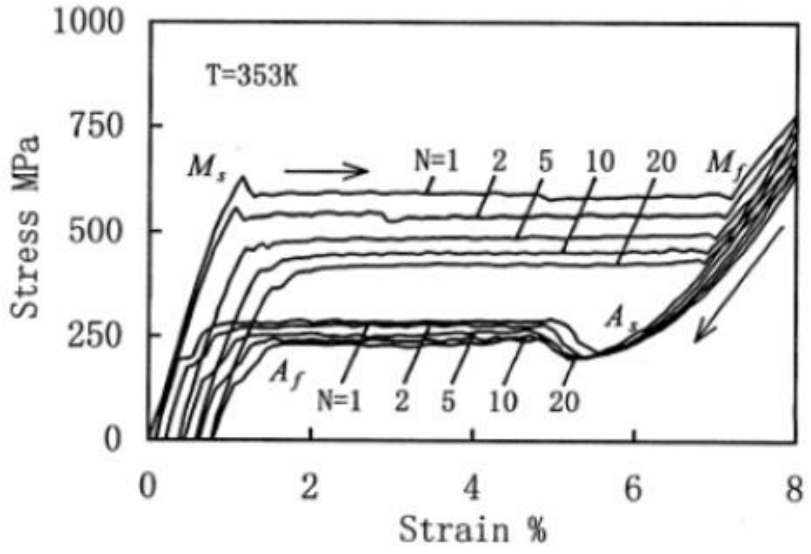

Figure 5-3: Stress strain curve of SMA specimen under tension cyclic (Tobushi et al. 1998)

5.3.2 Sample preparation for SMA wires training

SMA wires are prone to slippage and damage if teethed directly into the mechanical grips. In order to avoid both eventualities, SMA wires were grouped into a bundle and the ends were fastened together in a metal canopy (lead). Both the ends of the wire were frowned and then embedded in metal canopy, to avoid any slippage and out of plane alignment. A simple configuration made out of brass metal was developed in order to bunch and embed SMA wire ends in the metal canopy. Brass was selected as mould to make lead canopy because of its high temperature sustenance. The melting point for lead is 327.5^{o}C, while that of brass is 930^{o}C. High temperature flame was used to melt the lead and was then pour into the brass mould containing SMA wire ends. Before pouring the lead into the brass mould, the interior surface of the mould was sprayed with oil to avoid sticking of lead to the brass mould which will cause difficulties during the extraction process. The lead metal solidifies in few seconds after pouring and is able to be extracted along with the SMA wire ends. Same procedure is adopted for the other SMA wires end, while taking care of straightness of wire and ensuring that the wires are not in buckled position because of misalignment. Schematics of the brass mould and SMA wires configuration is shown in figure 5-4. Final configuration of bundled SMA wires along with lead canopy is shown in figure 5-5. Lead canopy is being used so that mechanical grips can bite on and keep the SMA wires secured during the tensile cyclic training. The methodology of bundling SMA wires for training process is illustrated with pictures in figure 5-6.

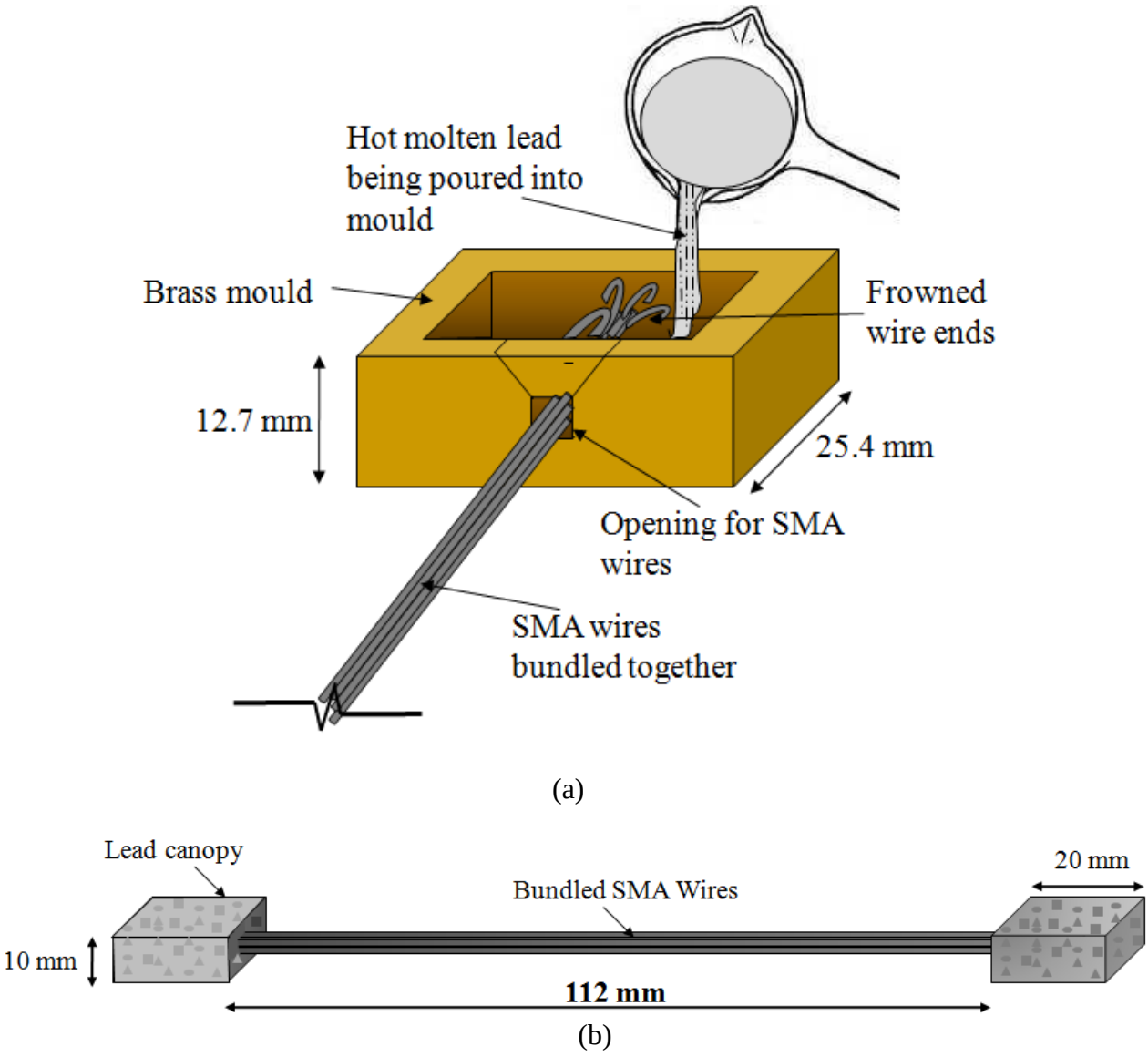

Figure 5-4: Schematics of (a) brass mould and SMA wires configuration (b) lead canopy at the both ends of bundled SMA wires

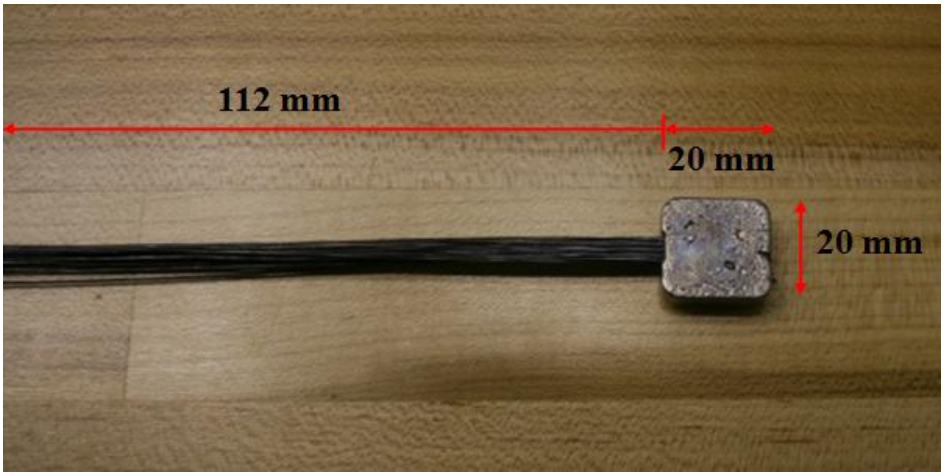

Figure 5-5: Final configuration of bundled SMA wires before training

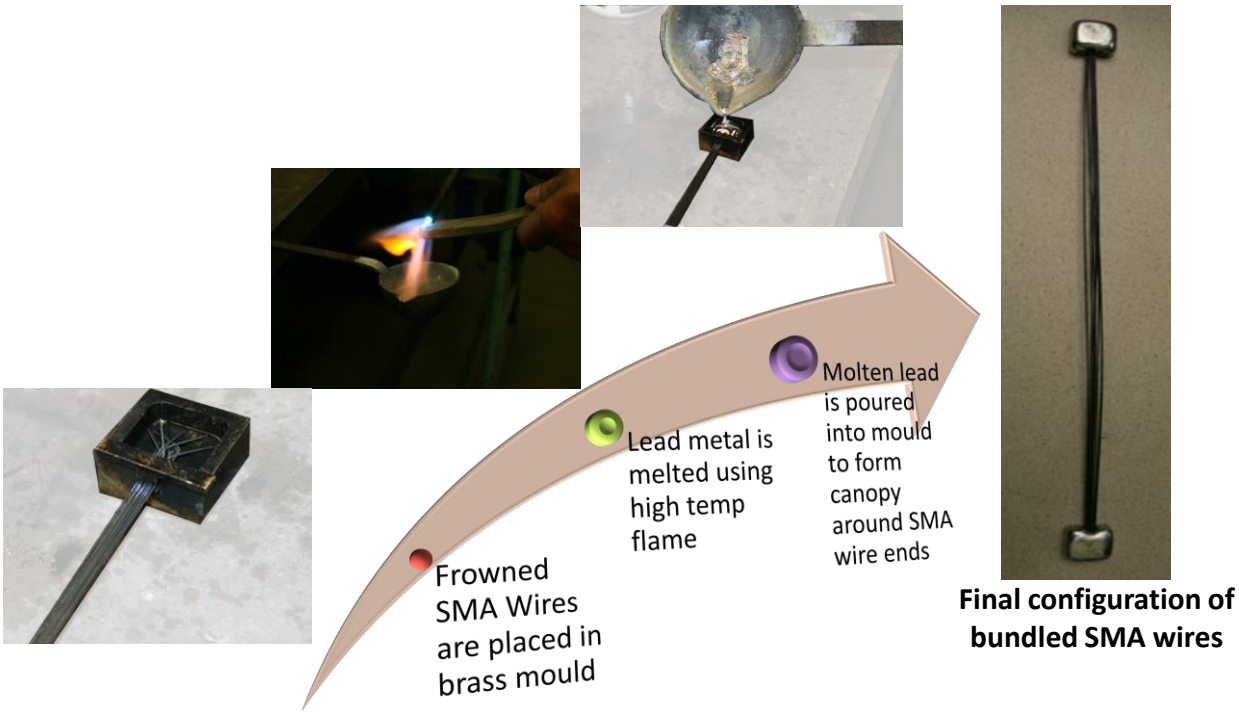

Figure 5-6: Methodology and sequence of bundling of SMA wires for training process

5.3.3 Results and discussion

In order to effectively implement superelastic NiTi SMAs into civil and structural applications, stable properties are typically required in order to meet performance based guidelines. This ensures predictable and reliable behavior of a structure during a seismic event. Results from studies conducted by Miyazaki et al. (1986) and Tobushi et al. (1998) show the degradation effects on SMA mechanical properties with continuous cyclic loading. This section addresses the issue of stabilization of SMA wire properties through 'training process', while exploring the degradation effects on SMA mechanical properties.

Numerous bundled SMA samples were manufactured with the procedure mentioned in section 5.3.2. Since all the composite manufacturing dog bone moulds were 115 mm long, the length of SMA wires needed to be of 112 mm. For this purpose, clear length of bundled SMA wires outside the lead grips was kept to be 224 mm to achieve double the trained SMA wires. Since the strains across the entire un-braced length of SMA wires are constant during tensile loading, length of wires were doubled to optimize output. These specimens were then gripped in the tensile loading platform and subjected to a training loading protocol. 102 mm long extensometer was utilized to measure the elongation in the wires during the testing. As the training process was strain controlled i.e. achievement of target strains at a certain strain rate, readings from extensometer were used to monitor the test. Close up of bundled SMA wire specimen loaded in the mechanical grips with attached extensometer is shown in figure 5-7.

Figure 5-7: Close up of bundled SMA wire specimen loaded in the mechanical grips with attached extensometer

The bundled SMA wires were subjected to constant strain of 5% in each cycle, till the residual strains were eliminated from the SMA wires. This results in accumulation of residual displacement, and will only effect in elongation of the SMA wires, which is not undesirable. Loading regime followed during the SMA training process is shown in figure 5-8. Both loading and unloading was governed by strain control, however limit detection was placed to stop the test cycle once the force reached zero. This was done to ensure that the specimen does not undergo compression during the test.

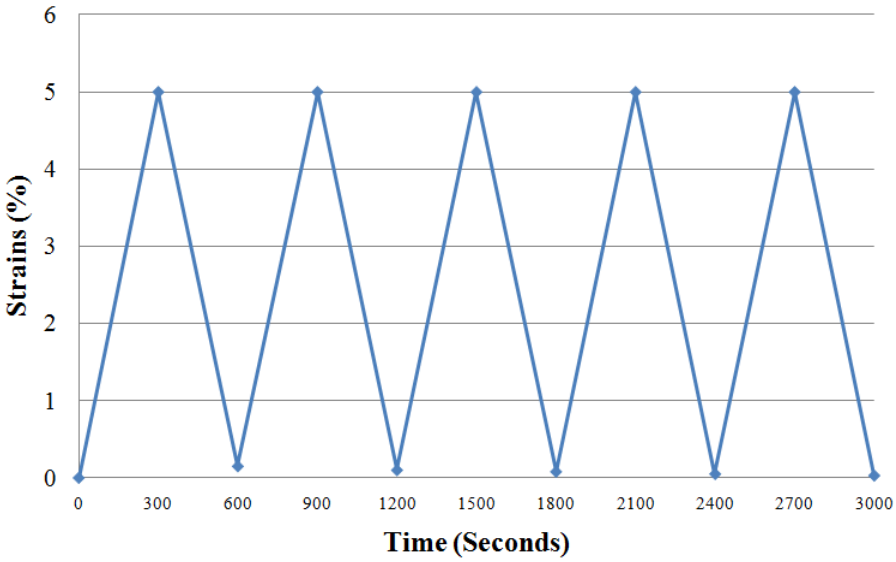

Figure 5-8: Loading and unloading protocol for training SMA wires

Initially, five SMA wire batches were prepared to undergo training process with varying number of wires. The numbers of wires in each batch were kept different in order to see the effect on initial modulus, austenite to martensite start stress (forward transformation stress) and residual displacement. Stress strain curves of batch-3 and batch-4 with 9 and 5 SMA wires, respectively, has been shown in figure 5-9 and 5-10. Figures show constant strain cycles of 0.05 mm/mm (5%) with strain rate of 0.254 mm/min (0.0083 Hz). In each subsequent cycles, the SMA wires show a trend of reduction of forward transformation stress also known as austenite to martensite start stress (σ_{AMs}). Reduction in young's modulus of the SMA wires was also observed during continued cyclic training process. The residual strain exhibited by SMA wires in each cycle also tends to reduce with every subsequent cycle. The residual strains were kept as bench mark to identify the SMA wires to be 'stable' or 'trained'. Table 5-1 shows the cyclic properties of trained and untrained SMA wire batches with different number of wires.

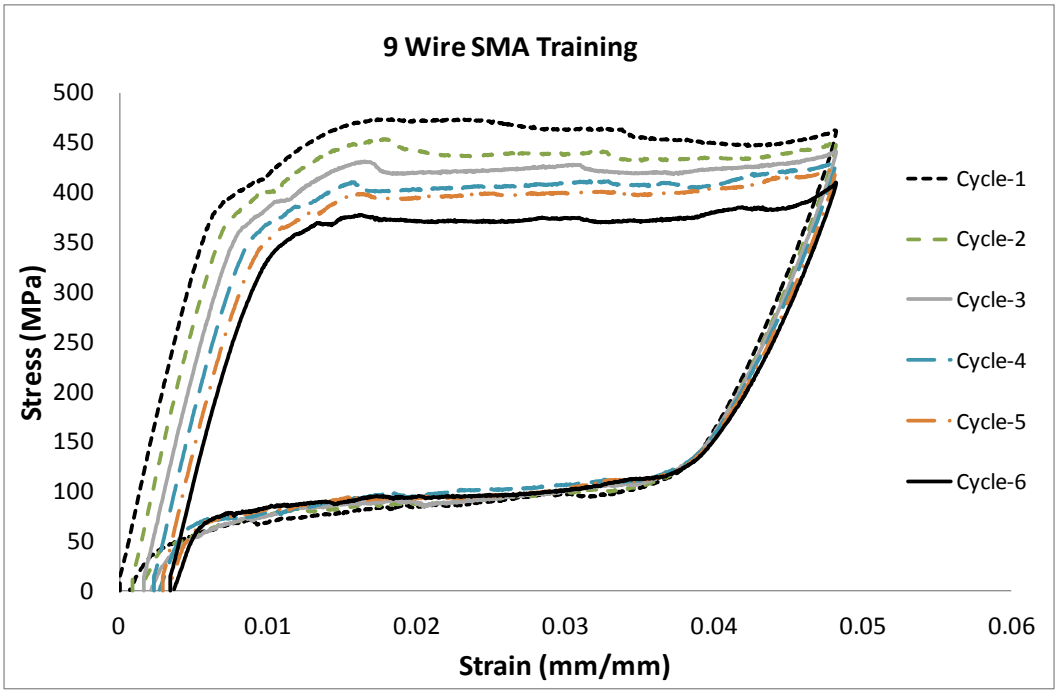

Figure 5-9: 6 cycles of stress strain curve for 9-wires SMA batch training

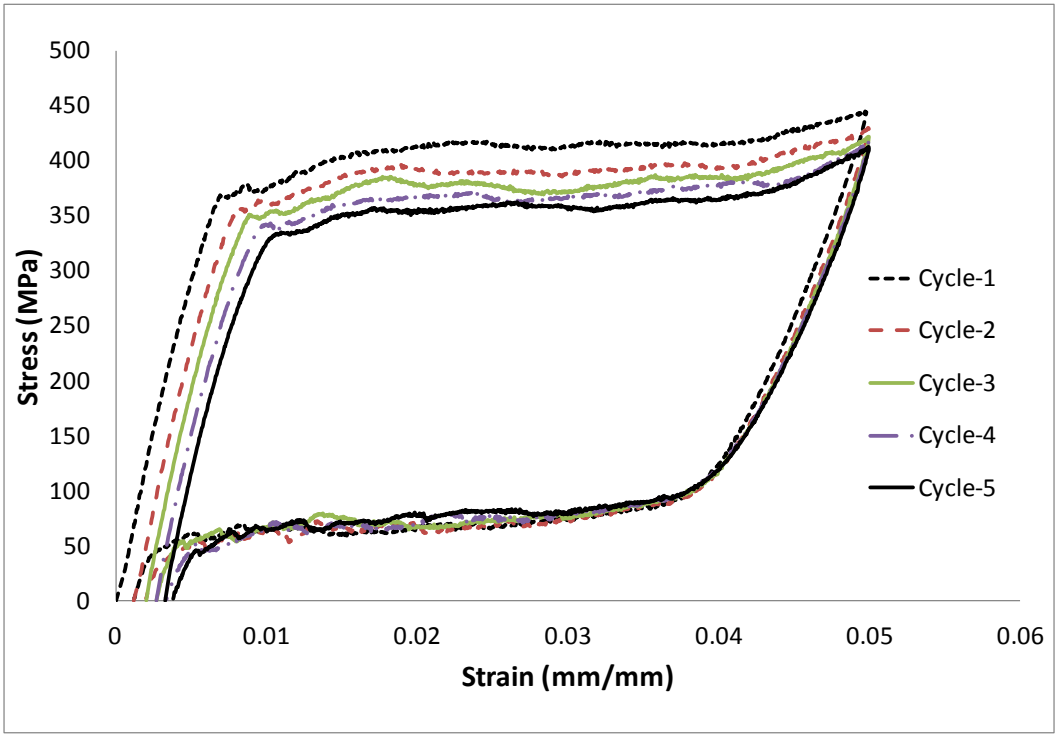

Figure 5-10: 5 cycles of stress strain curve for 5-wires SMA batch training

Table 5-1: Cyclic properties of trained and untrained SMA wire batches

SMA Wire Training Batches											
Batch	Number of wires	1st training cycle (Untrained)			Last training cycle (Trained)			Difference (%) Trained vs Untrained		
		Young's Modulus (E)	Forward transformation stress (σ_{AMS})	Residual strains	Young's Modulus (E)	Forward transformation stress (σ_{AMS})	Residual strains	Reduction in Young's Modulus	Reduction in Forward tranformation stress (σ_{AMS})	Reduction in Residual strains
		GPa	MPa	(mm/mm)	GPa	MPa	(mm/mm)			
1	14	64.98	422	0.001324	58.58	364	0.0008095	9.85	13.74	38.86
2	11	63.19	375	0.0034	55.04	330	0.00088	12.9	12	74.12
3	9	68.94	410	0.00242	62.35	360	0.000258	9.56	12.2	89.34
4	5	68.94	380	0.001196	60.12	330	0.000529	12.79	13.16	55.77
5	3	63.5	380	0.00233	56.31	328	0.000708	11.32	13.68	69.61
								11.28	**12.96**	**65.54**

For batch-3 with 9 SMA wires, 6 cycles were needed to bring the residual strains to negligible number of 0.00088 mm/mm (0.088%). During these 6 cycles, the wires experienced reduction in Young's modulus from 68.94 GPa to 62.35 GPa, a 9.56% reduction. Similarly, reduction in forward transformation was observed from being 410 MPa for untrained SMA wire to 360 MPa for trained SMA wires, a reduction of 12.2%. Almost identical pattern was observed in other SMA wire batches which were all trained to constant target strain of 5%. On average for all five SMA wire batches which were trained, the reduction in Young's modulus, forward transformation stress and residual strains between trained and untrained were 11.28%, 12.96% and 65.54%, respectively.

5.4 Uniaxial quasi-static testing and results

5.4.1 Resin matrix specimen

Various ingredients were explored during the manufacturing process of resin matrix in order to achieve desired elongation properties. Other properties such as stiffness, strength and

cyclic fatigue were also observed during the tests. An initial regime was developed to manufacture dog-bone resin specimens with different configuration, as shown in table 4-6. Out of these nine resin specimens; 1XE and 1YE were found to be too flexible even before any testing and hence were discarded. Remaining 7 specimens were subjected to cyclic tension until failure. Figure 5-11 shows image of specimen undergoing tension cyclic loading with mounted extensometer.

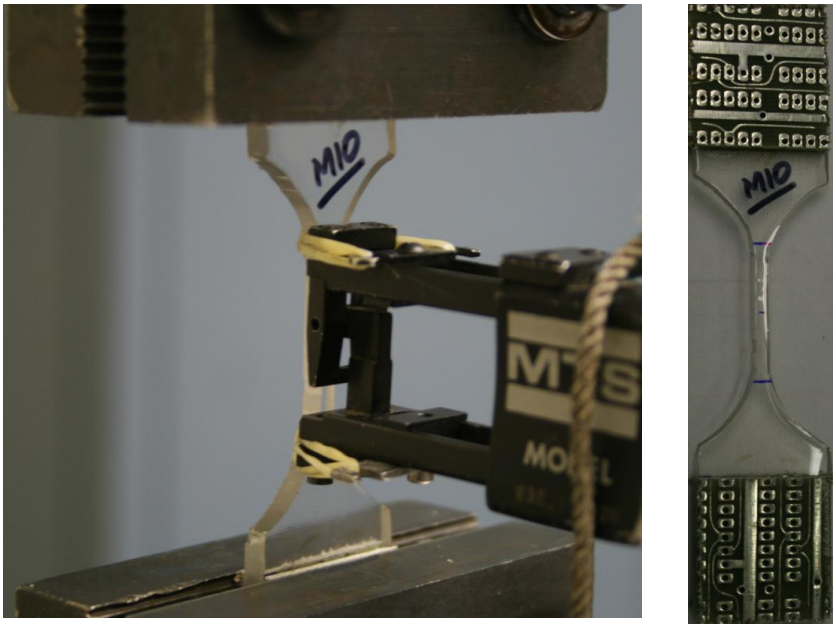

Figure 5-11: Dog bone resin specimen in loading grips with mounted extensometer

The loading protocol was set to have strain rate of 0.254 mm/min (0.0083 Hz) during the whole test with strains being incremented by 1% absolute strain (0.01 mm/mm) in every subsequent cycle. During the unloading phase in each cycle, special care was taken to avoid subjecting specimen to compression. This was enforced by stopping the test once the force levels

reached zero with small tolerance levels. In order to first classify the hardener, specimens 1XW, 2XW, 1YW and 2YW with EPIKURE W were tested. Stress strain plots for these specimens are shown in figure 5-12.

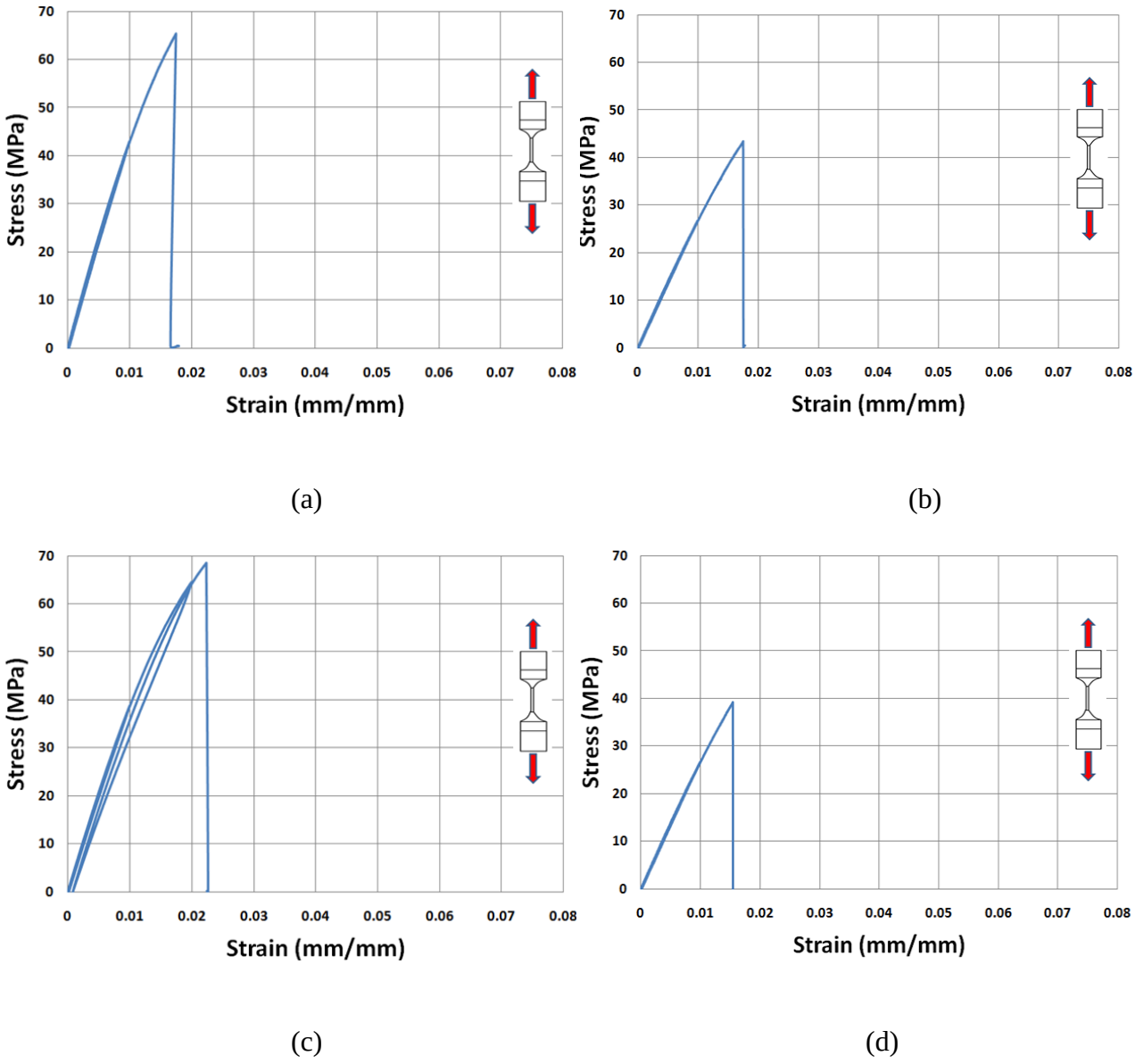

Figure 5-12: Stress strain plots of resin specimen with EPIKURE W as hardener. (a) Specimen 1XW (b) Specimen 2XW (c) Specimen 1YW (d) Specimen 2YW

As seen from figure 5-12, resin specimens with EPIKURE W hardener which is high temperature curing agent, although gives high strength and stiffness, but fails prematurely at low strains. In all four cases, the resin specimens failed close to 2% strains which is an undesirable property. For SMA-FRP composite applications, resin systems which can at least reach strains of 5% or more, are preferred to allow SMA to reach at least 50% of its elongation potential. Because of low strains, resin specimens configuration with EPIKURE W was not deemed suitable for further investigation and trial. The second type of hardener, EPIKURE 3274 which was used to produce specimens 2XE and 2YE were then tested. Stress strain curve for these specimens is shown in figure 5-13.

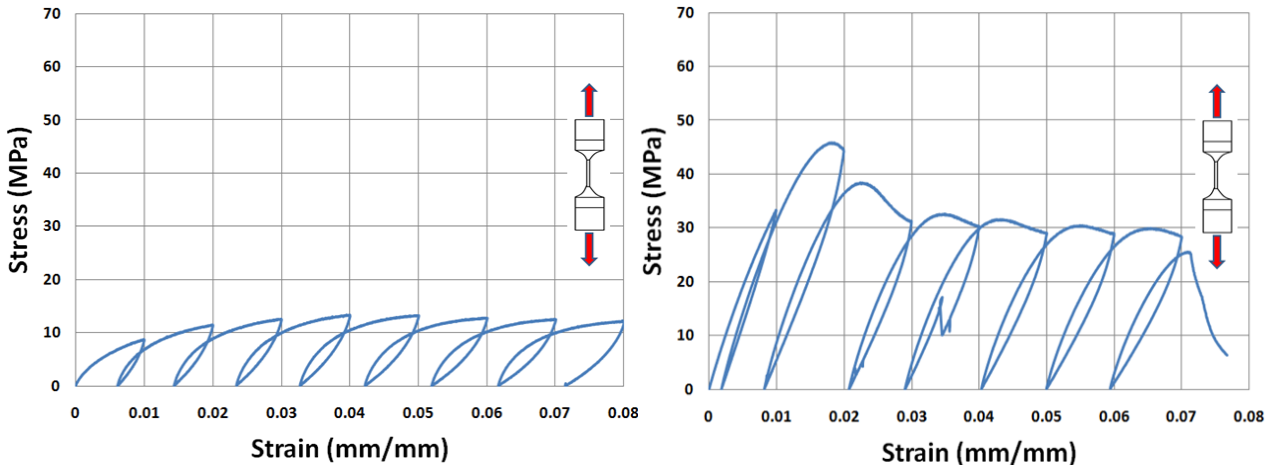

(a) (b)

Figure 5-13: Stress strain plots of resin specimen with EPIKURE 3274 as hardener. (a) Specimen 2XE (b) Specimen 2YE

Resin specimen with EPIKURE 3274 as curing agent showed much more promising results in terms of strain levels reached. Both 2XE and 2YE specimens were able to

exhibit strains of 8% and 7%, respectively. Although the strength and stiffness achieved during the tests showed variations, the prime property of elongation was enough to consider EPIKURE 3274 and both type of epoxy, EPON 862 and EPON 828 with or without addition of HELOXY modifier 48, for further investigation. The last specimen from this matrix, namely specimen U which was product of EPIKURE 3274 and EPON 815C neat mix, was tested. This specimen was discarded because of low strain levels reached during test (about 3.5%) before failure. Results are shown in figure 5-14.

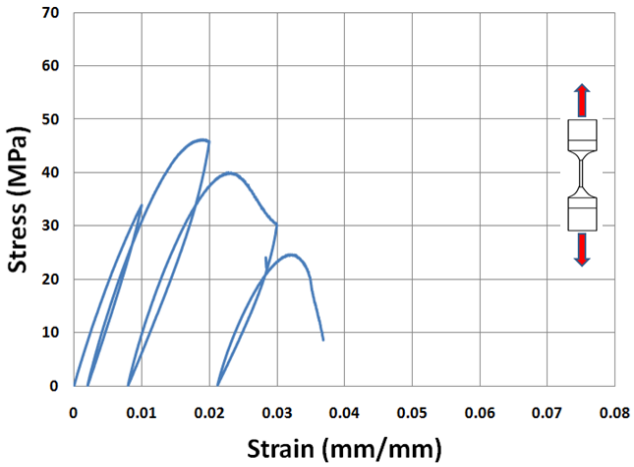

Figure 5-14: Stress strain plots of resin specimen U with EPIKURE 3274 and EPON 815C

Based on test results from 1st batch of resin specimens, a second regime was developed in which epoxy EPON 815C and curing agent EPIKURE W were discarded for producing high strength but brittle systems. Focus was then drawn on EPIKURE 3274 and its combination with EPON 862 and 828, with and without HELOXY diluents. The configuration of the constituents used in this 2nd batch were shown table 4-7. In this regime, the curing temperature was set at 35°C instead of being random room temperature. This allowed more consistency in addition to

reducing the required curing time to 24 hours for fully cured specimens with EPIKURE 3274. Loading protocol for the 2nd batch of resin specimens was kept the same as of 1st batch. Stress strain plots for M10, M30, N10 and N30 specimens are shown in figure 5-15.

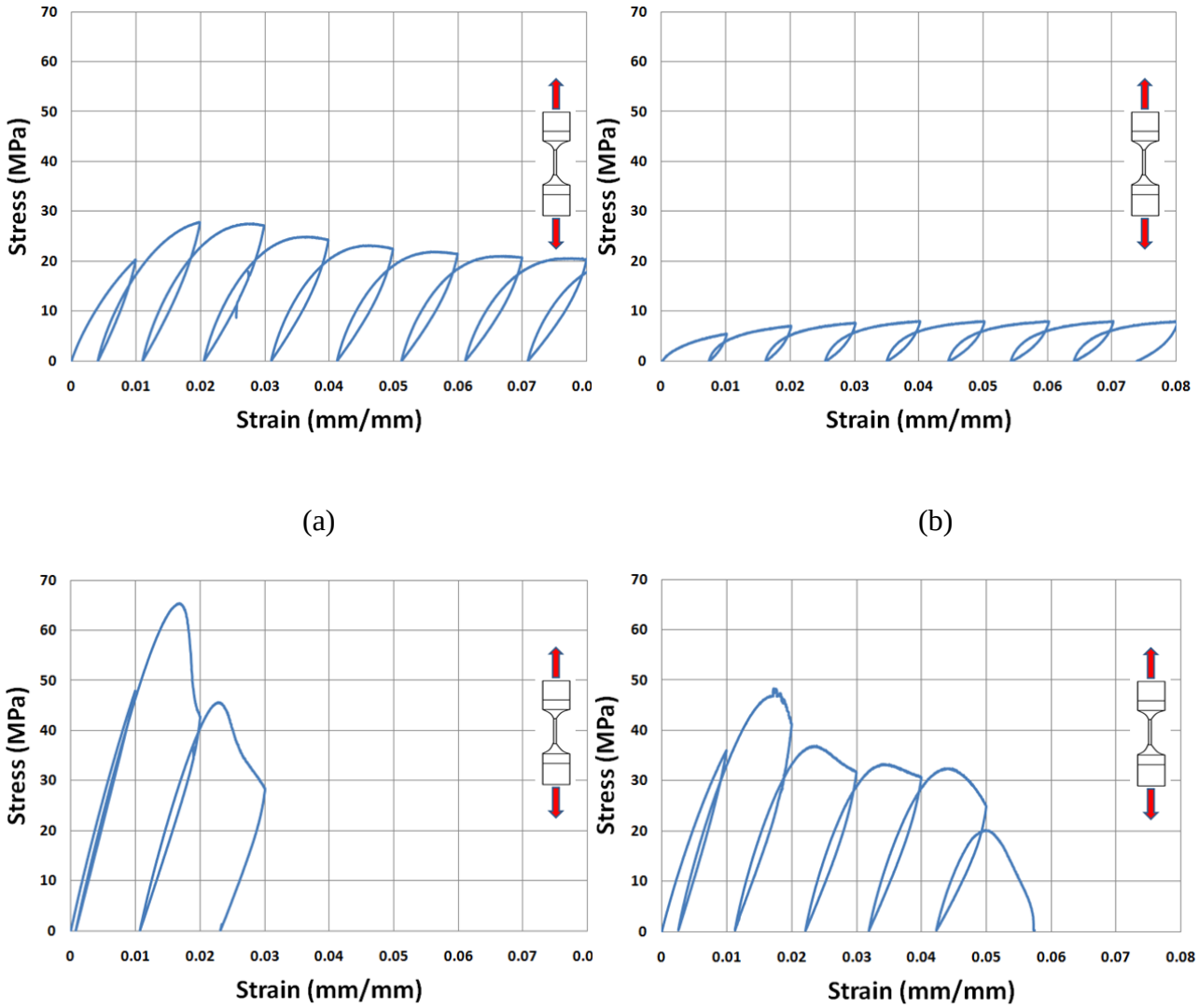

Figure 5-15: 2nd batch of resin specimen with EPIKURE 3274 as hardener. (a) Specimen M10 (b) Specimen M30 (c) Specimen N10 (d) Specimen N30

From figure 5-15, it is evident that the specimens M10 and M30 with EPON 862 epoxy system exhibited higher elongation capabilities as compared to specimens N10 and N30 with EPON 828 epoxy. Although specimen N10 and N30 showed higher strength and stiffness, prime characteristics of high strains was achieved using EPON 862 epoxy system. Based on results, M10 type resin matrix which showed ductility exceeding 4.7, was selected for all future composite manufacturing due to its excellent elongation properties, while maintain reasonably steady stiffness and strength in each subsequent cycle.

5.4.2 Pure (100%) SMA composite specimen

After a trial procedure involving SMA wire training and selection of resin system compatible with the superelastic behavior of SMA material, both materials were combined to form fully reinforced SMA composite (FRC). Detailed procedure of manufacturing and combination of SMA composite has already been explained in section 4.3.3. Table 4.8 showed the three SMA composite samples with 3, 7 and 13 trained embedded SMA wires, having as 8.46%, 20.3% and 6.48% reinforcement ratio, respectively. Initially, two specimen FRC-3 and FRC-7 were subjected to tensile loading protocol with each cycle incremented relatively by 1% strain. Later FRC-13 specimen was subjected to tension-compression cyclic loading protocol discussed in section 5.5. Figure 5-16 shows the schematics of close up of SMA-FRP composite specimen loaded in mechanical grips. Figure 5-17 shows the picture of FRC-7 specimen in mounted in the mechanical grips with extensometer. Figure 5-18 shows stress train curve of both, FRC-3 and FRC-7 specimens.

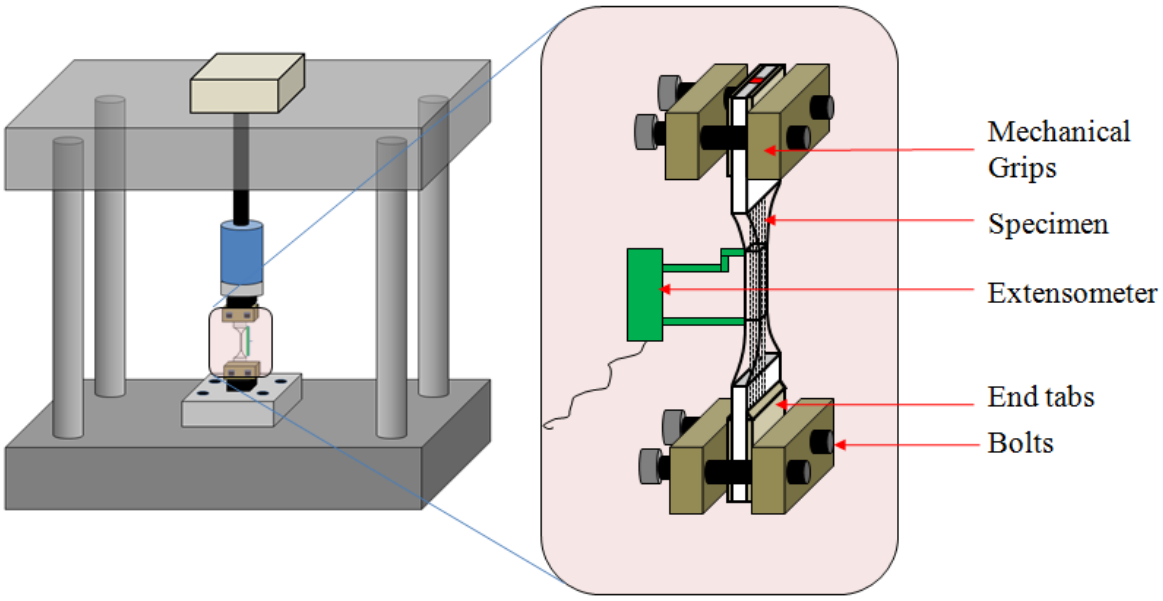

Figure 5-16: Schematics of close up of SMA-FRP composite specimen loaded in mechanical grips

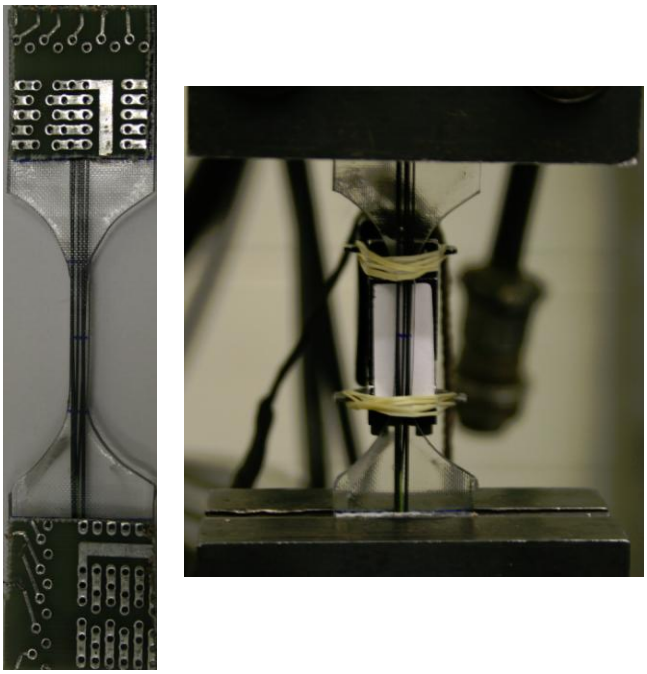

Figure 5-17: FRC-7 specimen in mounted in the mechanical grips with extensometer

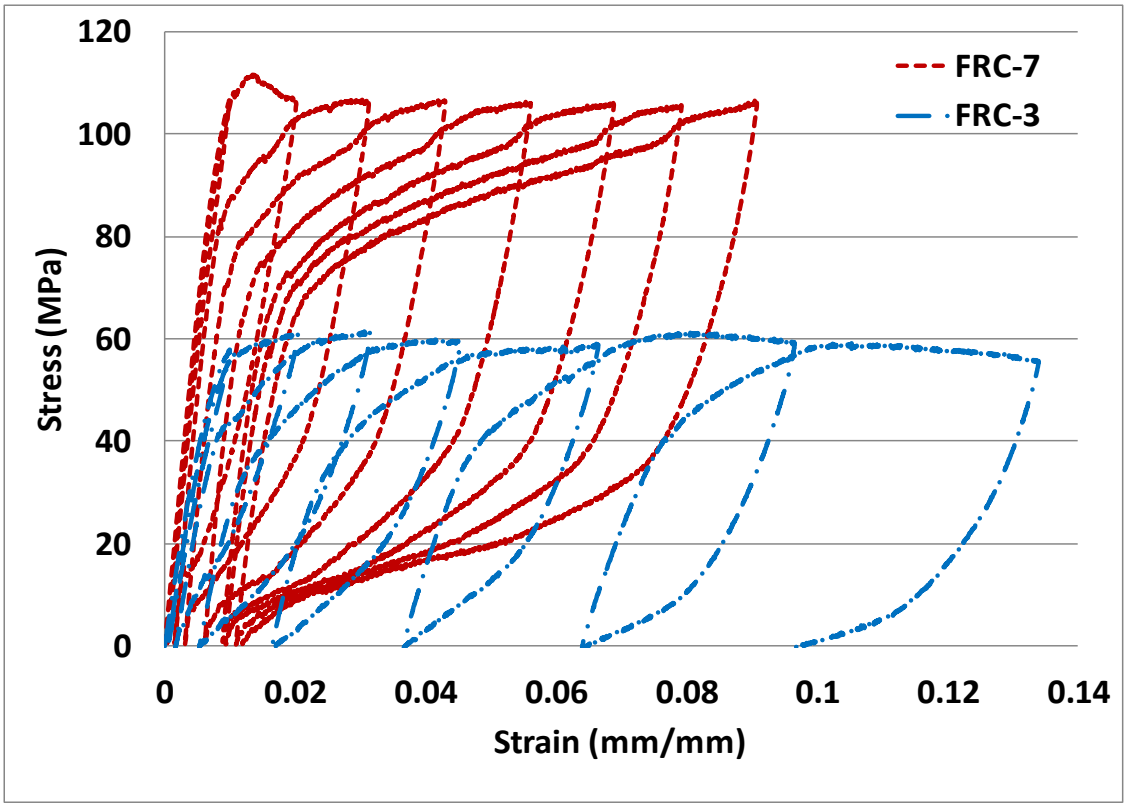

Figure 5-18: Stress strain curves of FRC-3 and FRC-7 specimens

Cycle wise comparison of FRC-3, FRC-7 and M10 resin system stress strain curves has been shown in figure 5-19 for strain levels of 1%, 3%, 5% and 7 %. Results show much improved performance of SMA composite (FRC-3 and FRC-7) in terms of stiffness, hysteresis area and residual strains as compared to resin specimen (M10). FRC-7 specimen showed much wider hysteresis as compared to both FRC-3 and M10 specimens. M10 specimen showed high accumulation of residual strain in each cycle as the specimen underwent more inelastic cycles. Once 3 SMA wires (FRC-3 with 8.46% reinforcement ratio) were embedded into the same resin, the residual strains were lowered significantly. Reduction in residual strains was further

improved by embedment of 7 SMA wires. Figure 5-20 shows plot between residual strains accumulated in each cycle for all three specimens.

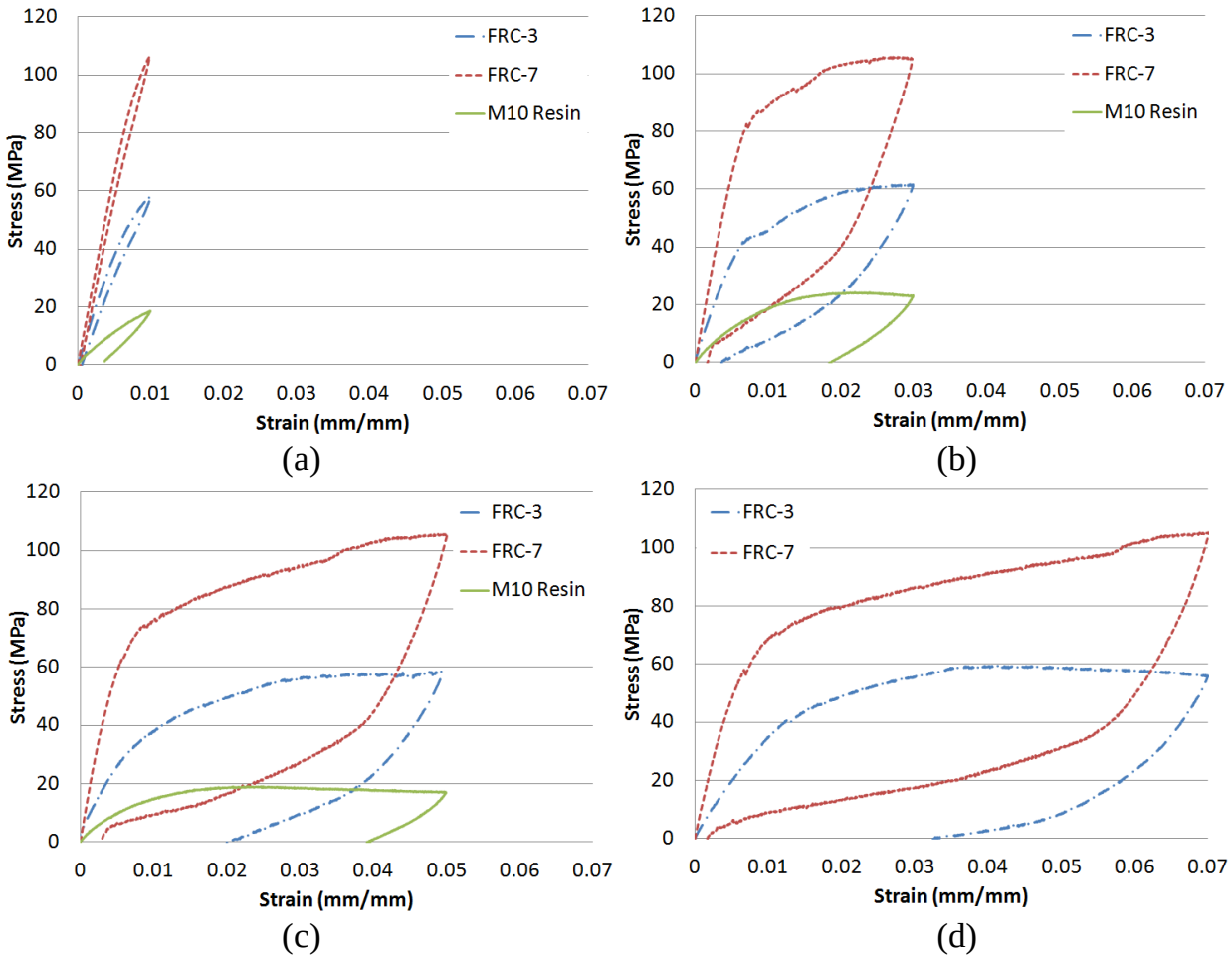

Figure 5-19: Cycle wises comparison of stress strain curves of FRC-3, FRC-7 and M10 resin specimens (a) 1% strain cycle (b) 3% strain (c) 5% strain (d) 7% strain

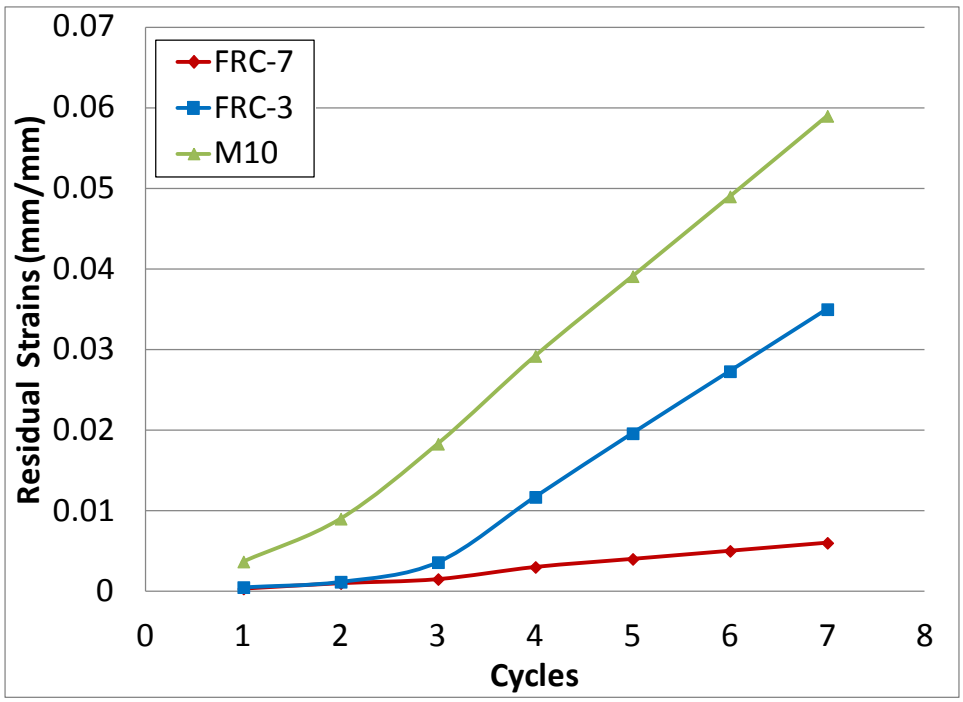

Figure 5-20: Plot of residual strains vs. cycles for FRC-7, FRC-3 and M10 specimens

Results show that FRC-3 and FRC-7 specimen had 45% and 89% less residual strain as compared to M10 specimen for the 7% strain (7^{th}) cycle. This reduction in residual strains, points out the re-centering capability of SMA composite reinforcement, which combined with wider hysteresis (energy dissipation) is an important characteristics, especially in the high seismic zones. Thus it can be concluded that, with increase in reinforcement ratio of SMA wires in composite, better composite behavior in terms of strength, stiffness and accumulation of residual strains is exhibited. Because of superior performance, FRC-7 composite specimen was considered as bench mark for additional manufacturing of SMA-FRP hybrid composite.

5.4.3 FRP composite specimen

Instead of embedding SMA wires into the resin matrix, conventional fibers are used as primary reinforcing material. As mentioned before, three types of conventional fibers, namely E-glass, S-glass and Kevlar were explored for manufacturing FRP composite.

5.4.3.1 E-glass composite

Resin matrix was embedded with E-glass fabric to produce composite specimen which was tested under cyclic tension until the rupture of the specimen. Stress strain curve for the E-glass composite is shown in figure 5-21. Plot shows failure of the composite specimen at strain of 2.2% with modulus of 14.7 GPa. Because of low elongation before rupture, E-Glass was not explored further as a constituent for fabrication of SMA-FRP hybrid composite.

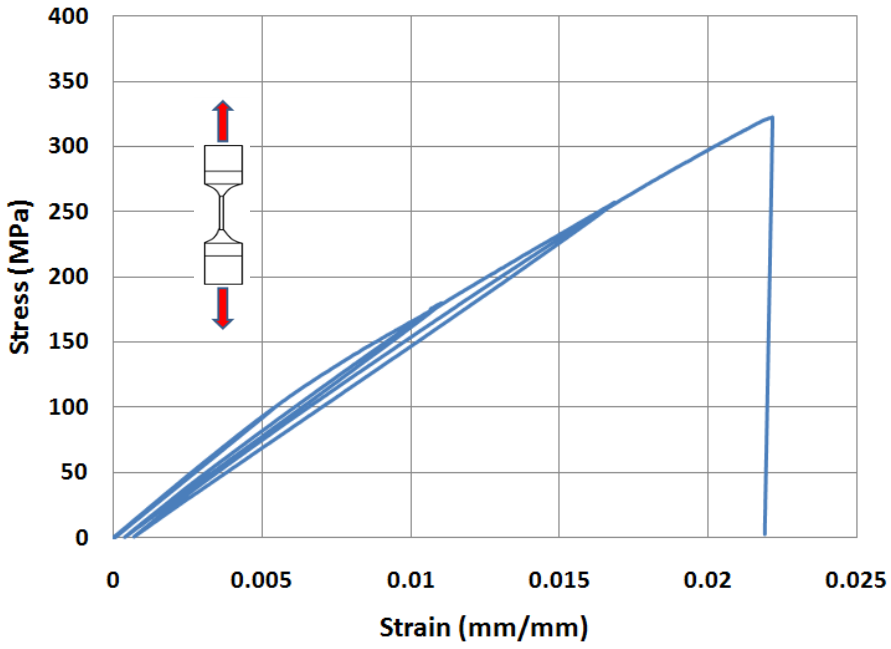

Figure 5-21: Stress strain curve of E-glass composite specimen

5.4.3.2 Kevlar composite

Kevlar fabric embedded resin composite was tested under cyclic loading until rupture of the specimen. Kevlar fibers are known for their toughness with decent stiffness and elongation characteristics. Stress strain curve of Kevlar based composite is shown in figure 5-22. Plot shows rupture of composite at strains of 2.5%. Kevlar composite also showed accumulation of residual strains in four cycles to which it was subjected to. Because of lower elongation before rupture, Kevlar was not explored further for SMA-FRP hybrid composite.

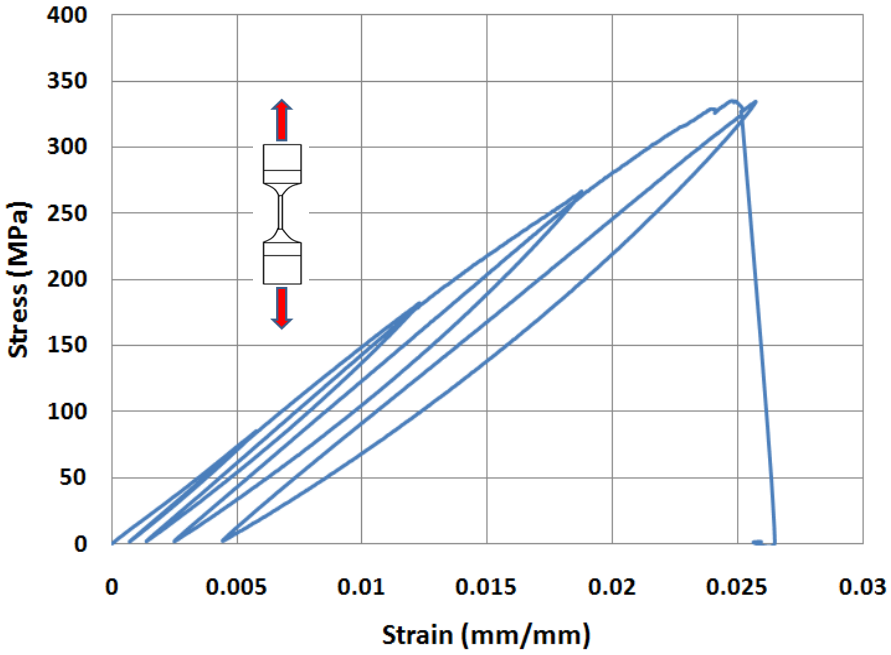

Figure 5-22: Stress strain curve of Kevlar composite specimen

5.4.3.3 S-Glass composite

Because of excellent elongation properties amongst all conventional fibers, S-Glass was investigated in more detail by manufacturing and testing, nine GFRP composite specimens.

GFRP unidirectional strands, as shown in figure 4-14 were used to manufacture these nine GFRP composite specimens. Stress strain curves for four of these specimens are shown in figure 5-23.

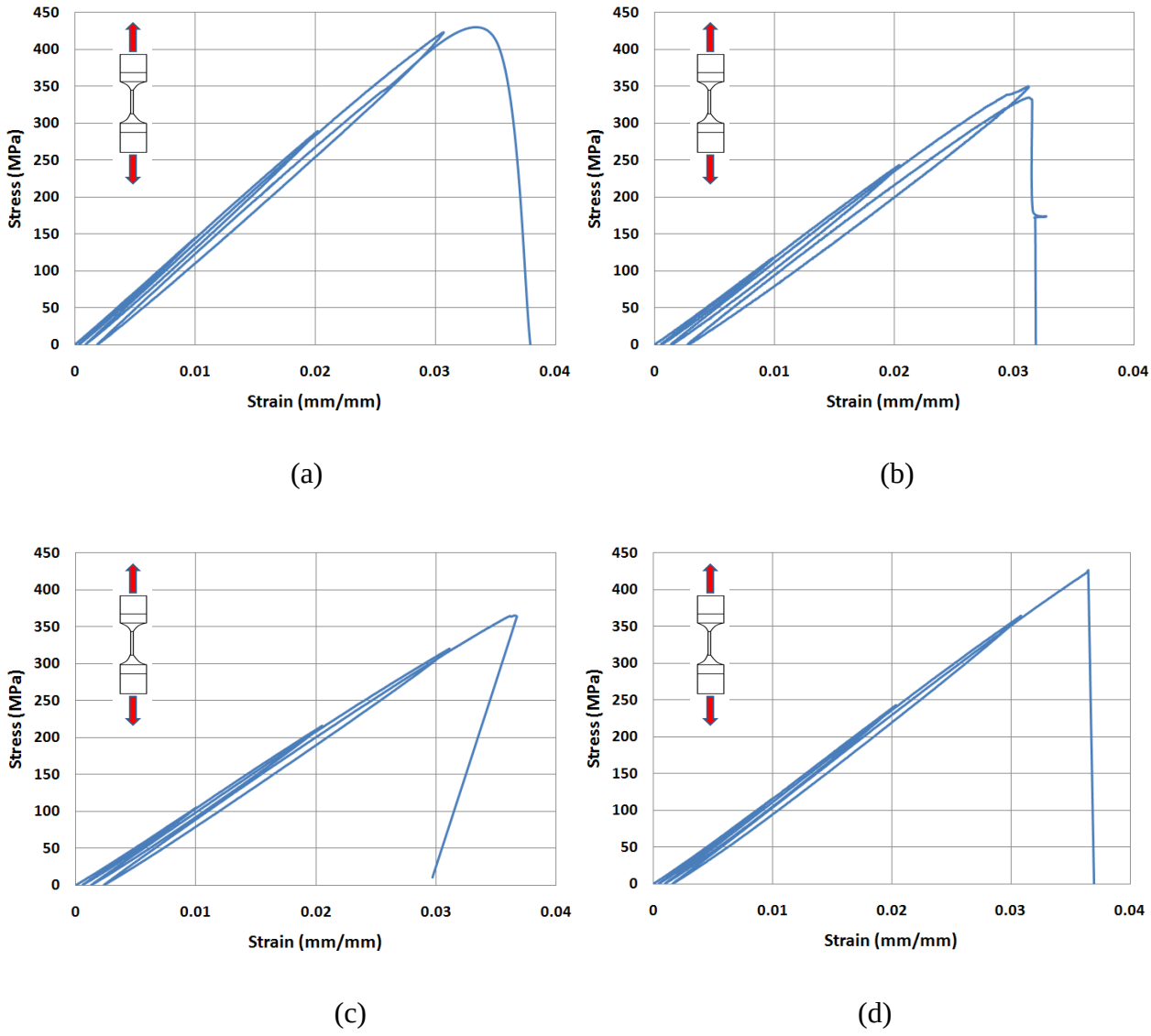

Figure 5-23: Stress strain curves of GFRP composite specimens (a) S-1 (b) S-2 (c) S-3 (d) S-4

A summary of the test results from all nine GFRP composite specimens is shown in Table 5-2. Table shows maximum stress corresponding to rupture strain, along with modulus of composite. The average rupture strain was 3.4%, while average modulus of these nine GFRP composite specimens was 11.94 GPa. Because of sustenance of high strains (3.4%) by fibers before rupture, glass fibers were considered ideal for manufacturing of SMA-FRP hybrid composite.

Table 5-2: Rupture strain and Young's modulus of GFRP composite specimens

Single Strand GFRP Composite Specimens					
Specimen	Stress (max)	Rupture Strain	Modulus (1st Cycle)		
	(MPa)	(mm/mm)	Stress (MPa)	Strain (mm/mm)	E (GPa)
S-1	420.5767	0.033	144.444	0.01	14.444
S-2	358.5244	0.032	117.968	0.01	11.797
S-3	365.4191	0.036	104.937	0.01	10.494
S-4	420.5767	0.036	115.969	0.01	11.597
S-5	579.1548	0.0375	157.613	0.01	15.761
S-7	324.0509	0.032	104.937	0.01	10.494
S-8	337.8403	0.032	105.006	0.01	10.501
S-9	311.64044	0.035	104.662	0.01	10.466
Average		**0.034**			**11.94**

5.4.4 Design of SMA-FRP hybrid composite specimen

After a tedious procedure of manufacturing and testing, ingredients for SMA-FRP hybrid composite were narrowed down to EPON 862, EPIKURE 3274 and Heloxy-48 resin type, S-glass FRP and NiTi SMA wires. However, since the reinforcement ratio of SMA and Glass fibers in the composite significantly affects the mechanical properties, composite was required to be designed to achieve desired target properties. As a bench mark, FRC-7 composite with 7

SMA wires was utilized in terms of setting target stiffness for the SMA-FRP hybrid composite. For this purpose, modulus (E) for S-glass along with relationship between fiber volume fraction (FVF) and quantity (by weight) of S-glass fiber is required. Six GFRP samples were produced by the combination of glass fibers and M10 resin matrix, with varying FVF. 112 mm long glass fiber strands were first weighted and then were embedded into the resin matrix. The quantity of glass fibers was intentionally varied with the aim to get a relationship between weight of glass fibers and their FVF for subsequent use in design of hybrid composite. After curing the specimens in hot press under constant pressure and temperature, specimens were tested under quasi-statically under tension. Results of stress strain plot of these weighted GFRP composite specimens are shown in figure 5-24. Summary of the test results has been shown in table 5-3.

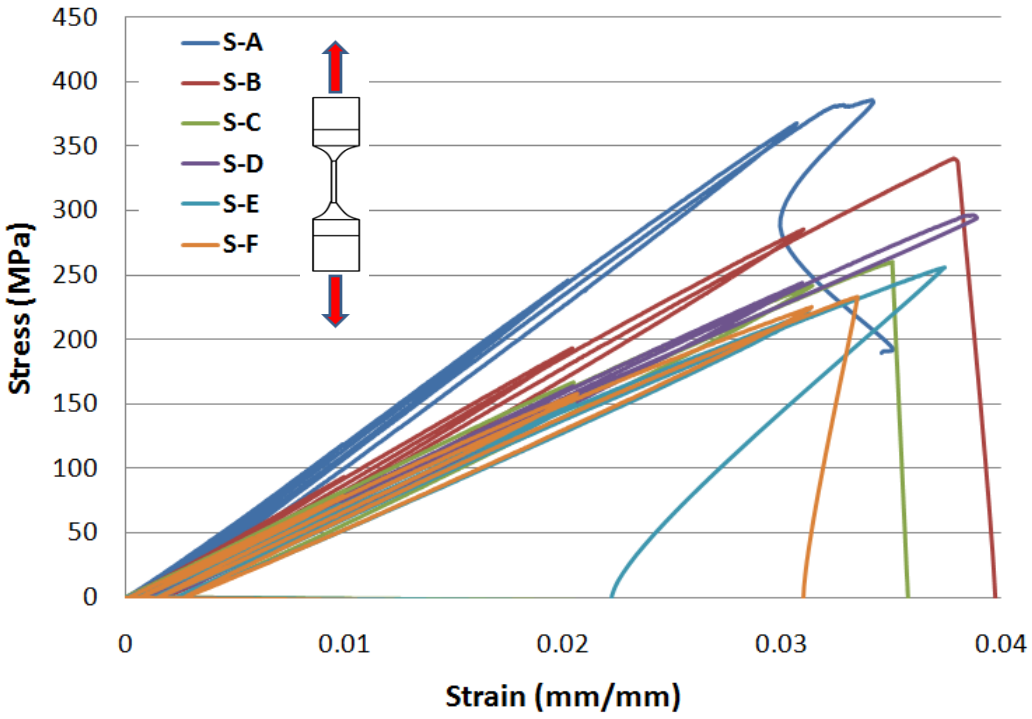

Figure 5-24: Stress strain curves of weighted GFRP composite specimens

Table 5-3: Rupture strains and Young's modulus of weighted GFRP composite specimens

Weighted GFRP Composite Specimens						
Specimen	Weights of 112 mm long (gm)	Stress (Max) (MPa)	Rupture Strain (mm/mm)	Modulus (1st Cycle) Stress	Strain	E_c (GPa)
S-A	0.2278	378.17	0.033	105	0.01	10.5
S-B	0.1945	337.91	0.037	93.49	0.01	9.349
S-C	0.1867	257.72	0.034	82.94	0.01	8.294
S-D	0.1678	293.51	0.0379	78.32	0.01	7.832
S-E	0.1589	253.72	0.0368	71.84	0.01	7.184
S-F	0.1186	231.52	0.033	70.95	0.01	7.095

As seen from, table 5-3 and figure 5-24, specimen S-A had the maximum glass fiber weight embedded during the manufacturing process and hence the maximum stiffness (modulus) amongst all six specimens. Specimen S-F had least weight of glass fiber strand, and hence the least modulus. From this test, a pattern emerged which suggested a correlation between the FVF of 112 mm long glass fibers embedded in the composite and modulus of composite (E_c). In order to conceive this relationship, a post processing technique to find out FVF by doing 'burn-off test' was conducted which has been explained in figure 4-11. Results from these tests have been summarized in table 5-4. Knowing the FVF, the relationship between modulus of composite and quantity of glass fibers in composite can be evaluated. This relationship has been shown in figure 5-25. Figure 5-25 also shows linear best fit for the relationship between modulus and FVF.

Table 5-4: Results from burn-off tests on weighted GFRP composite specimen

Sample	Original weight of Fiber	Weight of Container	Composite						GFRP			
			Length	Thickness	Width	Volume	Comp + container	Weight of Comp	GFRP + container	Weight of GFRP	Volume	FVF (%)
	(gm)	W (gm)	L (mm)	T (mm)	W (mm)	V1 (cm^3)	W1 (gm)	W2 (gm) =W1-W	W3 (gm)	W4 (gm) = W3-W	V2 (cm^3) =W4/D*	V2/V1
S-A	0.2278	16.5715	25.5	2.5908	2.286	0.1510255	16.7536	0.1821	16.6133	0.0418	0.01672	**10.8**
S-B	0.1945	17.6082	23.76	2.7432	2.667	0.17383088	17.8524	0.2442	17.6455	0.0373	0.01492	**9**
S-C	0.1867	16.7156	7.62	2.8956	2.6416	0.05828551	16.7928	0.0772	16.7245	0.0089	0.00356	**8.0041**
S-D	0.1678	16.4326	24.57	2.2606	2.7178	0.15095461	16.6632	0.2306	16.4718	0.0392	0.01568	**7.5**
S-E	0.1589	16.1008	15.47	3.1242	2.413	0.11662361	16.2461	0.1453	16.1196	0.0188	0.00752	**6.44809**
S-F	0.1186	2.6032	23.25	2.159	2.8956	0.14534971	2.8044	0.2012	2.6262	0.023	0.0092	**6.32956**

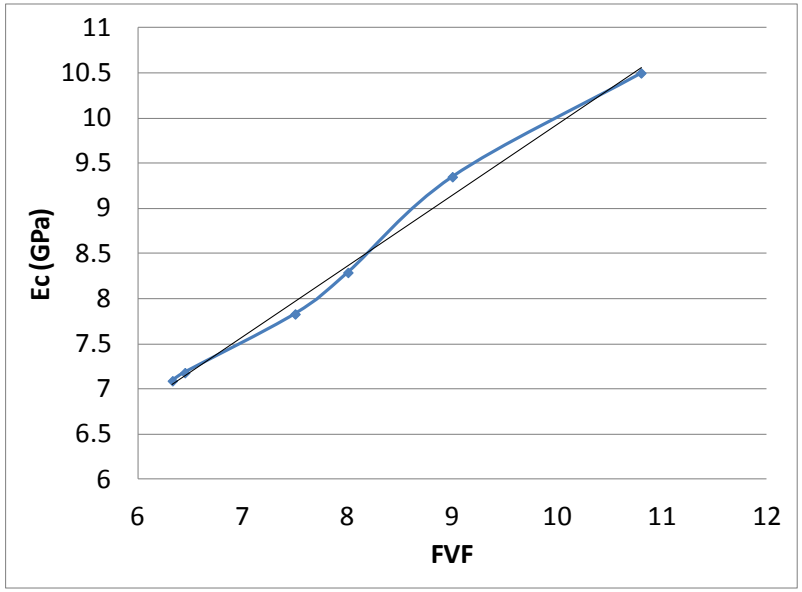

Figure 5-25: Relationship between FVF of glass fiber and modulus of composite (E_c)

Once glass fiber strand was embedded into resin matrix, the fibers were oriented to align with longitudinal axis of the specimen. In other words, the fibers are parallel to the direction of the load application. This configuration makes the constituents of composite behave in parallel and have been shown in a schematic in figure 5-26.

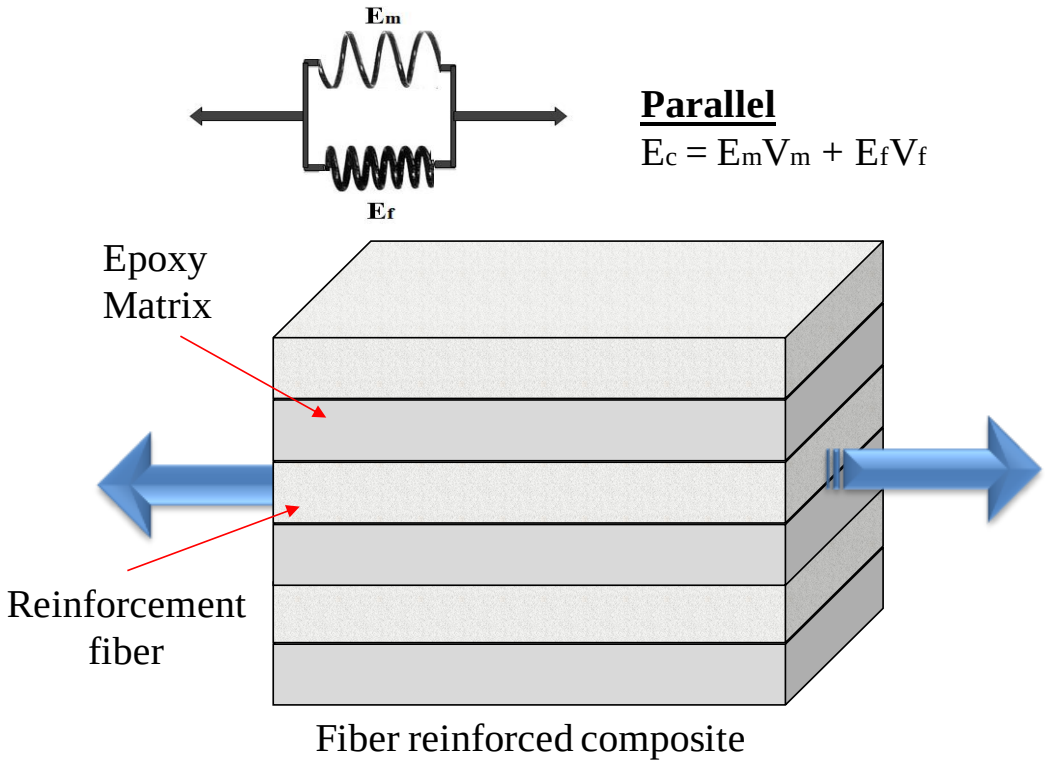

Figure 5-26: Schematics of composite behaving in parallel

In figure 5-26, E_c, E_m and E_f are the modulus of composite, resin matrix and glass fibers, respectively. V_m and V_f are the FVF of resin matrix and glass fibers. Having known all the parameters in the equation of parallel material, modulus of glass fibers strands (E_f) could be found for all six specimens. Summary of this calculation is shown in table 5-5. Calculations show very similar values of E_f (Average of 86.7 GPa), which is of course expected and confirms the role of mixtures for elastic modulus.

Table 5-5: Results from burn-off tests on weighted GFRP composite specimen

Specimen	Modulus of Elasticity				
	Fiber volume fraction	Matrix fraction	Modulus of Matrix	Modulus of Composite	Modulus of Glass Fiber
	(V_f)	(V_m)	(E_m)(GPa)	(E_c)(GPa)	(E_f)(GPa)
S-A	0.108	0.892	1.57	10.5	84.26
S-B	0.09	0.91	1.57	9.35	88.01
S-C	0.080041	0.919959	1.57	8.29	85.53
S-D	0.075	0.925	1.57	7.83	85.04
S-E	0.064480943	0.9355191	1.57	7.18	88.57
S-F	0.06329562	0.9367044	1.57	7.09	88.78
					86.7

Knowing the E_f (86.7 GPa), E_m (1.57 GPa) and FVF, a plot between modulus and FVF for GFRP composite was generated. Since this is a linear relationship, so the two extreme spectrum of this plot would be pure epoxy with zero fiber volume (V_f) and pure fiber with V_f equal to 1. Figure 5-27 shows this relationship with all computed E_c lying on this line. This also serves as a check for correctness of computation and experimental test results.

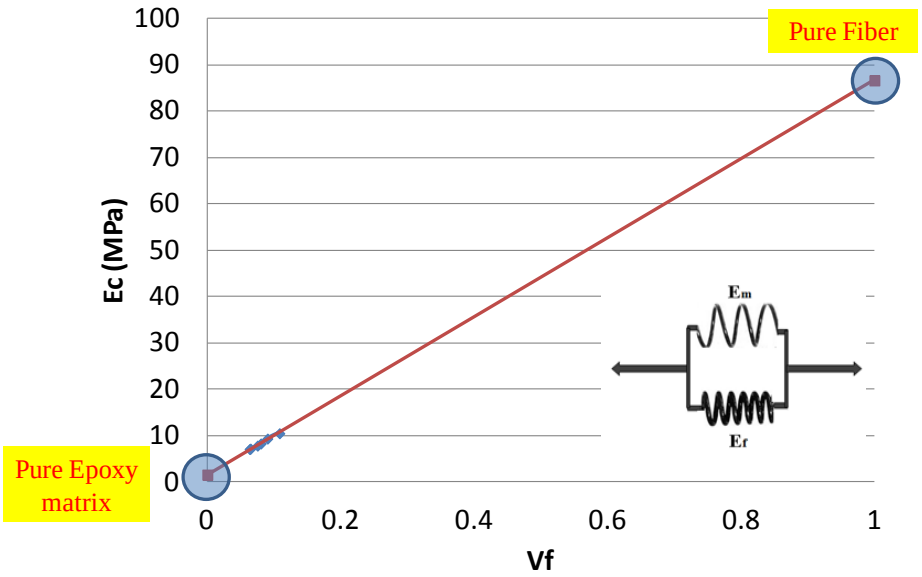

Figure 5-27: Schematics of composite behaving in parallel

Knowing the modulus of glass fibers (E_f) and relationship between modulus of composite (E_c) and FVF (V_f), design of SMA-FRP Hybrid can be conducted based on target modulus. SMA wires which were available for use in manufacturing of SMA-FRP hybrid composite was from batch-4 with 5-wires, shown in table 5-1. Since the wires have already been trained, so the modulus of SMA (E_{SMA}) wire at the end of last cycle, 60.12 GPa was taken as input for design calculations. The design of SMA-FRP hybrid composite was aimed at achieving a certain target modulus of composite (E_c) by varying the reinforcement ratio (SMA wires + Glass fibers). This target modulus was kept to be similar modulus achieved with FRC-7 composite (13.74 GPa). Equation 5-1 shows the relationship between SMA, GFRP and epoxy matrix constituents, once combined in parallel.

$$E_c = E_f V_f + E_{SMA} V_{SMA} + E_m V_m \qquad (5\text{-}1)$$

With SMA fraction known for different SMA wire combinations (known volume), equation 5-1 can be rearranged to find the volume fraction of glass fiber strand (V_f), needed to reach the target modulus (E_c) of 13.74 GPa. Equation 5-2 shows the rearranged version of equation 5-1.

$$V_f = \frac{E_c - E_{SMA}V_{SMA} - E_m V_m}{E_f} \tag{5-2}$$

Table 5-6, shows seven different options available for design of SMA-FRP hybrid composite with different number of SMA wires and different V_f of glass fiber strand. With volume of composite, % of reinforcement, modulus of composite, modulus of epoxy matrix, modulus of glass fibers and modulus of SMA wires known, fraction of glass fibers (V_f) required to reach target stiffness, can be estimated for different design options.

Table 5-6. Design options for SMA-FRP hybrid composite

Design Options	**SMA-FRP Hybrid Composite**				
	SMA Wires	**SMA Area (mm^2)**	**SMA Fraction (V_{SMA})**	**GFRP Fraction (V_f)**	**Constants**
Option 1	1	0.2	0.03	0.13	Area of specimen = 7.54 mm^2
Option 2	2	0.39	0.05	0.11	Percentage of reinforcement = 17%
Option 3	3	0.59	0.08	0.09	Area of reinforcement = 1.51 mm^2
Option 4	4	0.79	0.10	0.07	E_{SMA} = 60.12 GPa,
Option 5	5	0.98	0.13	0.05	E_m=1.57 GPa
Option 6	6	1.18	0.16	0.04	E_f = 86.7 GPa,
Option 7	7	1.38	0.18	0.02	E_c = 13.741 GPa

Table 5-4 gives relationship between FVF and weight of glass fiber strands. This relationship is plotted in figure 5-28, which shows linear relationship between the weight of glass fibers in the composite and the FVF.

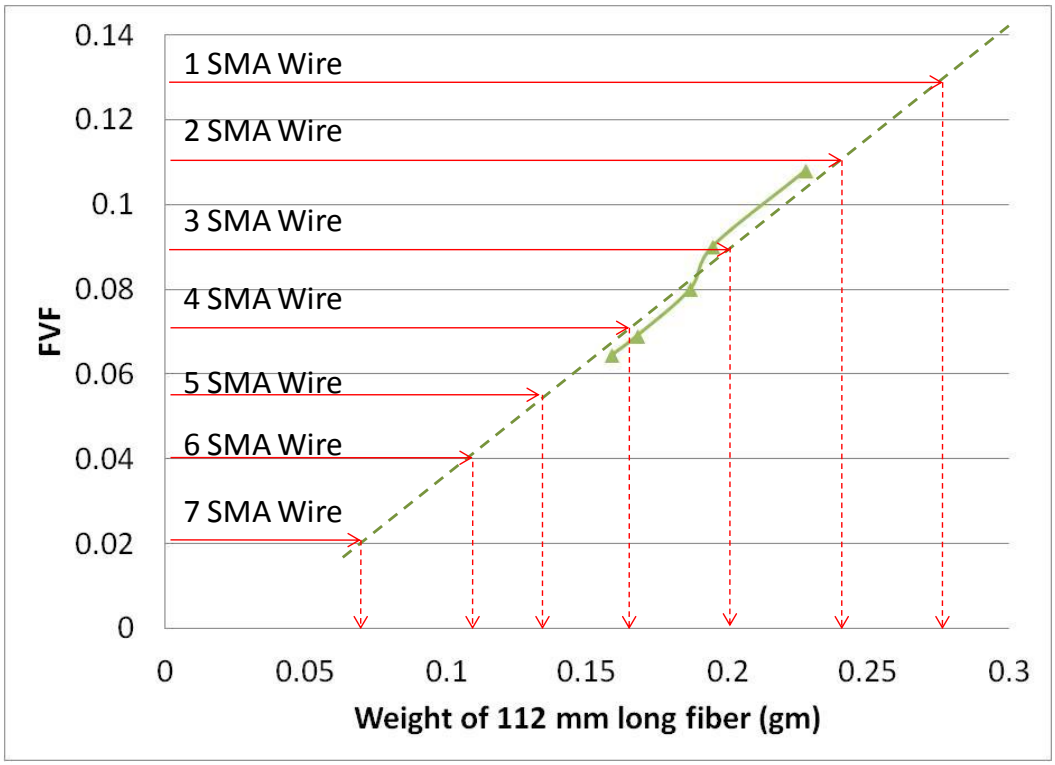

Figure 5-28: Relationship between FVF and weight of 112 mm long glass fibers

After the linear relationship was plotted, seven design options with varying number of SMA wires were plotted to find the weight of glass fiber needed in the composite to reach the target stiffness. Based on above findings, varying combinations of SMA and glass fiber strands could be used to manufacture SMA-FRP hybrid composite.

5.4.5 SMA-FRP hybrid composite specimen

Pure SMA (FRC-7) composite was able to dissipate energy due to hysteresis of SMA wire with negligible residual strains and is considered ideal for high seismic zone applications. However if high stiffness and strength, along with reasonable energy dissipation is needed, for a structure with low seismic hazard, then SMA-FRP hybrid composite named hereafter as partially reinforced composite (PRC) reinforcement will be a more preferable option. The main idea to manufacture SMA-FRP hybrid composite is to give the structure inherent stiffness and strength, which is associated with GFRP, but at same time be able to experience super-elastic behavior by dissipating energy. Two different configurations of SMA-FRP hybrid composite, option-3 and option-5, with 3 SMA wires with 0.19 gm of 112 mm long glass fiber (PRC-3) and 5 SMA wires with 0.13 gm of 112 mm long glass fiber (PRC-5), respectively and were embedded in resin matrix. The composite specimen PRC-3 and PRC-5 were tested under same loading protocol as discussed earlier in this chapter. The result of stress strain curve of PRC-3 is being shown only in figure 5-29. The PRC-3 specimen ruptured at a strain of 3.2%.

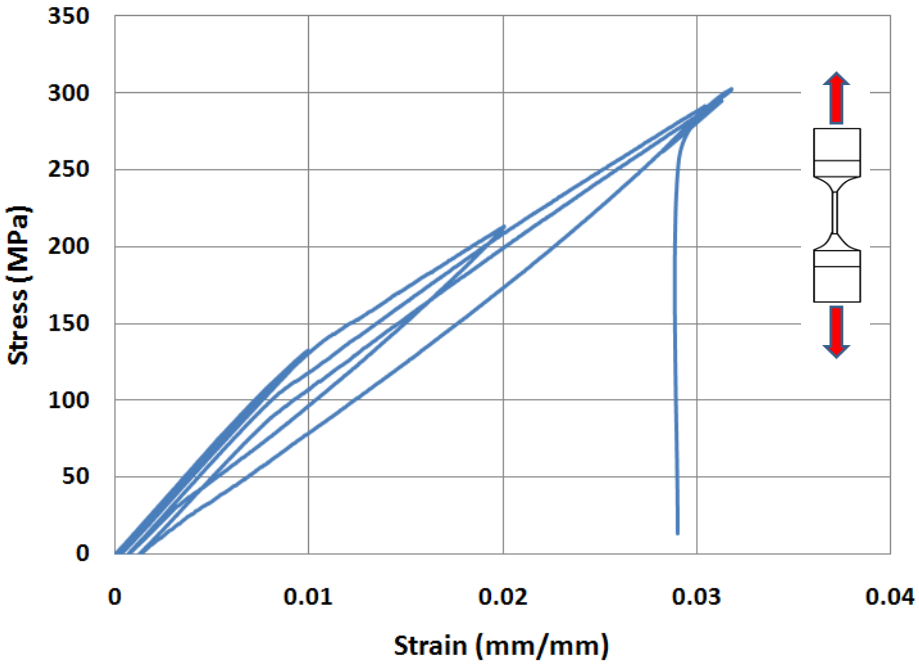

Figure 5-29: Stress strain plot of SMA-FRP hybrid composite (PRC-3)

In order to compare all the manufactured composites, a cycle wise stress strain plot has been shown in figure 5-30. PRC-3 and PRC-5 specimens ruptured at a strain of 3.2% and 3.3% respectively, with reasonable hysteretic area. The computed modulus of elasticity of PRC-3 and PRC-5 was found to be 13.5 GPa and 13.3 GPa, respectively, which was very close to the target modulus of 13.7 GPa. Results also show change in stiffness of composite after reaching strain of 0.8% due to forward transformation of SMA from austenite to martensite phase. Results reveal that the PRC specimens while exhibiting reasonable elongation and hysteretic properties also show higher stiffness and strength behavior in comparison with FRC specimens, while the SMA wires undergo austenite to martensite phase transformation (post-yield behavior). After experiencing elongation of up to 3% strains, residual strains were 0.08% and 0.21%, while maximum stress levels achieved were 302 MPa and 215 MPa for PRC-5 and PRC-3 specimens,

respectively. Both stiffness and strength of hybrid SMA-FRP composite specimen were improved compared to that of the 100% SMA-FRP, while the 100% SMA-FRP composite exhibited better ductility and energy dissipation capability. This shows that both types of composites have their own advantages; hence could be used for different applications.

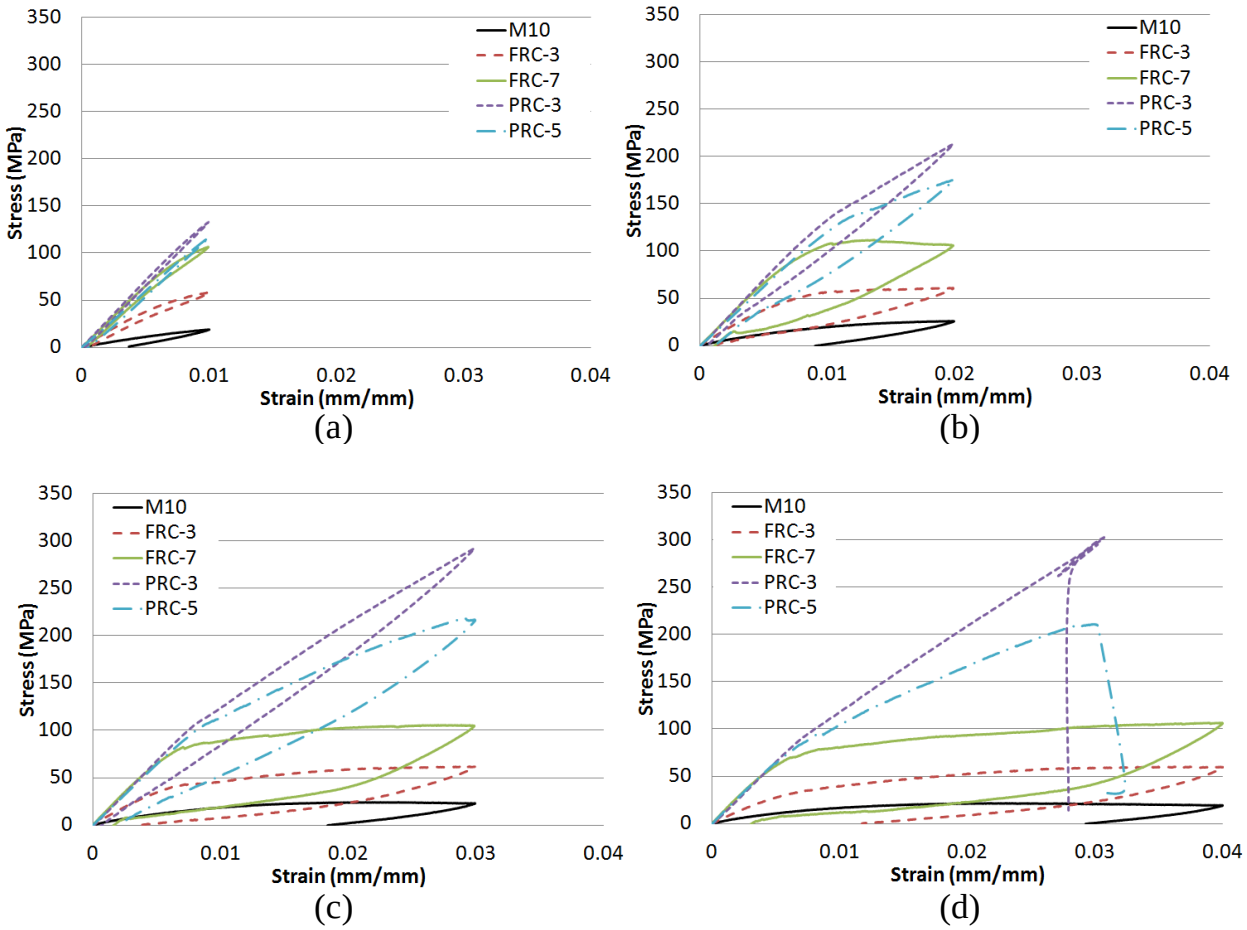

Figure 5-30: Cycle wises comparison of stress strain curves of FRC-3, FRC-7, M10 resin, PRC-3 and PRC-5 specimens (a) 1% strain cycle (b) 2% strain (c) 3% strain (d) 4% strain

5.5 SEM imaging of composite specimens

Scanning electron microscope (SEM) is a powerful magnification tool that utilizes focused beams of accelerated electrons to generate a variety of signals at the surface of solid specimens. A significant amount of kinetic energy is carried by these electrons, and this energy is dissipated as electrons de-accelerate resulting in variety of signals produced. These signals include secondary electrons (that produce SEM images), backscattered electrons (BSE), and diffracted backscattered electrons, photons and heat. These signals can then be used to generate high-resolution images that provide topographical, morphological and compositional information which makes them invaluable in a variety of science and industry applications. Electron microscopes utilize the same basic principles as light microscopes, but focus beams of energetic electrons rather than photons, to magnify an object. Areas ranging from approximately 1 cm to 5 microns in width can be imaged in a scanning mode using conventional SEM techniques (magnification ranging from 20X to approximately 200,000X, spatial resolution of 50 to 100 nm). Unlike optical electron microscopes, image magnification in the SEM is not a function of the power of the objective lens. SEM can also detect and analyze surface fractures, provide information in microstructures, examine surface contaminations, reveal spatial variations (void ratio) in chemical compositions and identify crystalline structures and crystal orientations.

Scanning electron microscope images have been used in the past to study the composite material characteristics. Otsuka et al. (2002) have used SEM images to study the manufacturing technique for SMA-CFRP composite specimens. The SEM images help in understanding delaminating, bond issues, void growth after cyclic loading, and damage to glass fibers in addition to any other potential issues with SMA-FRP hybrid composite reinforcement.

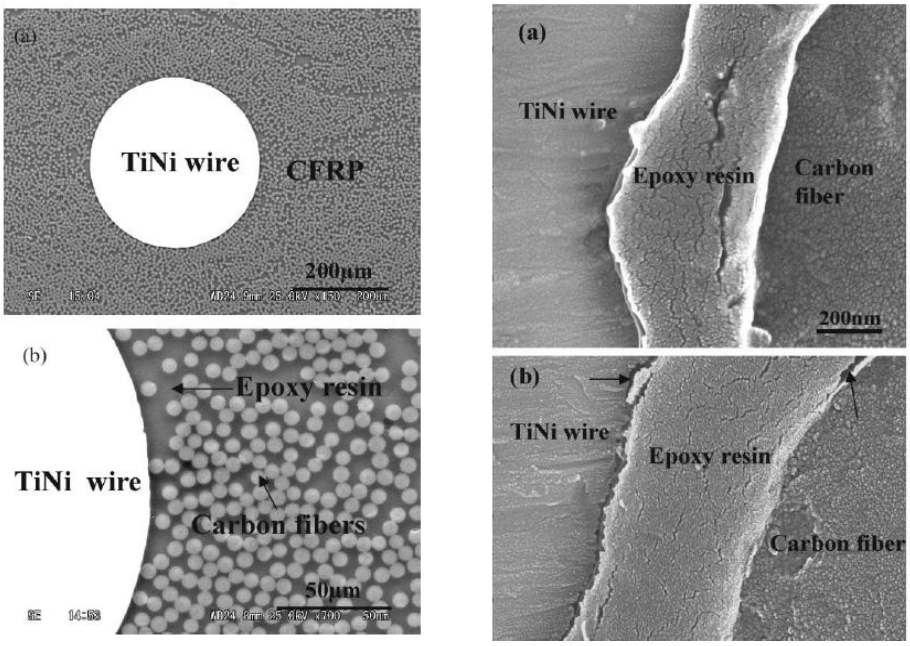

Figure 5-31: SEM images of SMA-CFRP composite (Otsuka et al. 2002)

SEM imaging can be used in variety of applications in the study of solid materials and are critical in all fields that require characterization of solid materials. Although they come with many advantages, they also have some limitations. Samples must be solid and they must fit into the microscope chamber. Maximum size in horizontal dimensions is usually on the order of 4 cm, vertical dimensions are generally much more limited and rarely exceed 40 mm. In most of the cases, an electrically conductive coating must be applied to electrically insulate the samples for study. Decent sample surface preparation is also needed for all the images, depending on application type. For this study, SEM images were being utilized to investigate the damages like de-bonding / de-lamination between resin and SMA, fracture of FRP fibers, efficacy of resin in filling all air voids and overall layout of composite specimen. For this purpose, all the composites specimens used for SEM imaging were acquired from tested / damaged specimens

and thus needed surface polishing and preparation. The equipment used to acquire SEM for this study has been shown in figure 5-32. The software used for getting SEM images was user friendly with wide range of options to allow focusing, aperture centering and removal of astigmatism, normally associated with SEM images.

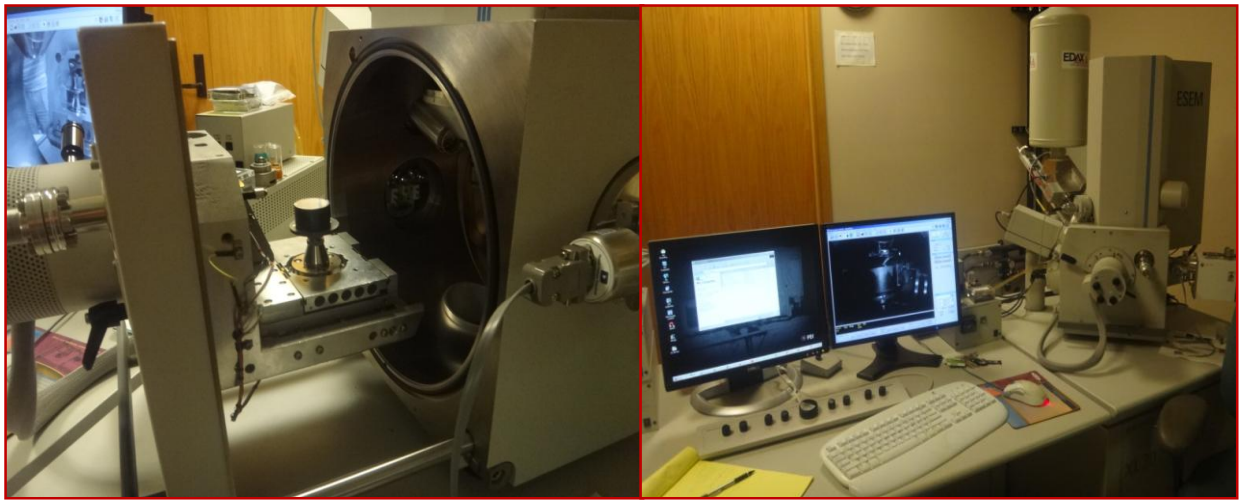

Figure 5-32: Imaging chamber and software module used to acquire SEM images

5.5.1 Sample preparation and polishing

In order to evaluate the surface of the composite, the damaged specimens were bisected to get a clean cut of the cross section area. For this purpose, carbide milling technique at 60000 RPM was used to first mill the composite specimen in order to get a fine cut. These acquired cross sections were then placed in a plastic circular mould with resin poured to act as support during polishing procedure in an automated polisher. Buehler ecomet polishing equipment was used to grind and polish six specimens at the same time. The polishing equipment allows control of RPM, time for polish, force level exerted on the specimen through polishing head and

direction of rotation. Since both the polishing head and polishing plate rotate, the direction can be controlled by either having it contrary to each other or complimentary to each other. Water sprinkler is used to keep the specimens wet during the polishing of the mounted specimens. Polishing setup along with mounted composite specimens is shown in figure 5-33.

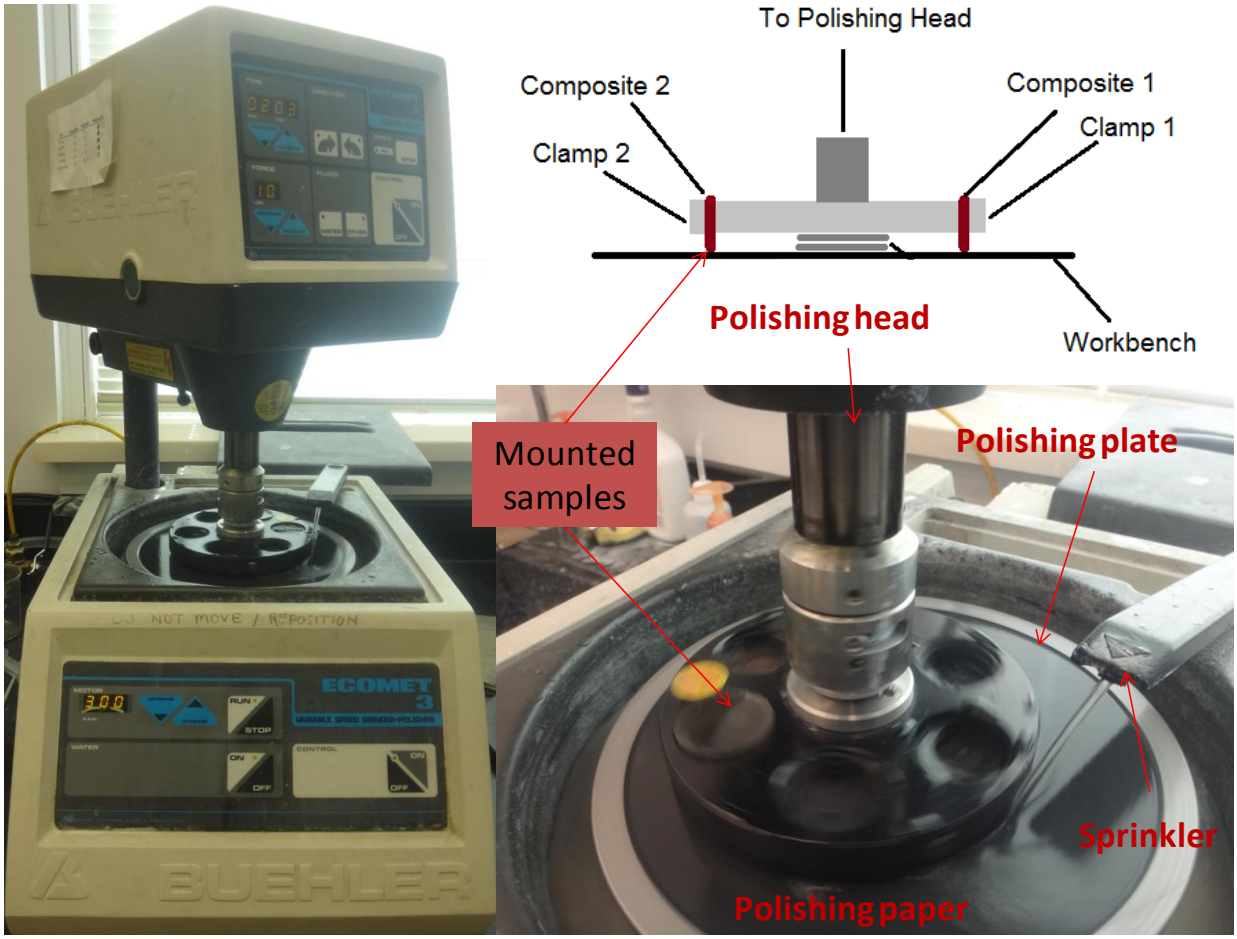

Figure 5-33: Polishing equipment along with mounted composite specimens

Four different polishing papers with 320, 600, 800 and 1200 grit were used to first grind the specimen. 320 grit paper being most course, is used first to grind the surface of the specimen.

In addition to these polishing papers, a polishing clot with 1.0 μm alumina suspension powder is used for fine polish of the specimen surface. The polishing protocol used for preparing samples for SEM images has been shown in table 5-7.

Table 5-7. Polishing protocol for preparation of composite samples for SEM imaging

Paper	**RPM**	**Approximate Time (min.)**	**Force (N)**	**Direction**
320 Grit	200-220	3-6	6-7	Contrary
600 Grit	200-220	4-5	6-7	Complimentary
800 Grit	220-250	4-5	5-6	Contrary
1200 Grit	220-250	4-5	5-6	Contrary
Polishing cloth with 1.0 μm alumina powder	120-140	5-10	4-5	5 min. contrary 5 min. complimentary

Once all the specimen requiring SEM images were grinded and polished, they were placed in the sonicator for 3 min with water and alconox solution. Sonicator uses ultrasound waves to rinse loose the residues, contaminations and alumina particles acquired during the polishing procedure. Next step is to mount the specimen on a metallic tab and are painted on the side with silver paint to create a path for conductivity of electrons. The top surface of the sample is sputter coated with a 7 nm film of Gold-Palladium in controlled chamber with negative pressure (vacuum). The specimens are now finally ready to be placed in SEM chamber to acquire images. The whole procedure is schematically explained in figure 5-34.

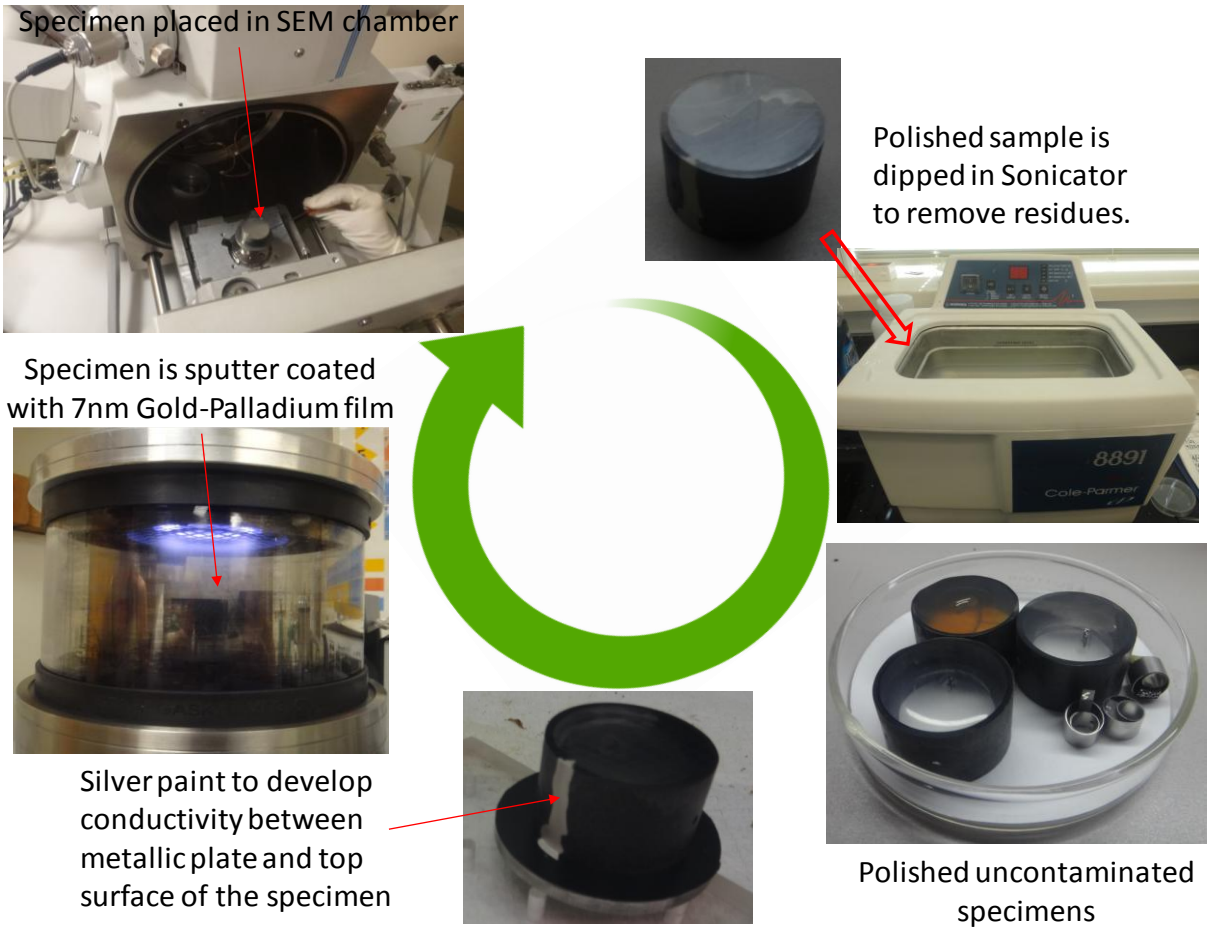

Figure 5-34: Preparation of composite specimen for SEM imaging

5.5.2 Images acquiring

In order to investigate any anomalies in manufacturing process, like de-bonding/de-lamination between resin and SMA and efficacy of resin in filling all air voids and cavities around glass fibers and SMA wires, scanning electron microscopic (SEM) images were taken of the composite specimens. These images acted as tools to confer the manufacturing technique which was established after many trials.

Secondary electrons and backscattered electrons are commonly used for imaging samples from the composite surfaces. Secondary electrons (SE) are most valuable for showing topography on the sample surface and backscattered electrons (BSE) are most valuable for illustrating contrasts in composition of the composite specimen. Signals from both of these electrons were used to acquire images. Figure 5-35 shows SEM images of PRC-3 composite specimen with both SE and BSE image at a 200X magnification. The image helps in understanding the layout of the specimen with different constituents. Figure 5-35(a) shows the contour of the PRC-3 specimen around SMA wires and glass fibers. Figure 5-35(b) shows contrast image of the PRC-3 sample, in which SMA wires are shown in white while resin which is opaque, is revealed in dark tone. Glass fibers can also be distinguished clearly in BSE image

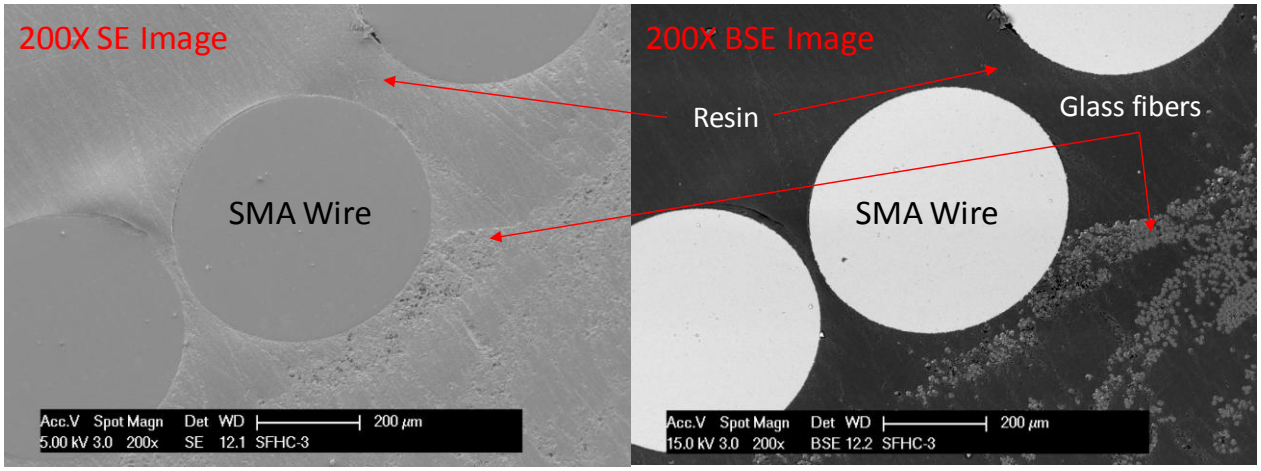

(a) (b)

Figure 5-35: SEM images of PRC-3 specimen at 200X magnification (a) SE (b) BSE

Figure 5-36a shows a back-scatter electron (BSE) image of PRC-3 composite specimen with 200X magnification and a blow up with 1200X and 5000X magnification in Figure 5-36c and Figure 5-36d, respectively. BSE images allow achieving contrasting images of the cross section which helps in identifying material with different densities. Figure 5-36b shows secondary electron (SE) image at 5000X magnification to see the depth and contours of the cross section.

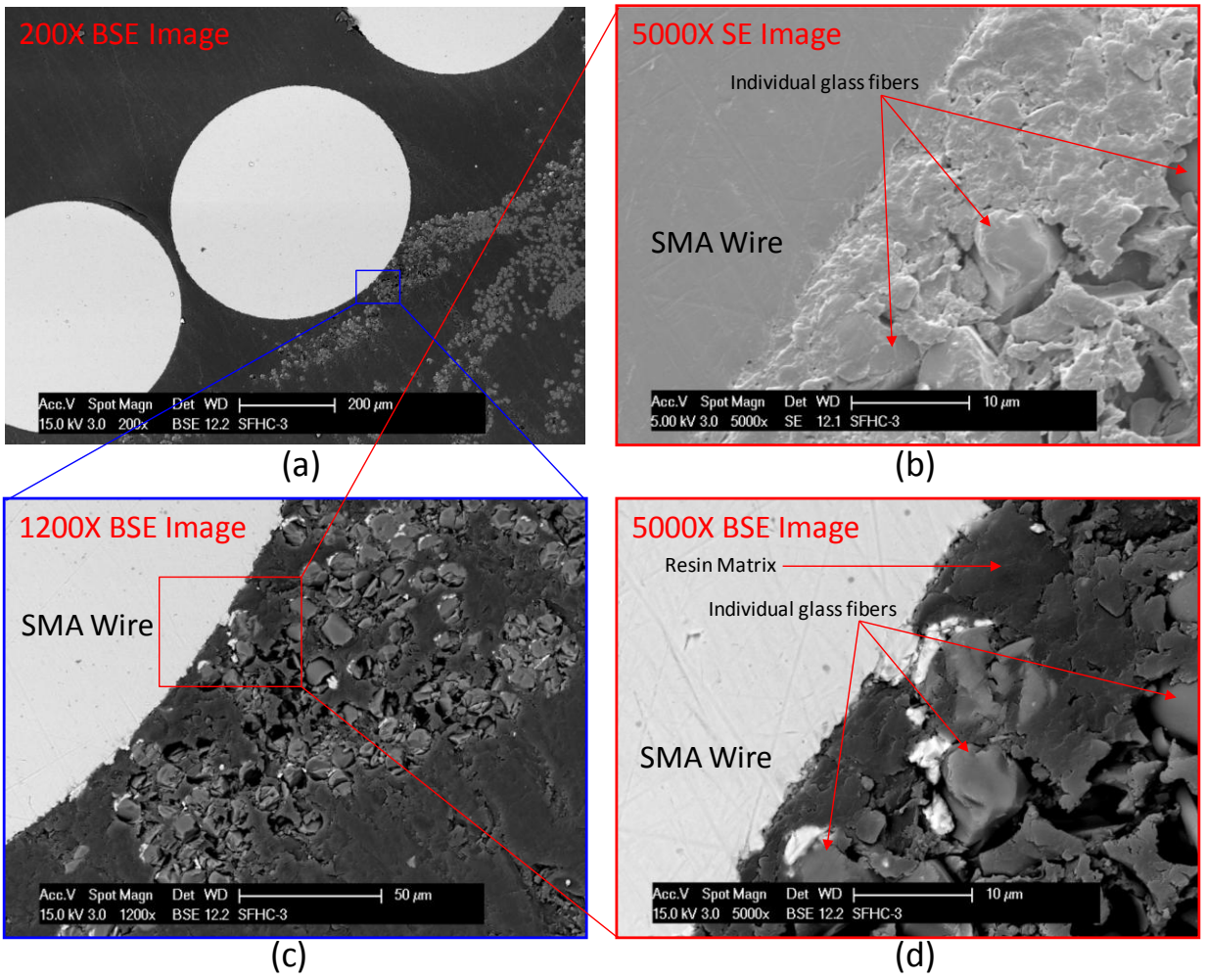

Figure 5-36: SEM images of PRC-3 composite. (a) BSE image with 200X. (b) SE image with 5000X. (c) BSE image with 1200X. (d) BSE image with 5000X.

As mentioned earlier, the images were observed after the specimen underwent tensile testing and show broken individual glass fibers spread around the SMA wires in resin matrix which is seen in the figure 5-36 with darker tone. Image also shows complete enveloping of resin around tiny glass fibers and SMA wire, proving good penetration capability and cavity filling of the selected resin matrix system (M10). Figure 5-37 shows BSE images with 1000X magnification of engulfing of resin around individual glass fibers. Images also show fractured and broken glass fibers which had ruptured during tensile testing.

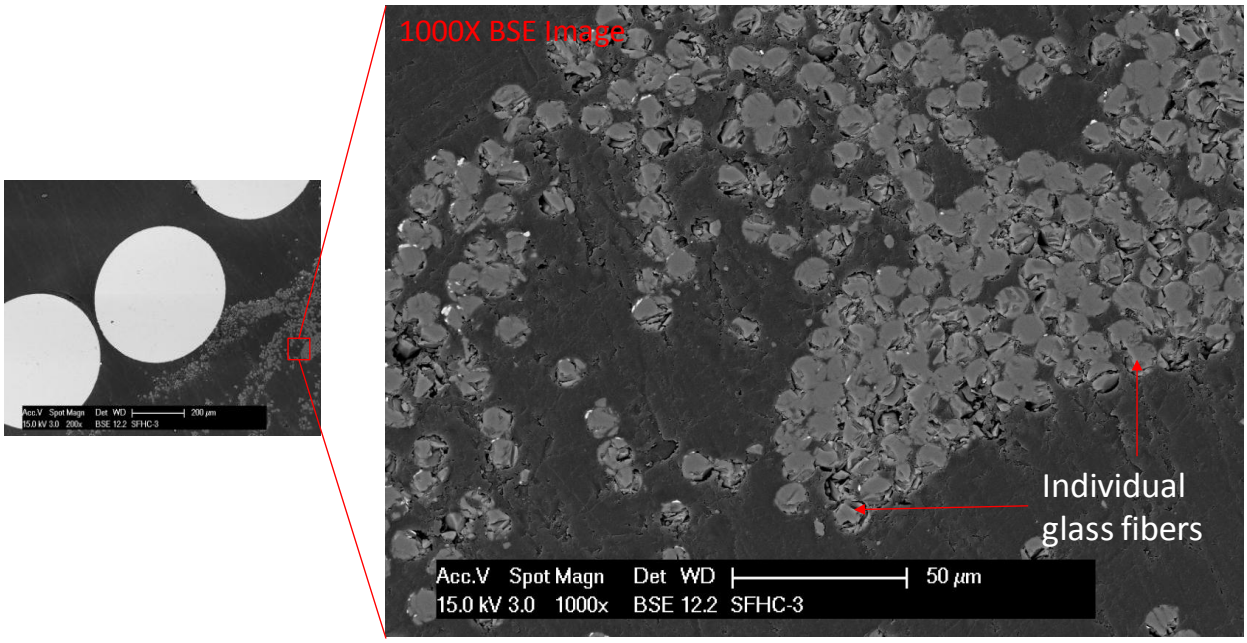

Figure 5-37: BSE image of PRC-3 with glass fibers at 1000X magnification.

Figure 5-38 highlights the penetration and surrounding of SMA wire and individual glass fibers by resin in PRC-3 specimen. Image is able to show all three constituents of the hybrid composite specimen i.e. SMA, glass fibers and resin. Figure 5-38 which is BSE image with

25000X magnification, also show absence of voids and de-lamination between SMA, glass fiber and resin matrix, depicting good bond.

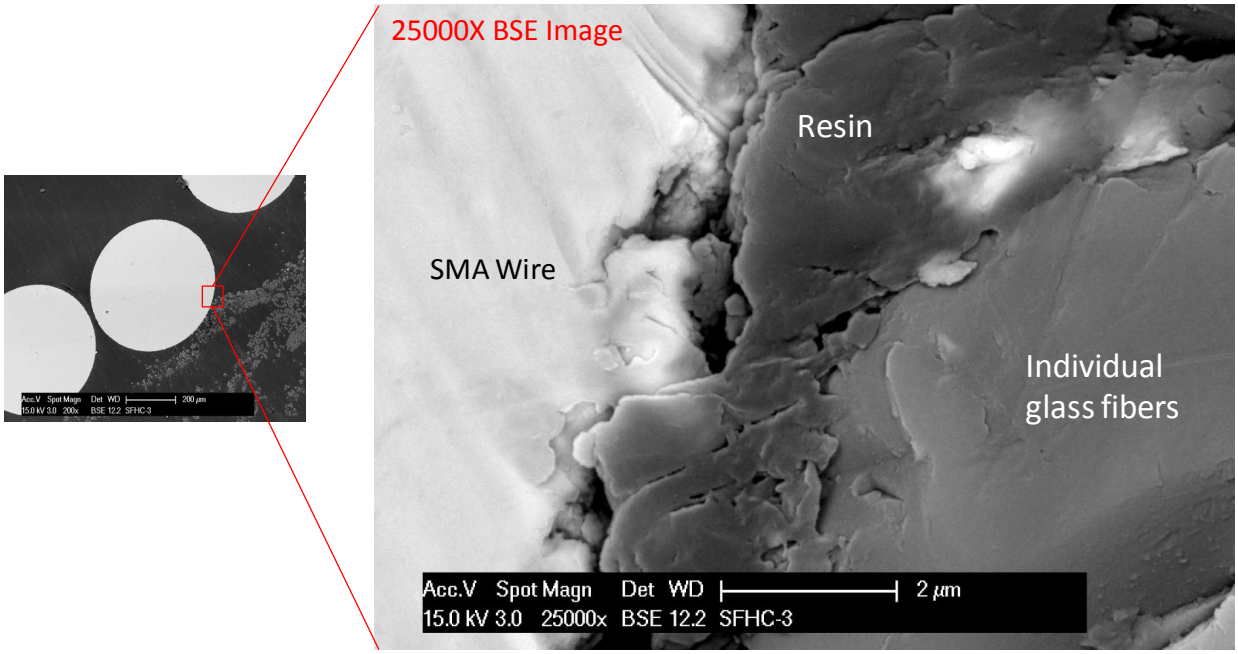

Figure 5-38: SEM images of PRC-3 composite with 25000X magnification.

5.6 Behavior of SMA composite under cyclic loading

There has been limited research on compression behavior of NiTi SMA material including the studies by Liu et al. (1998) and Lim & McDowell (1999). However no study exists which addresses the behavior of SMA-FRP composite under compression or under complete cyclic loading. Therefore, in order to make the study conclusive and complete, pure SMA composite, FRC-13 (Table 4-8) was manufactured and tested under complete cyclic behavior (tension and compression). Results from the tests helped in assessing the effects of compressive

behavior of composite on its tensile behavior. Same testing loading frame was used which has been used for tensile loading tests, discussed earlier in this chapter. Since the composite specimens will be undergoing buckling while under compressive loading, a loading protocol was developed to limit the compressive strains to around $1/10^{th}$ of tensile straining in each cycle. Although, no de-bonding was observed in all composite specimens tested so far in tension, addition of compressive loading will definitely make the slippage of SMA wires with its surrounding resin matrix more prominent. In order to study this effect, the specimen was subjected to six tensile and compressive loading cycles. The loading protocol followed during the test has been shown in figure 5-39. In the first cycle, the FRC-13 specimen was loaded in tension up to strain of 1% and there after it was incremented by 0.5% in every subsequent cycle.

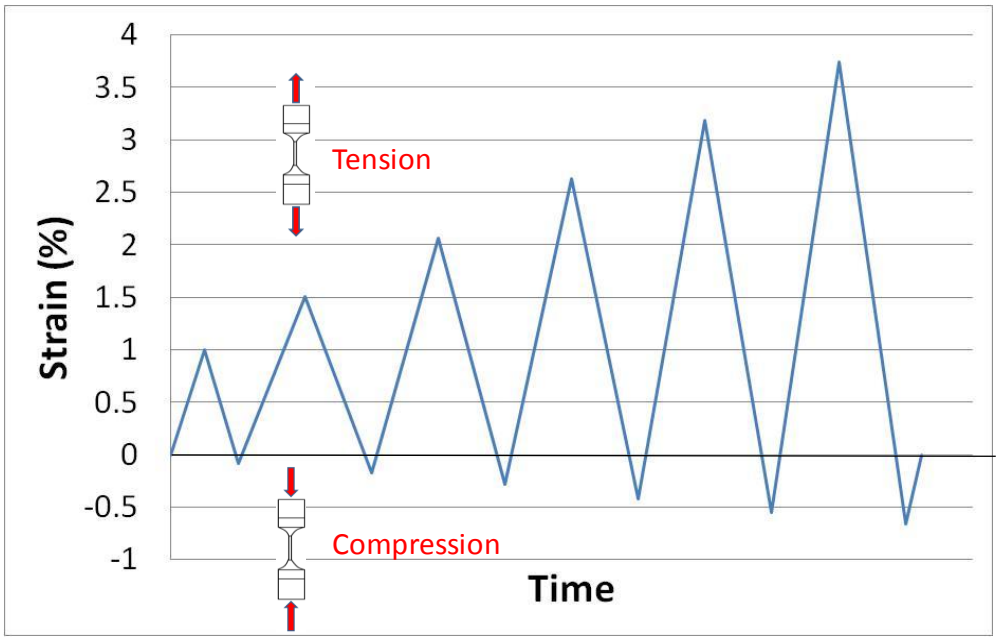

Figure 5-39: Loading protocol for uniaxial cyclic test

Cyclic stress strain curve of FRC-13 specimens has been shown in figure 5-40. As expected, the composite specimen was able to dissipate energy through hysteretic action of SMA and was able to recover residual strains due to superelasticity of SMA.

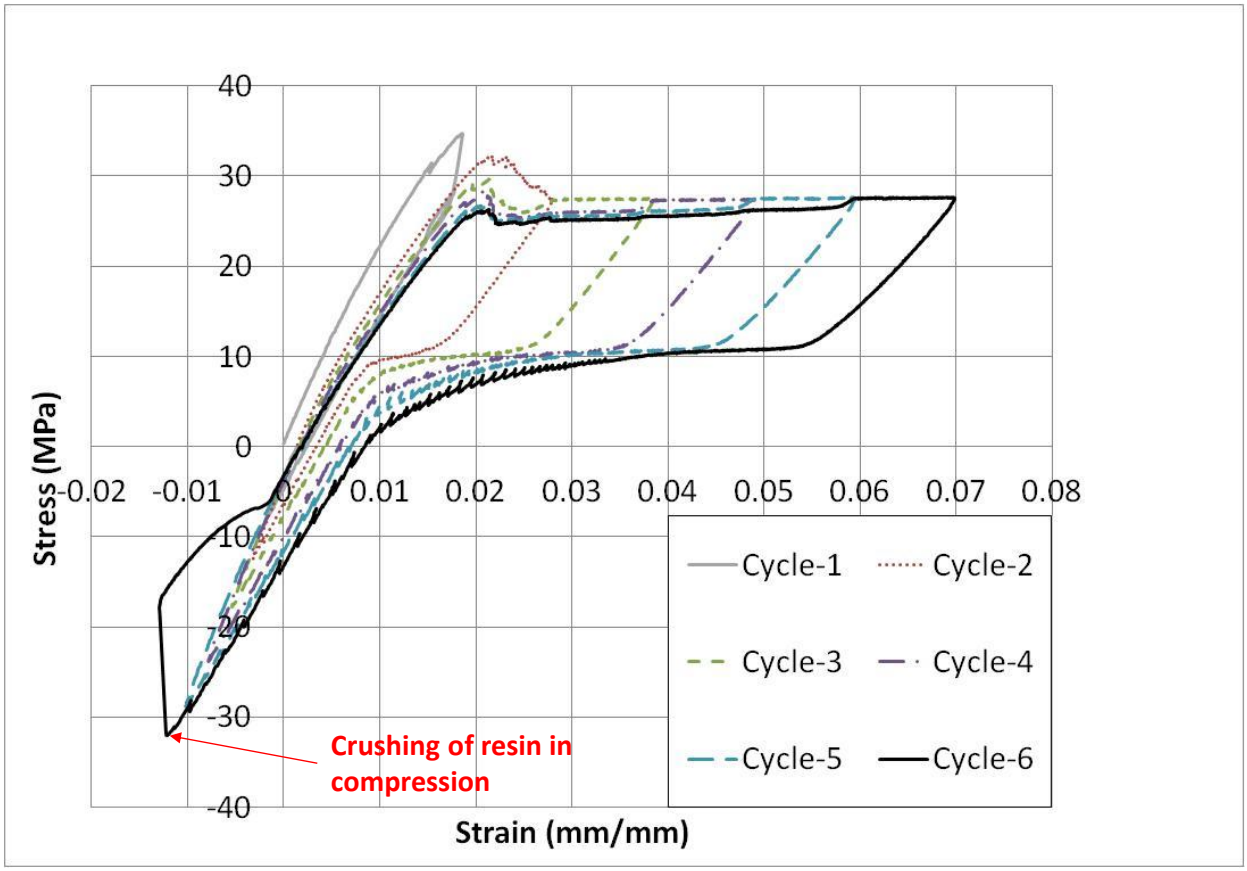

Figure 5-40: Cyclic stress-strain curve of FRC-13 specimen.

Due to addition of compressive loading and straining, de-bonding of SMA wire with resin matrix becomes an issue, as stated earlier. During all the compressive loading cycles, FRC-13 composite specimens experienced buckling, as expected which affected its tensile behavior. During the tensile unloading in 5th cycle, after experiencing reverse phase transformation by

SMA, the wires started to de-bond with its surrounding resin matrix because of buckling effects. This was evident from the jagged lines in 5^{th} and 6^{th} cycle of the test, as seen in the figure 5-40. Each drop in force / stress indicates de-bonding which continued once the specimen underwent compressive strains. By the end of the loading of specimen in compression in 6^{th} cycle, the composite specimen had experienced complete de-bonding, thus resulting in crushing of resin matrix in compression as seen in figure 5-40 with a jump to large strain value. Results show that the compressive loading does have impact on the tensile properties of the composite beyond strains of 5%. However in real application, the SMA-FRP composite rebar will be surrounded with concrete which will provide bracing along the length of the rebar. This bracing / confinement of rebar by concrete will prevent it from exhibiting buckling tendency, thus limiting de-bonding effects as seen in figure 5-40.

CHAPTER 6

Numerical Modeling Technique

6.1 Introduction

Finite element program, OpenSees (Mazzoni et al. 2009) which has been specifically designed for seismic analysis and earthquake simulations, was utilized to develop material constitutive and structural frame models. In this chapter, experimental results are utilized to develop numerical models to show hysteretic behavior of the composite. After calibrating these material models with experimental results, the models were then incorporated in 2D frame elements to perform the inelastic analyses on the moment resisting frame structures.

For calibrating material models, a simple cantilever beam was modeled using 'nonlinear beam-column element' defined in OpenSees library. This element is based on iterative force formulation, and considers the spread of plasticity along the element length. The integration along the element is based on Gauss-Lobatto quadrature rule (two integration points at the element ends). In OpenSees, 2-D beam-column elements have three degrees of freedom (2 translations and 1 rotation) at each end node. Cross-sections are modeled by defining geometric and material properties, while fibers form the basis of distributed plasticity models. For this study, five integration points were used for each beam and column element. The cross section at each integration point is then further discretized into fibers, which allows the section to be further divided into small areas with different constitutive models. In fiber-based formulations,

the area of the cross section is divided into finite regions (or fibers). Localizing nonlinearities of resin matrix due to post-peak softening, in SMA due to stress transformation and sudden rupture of FRP in a cross section can be easily accommodated by fiber models. Fiber section also allows the use of different constitutive models for different parts of the section such as epoxy, FRP and SMA reinforcement. For investigating analytical material behavior, a simple cantilever beam with a cross section was modeled with two nodes. Node 1 was considered fixed for all 3 DOF while node 2 was free for all 3 DOF. Element with length (L) with cross sectional area (A), underwent cyclic tensile elongation at node 2. Cross-sectional area was divided into various fibers and was assigned different material models (epoxy, FRP, SMA). Schematics of FE element model and fiber section modeling is shown in figure 6-1.

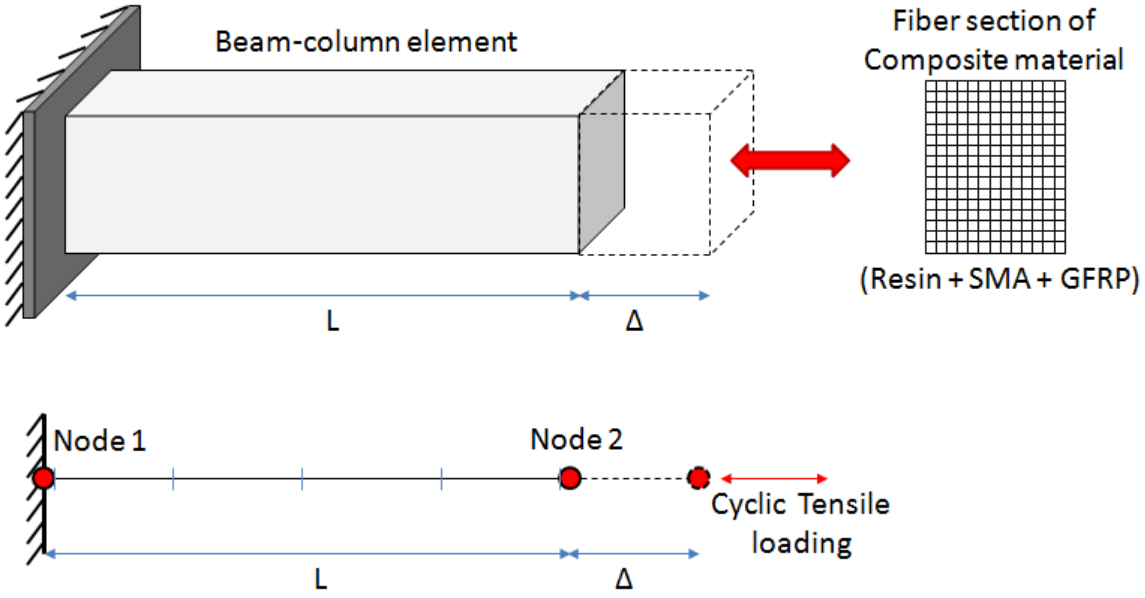

Figure 6-1: Beam-column element with boundary conditions and fiber section approach

6.2 Constitutive material properties and modeling

Properties related to all the materials were first identified and were then used to develop constitutive material models. The materials have been categorized as below:

6.2.1 Concrete material properties and modeling

Uni-axial material models which have been predefined in OpenSees have been utilized in defining the constitutive behavior of concrete and reinforcement materials. Concrete02 model, which considers concrete's tensile strength, was selected to represent the concrete behavior. This model is based on Kent-Park-Scott model (Scott et al. 1982) who derived the constitutive relationship based on low strain rate. The maximum stress Kf'_c attained is assumed to be reached at a strain of 0.002K. The explicit stress-strain relationship is shown in equations 6-1 and 6-2. As shown in figure 3, the core of the beam and column sections is typically confined with transverse reinforcement. For unconfined concrete, a compressive strength of 30 MPa and a strain of 0.002 mm/mm corresponding to peak compressive strength were assumed. Mander et al. (1988) model was used to determine the parameters for the generalized confined stress-strain curve as shown in figure 6-2. Variables, Kf'_c and ε_{cu} in figure 6-2 are the peak compressive strength and compressive strain of the confined concrete. Base model for confinement was developed for steel reinforcement and was then kept same for sake of consistency and comparison with SMA-FRP and GFRP sections.

$$f_c = Kf'_c\left[\frac{2\varepsilon_c}{0.002K} - \left(\frac{\varepsilon_c}{0.002K}\right)^2\right] \qquad (6\text{-}1)$$

$$K = 1 + \frac{\rho_s f_{yh}}{f'_c} \qquad (6\text{-}2)$$

Where, f_{yh} is the yield strength of the hoops, ρ_s is the ratio of volume of hoop reinforcement to volume of concrete core. f_c and ε_c are the longitudinal compressive stress and strain in concrete.

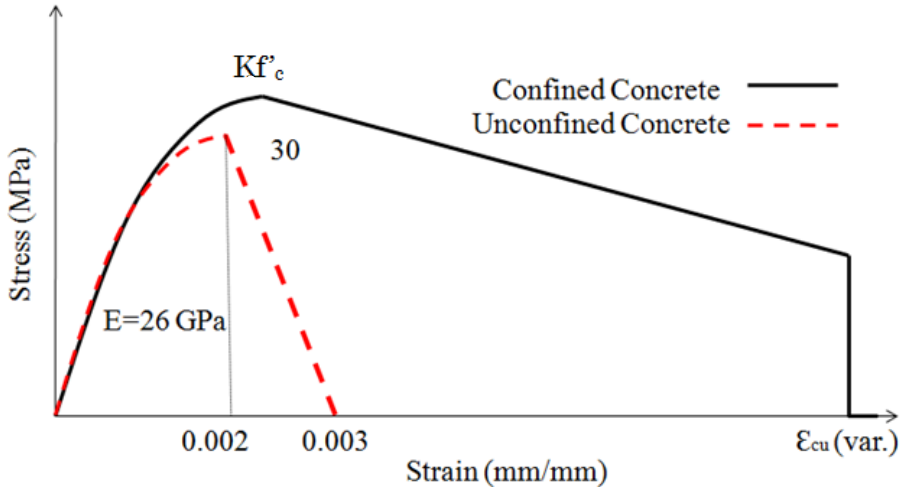

Figure 6-2: Confined and unconfined concrete stress-strain curves.

6.2.2 Reinforcing material properties and modeling

Three different reinforcing materials were used in this study namely, steel, SMA-FRP composite and GFRP. The steel behavior was described using Steel02 model predefined in OpenSees, which is based on the Giuffre-Menegotto-Pinto model with isotropic strain hardening (Menegotto and Pinto 1973). The stress-strain relationship defines the transition from initial elastic slope to another asymptote slope and is described as:

$$\sigma^* = b\varepsilon^* + \frac{(1-b)\varepsilon^*}{(1+\varepsilon^{*R})^{1/R}} \tag{6-3}$$

where, *R* is an independent parameter which defines the curvature of transition and *b* is the strain hardening ratio. The Menegotto-Pinto Model has been shown in figure 6-3. Grade 60 steel with modulus of elasticity (E_s) of 200 GPa was used for material modeling.

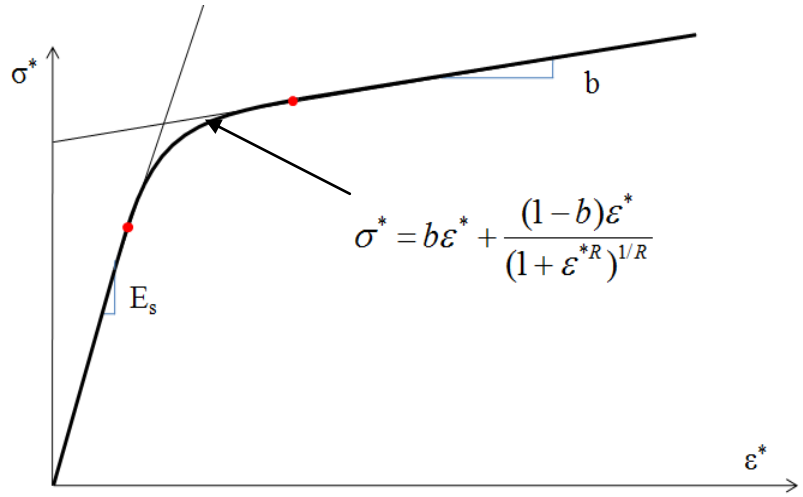

Figure 6-3: Menegotto-Pinto steel model.

GFRP was modeled using 'elastic linear material' models with rupture strain of 0.034 mm/mm and modulus of elasticity (E_f) of 86.7 GPa. SMA material was modeled using flag shape 'SMA' uniaxial material, predefined in OpenSees. Average values were used for NiTi transformation stresses, including, austenite to martensite start stress, σ_{AMS} = 365 MPa, austenite to martensite finish stress, σ_{AMF} = 425 MPa, martensite to austenite start stress, σ_{MAS} = 102 MPa, martensite to austenite finish stress, σ_{MAF} = 50 MPa. The modulus of elasticity of the NiTi SMA wires was 63.5 GPa as recorded during the training of SMA wires. Analytical material models of stress strain curve for SMA wires were developed in OpenSees as output. The analytical results were compared with experimental results and have been shown in figure 6-4. Results indicate

that the analytical model used in this study for SMA materials are capable of predicting closely, the initial stiffness and all the stresses and strains associated with phase transformations.

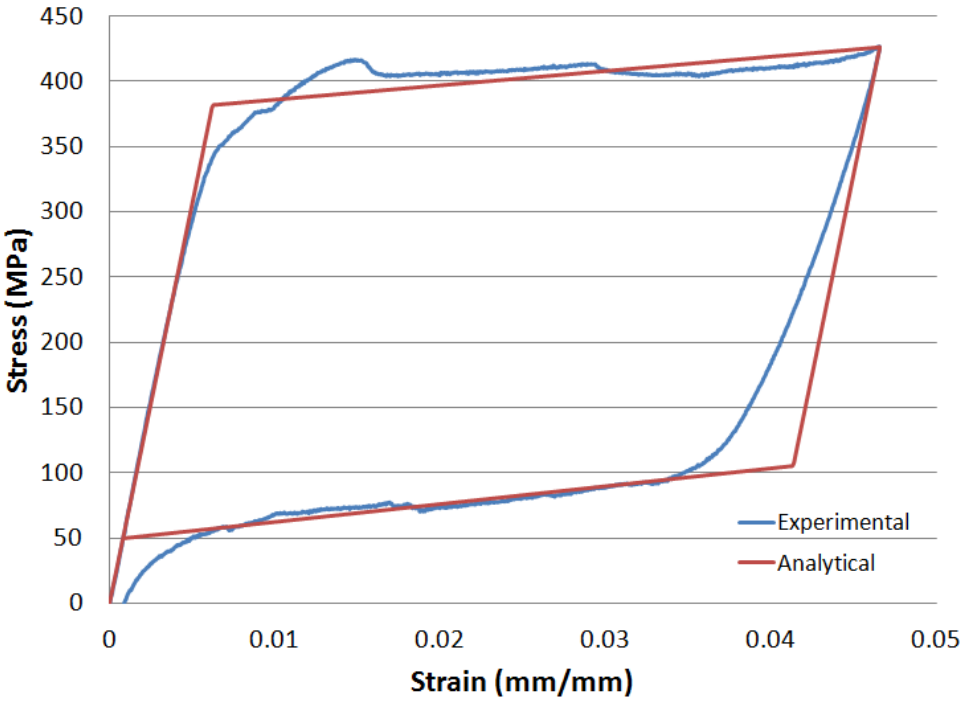

Figure 6-4: SMA material results; experimental and numerical model

As mentioned before that the type of epoxy which was deemed suitable for this research was one with high ultimate strain in order to match high strain capability of SMA material. Another important desired feature of resin was to have stable behavior over continued cyclic loading. The selected resin system (M10) shown in figure 5-15(a) had a high elongation property and its stiffness and strength remained stable over the course of continued straining. Elastic perfectly plastic (EPP) material model is able to capture the resin matrix behavior, well with initial stiffness and strength. Modulus of resin (E_m) was assigned to be 1.57 GPa while strain at

yield was 0.01 mm/mm, in the EPP input for analytical model. Comparison of results between experimental results and analytical model are shown in figure 6-5. Results indicated that the analytical model (EPP) used in this study for resin materials is able to capture the initial stiffness and material behavior as a whole. Table 6-1shows the summary of all the material properties used in this chapter for developing numerical models.

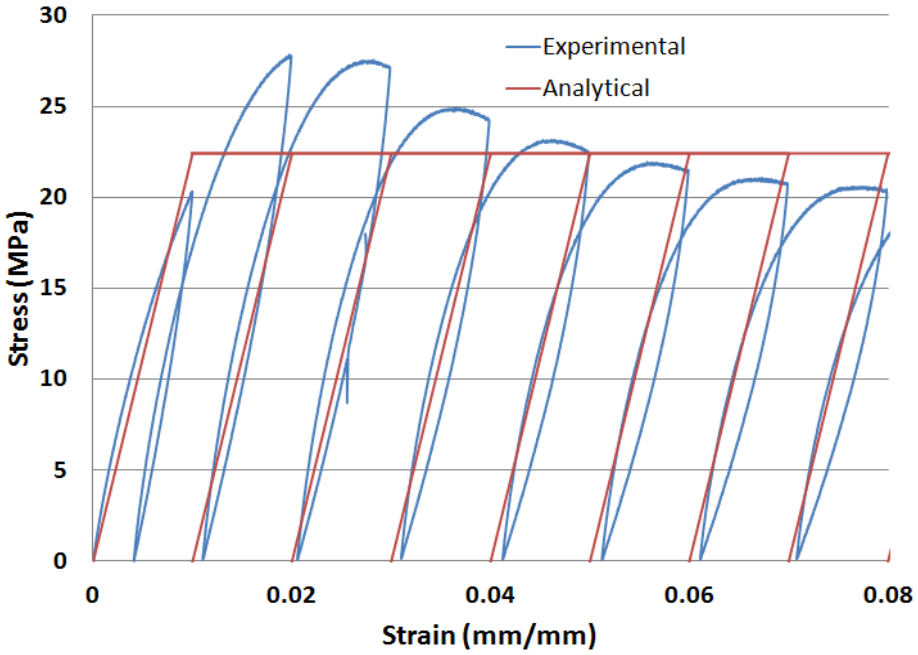

Figure 6-5: Resin matrix material results; experimental and numerical model

Table 6-1: Material properties used in numerical models obtained from experimental tests

Material	Properties	Abvn.	Values
Concrete	Young's Modulus	E_{conc}	26 GPa
	Ultimate strain	$\varepsilon_{cu.}$	1.50%
	Compressive Strength	f'_c	30 MPa
Resin	Young's Modulus	E_m	1.57 GPa
	Yield Stress	F_{ym}	22 MPa
SMA	Young's Modulus	E_{SMA}	63.5 GPa
	Austenite to Martensite start stress	σ_{AMs}	365 MPa
	Austenite to Martensite finish stress	σ_{AMf}	425 MPa
	Martensite to Austenite start stress	σ_{MAs}	102 Mpa
	Martensite to Austenite finish stress	σ_{MAf}	50 Mpa
Glass fibers	Young's Modulus	E_f	86.7 GPa
	Rupture strain	ε_{Glass}	3.20%
Steel	Young's Modulus	E_s	200 GPa
	Yield Stress	Fy	420 MPa

6.3 Comparison of material models with experimental results

Parallel material command was used to join the epoxy and SMA / FRP material models, in which the strains are equal while stresses and stiffness's are additive. Schematic of use of parallel material to combine different materials, namely resin, SMA and glass fibers, to get SMA-FRP hybrid composite is shown in figure 6-6.

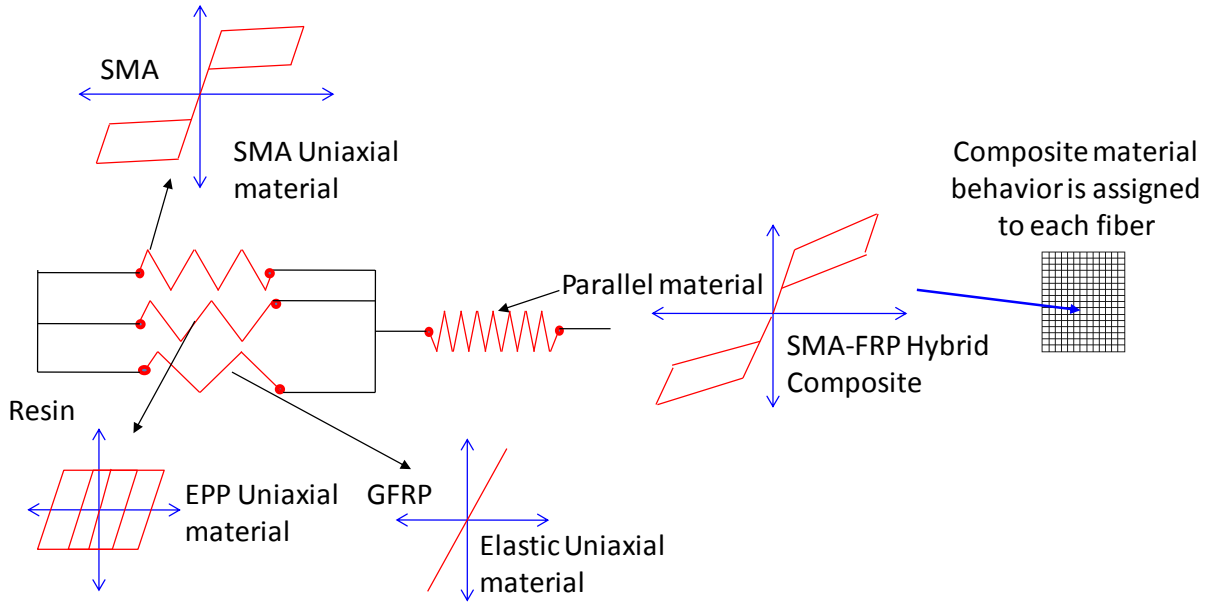

Figure 6-6: Parallel material used to combine epoxy resin with SMA and glass fiber material.

Figure 5-19 shows experimental results of pure SMA composite (FRC-7) with 20.3% reinforcement ratio. In order to capture this composite behavior numerically, FE models with fiber section approach were used again, by combining SMA and resin material in parallel. Numerical models were calibrated with experimental results. Figure 6-7 shows comparison of experimental results of FRC-7 and numerical model developed for SMA composite material.

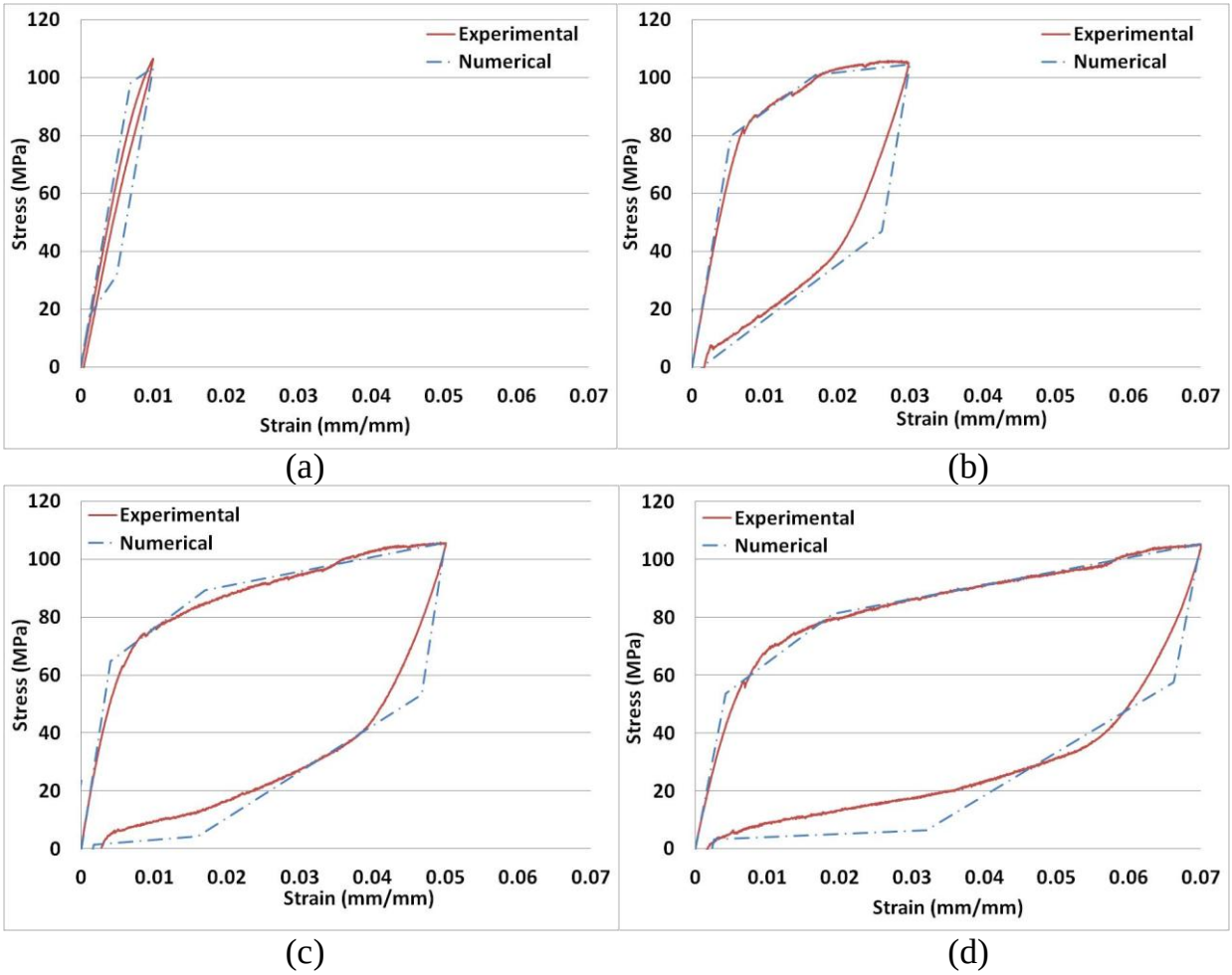

Figure 6-7: Cycle wises comparison of stress strain curves of experimental results and numerical model of FRC-7 composite. (a) 1% strain cycle (b) 3% strain (c) 5% strain (d) 7% strain

Results indicated that the numerical models used in this study are capable of predicting closely, the initial stiffness, transformation stresses and strains, and the post-yield behavior. Figure 5-29 shows the results of SMA-FRP hybrid composite (PRC-3) subjected to 4 cycles of tensile loading. In order to capture behavior of this composite material SMA was combined with glass fibers and resin material in parallel, as described in figure 6-6. Results from numerical modeling and experiments are shown in figure 6-8 for PRC-3 material.

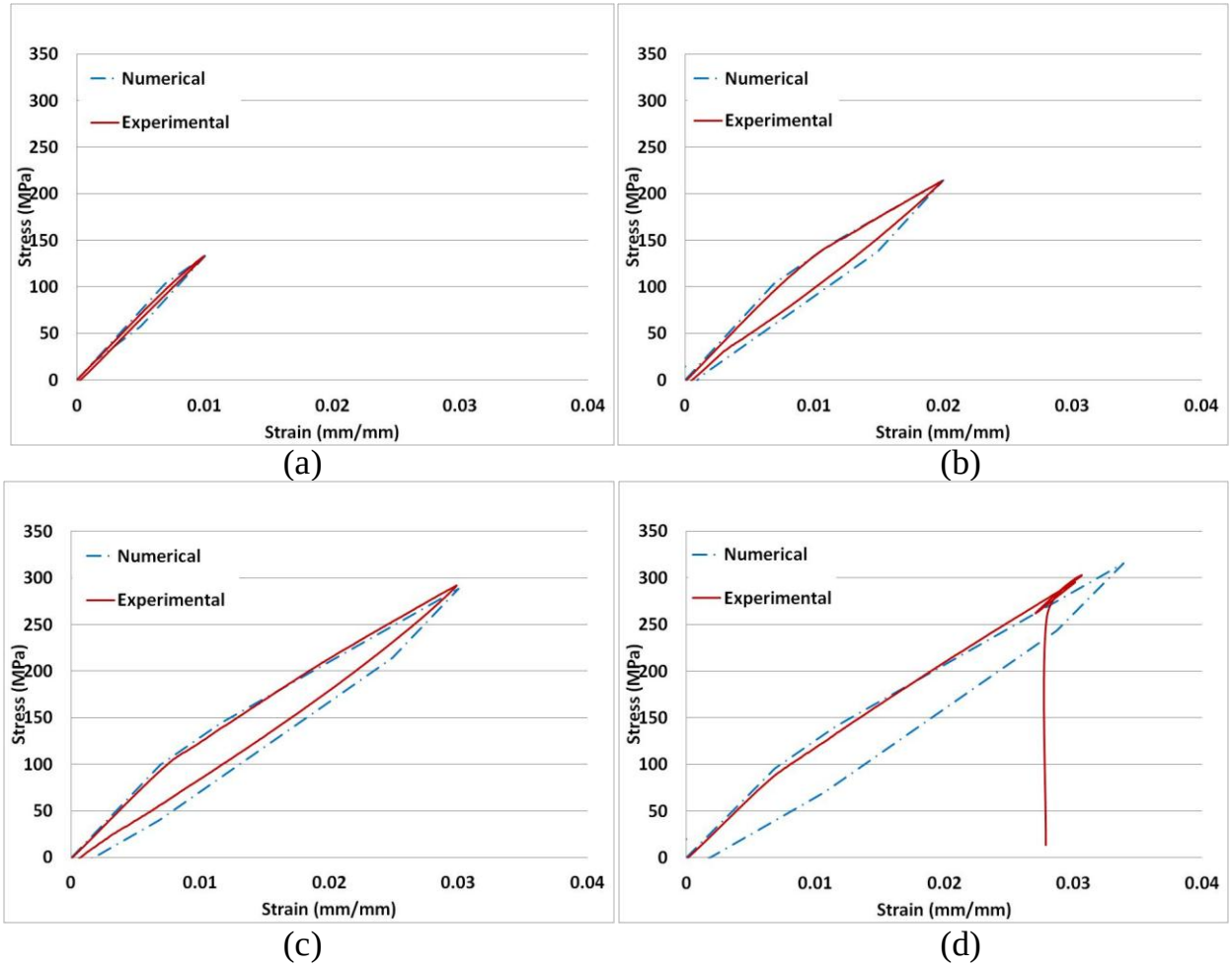

Figure 6-8: Cycle wises comparison of stress strain curves of experimental results and analytical model of PRC-3 composite. (a) 1% strain cycle (b) 2% strain (c) 3% strain (d) 4% strain

Results show that the numerical models developed are well capable of predicting the SMA-FRP hybrid composite material behavior. In figure 6-8(d) the experimental specimen failed at 3.2% strain and was not able to complete the whole cycle, because of rupture of glass fibers. These calibrated numerical models can now be used with confidence in the seismic analyses of structural buildings.

6.4 Finite element modeling at member and structural levels

A 2-D three storey one bay (3S1B) and a six storey two bay (6S2B) reinforced concrete MRFs were investigated to explore the behavior of steel, GFRP and SMA-FRP composite reinforcement. The prototype MRFs used in the seismic simulation done in this research are shown in figure 6-9. 6S2B MRF was selected for modeling in addition to 3S1B, in order to investigate the response of a building with a higher fundamental period and also to incorporate behavior of the interior joint into the model, subjected to earthquake loading.

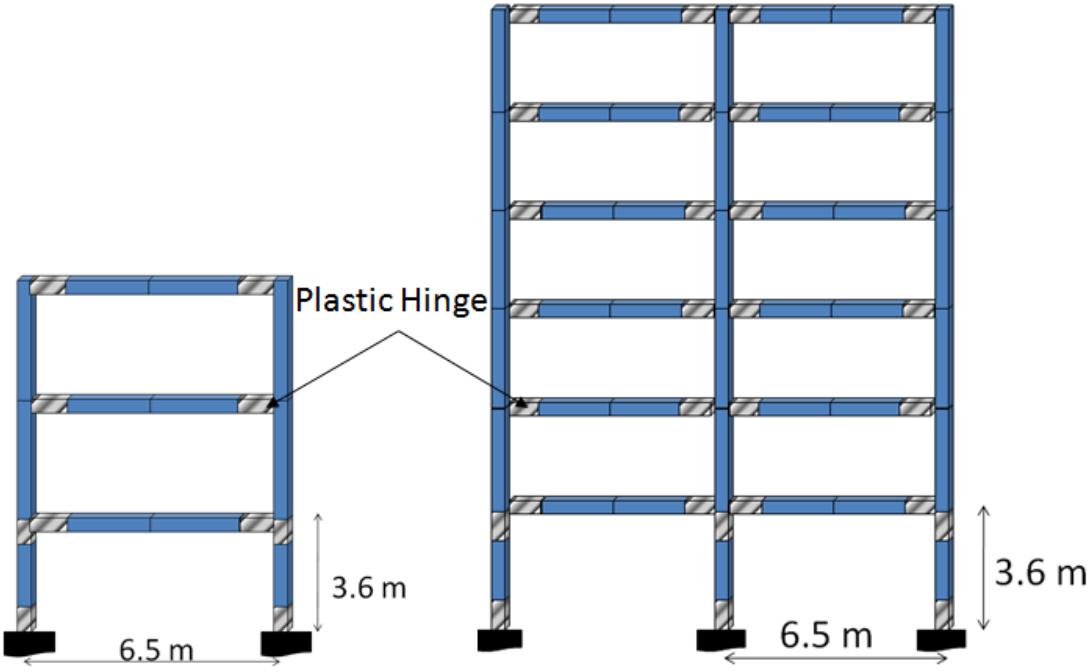

(a) 3S1B (b) 6S2B

Figure 6-9: Prototype reinforced concrete moment resisting frames

Finite element program, OpenSees (Mazzoni et al. 2009) was utilized to perform the inelastic analyses on the MRF structures considered in this study. Fiber section approach and

nonlinear beam-column elements were utilized to define the cross-section and the elements, respectively. Nonlinear beam-column elements with fiber sections were used to model the moment resisting frame elements with distributed plasticity. Schematics of the technique utilized to model the MRFs at structural, element and sectional level are shown in figure 6-10.

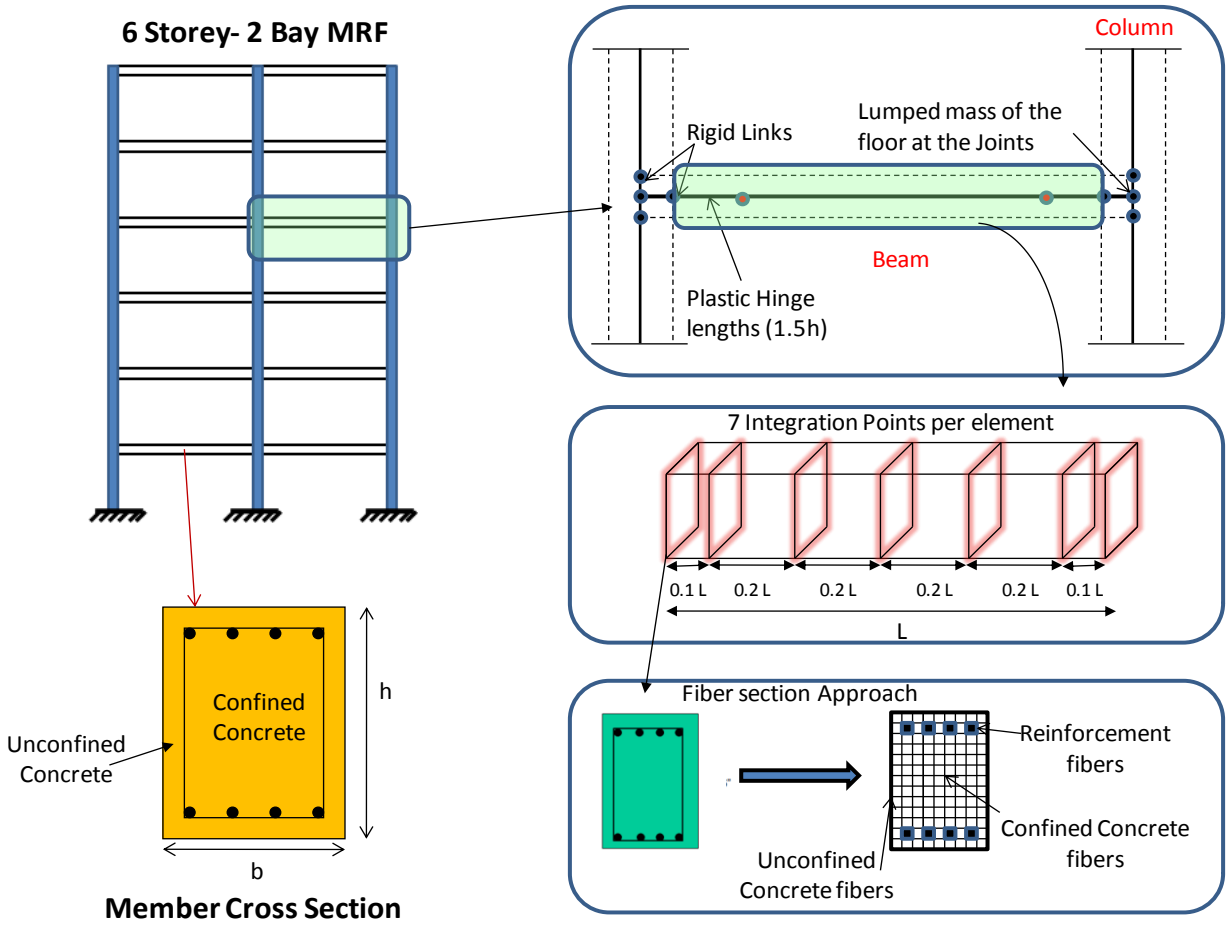

Figure 6-10: Analytical modeling technique utilized in OpenSees.

Both beams and columns were modeled using 'nonlinear beam-column element' defined in OpenSees library. This element is based on iterative force formulation, and considers the

spread of plasticity along the element length. Cross-sections are modeled by defining geometric and material properties, while fibers form the basis of distributed plasticity models. For this study, seven integration points were used for each beam and column element. The cross section at each integration point is then further discretized into fibers, which allows the section to be further divided into small areas with different constitutive models Fiber section also allows the use of different constitutive models for different parts of the section such as unconfined concrete, confined concrete and steel reinforcement.

As mentioned earlier, in order to restrict the cost of material associated with use of NiTi in SMA-FRP composite, the reinforcing composite is only provided in the plastic hinge zones of MRF where high inelasticity is expected to accumulate. Generally, the length of plastic hinge varies between 1.2h to 2h, where h is the depth of the section (Paulay & Priestley 1992). Location of plastic hinge zone in all the beams and 1^{st} storey column only is shown in figure 6-9, with cross hatch. A more detailed view of use of suggested composite surrounding the plastic hinge zone of the beam is shown in figure 6-11.

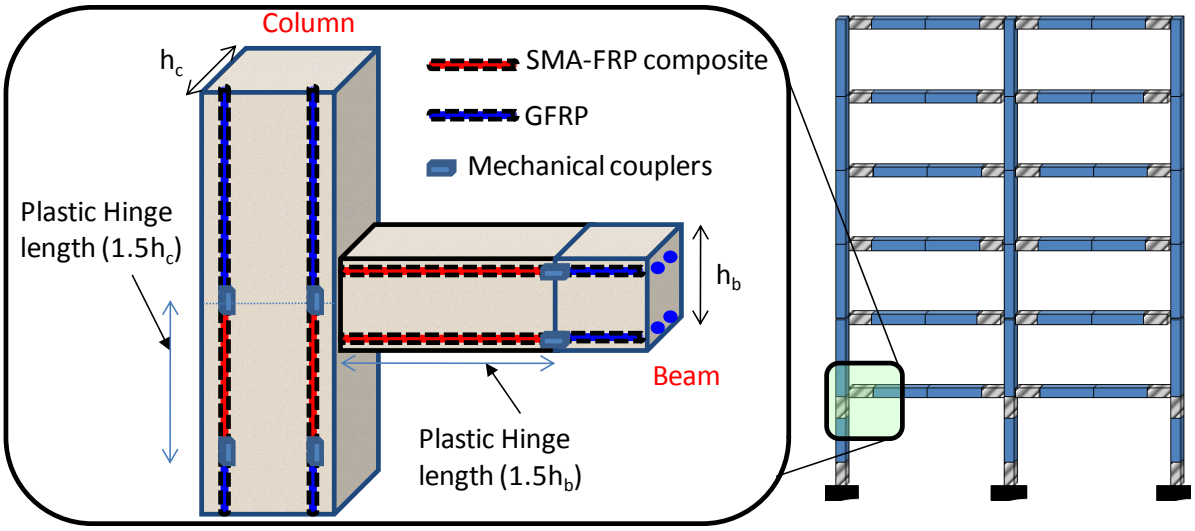

Figure 6-11: Use of SMA-FRP composite in beam plastic hinge zone.

Mechanical couplers can be used to tie the two different types of reinforcement after their cutoff points outside the plastic hinge zone, which for this study was kept constant to be 1.5h. Also in this study it is assumed that no slippage occurs at the mechanical coupler and a perfect bond exists between all reinforcement types and concrete material. Although FRP reinforcement has inferior performance in terms of bond strength with concrete as compared to steel, this characteristic can be improved upon by use of better surface interlock strategy like ribbed or grooved rebars. Wang and Belarbi (2010) found out that bond characteristics between FRP bars and concrete are strongly dependent on the mechanical and physical properties of the external layer of FRP bars. Thus for this study it was assumed that the composite reinforcement used has deformed outer cladding which enhances the bond characteristics and thus there is no slippage issues with concrete.

CHAPTER 7

Force Based Design and Seismic Analysis

7.1 Introduction

Typical reinforced concrete moment resisting frame (RC MRF) displays non-linear behavior through beam-column joint interaction and by lumping majority of inelasticity at the plastic hinge zones of member elements. Many modern mid and high rise buildings have moment resisting frames (MRFs) as the primary lateral load resisting system. This type of construction was considered the safest one for earthquake resistance, as beam-column joints in MRF's are expected to sustain large plastic deformations in bending and shear before collapse. This performance can further be enhanced by providing better confinement to core concrete in the plastic hinge lengths causing MRF to behave in a very ductile manner. Thus, ductility of the frame is dependent on flexural yielding of reinforced beams and columns. These permanent damages exhibited in steel reinforced RC MRF due to plasticity, leads to undesirable residual displacements during earthquake events. Collapse of RC structures as exhibited in figure 2-2 is direct result of yielding of reinforcement and crushing of concrete which leads to development of plastic hinge and progressive collapse of the structure. Excessive steel deformation (beyond yielding) in RC MRFs, for example often results in permanent residual drifts, which not only cause overall capacity degradation but also pose safety issues for the occupants even under gravity loads. This chapter addresses the potential issues associated with development of plastic hinge in steel reinforced MRF and replaces it with proposed SMA-FRP composite. Response of

these MRF's once subjected to different natural earthquake records are evaluated and compared. In addition, GFRP reinforced MRF is also analyzed under same seismic loading. All three reinforcement types i.e. steel, SMA-FRP and GFRP are first designed for the two prototypes (3S1B and 6S2B) MRF using guidelines from current seismic codes. These codes primarily dictate forced based design approach which focuses on ductility of structure by first assessing elastic demands and then modifying the demands by response modification factor (R_m factor). According to traditional seismic design codes like International Building Code (IBC) (IBC-2006), the structures are analyzed elastically under a reduced level of equivalent lateral force based on equal energy rule according to the fundamental period of the structure. It is then designed by ultimate stress design method to provide sufficient strength to withstand the design earthquake. This chapter adopts this methodology to design the MRFs and then investigate their behavior based on global and story response parameters. Elastic modal properties, pushover analysis results, and nonlinear time history analyses are presented. The emphasis is made on inter-story drift (IDR) ratios of each designed MRF subjected to varying levels of ground excitation. These IDR and cumulative damage in terms of residual drifts are used to assess the performance of these MRFs. Work done in this chapter including numerical modeling has been presented in Zafar and Andrawes (2012).

7.2 Design philosophy – force based approach

2-D three story one bay (3S1B) and six story two bay (6S2B) RC MRFs were designed to investigate the behavior of steel, GFRP and SMA-FRP composite reinforcement. Initially, the frame was design assuming steel reinforcement, as all the guidelines for design are available for

concrete members reinforced with steel rebars. Later, steel reinforcement was replaced by SMA-FRP and GFRP composite rebars, based on adopted design technique.

7.2.1 Calculation of loads and base shear for design

Loads were considered on the structure assuming it to be an office building with values of loads based on American Society of Civil Engineers (ASCE-7) standard guidelines (ASCE 2005). Values of 2.63 kPa of distributed live load and 0.478 kPa of distributed dead load and partition load were assumed at each floor. International Building Code (IBC) (IBC 2006) was used to compute the base shear for the structure. For purpose of calculation, it was assumed that the structure is located on a rock soil profile, in a high seismic zone of California, USA for which the maximum spectral response acceleration maps are available in IBC-2006. The base shear equation in IBC-2006 is given by equation 7-1:

$$V = C.W \qquad (7\text{-}1)$$

where, V is the base shear, C is the seismic response coefficient and W is the weight of the structure. C is given by equation 7-2:

$$C = S_{DS}.\, I / R_m \qquad (7\text{-}2)$$

where, S_{DS} is the design spectral response acceleration at short period, I is importance factor and R is the response modification factor. S_{DS} is given by equation 7-3:

$$S_{DS} = 2/3.F_a.S_S \qquad (7\text{-}3)$$

where, S_S is the maximum spectral response acceleration and F_a is the site coefficient.

After computation of base shear, special seismic load combination given by IBC-2006 was used to incorporate effects of seismic ground motion in addition to gravity loads. Equation 7-4 gives the load combination:

$$1.2D+f_1.L+E \qquad (7\text{-}4)$$

where D is the deal load, L is live load, f_1 is the reduction factor for live load and E is the seismic load effect. Since vertical acceleration was not considered in this study and only effects of horizontal forces were considered, the seismic load E is given by IBC-2006 in equation 7-5.

$$E = \rho_r.Q_E \qquad (7\text{-}5)$$

where ρ_r is the redundancy coefficient defined in both IBC-2006 and ASCE-7. The value of ρ_r varies between 1.0 and 1.5 depending on structure type. For design of 3S1B and 6S2B, 1.3 and 1.5 was used as ρ value, respectively. Q_E is the effect of horizontal seismic forces from V.

Equivalent static force (ESF) procedure, as described in IBC-2006 and ASCE 7 was used to distribute the design base shear along the height of the structure using inverted triangular distribution, corresponding to the first mode of the structure. Structural analysis was performed to obtain the design moment and shear with the special seismic load combination allowed by IBC-2006. The strong column weak beam design approach was followed as described in ACI-318 code (ACI 2011). Design acceleration response spectrum was plotted to design the frame for computed base shear using procedure defined in IBC-2006. Figure 7-1 shows the design

acceleration response spectrum for a site in California with rock bed as soil profile. IBC-2006 classifies this soil profile as site class B for finding corresponding site coefficient values.

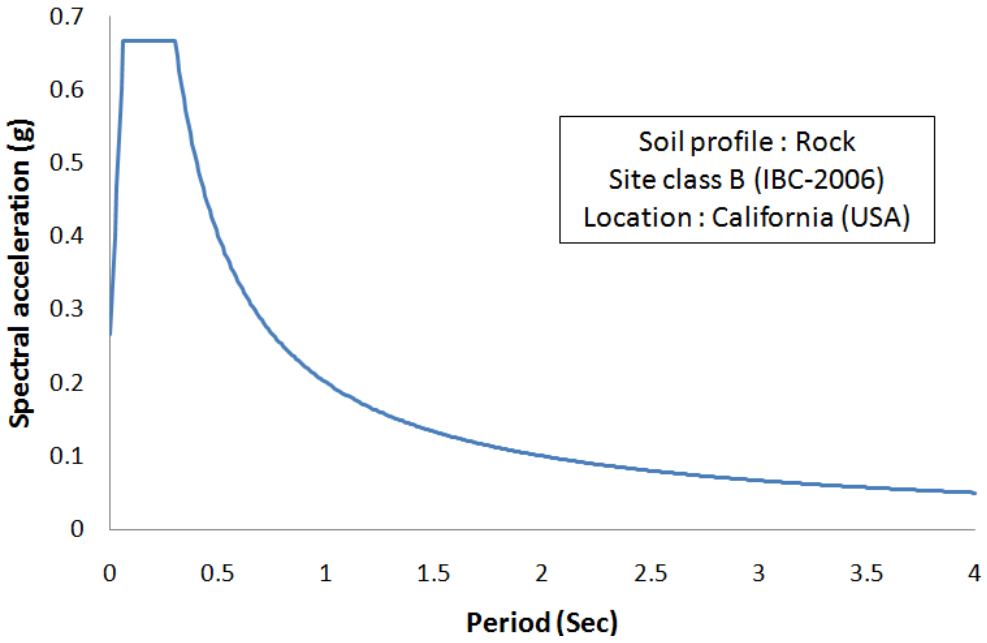

Figure 7-1: Design acceleration response spectrum used in the design of MRFs.

MRF with steel reinforcement was designed based on the response spectrum shown in figure 7-1. An iterative process was carried out next using the design response spectrum to determine the area of the SMA-FRP and GFRP reinforcement. In this process, the area of the steel reinforcement was used as an initial estimate. Modal analysis is then performed in OpenSees where the fundamental periods of the MRFs with SMA-FRP and GFRP are computed and a corresponding spectral acceleration is determined from the design spectrum and used in updating the area of SMA-FRP and GFRP reinforcement. The process is repeated until a satisfactory convergence of the area of reinforcement is reached. The procedure for determining

the area of SMA-FRP and GFRP reinforcement is explained in the flow chart shown in figure 7-2. Final periods of designed MRFs just after cracking for all three types of reinforcement are also shown in table 7-1. It is obvious from the table that the structure is required to be designed for lesser base shear value, as the period of the structure increases.

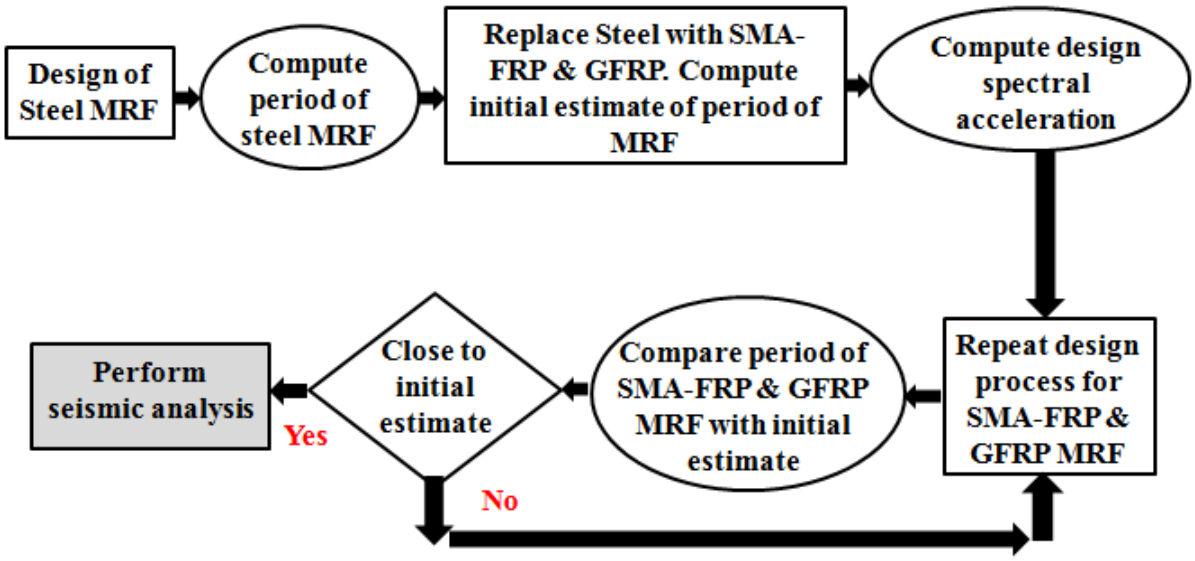

Figure 7-2: Design procedure for MRF with SMA-FRP and GFRP composite reinforcement.

Table 7-1: Fundamental periods of 3S1B and 6S2B MRFs.

Reinforcement type	3S1B MRF		6S2B MRF	
	Fundamental Period	Design Base Shear	Fundamental Period	Design Base Shear
Steel	0.49 sec	263 kN	0.86 sec	739 kN
SMA-FRP	0.58 sec	205 kN	0.97 sec	534 kN
GFRP	0.60 sec	187 kN	1.01 sec	503 kN

7.2.2 Sectional level analysis for design

Moment-curvature analysis (M-φ analysis) was performed in order to find the reinforcement ratio which would give the desired design moment capacity for both beam and column cross-section computed from structural analysis of frames using ESF procedure. Moment curvature curves were developed for various reinforcement ratios for both column and beam and for each reinforcement type, i.e. steel, SMA-FRP and GFRP. Axial loads due to gravity loads were also considered during the sectional analysis for the columns. The M-φ behavior of a beam cross-section for both 3S1B and 6S2B frames at 1st story level is shown in figure 7-3(a) and figure 7-3(b), respectively. It is evident that the GFRP cross section showed linear elastic behavior till the rupture of GFRP reinforcement. It can also been seen that the steel cross section was designed for higher moment as compared to SMA-FRP and GFRP cross sections. This is due to the fact that the steel has much higher stiffness and has been designed for higher demand as compared to other two categories. Due to this inherent variation in stiffness of the three reinforcements, the frames were not designed for same seismic force levels. ACI code was used to ensure that the designed section is not critical in shear.

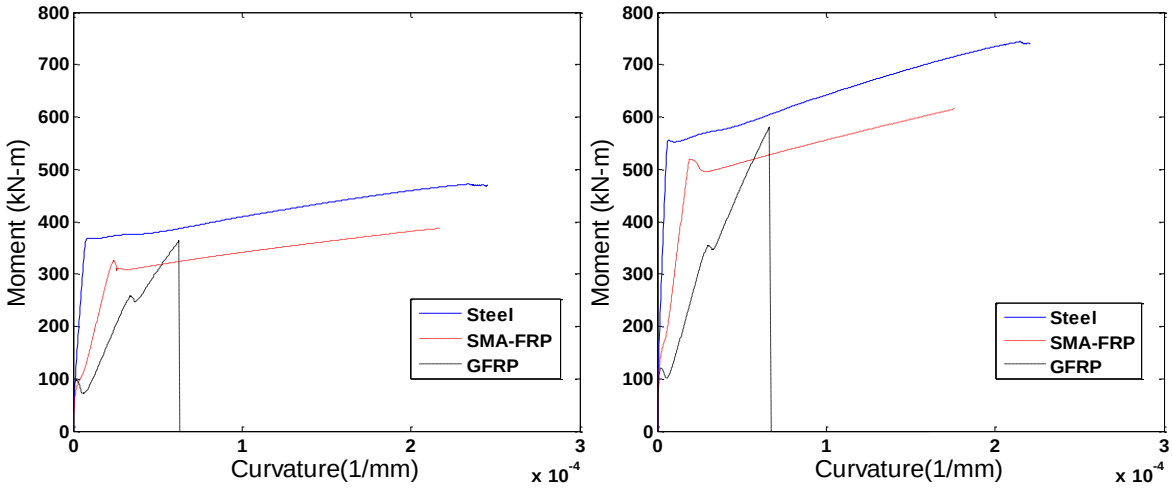

(a) 3S1B (b) 6S2B

Figure 7-3: M-φ analysis of beam cross section at 1st story level.

Same cross section was used for the entire length of beam and column in all the floors for both frames. For 3S1B frame, the beam cross section had a height of 500 mm and width of 300 mm, while the column had a height and width of 400 mm. Both beam and columns had a concrete cover of 50 mm on each side. For 6S2B frame, the beam cross section had a height of 600 mm and width of 350 mm, while the column had a height and width of 600 mm. The final reinforcement ratio (ρ), which is ratio of area of reinforcement to area of concrete are shown in table 7-2 for both beams and columns inside the plastic hinge zones.

Table 7-2: Reinforcement ratio for the designed column and beam cross-sections

Details of Reinforcement Ratio						
	Beam			Column		
Reinforcement type	**Steel**	**SMA-FRP**	**GFRP**	**Steel**	**SMA-FRP**	**GFRP**
3S1B ρ_total (%)	1.6	1.4	1.4	2.6	2.3	2.3
6S2B ρ_total (%)	2.4	2.2	2.2	4.2	4	3.9

7.3 Properties of selected ground motion records

Four ground motion records were used to conduct nonlinear time history analysis on the two frames. These selected natural earthquake records were from Kashmir-2005, Northridge-1994, Tabas-1978, and Kocaeli-1999 earthquakes. The ground motion characteristics are shown in table 7-3. The records were used to perform non-linear time history analysis on MRFs discussed in section 7.2. Acceleration response spectra for all four ground motions are shown in figure 7-4.

Table 7-3: Characteristics of selected ground motion records

Earthquake	Station	PGA(g)	Predominant Period
2005 Kashmir	Abbotabad	0.236	0.85 sec
1994 Northridge	24278 Castaic	0.516	0.55 sec
1978 Tabas	9101 Tabas	0.835	0.24 sec
1999 Kocaeli	Kocaeli	0.219	0.31 sec

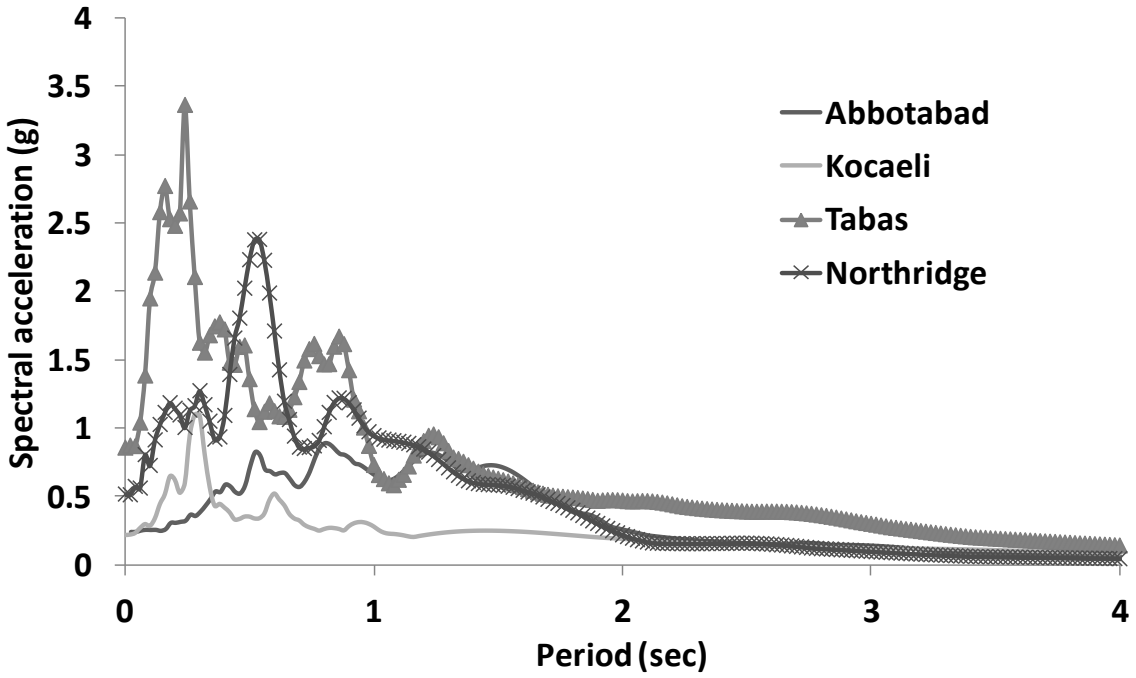

Figure 7-4: Acceleration response spectra for selected ground motion records

The four ground motion records were selected to have variation in predominant period as well as the frequency content of the record, in order to assess variation in response of 3S1B and 6S2B MRFs. Predominant period of the earthquake records were found by performing Fourier transformation of the input excitation (Chopra 2006). The ground motion records represent a sample of earthquake with low, medium and high frequency content. For instance, the Kashmir ground motion record had lower PGA and spectral acceleration value but had a higher predominant period, while Tabas record had a much higher PGA and spectral acceleration value but had a smaller predominant period. This variation was considered critical in evaluating response of the two MRFs under various seismic hazard parameters.

7.4 Incremental dynamic analysis and results

Incremental dynamic analysis (IDA) method was used in this study to evaluate the response of the frames under varying seismic loading. IDA has been in use as early as 1977 but has become more popular recently due to advancement in computational capability. Vamvatsikos and Cornell (2001) showed the benefits of using IDA by changing the level of intensity of a specific ground motion. IDA method involves subjecting a structural model to one or more ground motion records. Each record is then scaled to multiple levels of intensity, thus producing one or more load displacement curves. The three 3S1B and 6S2B frames reinforced with steel, SMA-FRP and GFRP were subjected to IDA using the four ground motions (see Table 7-3). IDA curves for steel, SMA-FRP and GFRP frames were developed to find the corresponding PGA which would cause collapse. For this chapter, collapse was defined as the crushing of core concrete in the column or rupture of reinforcement whichever is earlier. From the analyses, the focus was drawn to the results of maximum inter-story drifts (ID), the PGA causing those maximum drifts, dynamic pushover curves, residual inter-story drifts and energy dissipated due to hysteresis behavior of the frames.

7.4.1 Maximum inter-story drift ratio

From the analyses results, IDA curves were generated for 3S1B and 6S2B frames, which are a plot between maximum inter-story drift (IDR%) and the PGA(g) for each record as shown in figures 7-5 and 7-6. Inter story drifts are defined as the ratio between relative displacement of two immediate floor levels and the height of that floor. Figure 7-5(a) which is the response of 3S1B subjected to Kashmir ground motion shows that for the lower value of PGA, steel-

reinforced frame shows less ID values as compared to both SMA-FRP and GFRP reinforced frames. This could be attributed to lower stiffness of both SMA-FRP and GFRP material as compared to steel. However, after a PGA of about 0.6g, SMA-FRP-reinforced frame exhibited less ID values as compared to frame with steel reinforcement. At a PGA value of 1.2g, SMA-FRP frame exhibited less ID by 7%, despite having 60% less initial modulus of elasticity as compared to steel. This can be attributed to lower damage to the SMA-FRP reinforced frame due to lesser residual drifts, discussed further in section 7.4.3. On the other hand GFRP-reinforced frame experienced much higher ID as much as 21% as compared to steel and SMA-GFRP frame despite the fact that it was able to sustain lesser PGA intensity before collapse. Figure 7-5(b) which is the response of frame subjected to Northridge ground motion also exhibits high ID values for GFRP-reinforced frame. However, for this record the steel and SMA-FRP-reinforced frames showed comparable ID values at same PGA. In this case GFRP-reinforced frame exhibited much higher ID as compared to both steel and SMA-FRP. Figure 7-5(c) is the response of frames subjected to Tabas ground motion record. The results show that the steel-reinforced frame experienced an ID of 4.16% at a PGA of 2.42g when core concrete in columns started to experience crushing. However SMA-FRP-reinforced frame experienced maximum ID of 4.2% before reaching collapse at a PGA of 2.08g. While GFRP-reinforced frame, which experienced ID of 4.8%, suffered collapse at a lower PGA of 1.54g due to rupture of GFRP within plastic hinge zone. Similar results were observed for the response of 3S1B frame subjected to Kocaeli ground motion record. Maximum drifts experienced by steel, SMA-FRP and GFRP reinforced frames were 3.24%, 4.16% and 4.8%, respectively, before collapse. Higher IDs in GFRP frames

are attributed to lower material stiffness and sudden rupture of GFRP in beams, leading to higher drifts in the frame.

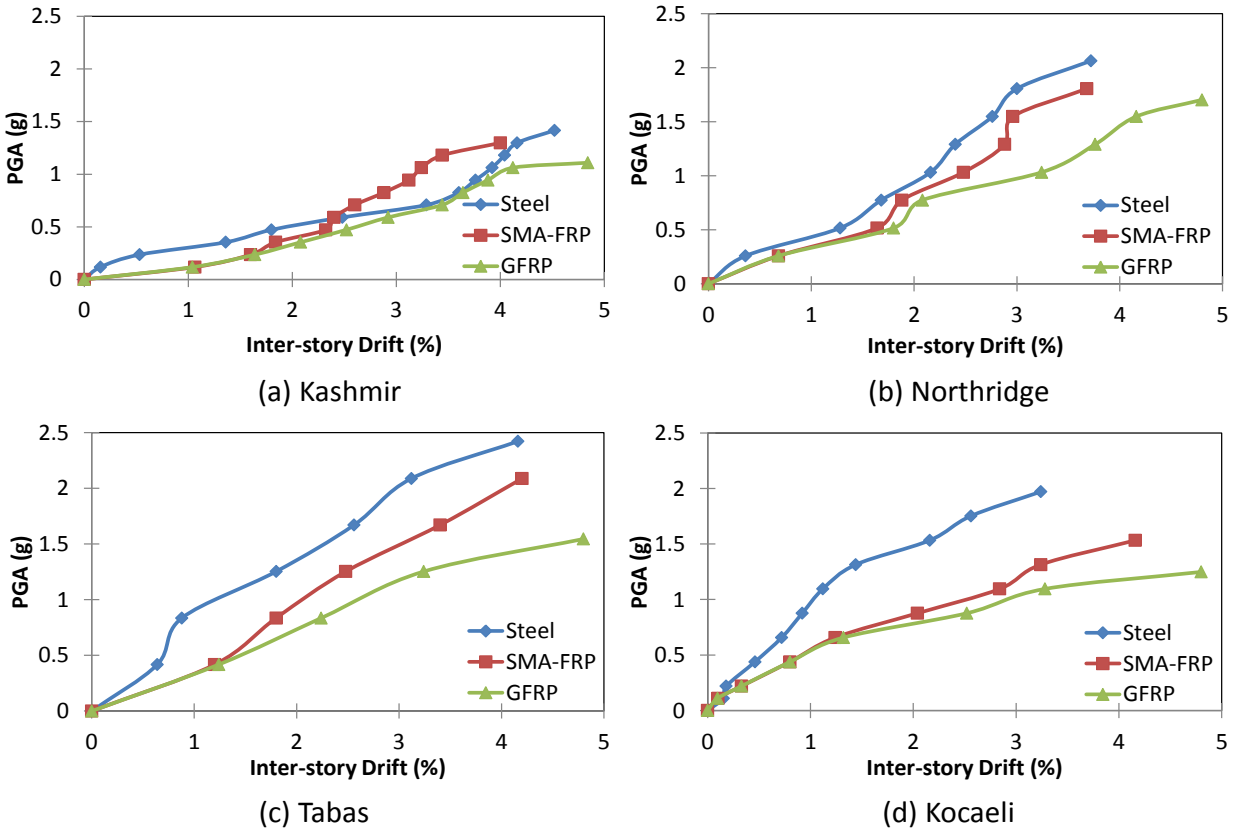

Figure 7-5: IDA curves for 3S1B MRF subjected to ground motion records.

Results for 6S2B MRF shown in figure 7-6 reveal that the steel-reinforced frame experienced smaller ID compared to its counterparts because of higher initial stiffness and higher yield strength. From the analyses results, it is observed that steel and SMA-FRP frames were able to experience 30% and 17%, respectively less average ID as compared to GFRP-reinforced frame. The lower drift values exhibited by SMA-FRP frame could be attributed to the prime property of SMA material to recover strains. This leads to overall less damage to the frame and

thus leads to lesser overall ID. From the results it can be stated that the steel and SMA-FRP reinforced frames exhibited close performance in terms of inter-story drifts at same PGA values, however GFRP-reinforced frame exhibited much higher inter-story drift values despite reaching failure limit state at lower PGA values as compared to steel and SMA-FRP reinforced frames.

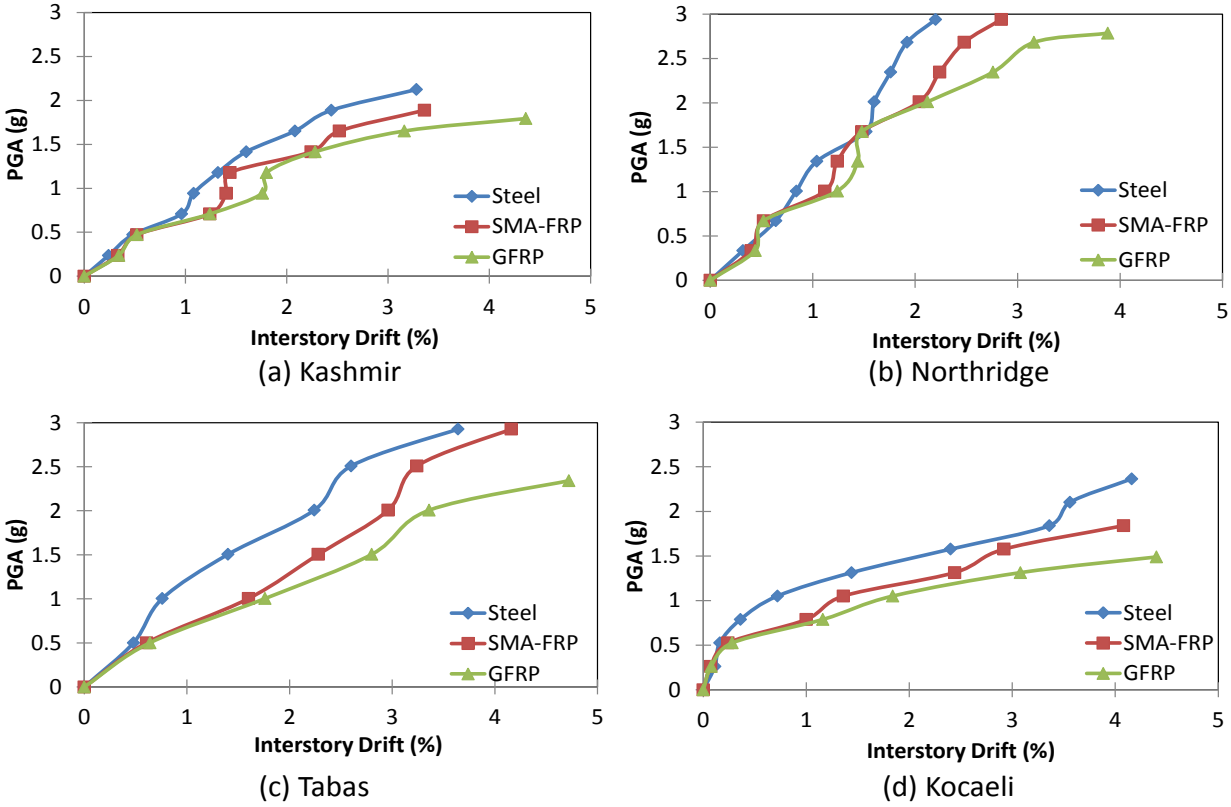

Figure 7-6: IDA curves for 6S2B MRF subjected to ground motion records.

As mentioned earlier, the collapse of the frame was defined as development of plastic hinge in column, which is triggered by yielding of reinforcement and crushing of core concrete at the same location or rupture of reinforcement. By running IDA technique, this collapse

mechanism was corresponded to maximum PGA which the frames can sustain just before their collapse (or causing collapse). 6S2B frame was able to sustain higher maximum PGA before reaching collapse as compared to 3S1B frame. The aforementioned results can be attributed to higher redundancy in 6S2B frame as compared to 3S1B frame. Because of strong column weak beam design approach which was followed in designing the frames, more number of beams were able to sustain collapse before the plastic hinge could develop in the columns, as compared to 3S1B frame. This observation was common for all four earthquake records. Also from the results it can be stated that steel reinforced frames were able to sustain higher maximum PGA for all four earthquake records. This performance was then followed by SMA-FRP and then lastly by GFRP reinforced frame. This performance behavior can be attributed to higher ductility and strength capacity of steel reinforcing material. The average increase in maximum PGA for 3S1B frame reinforced with steel and SMA-FRP was 42% and 20% respectively, as compared to GFRP reinforced frame. However for 6S2B frame, this difference was 23% and 14% for steel and SMA-FRP reinforced frames, respectively. This can be attributed to more redundancy in the 6S2B frame as compared to 3S1B frame. Figure 7-7 shows the PGA causing collapse of 3S1B and 6S2B MRFs.

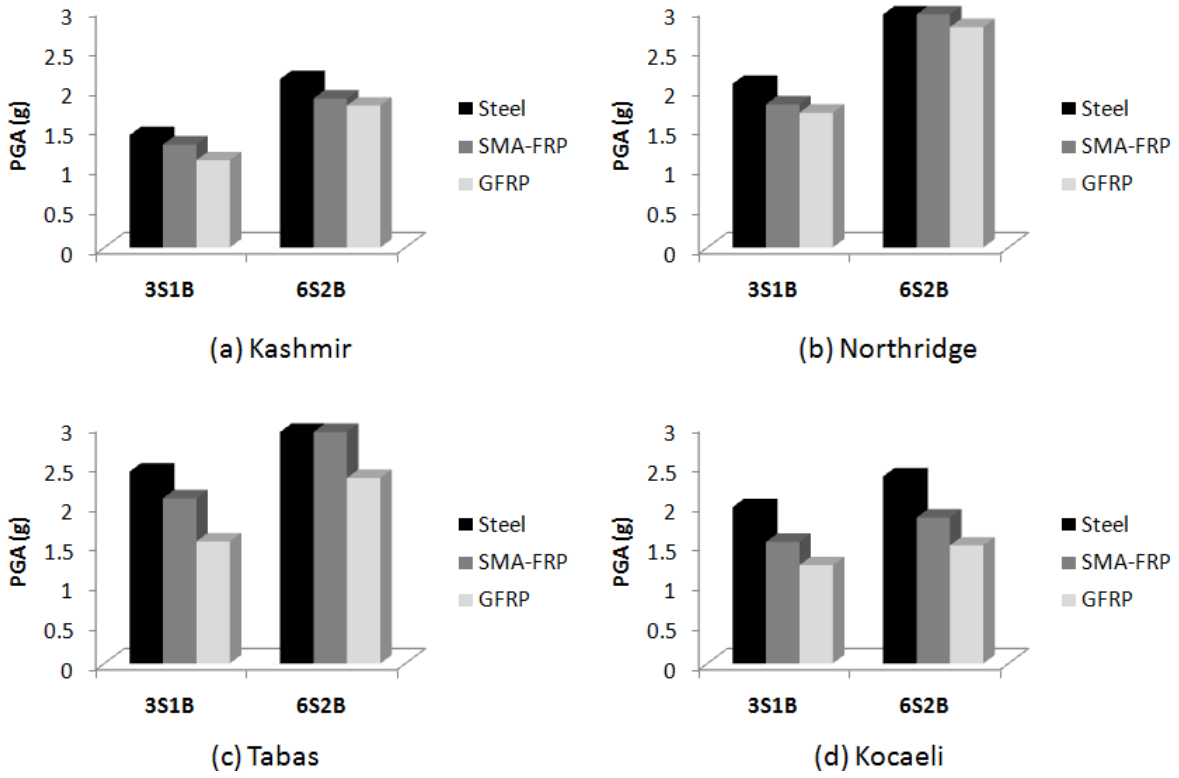

Figure 7-7: PGA causing collapse of 3S1B and 6S2B MRFs.

7.4.2 Dynamic pushover

Dynamic pushover curve is a plot between maximum drift vs. corresponding base shear obtained from IDA analyses technique while being subjected to an earthquake record (Elnashai and Luigi 2008). These curves can be utilized to estimate the structural capacity under specific earthquake loading. Unlike static pushover curves, dynamic pushover curves incorporate the frequency content of the earthquake excitation in the response. Dynamic pushover curves resulted from IDA technique for steel, SMA-FRP and GFRP reinforced frames were developed and are shown for 3S1B and 6S2B frames in figure 7-8 and figure 7-9, respectively.

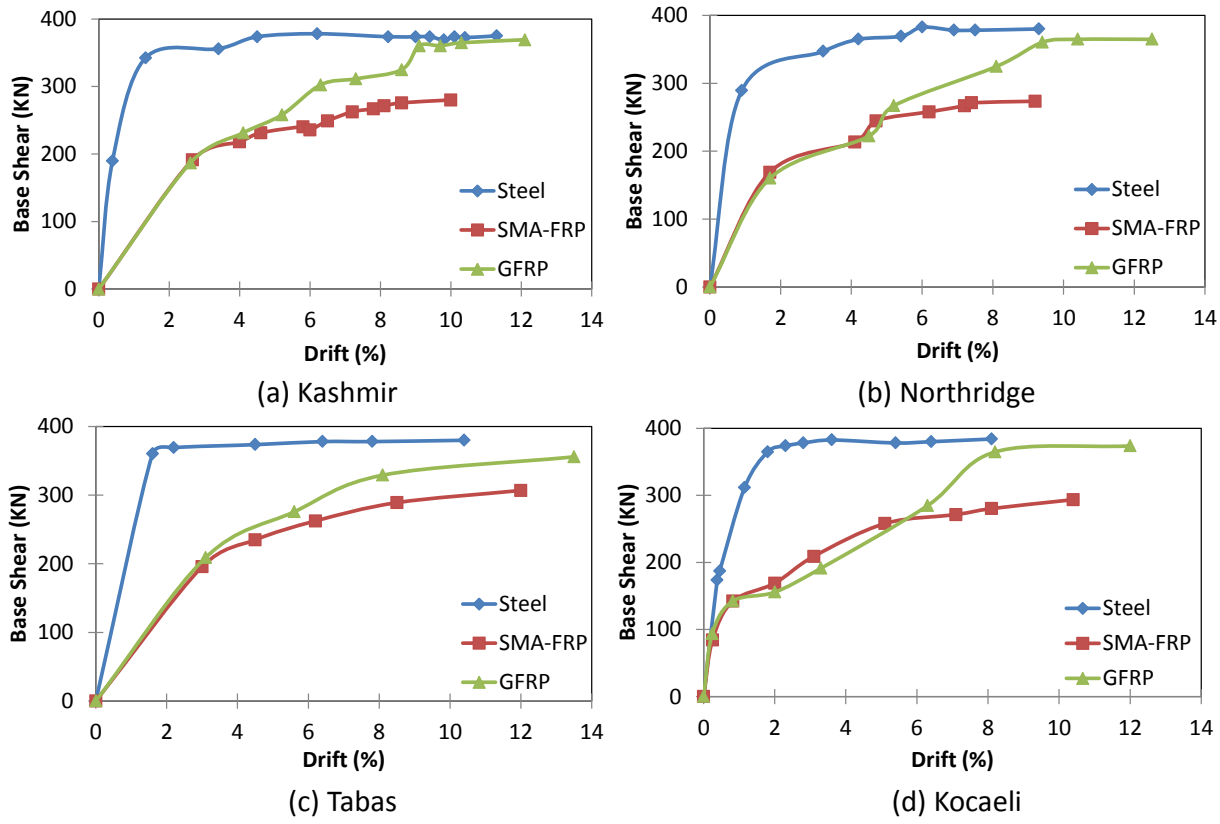

Figure 7-8: Dynamic pushover curves for 3S1B MRF.

The results of analyses show that the value of maximum base shear for 3S1B is not influenced much by change of ground motion frequency content. From figure 7-8, it is evident, that the response of all three frames is similar for all four earthquake records with maximum base shear variation within 5%, which is insignificant variation. However for 6S2B frame, this variation was more significant, (close to 10% for all three frames) as shown in figure 7-9. Thus it is reasonable to say that the maximum base shear value is affected by the frequency content of the earthquake record used for structures which have higher period and are more flexible. Also from the figure it is evident that steel reinforced frames have much higher initial stiffness as

compared to both SMA-FRP and GFRP reinforced frames. This is primarily due to higher material modulus of steel as compared to SMA-FRP and GFRP. It is also observed that unlike steel and SMA-FRP reinforced frames which do exhibit a yielding behavior, GFRP reinforced frame continues to show near linear response till the rupture of GFRP reinforcement in the column, which is considered as ultimate limit state for the frame.

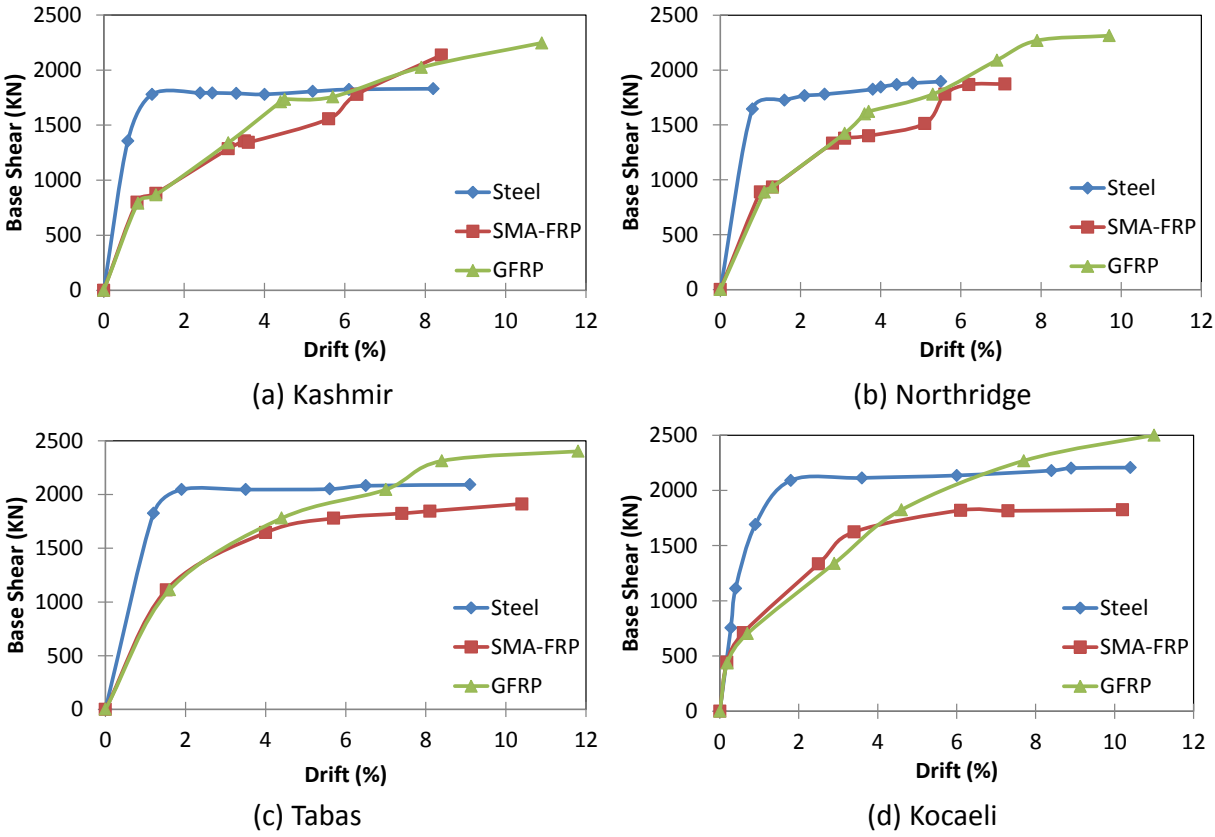

Figure 7-9: Dynamic pushover curves for 6S2B MRF.

7.4.3 Residual inter-story drifts

During any seismic event structures which get severely damaged, exhibit permanent deformations. For MRFs permanent deformations are generally quantified in terms of residual drifts. Residual inter-story drifts (IDs) are therefore a good signal of the level of permanent damage sustained by the structure and are sourced by nonlinear behavior and yielding of reinforcement, development of cracks in concrete and crushing of concrete within plastic hinge zone. Figures 7-10 and 7-11 show the residual ID plots of 3S1B and 6S2B frames, respectively when subjected to the four earthquake records.

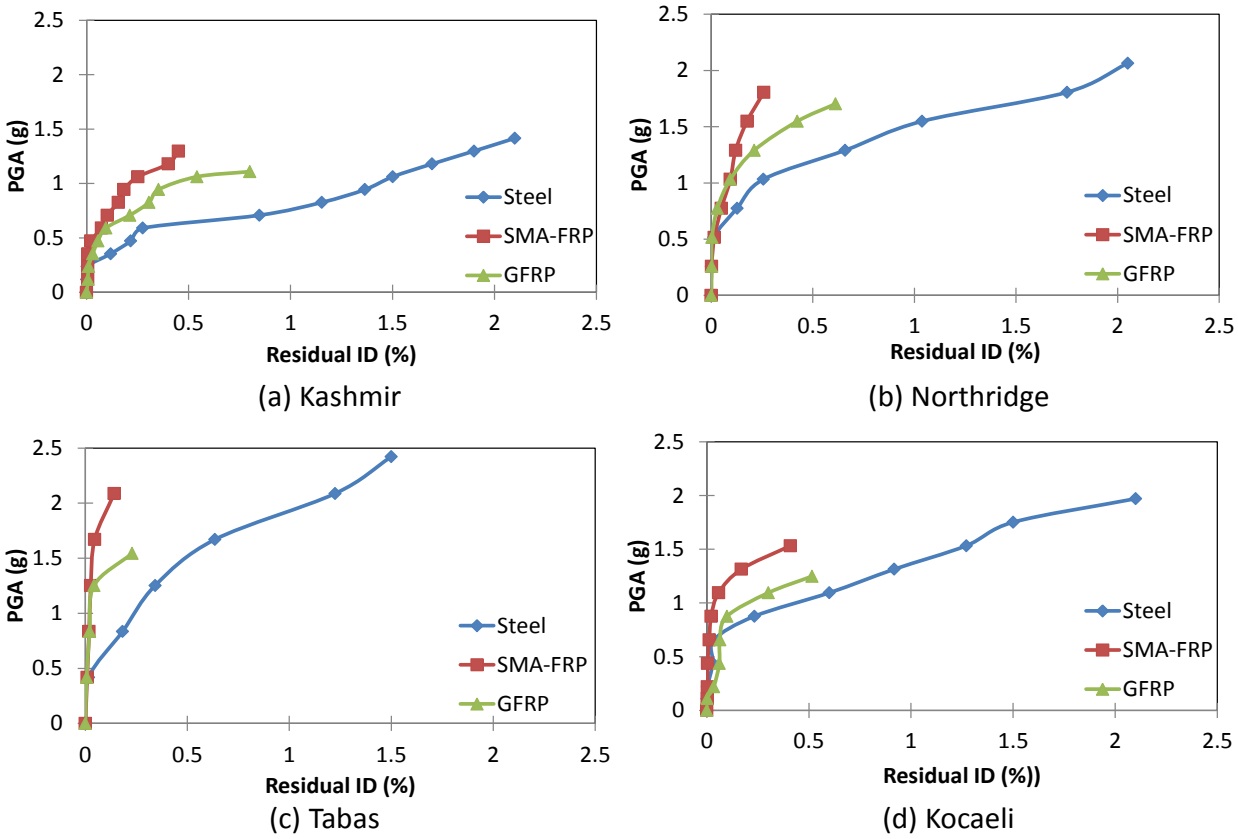

Figure 7-10: Residual inter-story drifts for 3S1B MRF.

By comparing the residual ID values, it was observed that, SMA-FRP-reinforced frame exhibit about 84% and 82% less residual ID compared to 3S1B and 6S2B steel reinforced frame. Frame with steel reinforcement initially experienced less residual ID as compared to SMA-FRP and GFRP reinforced frames till the PGA range of 0.4g-0.5g due to high stiffness. However once the steel reinforcement started to yield, it developed higher residual ID, for the same value of PGA, as compared to SMA-FRP reinforced frame. Because SMA exhibit almost negligible amount of residual strains, the behavior of frame with SMA-FRP composite reinforcement in plastic hinge zone was found to be much superior. On the other hand, GFRP reinforced frame, which reached collapse limit state at a lower PGA value, exhibited on average 49% higher residual inter story drift values when compared to SMA-FRP reinforced frame but 62% lesser residual inter story drift values when compared to steel reinforced frame.

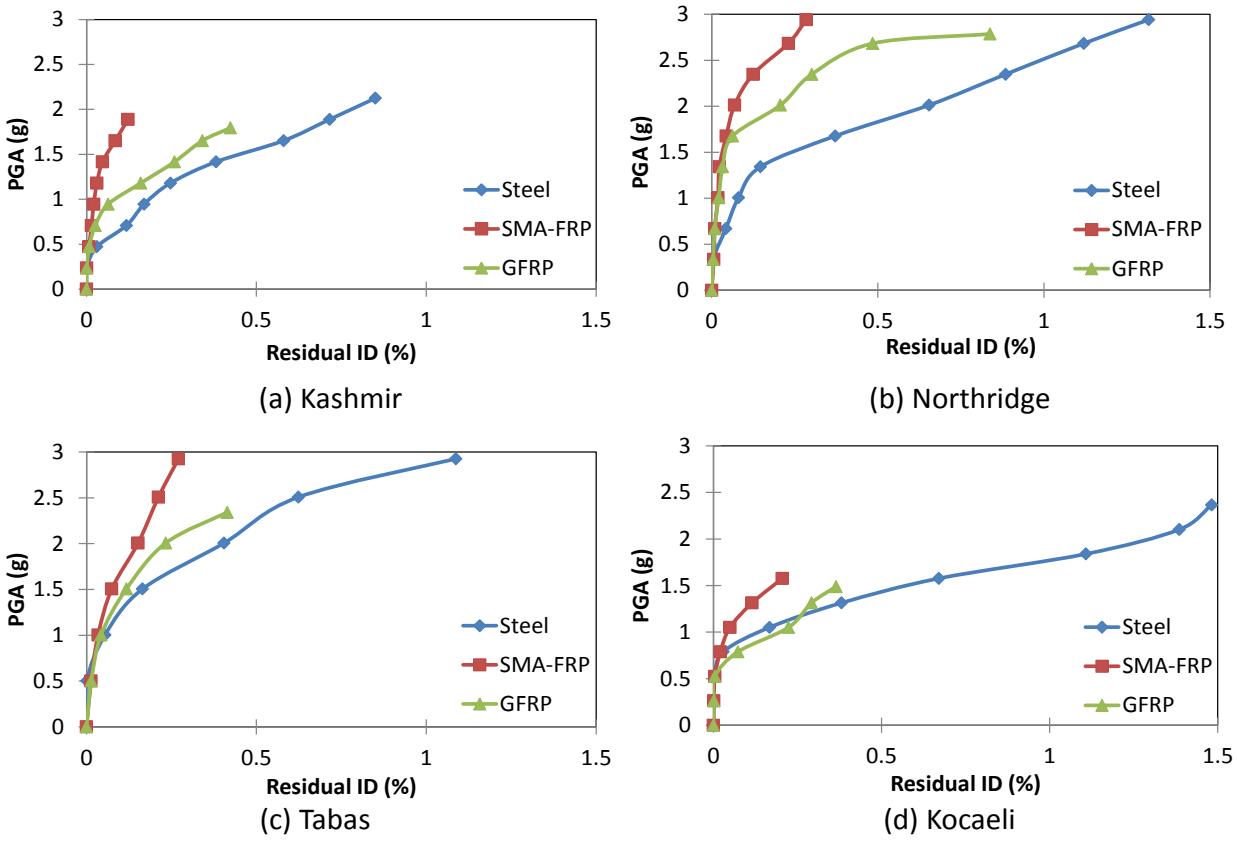

Figure 7-11: Residual inter-story drifts (ID) for 6S2B MRF.

Irrespective of frequency content of earthquake excitation, SMA-FRP-reinforcement showed much better performance in ways to curb damage by recovering the applied strains. This tendency and property to re-center itself after experiencing inelasticity is the hallmark of SMA material and is that which distinguishes it from GFRP and steel as reinforcing material.

7.4.4 Dissipated hysteretic energy

The ability of a structure to dissipate energy during a seismic event is also an important desirable seismic parameter. This dissipated energy is the direct result of damping and hysteretic

nature of the material. But energy alone will not be enough indication to show the desirable characteristic of SMA-FRP reinforcement. In order to illustrate the concept, hysteretic behavior of 3S1B frame reinforced with steel, SMA-FRP and GFRP when subjected to Kocaeli earthquake record is shown in figure 7-12. This figure is a plot between roof drift (ratio between displacement and height of frame) and base shear reaction. The response shown in the figure is governed by the hysteretic nature of material response and is shown for the PGA level causing failure in GFRP frame. Figure 7-12(a) clearly shows superior performance of steel reinforcement followed by SMA-FRP composite, in terms of energy dissipation, which is calculated, based off of cumulative area enclosed within the displacement vs. base shear plot. This improved potential comes from the fact that the stress-strain curve of steel and SMA-FRP contains more hysteretic area than GFRP.

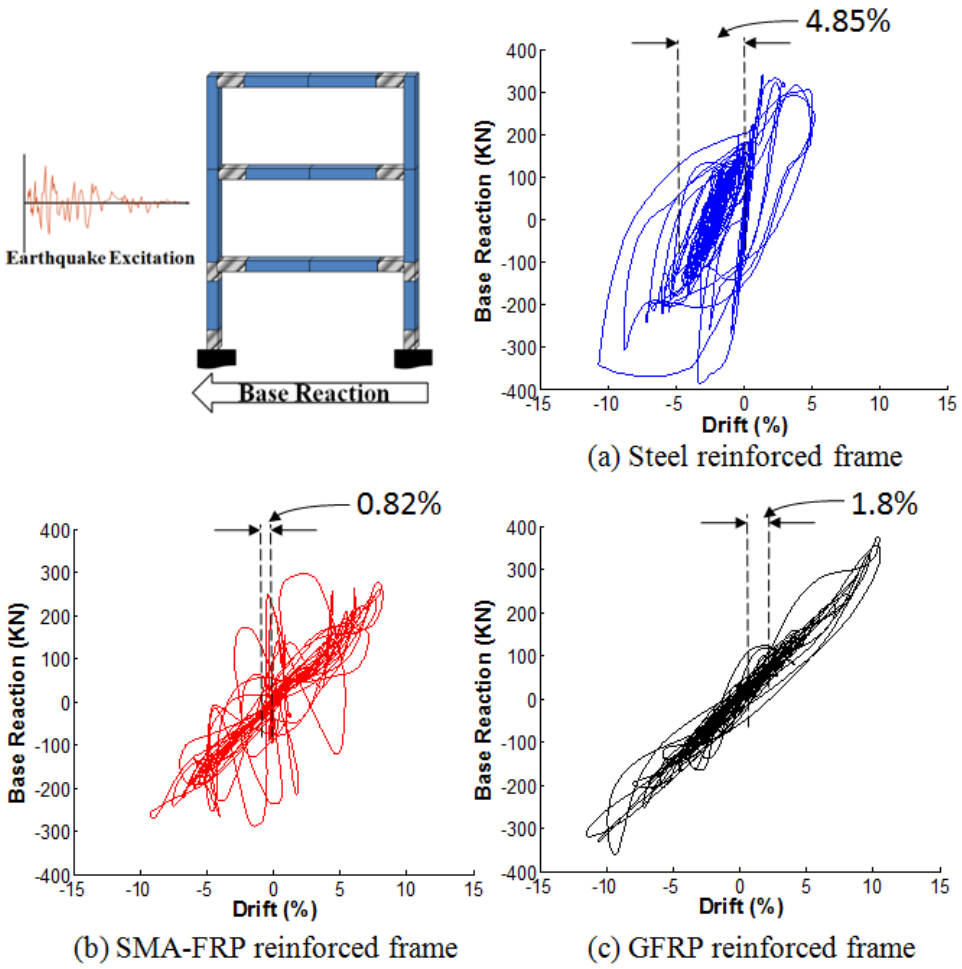

Figure 7-12: Base shear vs. roof drift for 3S1B MRF subjected to Kashmir earthquake record.

Steel and SMA-FRP reinforced frame when compared with GFRP frame showed 108% and 65% more energy dissipation, respectively. As mentioned before, the response of the three frames should be seen in light of energy dissipated and the permanent residual drifts, as both parameters govern the desirable response of a structure under seismic loading. Figure 7-12 shows that although steel frame was able to dissipate much more energy as compared to other two frames, it suffered residual drifts of 4.85% measured at the roof level. On the other hand, GFRP

frame suffered 1.8% permanent drifts and failed at much lower PGA. Figure 7-12(b) shows the main benefits of using SMA-FRP composites which is their ability to dissipate energy with minimal permanent damage / residual drifts (0.82% residual drift). For the purpose of illustration, a plot of material stress-strain is shown in figure 18 for 3S1B frame when subjected to Kocaeli earthquake record. In figure 7-13(a), stress-strain plot of core concrete of the 1st story column at the location of plastic hinge is shown. The response shows core concrete reaching peak stress of 33MPa and the crushing strains at a value of 0.016 mm/mm. Figure 7-13(b-c-d) shows material response of steel, SMA-FRP and GFRP reinforcement at the same plastic hinge location in the column. Steel material response shows residual strains due to permanent damage to the RC column. The material response of SMA-FRP shows typical flag shape hysteresis with some hardening and with maximum strain reaching up to range of 6%. GFRP material response shows linear elastic behavior until rupture.

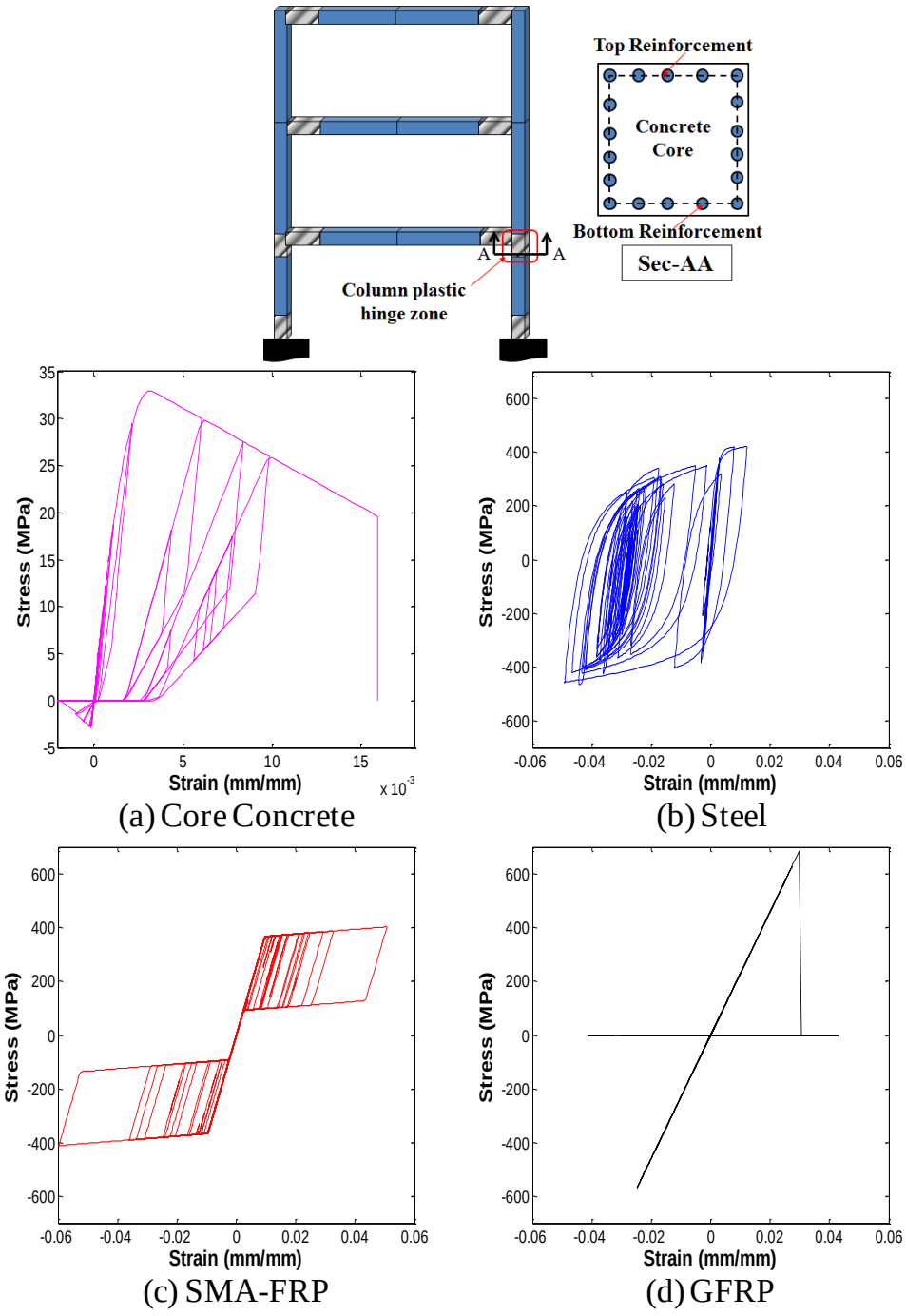

Figure 7-13. Stress strain curves of base column cross section A-A during the response from Kocaeli record (a) Core concrete (b) Steel reinforcement (c) SMA-FRP composite reinforcement (d) GFRP reinforcement

CHAPTER 8

Performance Based Design and Sequential Seismic Analysis

8.1 Introduction

Structural seismic performance is often based on response of structures to single major main shock seismic event. However, it is a common fact that aftershocks are often strong enough to cause serious damage and even collapse of structures, especially those which were already damaged during the main shock (Li and Ellingwood 2007). For example, many RC buildings during the September 1985 Mexico City earthquake were brought down using controlled demolition because of permanent damage and residual drifts from strong shaking, making them uneconomical to repair (Rosenblueth 1986). This chapter thus utilizes the effects of multiple seismic hazards as a way to assess level of damage expected in MRFs. Accumulation of permanent drifts, indicates permanent damage to the structure and could be utilized as a realistic way to incorporate effects of multiple earthquake hazards. Moreover, assessment of post earthquake damage from multiple seismic events, allows examination of structural integrity for subsequent use. Recent earthquakes (Christchurch 2010, Tohoku 2011 etc.) have shown effects of aftershocks on reinforced concrete (RC) buildings in terms of damage accumulation and permanent residual drifts due to plasticity of reinforcing steel. Hence, there is a need to revisit the performance of reinforcing material in RC structures and development of a robust reinforcement which has ability to withstand seismic forces while maintaining re-centering capability. Despite the fact that the problem has been acknowledged, very few studies have been published regarding main shock-aftershock sequences. Most of the recent studies (Amadio et al.

2003, Beskos & Hatzigeorgiou 2009) focused on nonlinear response of single degree of freedom (SDOF) systems to seismic sequence. Garcia et al. (2008) studied the performance of highway bridges under main shock-aftershock seismic sequence. Lee et al. (2009) conducted analytical research on repair and retrofitting of bridge pier under multiple seismic hazard. Recently, Garcia and Manriquez (2011) conducted research aimed at evaluating the effect of aftershock on steel framed buildings. Hatzigeorgiou and Liolios (2010) conducted a study which focused on behavior of RC frames subjected to repeated ground motions. Their study showed that the RC structures reinforced with steel are very much vulnerable to impact of aftershocks as they already are weakened due to damage accumulation and residual inter-story drifts (IDR). Lack of any experimental research and absence of guidelines by any governing body to account for multiplicity earthquake effect has made this problem more challenging. First step to meet the challenges offered by multiplicity earthquake effects is to develop a more robust reinforcing material. This chapter utilizes the proposed SMA based composite as a potential solution which has capability of dissipating energy through hysteretic action and re-centering under multiple seismic loading.

Recent trends in earthquake engineering have brought displacement based design approach into lime light as a replacement to conventional force based design (FEMA-445, 2006). As mentioned earlier in chapter 7, the current seismic design codes like IBC, first analyze the structure elastically under a reduced level of equivalent lateral force using R factor. The design base shear obtained through this procedure is used to determine member sizes and reinforcement through sectional analysis. It is then designed by ultimate stress design method to provide sufficient flexural strength followed by checking for shear capacity. Lately, a more modern and a

popular approach, in which performance based assessment methodologies for evaluation of existing and design of new structures are based on peak lateral displacement demands. Performance based engineering (PBE) involves use of these displacement demands and capacities with additional guidelines for designs, expressed in terms of achieving performance objectives. Generally, performance objectives are pre-quantified by the inter story drift ratio (IDR) limits. Present seismic design practice advocates use of displacement based criteria's bounded by certain performance limit states (LS). FEMA-273 (FEMA-273, 1997) defines these limit states in terms of three structural performance levels namely immediate occupancy (IO), life safety / damage control (DC) and collapse prevention (CP). For this study, collapse prevention was selected as limit state which is generally associated with severe structural damage and ductility. Since the focus of this study is to develop a new SMA based composite reinforcement which can exhibit better performance at higher ductility demands and damage during aftershock event, CP has been chosen as LS. Local LS such as crushing of concrete, buckling and residual drifts could all be associated with CP performance level. The primary focus of this chapter is to explore the use of SMA-FRP bars as reinforcement in RC MRF structures subjected to sequential earthquakes.

8.2 Design philosophy – performance based design approach

Performance based approach guidelines were used for designing 3S1B MRF with steel, SMA-FRP and GFRP reinforcement. IDR has become a common earthquake demand parameter (EDP) that is used for assessing the damage in structures (Elnashai and Luigi 2008). Since values of inter-story drift ratio (IDR) larger than 4% may result in irreparable structural damage or

collapse (Sozen 1981) so the two limit states adopted in this study for all types of frames was 3% and 4% IDR. Displacement based design approach was adopted by incorporating capacity spectrum method (CSM) as defined in Applied Technology Council, ATC-40 (ATC-40 1996). The procedure compares the capacity of the structure (in the form of pushover curve up to target IDR) with the demands on the structure (in the form of response spectrum). The graphical intersection of the two curves dictates the design of the frame by approximating the response. In order to imitate a nonlinear response of the MRF, effective damping values are used to reduce the linear elastic response spectrum (LERS - 5% damped) to inelastic response spectrum (IRS). The effective damping ratios can be related to ductility ratios for various characteristics of hysteretic behavior and can be used to determine spectral reduction factors. The original procedure as an evaluation tool has been explained in detail in ATC-40 and later modified as design tool by Freeman (1998). A schematics representing the whole design procedure using capacity spectrum method has been depicted in figure 8-1. After the initial estimate of cross sections and reinforcement ratio, the frames were analyzed to get pushover curves and dynamic response characteristics such as fundamental elastic period, modal participation factor and effective modal weight ratio for target IDR of 3% and 4%. The pushover curves which were converted to capacity spectrum (Acceleration vs. displacement) format (A-D) were then matched up with inelastic response spectrum (A-D format) for target IDR. The elastic response spectrum was developed based on International Building Code (IBC) (IBC-2006) for a high seismic zone with site classification B in California. The mapped spectral acceleration for short period (S_s) was 1.15g and mapped spectral acceleration for 1-second period (S_1) was 0.5g. The frames were then redesigned to get capacity spectrum which would exactly intersect inelastic response

spectrum at target IDR. This iterative process not only requires change in member sizes but also in reinforcement ratio. A flow chart explaining the overall design process using capacity spectrum method is shown in figure 8-2.

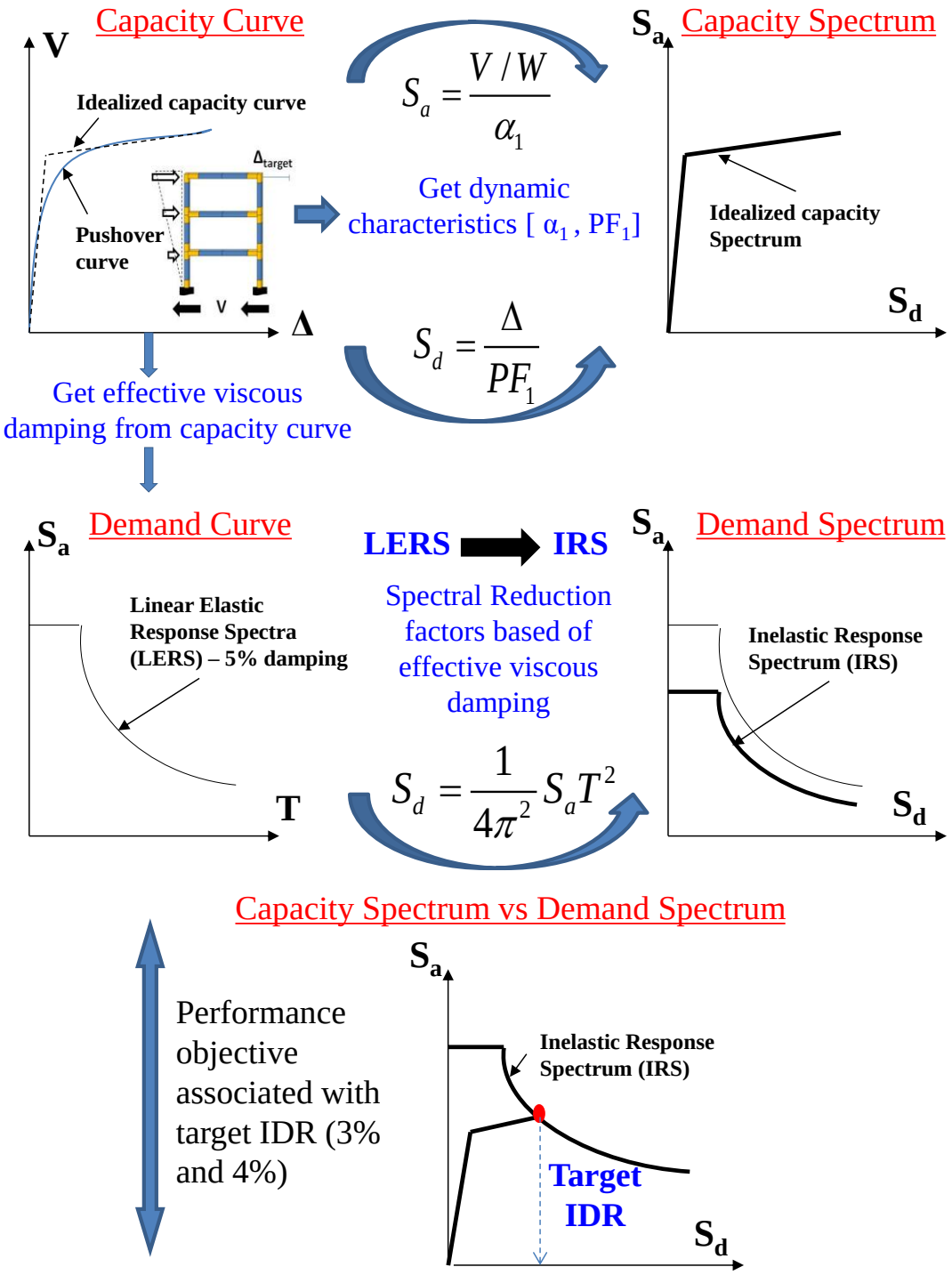

Figure 8-1: Schematics of Capacity Spectrum Method (CSM) adopted for design of MRF

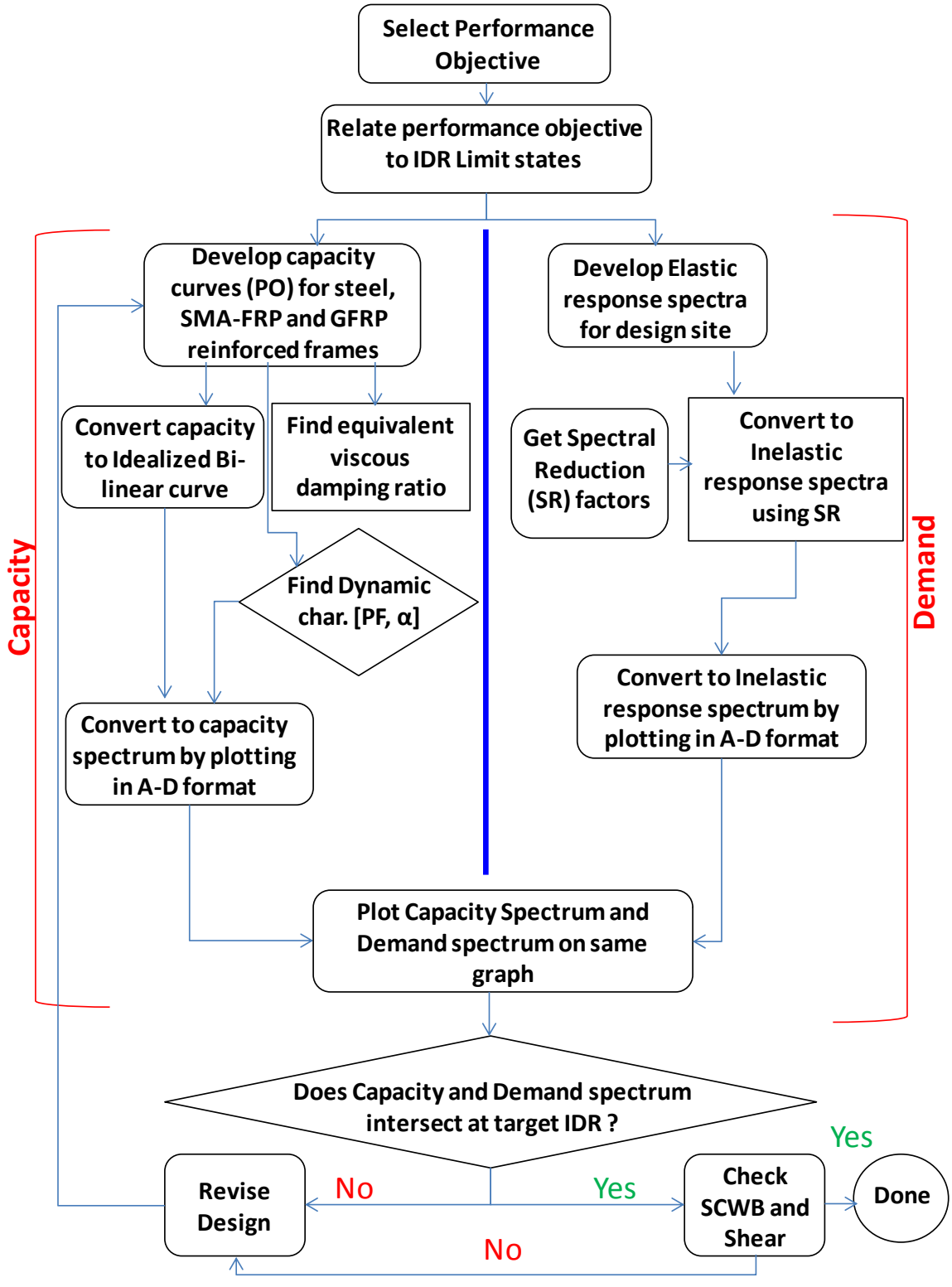

Figure 8-2: Flowchart for adopted design process using Capacity Spectrum Method (CSM)

The reinforcement ratio for beam and columns in both the frames is shown in table 8-1 after final iteration. The selected beam and column dimensions for MRF designed for 3% IDR demand were 300x525 mm and 475x475 mm, respectively for all three frames. For MRF designed for 4% IDR, the beam and column dimensions for MRF designed for 3% IDR demand were 300x500 mm and 450x450 mm, respectively.

Table 8-1: Reinforcement ratio for the designed column and beam cross-sections

Performance Limit State	**Reinforcement Ratio (ρ-%)**						**Fundamental Period (Sec.)**			**Ultimate Strain in Column Core Concrete**
	Beam			**Column**						
	Steel	**SMA -FRP**	**GFRP**	**Steel**	**SMA-FRP**	**GFRP**	**Steel**	**SMA-FRP**	**GFRP**	
3% IDR Design (MRF-3%)	1	1.5	1.2	2.56	3.8	3.52	0.46	0.52	0.51	1.4%
4% IDR Design (MRF-4%)	0.9	1.4	1.1	2.56	3.52	3.2	0.49	0.57	0.55	1.6%

The final capacity spectrum and design spectrum for steel, SMA-FRP and GFRP reinforced frame with 3% IDR performance limit state has been shown as an example in figure 8-3, 8-4 and 8-5, respectively.

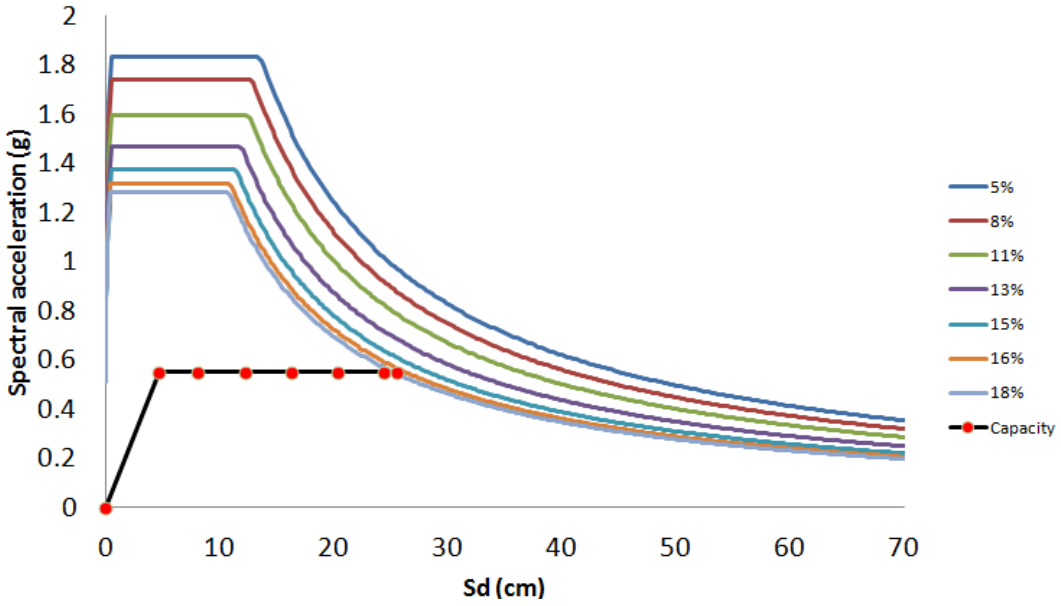

Figure 8-3: Capacity spectrum vs. response spectrum for various effective damping ratio for steel reinforced MRF at 3% target IDR

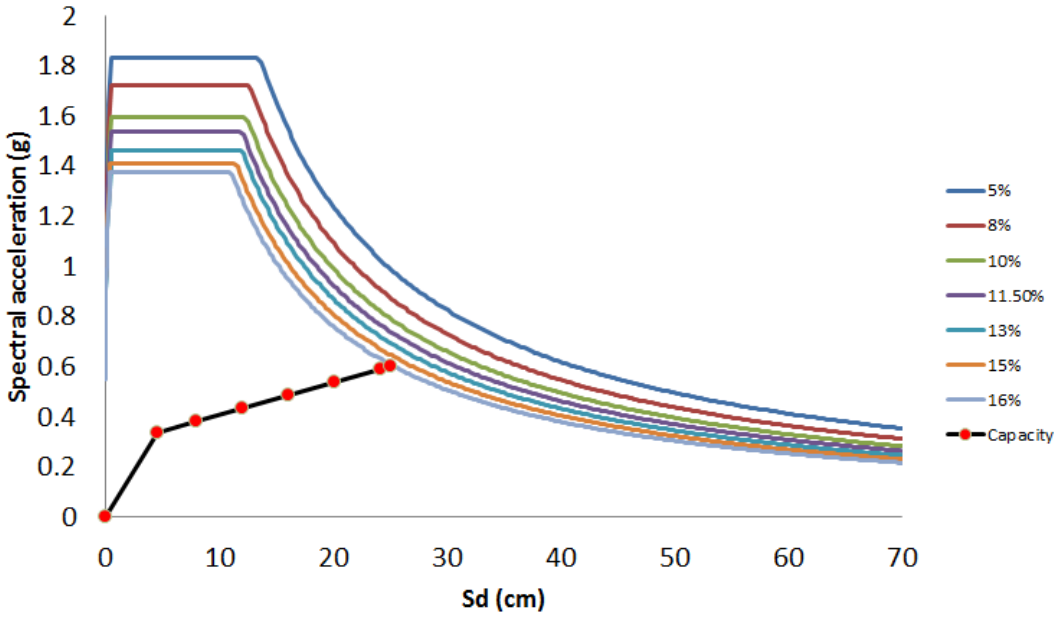

Figure 8-4: Capacity spectrum vs. response spectrum for various effective damping ratio for SMA-FRP composite reinforced MRF at 3% target IDR

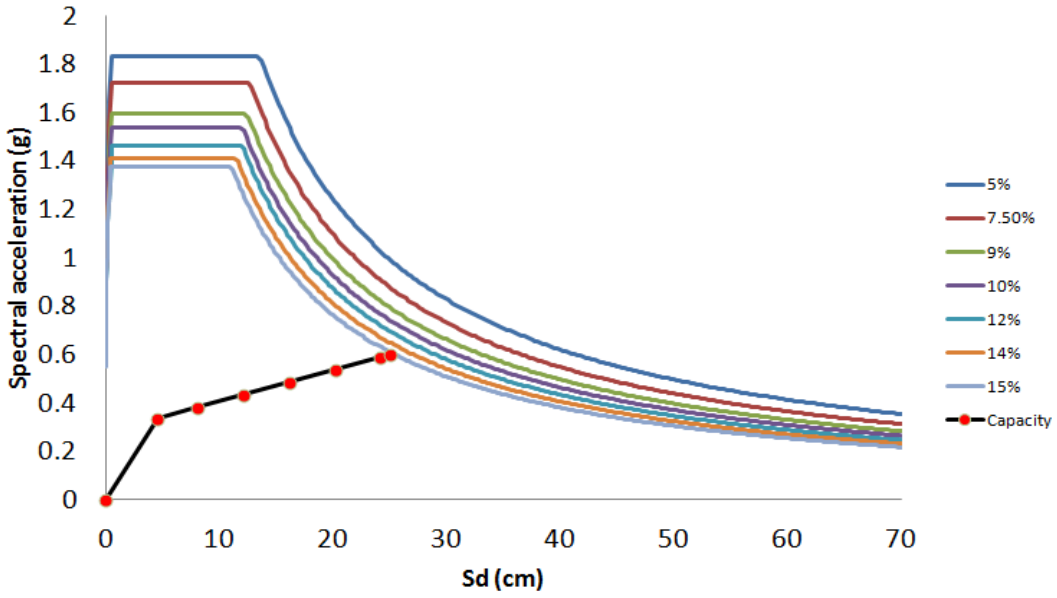

Figure 8-5: Capacity spectrum vs. response spectrum for various effective damping ratio for GFRP reinforced MRF at 3% target IDR

8.3 Selection of ground motions representing sequential seismic input

Natural ground motion records from six earthquakes were chosen as seismic input for sequential nonlinear time history analysis. The sequential records i.e. the main shocks and the aftershocks were recorded by same station and in same direction. The seismic sequences used in this study are from Imperial Valley events (1979), Mammoth Lake events (1980), Coalinga events (1983), Chalfant Valley events (1986), Christchurch events (2010) and Tohoku events (2011). The Christchurch event from CCC recording station is a 4-event sequence while all others are 2-event sequences. The details of these records and their characteristics (magnitude, PGA and predominant period) are listed in table 8-2.

Table 8-2: Sequential seismic input and their characteristics

# of Events	Earthquake	Record Station	Sequence	Date	Magnitude (Mw)	PGA (g)	Predominant Period (sec)
2-Event Sequence	1979 Imperial Valley	5055 Holtville P.O.	Main	10/15/1979	6.6	0.601	1.32
			After	10/15/1979	5.2	0.12	0.28
	1980 Mammoth Lake	54099 Convict Creek	Main	5/25/1980	6.1	0.441	0.13
			After	5/25/1980	6	0.178	0.33
	1983 Coalinga	Pleasant valley pump yard-1162	Main	5/2/1983	6	0.591	0.49
			After	7/22/1983	5.3	0.602	0.69
	1986 Chalfant Valley	54428 Zack Brothers Ranch	Main	7/21/1986	5.9	0.447	0.58
			After	7/31/1986	6.3	0.064	0.95
	2010 Christchurch	Christchurch Botanic Garden	Main	9/3/2010	7.1	0.149	0.42
			After	2/21/2011	6.3	0.529	0.48
	2011 Tohoku	FKS 013	Main	3/11/2011	9	0.36	0.44
			After	4/7/2011	7.4	0.096	0.4
4-Event Sequence	2010 Christchurch	Christchurch Cathedral College (CCC)	Main	9/3/2010	7.1	0.149	0.42
			After-1	9/7/2010	5.13	0.126	0.14
			After-2	10/18/2010	5.03	0.081	0.34
			After-3	12/25/2010	4.9	0.216	0.31

Earthquake records are generally characterized by peak ground acceleration (PGA) and the response spectra. However, the seismic response of structures is significantly affected by duration and number of cycles of the ground motion (Jeong and Iwan 1988). For structures responding in nonlinear range, the sustenance of drifts and magnitude of permanent deformation depends on the duration of shaking. It is therefore crucial to account for effects of duration and number of cycles of ground motion records on the structure. Numerous definitions of ground motion record durations have been proposed, but for this research 'significant duration' was used as threshold to compute duration. It is defined as the time interval over which a portion of the total energy integral is accumulated. The accumulation of energy in earthquake record can be

computed as the integral of the square of the ground acceleration and this quantity is related to Arias intensity, AI (Arias 1970) given by following expression:

$$AI = \frac{\pi}{2g}\int_0^{tr} a^2(t)dt \qquad (8\text{-}1)$$

where, a(t) is the acceleration time history and tr is the total duration of the record. Generally, the significant duration is assumed equal to the build-up of the Arias intensity between two arbitrary limits. For this study, limits used are 5% and 95%, and are referred as Husid plot (Husid 1969). Since the ground motion records are required to be scaled for analysis (discussed later), use of significant duration seems more appropriate and justified. Based on above mentioned definition, significant duration of all ground motion records were computed and have been shown in Table 8-3. A ratio between durations of main and aftershock records was computed for all the records. A ratio less than 1 implies longer aftershock record and more number of cycles as compared to main shock, thus more potential to accumulate damage after an initial main shock event. The records have been listed in Table 8-3 based on ascending duration ratio between main and aftershock records. Duration ratio for earthquake record from Christchurch Cathedral College (CCC) with 4-event sequence has been computed by adding duration from all three aftershocks and comparing the total duration with main shock duration.

Table 8-3**:** Significant duration Ratio of sequential ground motion records

Earthquake	Sequence	Significant Duration (sec)			Duration Ratio (Main/After)
		5% AI	95% AI	Net	
1986, Chalfant Valley	Main	3.48	9.64	6.16	0.37
	After	2.95	19.68	16.73	
2011 Tohoku	Main	56.15	156.46	100.31	1.01
	After	15.74	115.3	99.56	
1980 Mammoth Lake	Main	1.36	10.7	9.34	1.22
	After	1.61	9.24	7.63	
1979 Imperial Valley	Main	5.4	12.17	6.77	1.57
	After	3.96	8.27	4.31	
Christchurch Cathedral College (CCC)	Main	23.69	47.61	23.92	2.09
	After-1	7.82	11.43	3.61	
	After-2	7.94	13.2	5.26	
	After-3	7.74	10.31	2.57	
1983, Coalinga	Main	3.86	11.78	7.92	2.19
	After	4.7	8.31	3.61	
2010 Christchurch	Main	23.69	47.61	23.92	2.47
	After	13.58	23.25	9.67	

8.4 Preliminary study on importance of sequential seismic analysis

Aftershocks have been known to cause increase in damage to the structure which may lead to collapse. In order to show that sequential seismic input leads to varying response once compared to single main shock event, incremental dynamic analysis (IDA) technique was utilized. IDA technique allows focusing on the frequency content of the ground motion as the whole record is scaled with same intensity level. The primary goal of IDA technique is to quantify the reserve capacity of the structure against collapse. As a sample, steel reinforced MRF

was selected and subjected to Coalinga earthquake records. The frame was first subjected to scaled main shock using IDA technique till the response of the structure reached a target limit state. For this section only, the target limit state was defined as failure of any column in the structure which in turn means yielding of reinforcement followed by crushing of core concrete. Then the same original frame was subjected to aftershock from the same record using IDA technique to reach the target limit state. After recording the response from the main and aftershock, the original frame was subjected to sequential ground motion record. A single sequential ground motion record was created by adding the aftershock to the main shock record with 50 seconds time gap. This sequential serial array allowed combining the two consecutive seismic events and scaling them so that the ratio of frequency content of main and aftershock records remain the same. The time gap was necessary to minimize the transient vibration from the main shock. Figure 8-6a shows the maximum IDR experienced by steel reinforced MRF once subjected to all three earthquake records associated with Coalinga earthquake. Figure 8-6b compares the accumulation of residual drifts during the course of IDA analysis for all three records.

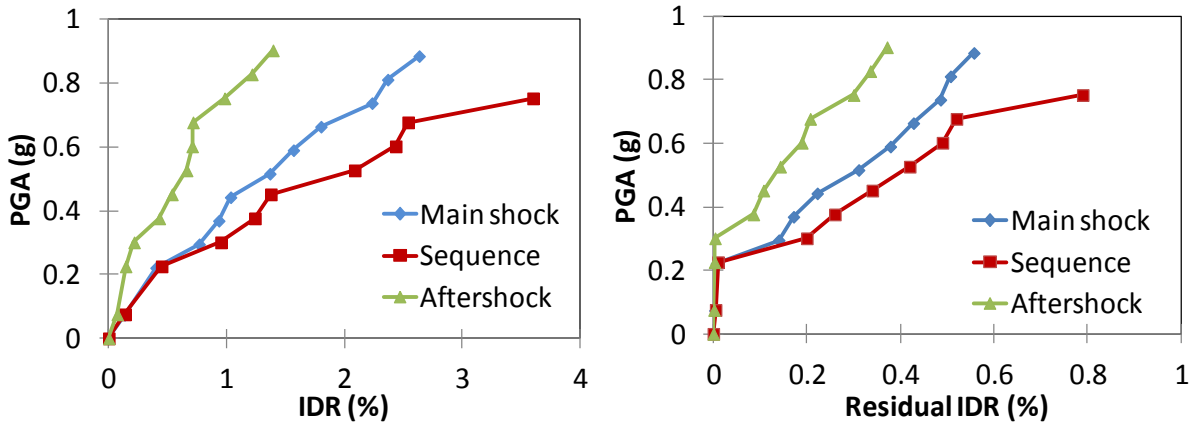

(a) (b)

Figure 8-6: Response of steel reinforced MRF subjected to Coalinga earthquake records (a) IDR vs PGA (b) Residual IDR vs PGA

Figure 8-6a shows that the frame subjected to sequential record reached limit state at a PGA of 0.753g. For same value of PGA, frame subjected to main and aftershock did not experience reaching of limit state i.e. development of plastic hinge in any column in the frame. This early failure of the frame once subjected to sequential record is indicative of the fact that there is higher displacement demands exerted on the frame due to effect of considering aftershock. Also for same value of PGA, frame subjected to sequential record experienced more IDR value (3.6%) as compared to main shock which experienced 2.6% IDR. This reduction of 27.7% in IDR for same value of PGA between sequential and main shock indicates the significance of sequential seismic analysis. Similar pattern is observed in figure 8-6b for residual IDR values between main and sequential records. Till PGA of 0.22g, when steel did not yield, the residual IDR is about the same in both frames subjected main and sequential record. However after yielding of steel, the demand exerted on frame subjected to sequential record increases, thus increase in IDR and residual IDR as compared to other two frames. It is evident

from the results that the sequential record causes the MRF to experience more IDR as compared to any single seismic event (main shock) as it is subjected to more displacement demands. Increased displacement demand leads to higher values of IDR and residual drifts, indicating more damage.

8.5 Sequential analysis technique

The inelastic response of the examined MRFs was investigated using sequential incremental dynamic analysis (IDA). In step-1, all three designed MRFs with steel, SMA-FRP and GFRP reinforcement were first subjected to main shock records, till the time the scaled ground motion record caused 3% and 4% IDR. In the subsequent analysis in step-2, the scaled main shock (from step-1) and aftershocks were combined together to develop a single sequential ground motion record and was again subjected to each MRF. A time gap was applied between each scaled main and aftershock record of 50 seconds to curb any transient vibration. The aftershock part of the sequential record was again scaled to different intensity levels, till the time the scaled sequential ground motion record again causes 3% and 4% IDR. The analysis technique being used in this study is further explained in the illustration in figure 8-7. For the case with 4-event sequence, similar analysis procedure was adopted as mentioned earlier. After scaling the main shock so as to cause 3% and 4% IDR, first aftershocks were scaled to result in 3% and 4% IDR. The damaged frames were again subjected to 2nd and 3rd aftershocks sequence till the target IDR LS is achieved. Drift time history for steel, SMA-FRP and GFRP reinforced frames were developed to find the corresponding PGA which would satisfy the targeted

performance level (3% and 4% IDR). Accumulations of residual IDR in frames were also recorded for each earthquake sequence.

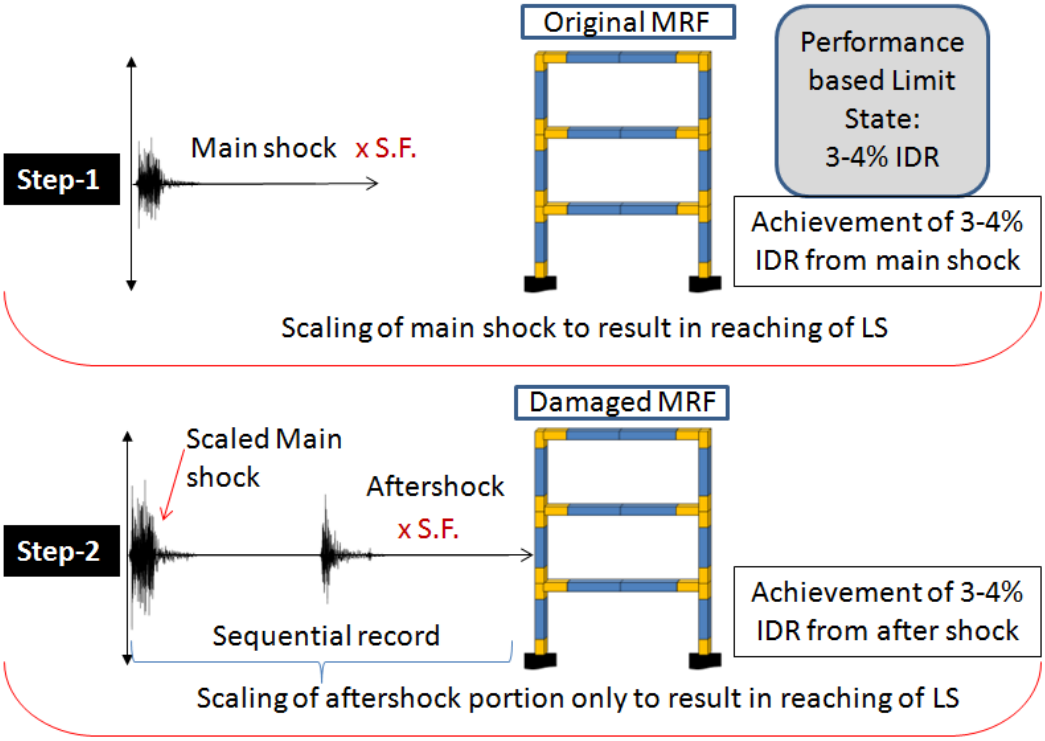

Figure 8-7: Illustration of sequential seismic analysis technique

8.6 Results and discussion

All the six MRF's with steel, SMA-FRP and GFRP reinforcement designed for 3% IDR (MRF-3%) and 4% IDR (MRF-4%) were subjected to the sequential records shown in table 8-3. Response of MRF's in terms of IDR time history and accumulation of residual IDR were evaluated in relation to PGA. Other ground motion record parameters such as duration ratio were correlated with response of the structure. All these parameters and characteristics are discussed below in detail.

8.6.1 IDR time history and residual IDR

IDR time history response of the MRF reinforced with steel, SMA-FRP and GFRP reinforcement were investigated, when subjected to earthquake records listed in table 8-3. Aforementioned analysis technique was adopted for all the cases to satisfy both 3% and 4% IDR limits. Examined IDR and residual IDR values include the multiplicity earthquake effects. Figure 8-8 shows the IDR time history of all three frames when subjected to Tohoku earthquake sequential records. Main shock from Tohoku was required to be scaled to a PGA of 1.51g, 1.48g and 1.33g to cause 3% IDR for steel, SMA-FRP and GFRP reinforced frames, respectively. Because of inherent higher stiffness and lower fundamental period, steel frame required higher seismic input (PGA / scaling factor) from main shock record to reach to 3% IDR as compared to SMA-FRP and GFRP reinforced MRF-3%. Hereafter the scaled main shock was kept unchanged while the aftershock was scaled till all three frames again experienced 3% IDR. The aftershock from Tohoku earthquake had to be scaled to a PGA of 0.93g, 1.16g and 1.02g to reach the target performance limit state for steel, SMA-FRP and GFRP reinforced frames, respectively. It is worth noting that steel reinforced frame accumulated 0.41% residual IDR from main shock and this permanent drift increased to 0.56% by the end of aftershock. This net residual IDR increase by 37% is due to sequential earthquake influence. On the other hand, because of re-centering capability of SMA composite reinforcement, there was no accumulation of permanent damage or drift in SMA-FRP reinforced MRF-3%.

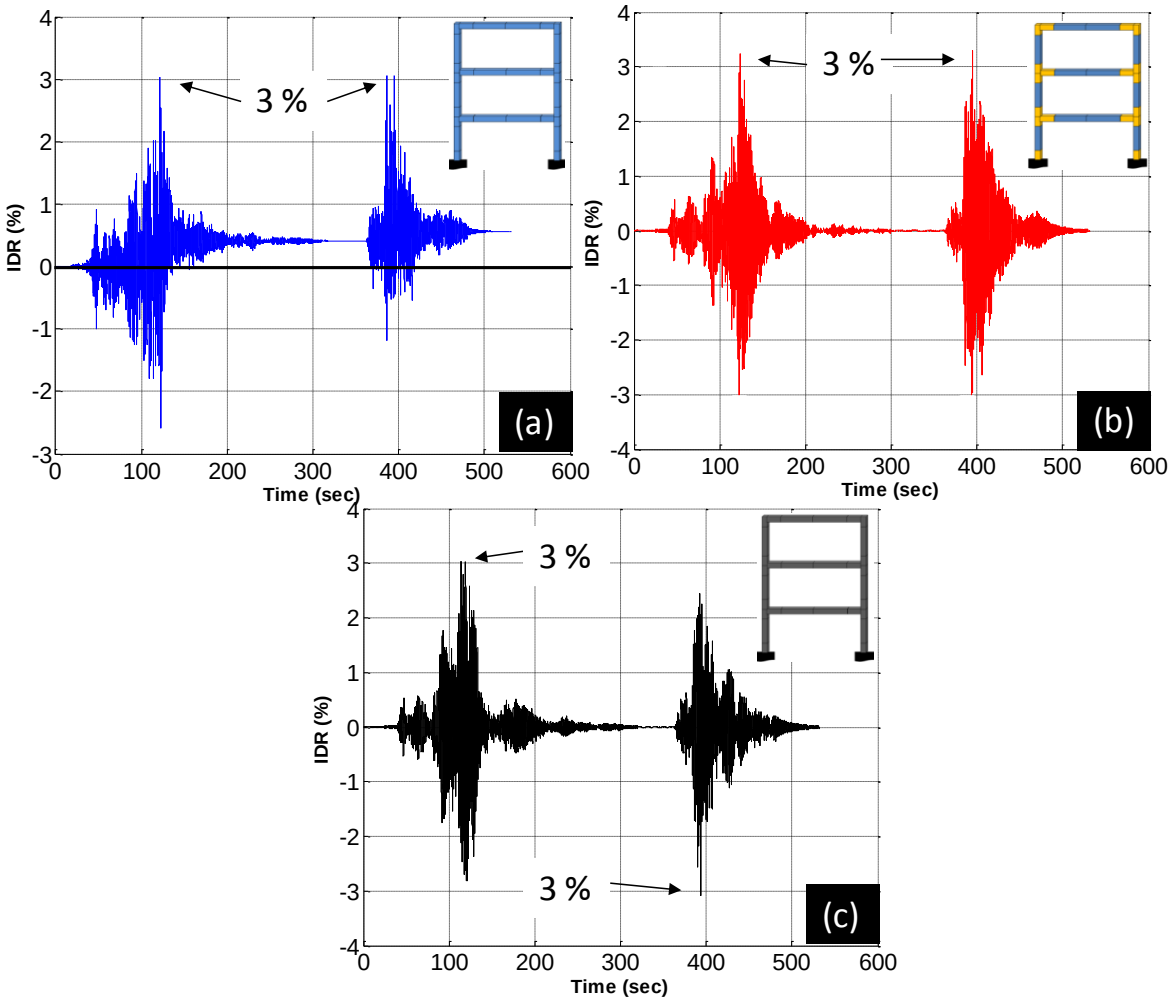

Figure 8-8: IDR time history response of MRF-3% subjected to Tohoku sequential records (a) Steel (b) SMA-FRP (c) GFRP

Figure 8-9 shows the IDR time history of all three frames designed based on 4% IDR, when subjected to Tohoku earthquake sequential records.

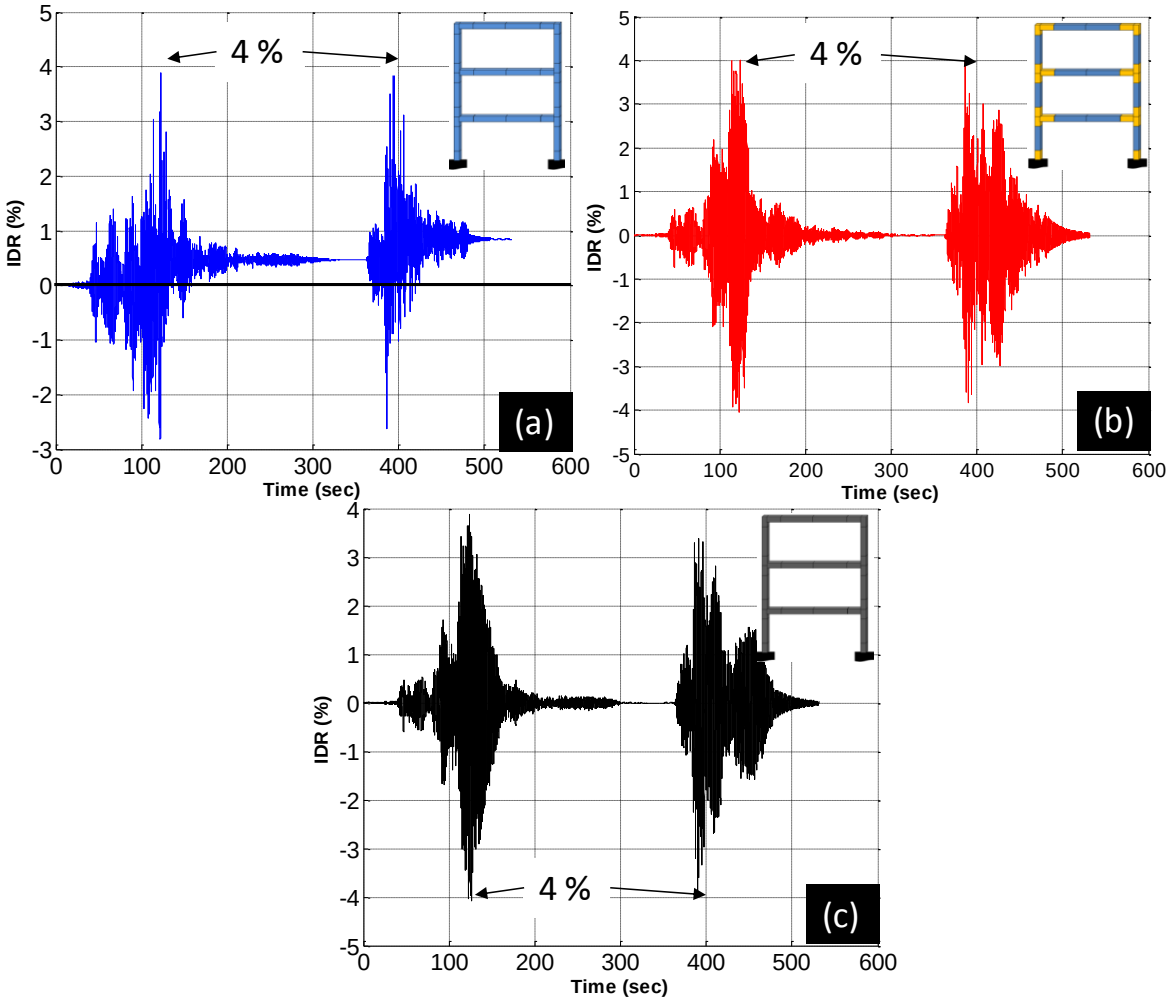

Figure 8-9**:** IDR time history response of MRF-4% subjected to Tohoku sequence event (a) Steel (b) SMA-FRP (c) GFRP

Main shock from Tohoku earthquake was required to be scaled to a PGA of 2.27g, 1.55g and 1.4g to cause 4% IDR for steel, SMA-FRP and GFRP reinforced frames, respectively. The aftershock from Tohoku earthquake had to be scaled to a PGA of 1.29g, 1.61g and 1.19g to reach the target performance limit state for steel, SMA-FRP and GFRP reinforced MRF-4%, respectively. In this case also, steel MRF-4% accumulated 0.47% and 0.84% residual IDR from main and aftershock sequence, respectively. Figure 8-10 shows the IDR time history of all three

frames designed based on 3% IDR, when subjected to Chalfant Valley earthquake sequential records.

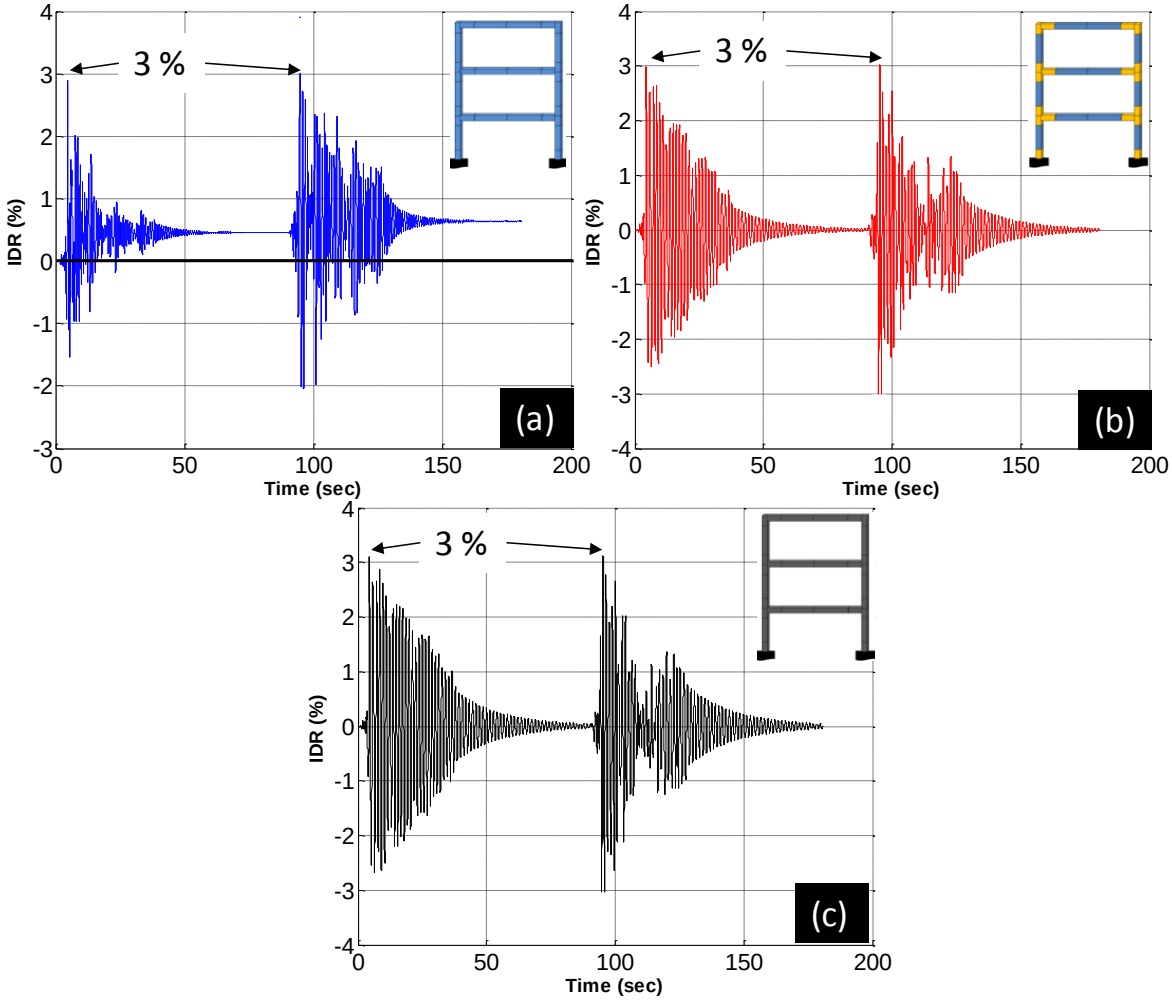

Figure 8-10**:** IDR time history response of MRF-4% subjected to Chalfant Valley sequence event (a) Steel (b) SMA-FRP (c) GFRP

Main shock from Chalfant Valley earthquake was required to be scaled to a PGA of 1.39g, 1.16g and 1.21g to cause 3% IDR for steel, SMA-FRP and GFRP reinforced frames, respectively. The aftershock from Chalfant Valley earthquake had to be scaled to a PGA of 1.03g, 1.41g and 1.29g to reach the target performance limit state for steel, SMA-FRP and GFRP

reinforced MRF-3%, respectively. Steel reinforced MRF-3% accumulated 0.52% and 0.74% residual IDR from main and aftershock sequence, respectively. This net residual IDR increase by 42% is due to sequential earthquake influence. Figure 8-11 shows the IDR time history of all three frames designed based on 4% IDR, when subjected to Chalfant Valley earthquake sequential records. Main shock from Chalfant Valley earthquake was required to be scaled to a PGA of 1.43g, 1.3g and 1.12g to cause 4% IDR for steel, SMA-FRP and GFRP reinforced frames, respectively. The aftershock from Chalfant Valley earthquake had to be scaled to a PGA of 0.96g, 1.54g and 1.16g to reach the target performance limit state for steel, SMA-FRP and GFRP reinforced MRF-4%, respectively. Steel reinforced MRF-4% accumulated 0.78% and 1.21% residual IDR from main and aftershock sequence, respectively. This net residual IDR increase by 55% is due to sequential earthquake influence.

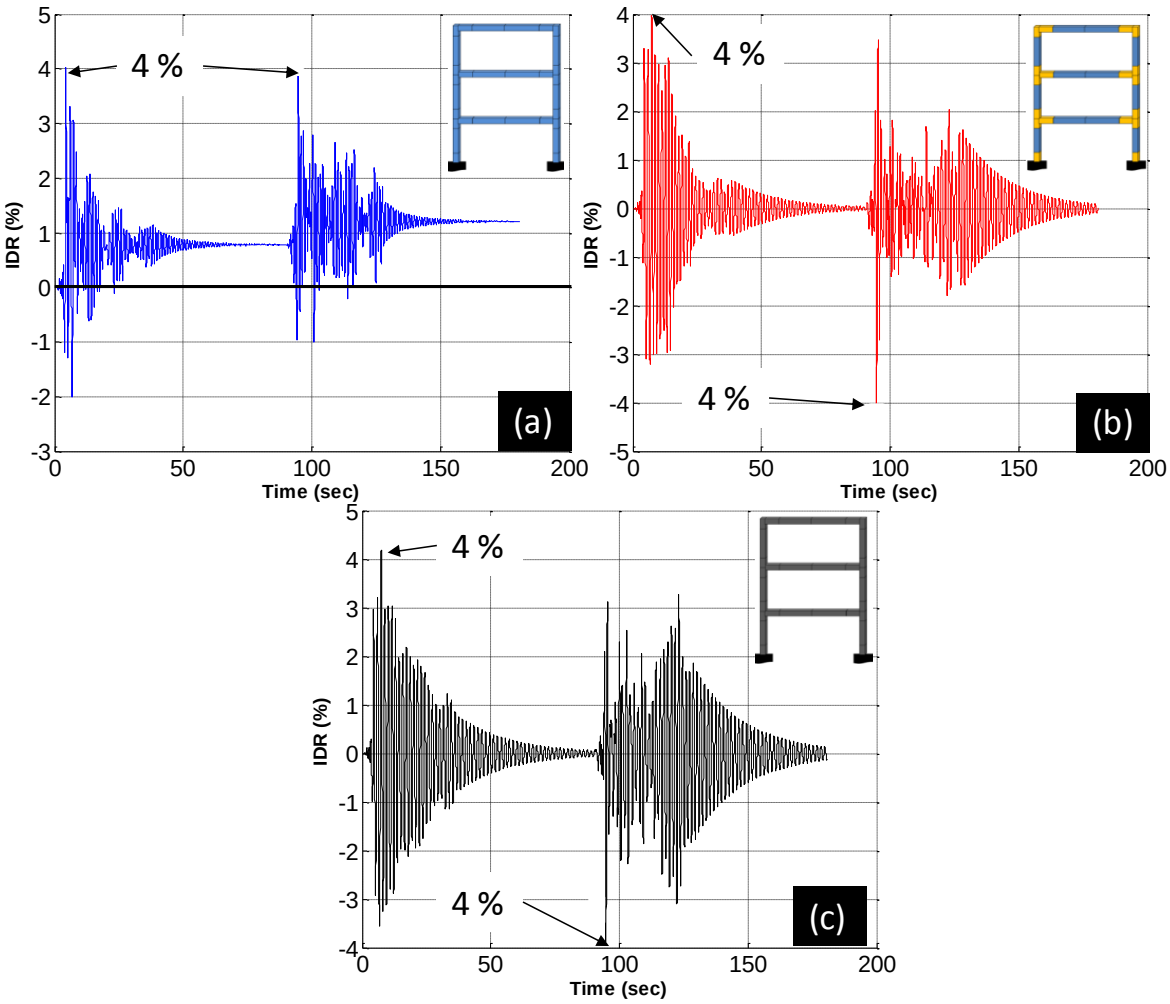

Figure 8-11**:** IDR time history response of MRF-4% subjected to Chalfant Valley sequence event (a) Steel (b) SMA-FRP (c) GFRP

Figure 8-12 shows response of MRF-3% for all three reinforcement types, to the 2-event sequence from Mammoth Lake earthquake. Main shock from Mammoth lake earthquake was required to be scaled to a PGA of 2.74g, 2.21g and 2.21g to cause 3% IDR for steel, SMA-FRP and GFRP reinforced frames, respectively. The aftershock from Mammoth Lake earthquake had to be scaled to a PGA of 1.07g, 1.09g and 1.01g to reach the target performance limit state for steel, SMA-FRP and GFRP reinforced MRF-3%, respectively. Steel reinforced MRF-3%

accumulated 0.13% and 0.16% residual IDR from main and aftershock sequence, respectively. This net residual IDR increase by 23% is due to sequential earthquake influence.

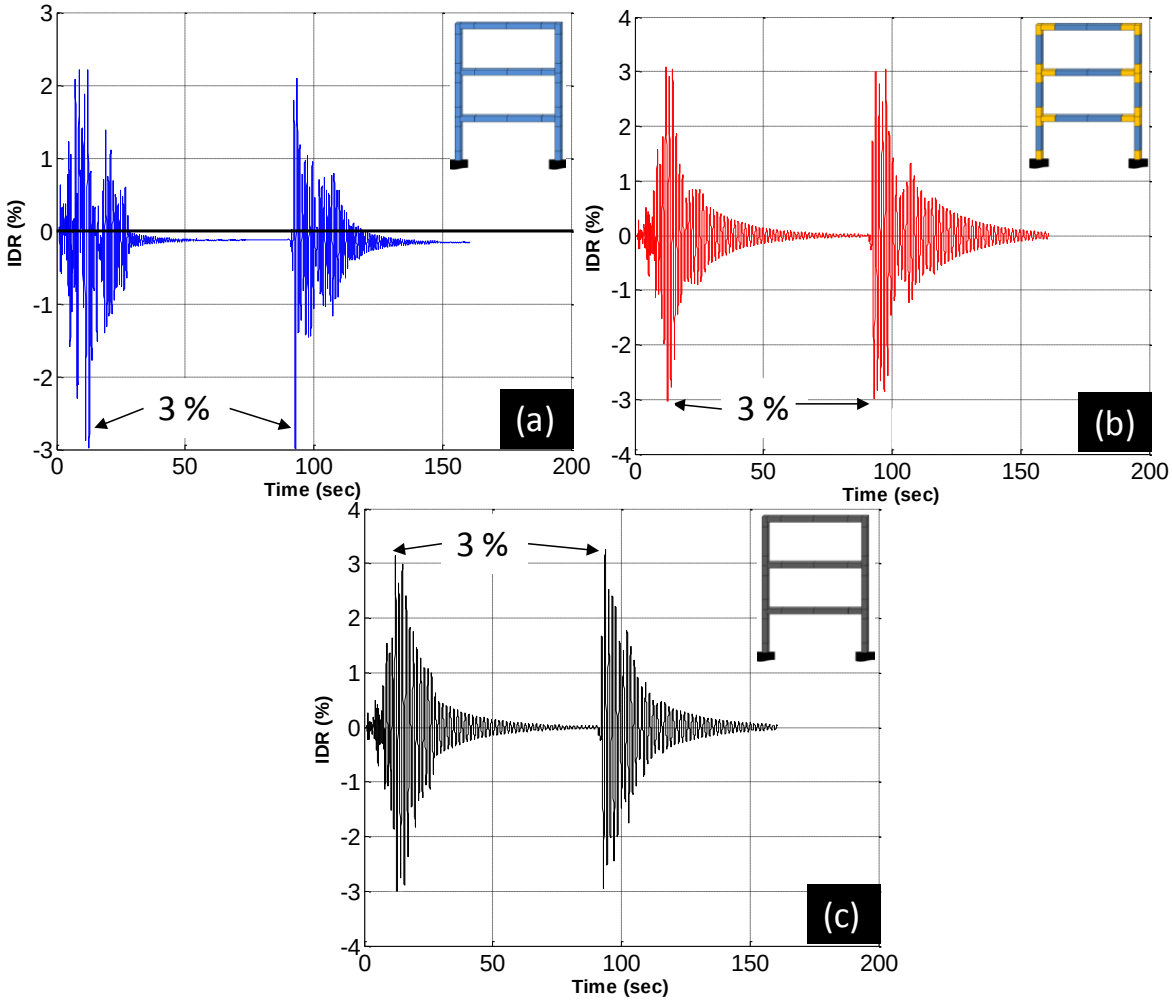

Figure 8-12**:** IDR time history response of MRF-3% subjected to Mammoth Lake sequence event (a) Steel (b) SMA-FRP (c) GFRP

Figure 8-13 shows response of MRF-4% for all three reinforcement types, to the 2-event sequence from Mammoth Lake earthquake. Main shock from Mammoth lake earthquake was required to be scaled to a PGA of 2.78g, 1.85g and 1.81g to cause 4% IDR for steel, SMA-FRP and GFRP reinforced frames, respectively. The aftershock from Mammoth Lake earthquake had

to be scaled to a PGA of 1.09g, 1.05g and 0.89g to reach the target performance limit state for steel, SMA-FRP and GFRP reinforced MRF-4%, respectively. Steel reinforced MRF-4% accumulated 0.54% and 0.74% residual IDR from main and aftershock sequence, respectively. This net residual IDR increase by 37% is due to sequential earthquake influence.

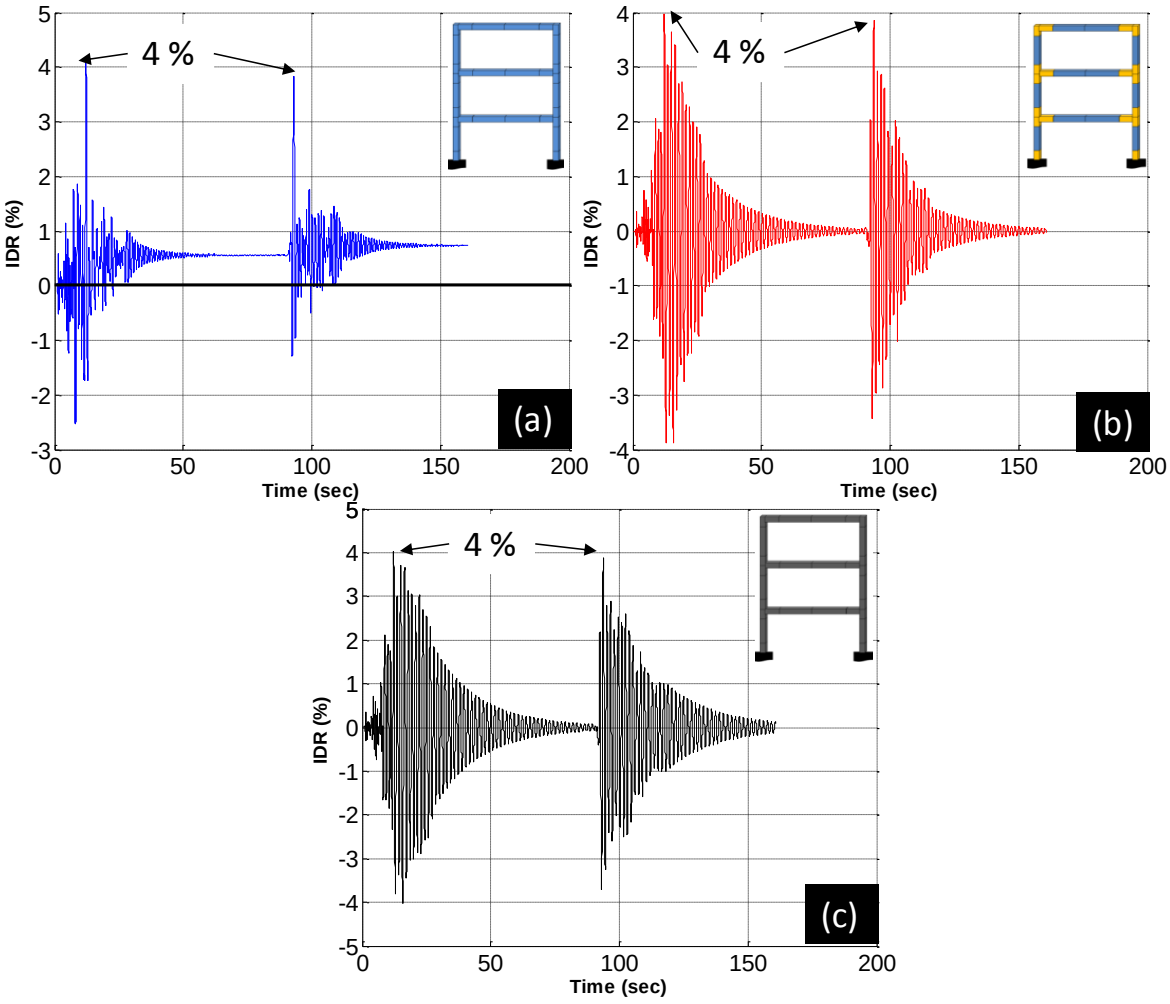

Figure 8-13**:** IDR time history response of MRF-4% subjected to Mammoth Lake sequence event (a) Steel (b) SMA-FRP (c) GFRP

Figure 8-14 shows response of MRF-3% for all three reinforcement types, to the 2-event sequence from Imperial Valley earthquake.

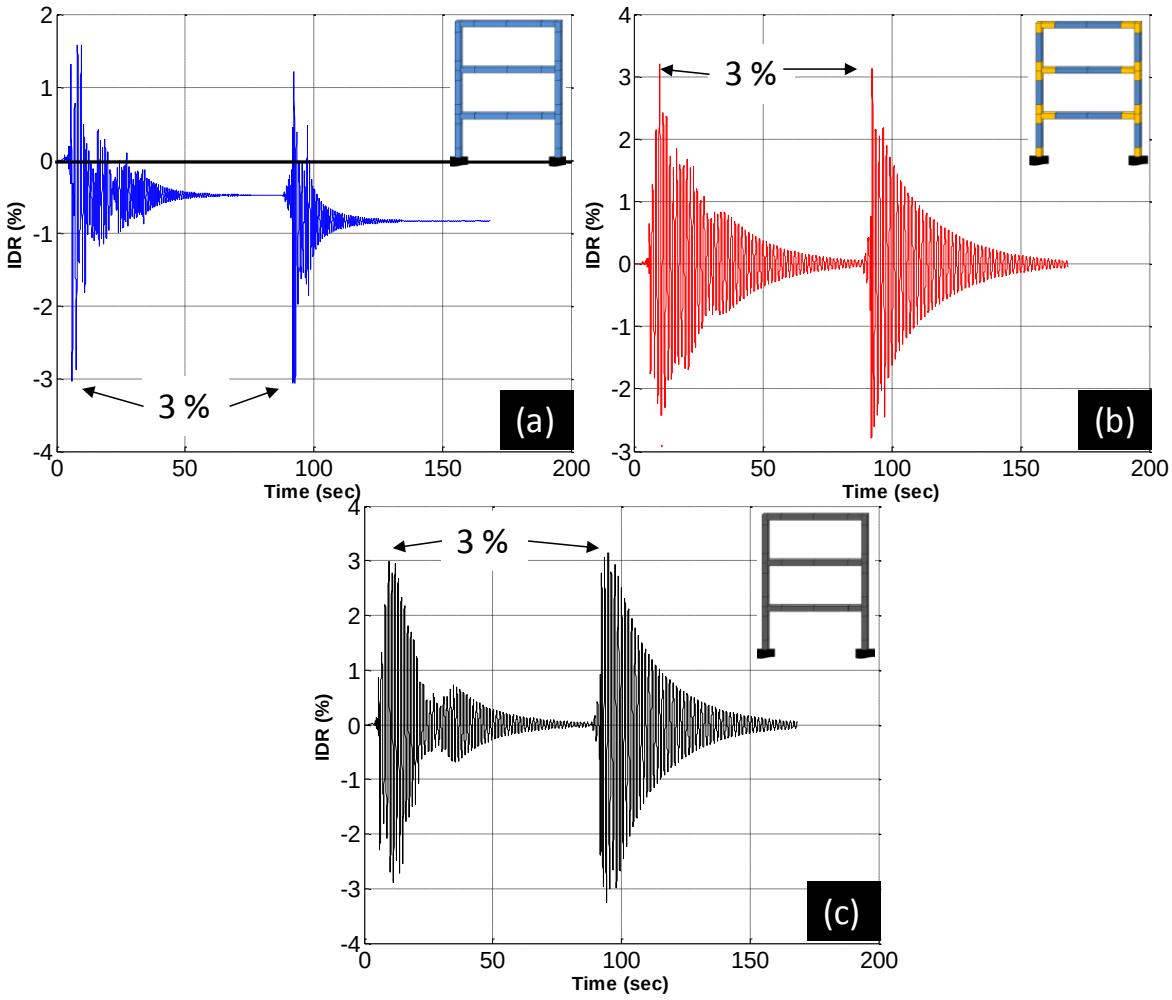

Figure 8-14**:** IDR time history response of MRF-3% subjected to Imperial Valley sequence event (a) Steel (b) SMA-FRP (c) GFRP

Main shock from Imperial Valley earthquake was required to be scaled to a PGA of 1.56g, 1.32g and 1.26g to cause 3% IDR for steel, SMA-FRP and GFRP reinforced frames, respectively. The aftershock from Imperial Valley earthquake had to be scaled to a PGA of 1.32g, 1.52g and 1.32g to reach the target performance limit state for steel, SMA-FRP and GFRP reinforced MRF-3%, respectively. Steel reinforced MRF-3% accumulated 0.49% and 0.84% residual IDR from main and aftershock sequence, respectively. This net residual IDR increase by

71% is due to sequential earthquake influence. Figure 8-15 shows response of MRF-4% for all three reinforcement types, to the 2-event sequence from Imperial Valley earthquake.

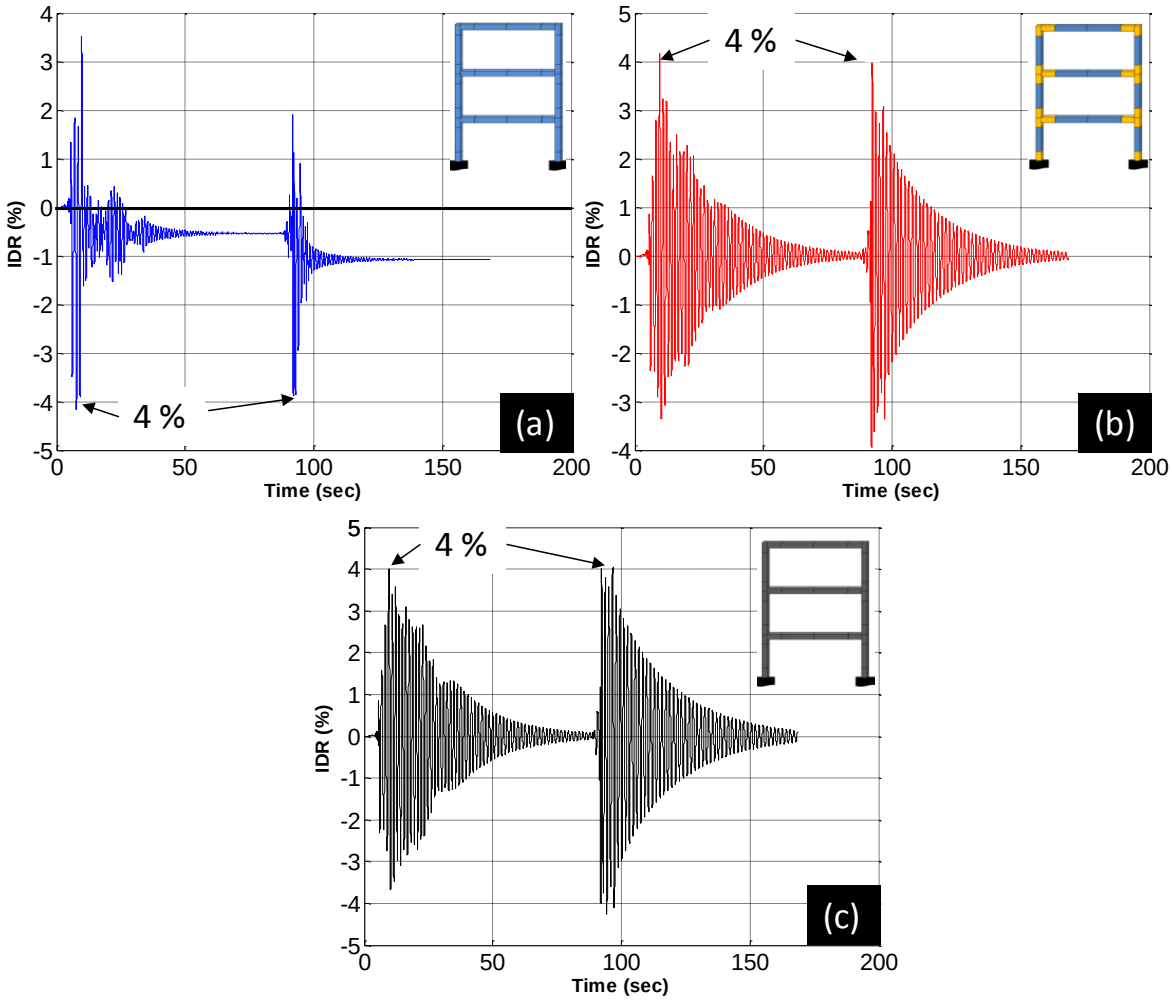

Figure 8-15**:** IDR time history response of MRF-4% subjected to Imperial Valley sequence event (a) Steel (b) SMA-FRP (c) GFRP

Main shock from Imperial Valley earthquake was required to be scaled to a PGA of 1.62g, 1.26g and 1.19g to cause 4% IDR for steel, SMA-FRP and GFRP reinforced frames, respectively. The aftershock from Imperial Valley earthquake had to be scaled to a PGA of

2.12g, 2.44g and 2.28g to reach the target performance limit state for steel, SMA-FRP and GFRP reinforced MRF-4%, respectively. Steel reinforced MRF-4% accumulated 0.56% and 1.08% residual IDR from main and aftershock sequence, respectively. This net residual IDR increase by 93% is due to sequential earthquake influence. Figure 8-16 shows response of MRF-3% for all three reinforcement types, to the 2-event sequence from Coalinga earthquake. Main shock from Coalinga earthquake was required to be scaled to a PGA of 0.83g, 0.65g and 0.65g to cause 3% IDR for steel, SMA-FRP and GFRP reinforced frames, respectively. The aftershock from Coalinga earthquake had to be scaled to a PGA of 2.01g, 1.85g and 1.69g to reach the target performance limit state for steel, SMA-FRP and GFRP reinforced MRF-3%, respectively. Steel reinforced MRF-3% accumulated 0.5% and 0.82% residual IDR from main and aftershock sequence, respectively. This net residual IDR increase by 64% is due to sequential earthquake influence.

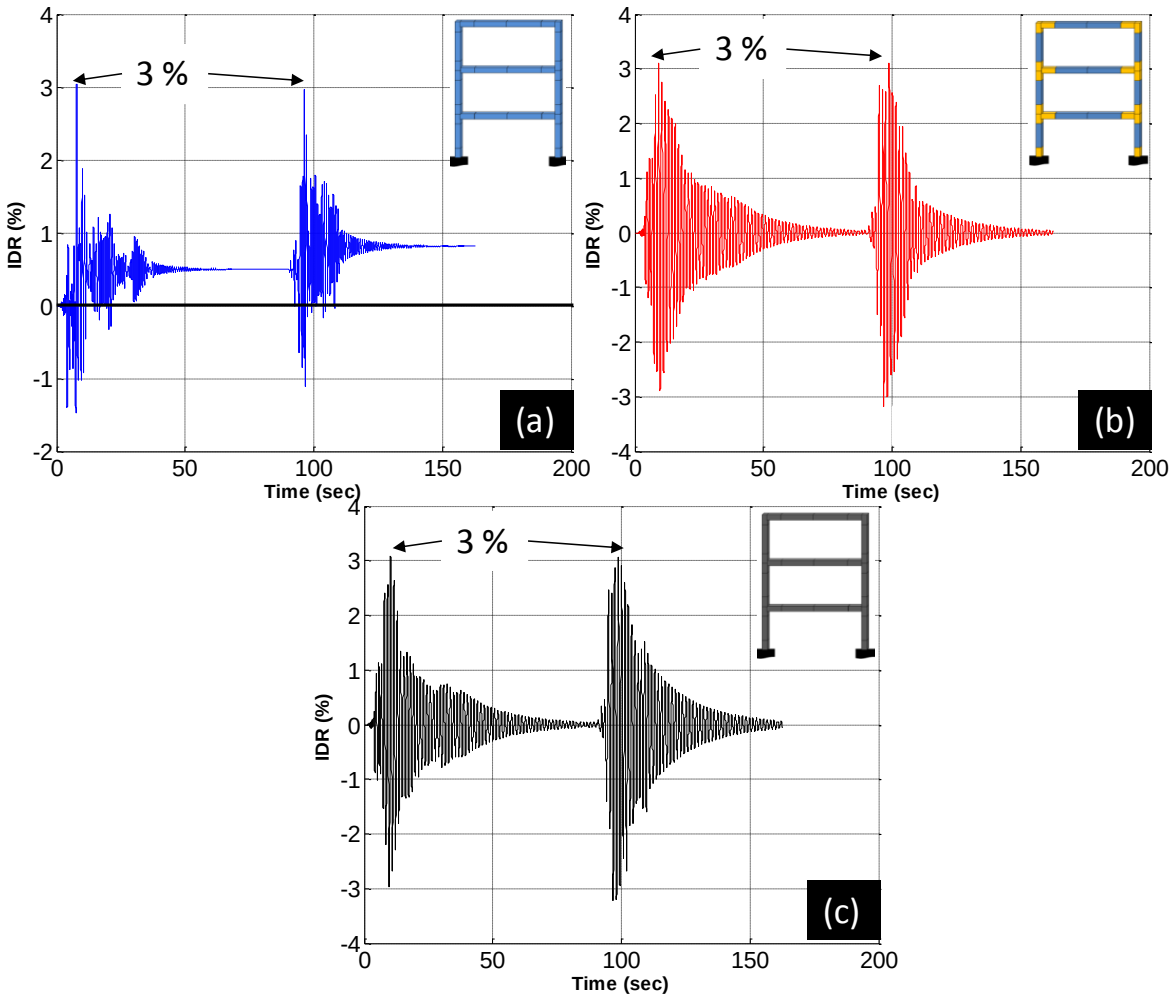

Figure 8-16**:** IDR time history response of MRF-3% subjected to Coalinga sequence event (a) Steel (b) SMA-FRP (c) GFRP

Figure 8-17 shows response of MRF-4% for all three reinforcement types, to the 2-event sequence from Coalinga earthquake. Main shock from Coalinga earthquake was required to be scaled to a PGA of 0.96g, 0.92g and 0.86g to cause 4% IDR for steel, SMA-FRP and GFRP reinforced frames, respectively. The aftershock from Coalinga earthquake had to be scaled to a PGA of 2.21g, 2.57g and 2.17g to reach the target performance limit state for steel, SMA-FRP and GFRP reinforced MRF-4%, respectively. Steel reinforced MRF-4% accumulated 0.86% and

1.29% residual IDR from main and aftershock sequence, respectively. This net residual IDR increase by 50% is due to sequential earthquake influence.

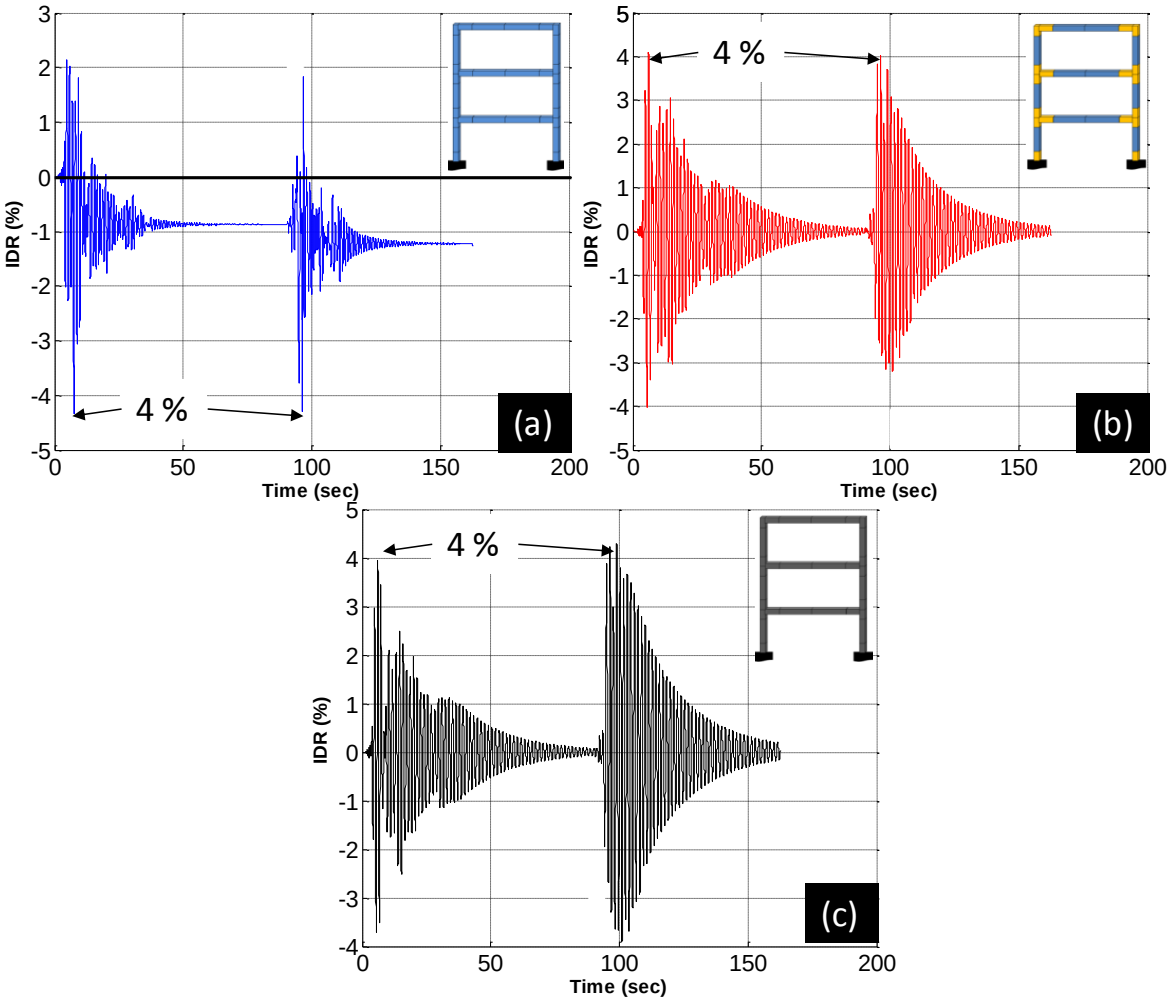

Figure 8-17**:** IDR time history response of MRF-4% subjected to Coalinga sequence event (a) Steel (b) SMA-FRP (c) GFRP

Figure 8-18 shows response of MRF-3% for all three reinforcement types, to the 2-event sequence from Christchurch earthquake.

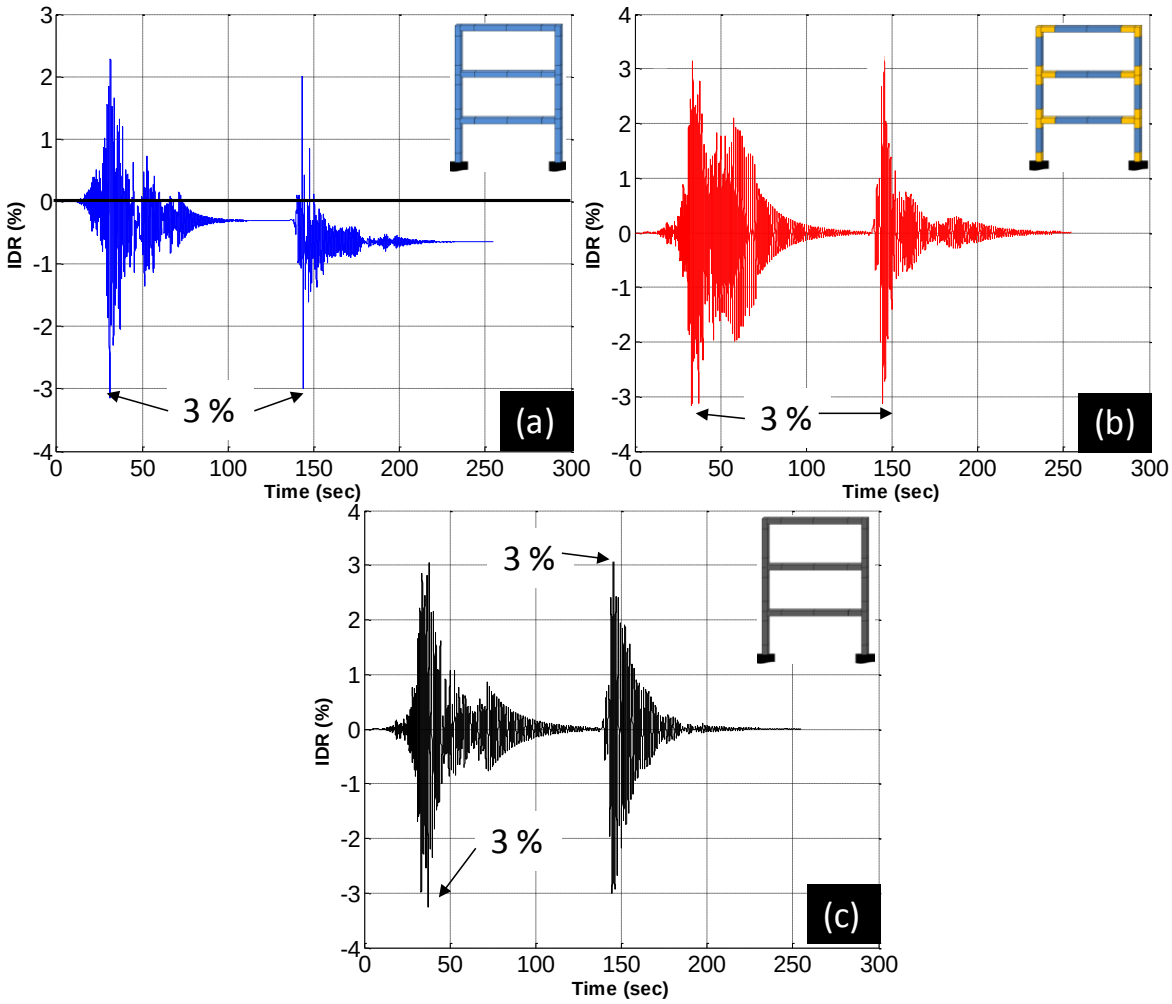

Figure 8-18**:** IDR time history response of MRF-3% subjected to Christchurch sequence event (a) Steel (b) SMA-FRP (c) GFRP

Main shock from Christchurch earthquake was required to be scaled to a PGA of 0.61g, 0.52g and 0.48g to cause 3% IDR for steel, SMA-FRP and GFRP reinforced frames, respectively. The aftershock from Christchurch earthquake had to be scaled to a PGA of 0.53g, 0.5g and 0.45g to reach the target performance limit state for steel, SMA-FRP and GFRP reinforced MRF-3%, respectively. Steel reinforced MRF-3% accumulated 0.3% and 0.65% residual IDR from main and aftershock sequence, respectively. This net residual IDR increase by

117% is due to sequential earthquake influence. Figure 8-19 shows response of MRF-4% for all three reinforcement types, to the 2-event sequence from Christchurch earthquake.

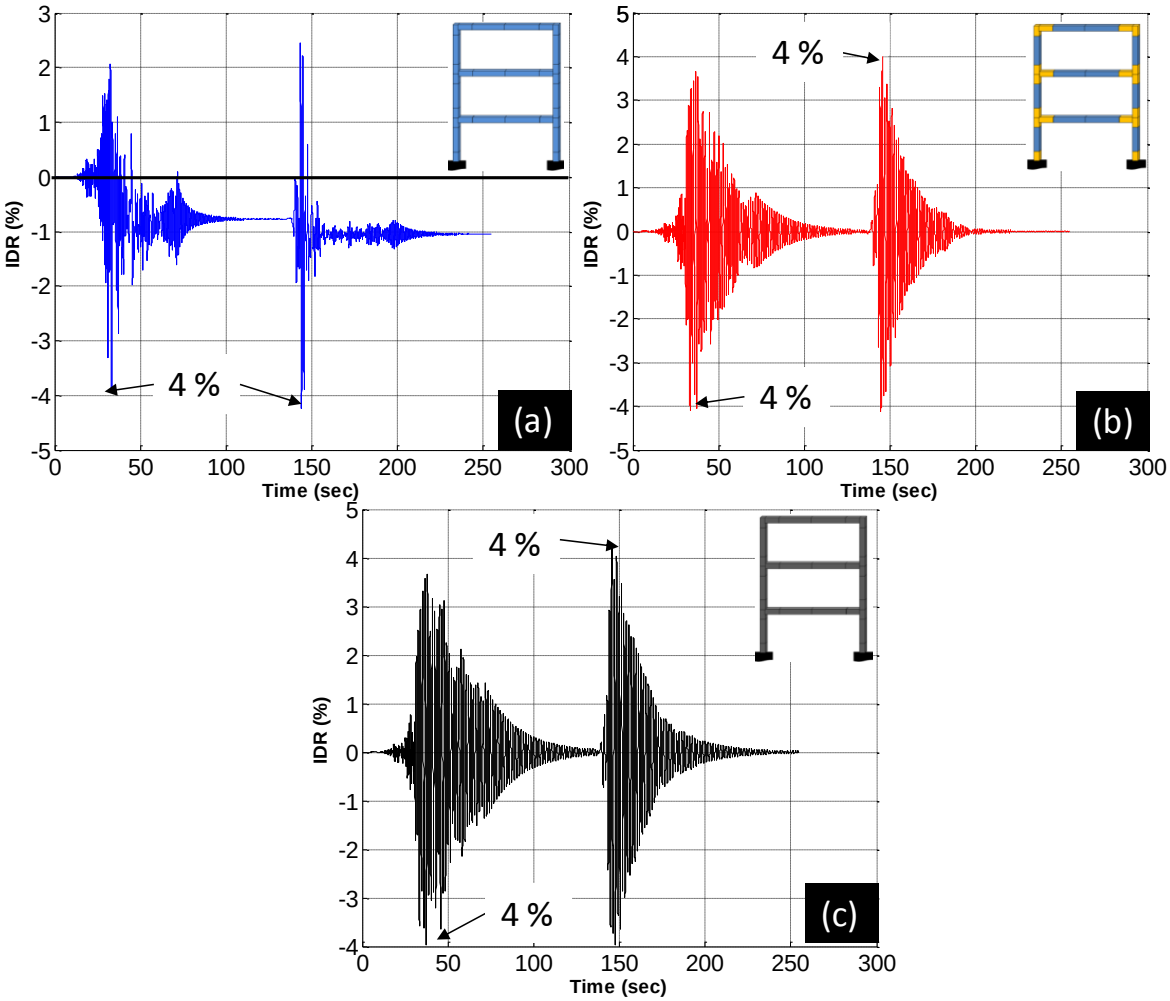

Figure 8-19**:** IDR time history response of MRF-4% subjected to Christchurch sequence event (a) Steel (b) SMA-FRP (c) GFRP

Main shock from Christchurch earthquake was required to be scaled to a PGA of 0.64g, 0.48g and 0.42g to cause 4% IDR for steel, SMA-FRP and GFRP reinforced frames, respectively. The aftershock from Christchurch earthquake had to be scaled to a PGA of 0.58g,

0.53g and 0.48g to reach the target performance limit state for steel, SMA-FRP and GFRP reinforced MRF-4%, respectively. Steel reinforced MRF-4% accumulated 0.61% and 1.24% residual IDR from main and aftershock sequence, respectively. This net residual IDR increase by 103% is due to sequential earthquake influence. Figure 8-20 shows response of MRF-3% for all three reinforcement types, to the 4-event sequence from Christchurch earthquake. Results from analysis show accumulation of permanent drift in steel frame when subjected to multiple sequential records each scaled to cause 3% IDR. After the fourth ground motion record in Christchurch sequence (After-3), the residual IDR accumulated is 0.81%. This is an increase of 224% in permanent deformation as compared to main shock response. It has been seen that the accumulation of residual drifts after each record makes the steel frame vulnerable and prone to collapse even with smaller intensity aftershock. This is primarily due to the plasticity of steel and accumulation of permanent strains due to yielding resulting in damage to steel reinforcement at material level.

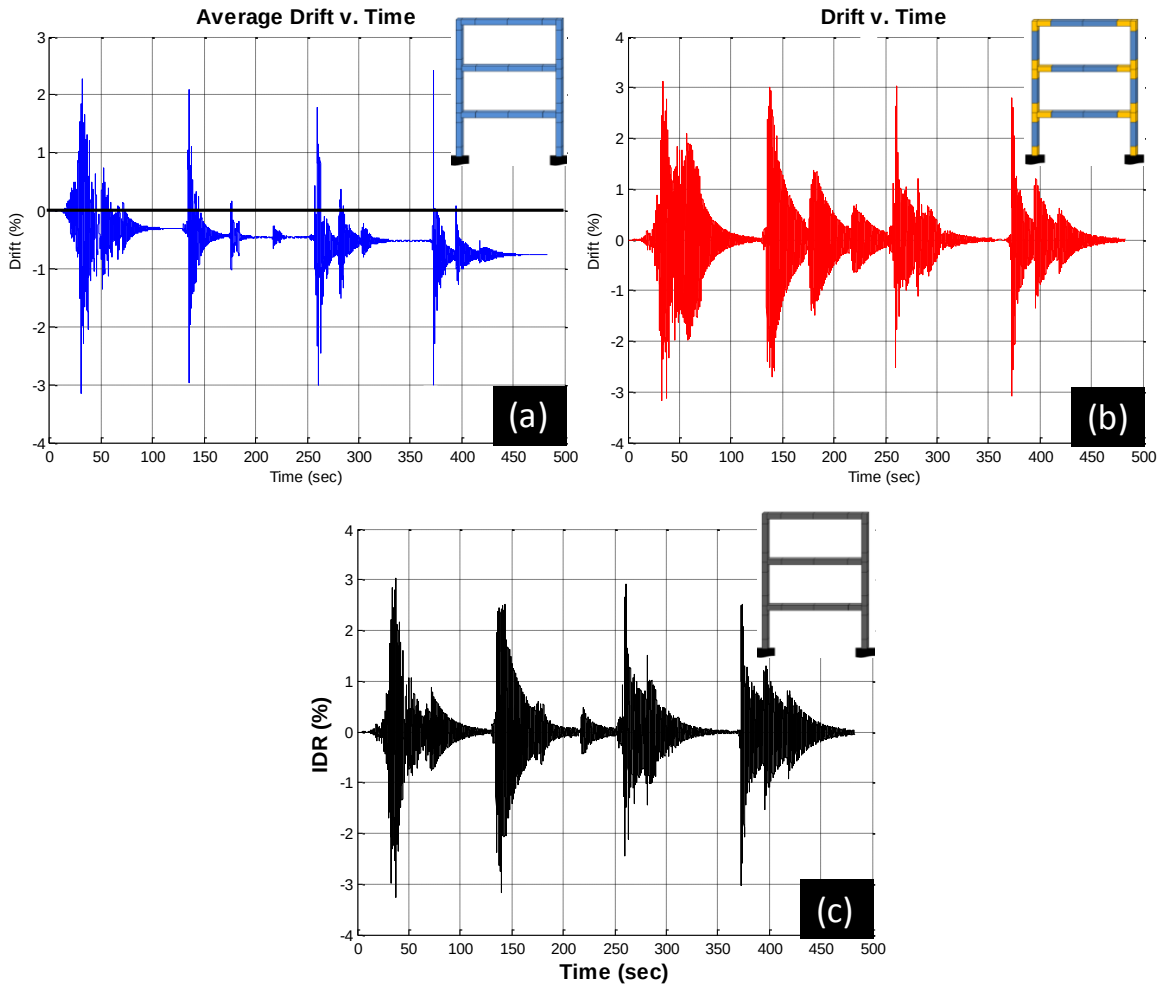

Figure 8-20: IDR time history response of MRF-3% subjected to CCC 4 sequence event (a) Steel (b) SMA-FRP (c) GFRP

Figure 8-21 shows response of MRF-4% for all three reinforcement types, to the 4-event sequence from Christchurch earthquake. Results from analysis show accumulation of permanent drift in steel frame when subjected to multiple sequential records each scaled to cause 4% IDR. After the fourth ground motion record in Christchurch sequence (After-3), the residual IDR accumulated is 1.25%. This is an increase of 229% in permanent deformation as compared to main shock response.

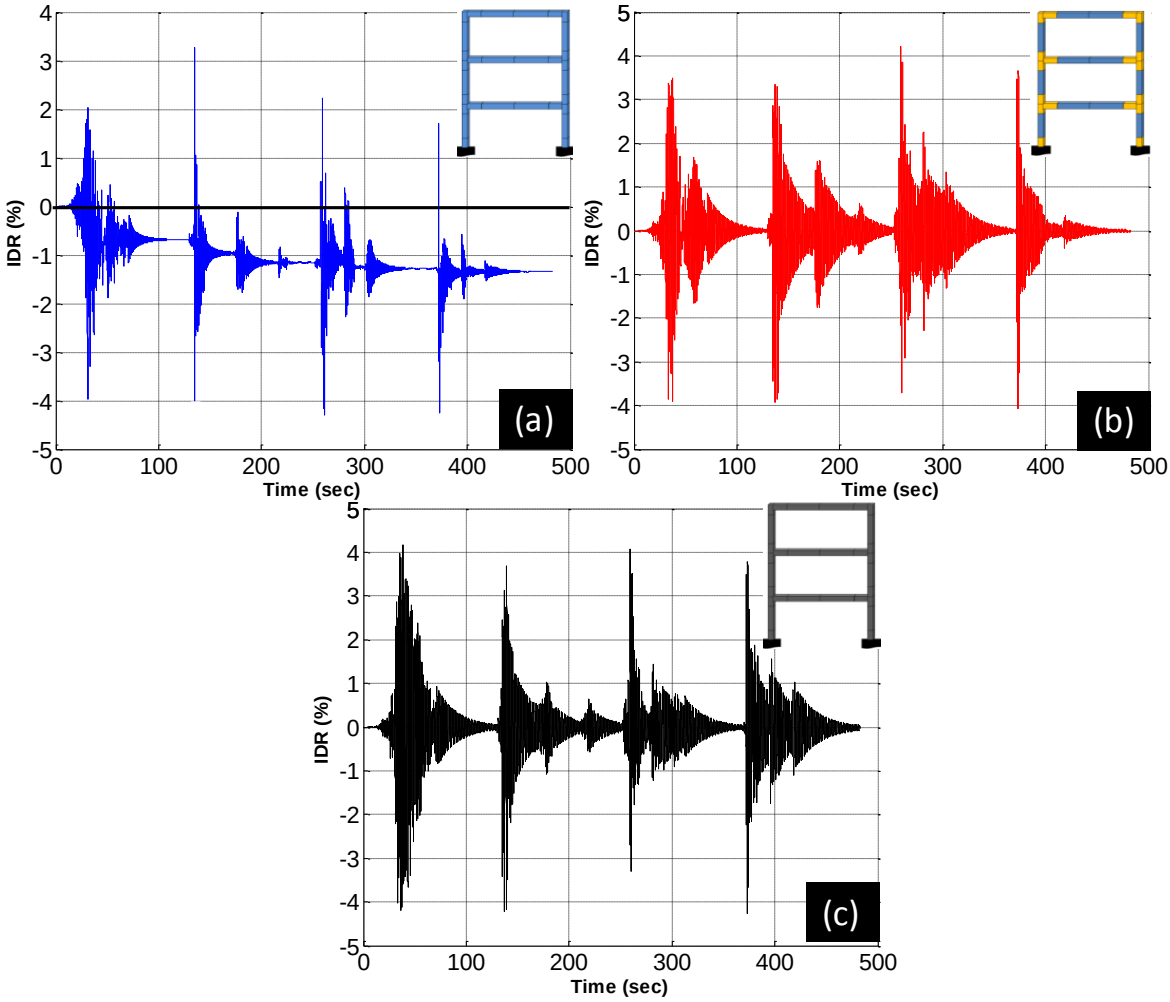

Figure 8-21: IDR time history response of MRF-4% subjected to CCC 4 sequence event (a) Steel (b) SMA-FRP (c) GFRP

8.6.2 Comparison of accumulation of residual IDR

Because of yielding and permanent damage, steel MRF experienced residual IDR for both main and aftershocks once scaled to target drifts. For steel reinforced MRF-4% once subjected to Tohoku earthquake records, residual IDR from main shock was 0.47% and by end of aftershock it was 0.84%, resulting in an increase of 79%. For MRF-3%, the residual IDR from

main shock was 0.41% and by end of aftershock it was 0.56%, resulting in an increase of 37%. Comparing accumulation of residual IDR from steel reinforced MRF-3% (37% increase in residual IDR), the MRF-4% experienced an increase of 108%, which is substantial considering that the increase in design limit state was only by 1% drift, going from 3% to 4% IDR. This shows that more the drift values experienced by steel frame, more residual IDR is likely to be accumulated, thus leading to more damage. Analysis results from other remaining sequential ground motion records showed similar behavior. Summary of accumulation of residual IDR by steel reinforced for both MRF-3% and MRF-4 % IDR, subjected to all the sequential earthquake records has been shown in table 8-4. Figure 8-22 and 8-23 shows graphical comparison of accumulated residual IDR from main and sequential records for both MRF-3% and MRF-4%, respectively.

Table 8-4**:** Residual IDR in steel reinforced MRF experiencing 3% and 4 % IDR

Residual IDR (%) in Steel MRF						
Earthquake	**3% IDR**			**4% IDR**		
	Main	**After**	**% increase**	**Main**	**After**	**% increase**
Chalfant	0.52	0.74	42	0.78	1.21	55
Tohoku	0.41	0.56	37	0.47	0.84	79
Mammoth	0.13	0.16	23	0.54	0.74	37
Imperial	0.49	0.84	71	0.56	1.08	93
CCC 4-event	0.25	0.81	224	0.38	1.25	229
Coalinga	0.5	0.82	64	0.86	1.29	50
Christchurch	0.3	0.65	117	0.61	1.24	103

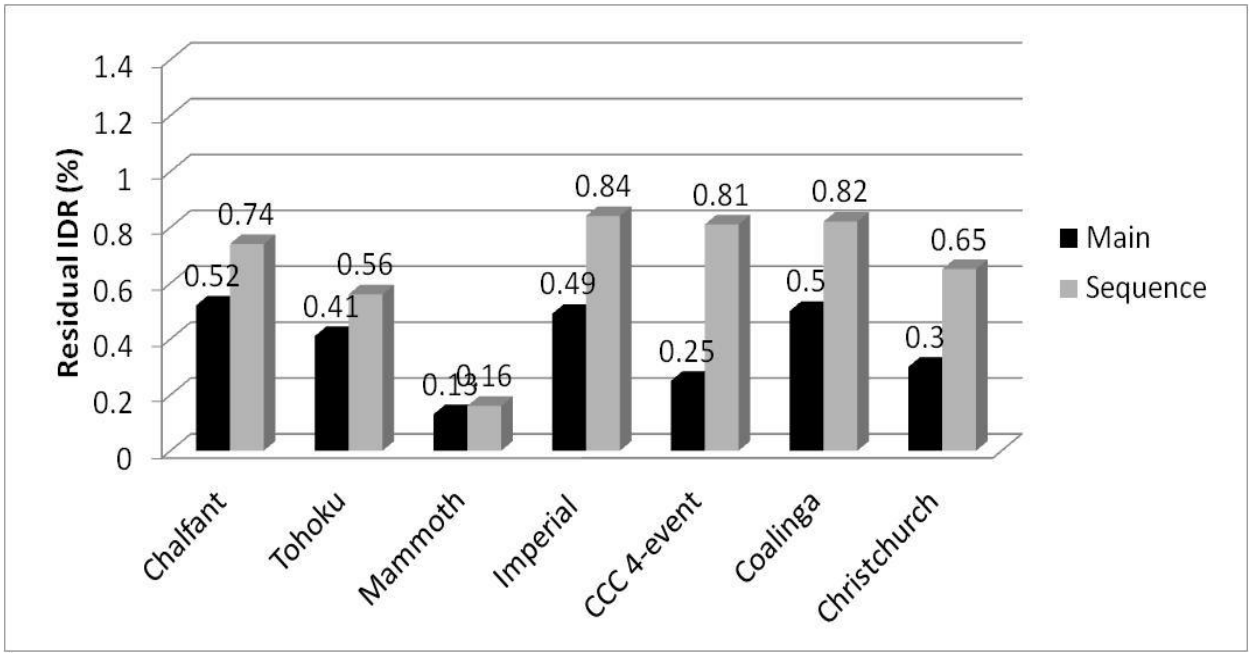

Figure 8-22: Accumulation of residual IDR for steel reinforced MRF-3%

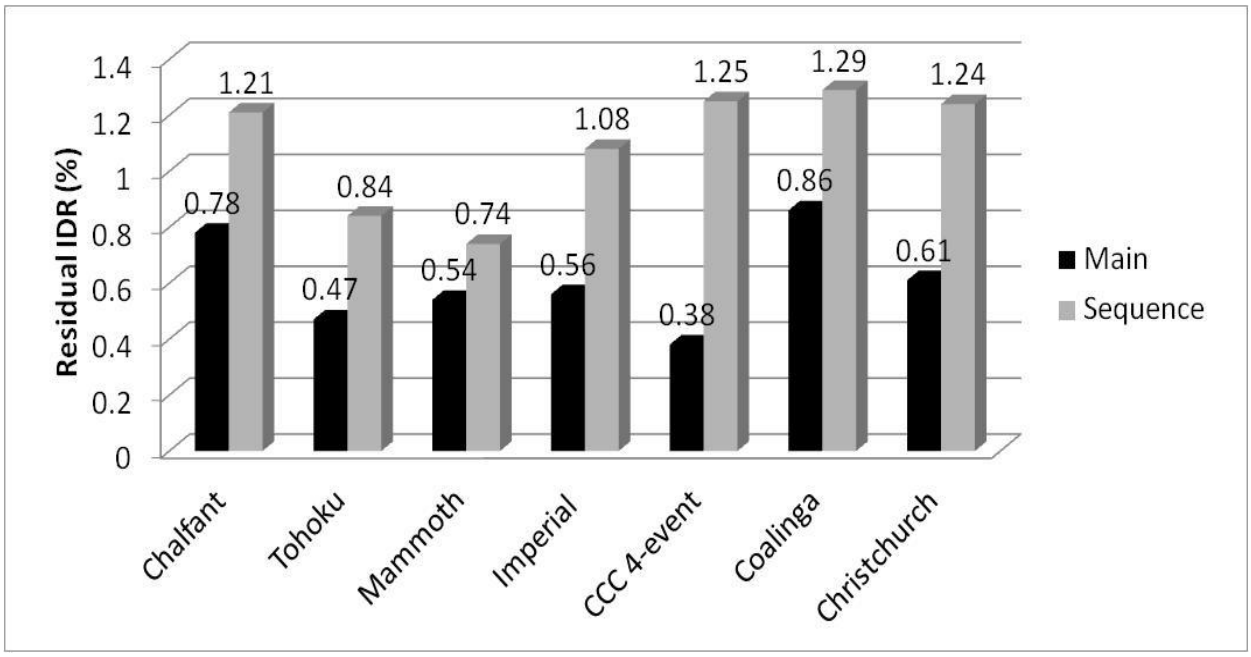

Figure 8-23: Accumulation of residual IDR for steel reinforced MRF-4%

8.6.3 Reduction factor and duration ratio

The accumulation of residual permanent drifts in steel reinforced frame due to multiple seismic sequence, results in decreased demand, needed in order to reach 3% and 4% IDR. This multiplicity earthquake effect is quantified in terms of reduction factor (%) once compared to other two type of reinforcements. This reduction is a function of $(PGA)_{Steel}$ / $(PGA)_{Rft}$ which causes 3% and 4% IDR and corresponds to reduction in PGA required, going from main to aftershock for the same earthquake. Equation 8-2 represents the definition of reduction factor used in this study:

$$\text{Reduction Factor} = 1 - \frac{[(PGA)_{Steel} / (PGA)_{Rft}]_{Sequence}}{[(PGA)_{Steel} / (PGA)_{Rft}]_{Main}} \qquad (8\text{-}2)$$

In equation 8-2 , $(PGA)_{Rft}$ can either be replaced by SMA-FRP or GFRP reinforcement to get corresponding reduction factor in relation to steel. This reduction factor allows taking into account the phenomena of residual IDR accumulation and thus requiring lesser demand by steel reinforced frame to reach target performance levels. Reduction factor computed for all the seven considered cases causing 3% IDR in MRF-3% have been tabulated in table 8-5. For 2-event sequence the maximum reduction factor was exhibited by MRF-3% once subjected to Chalfant valley earthquake sequence. The reduction for steel frame comes out to be 39%, 30% when subjected to Chalfant valley earthquake sequences for SMA-FRP and GFRP reinforced MRF, respectively. Similarly, results from 4-event sequence from Christchurch earthquake shows reduction factors to be 43% and 41% once PGA required by steel MRF to reach performance

levels is compared to SMA-FRP and GFRP reinforcement, respectively. Figure 8-24 shows the bar chart for reduction factors once MRF-3% is subjected to the various sequential inputs.

Table 8-5: PGA causing 3% IDR in steel, SMA-FRP and GFRP reinforced MRF

Earthquake	Sequence	PGA (g) causing 3% IDR in MRF-3%			PGA Ratio	
		Steel	SMA-FRP	GFRP	PGA(Steel)/ PGA(SMA-FRP)	PGA(Steel)/ PGA(GFRP)
1986, Chalfant Valley	Main	1.39	1.16	1.21	1.2	1.15
	After	1.03	1.41	1.29	0.73	0.8
			Reduction factor		**39**	**30**
2011 Tohoku	Main	1.51	1.48	1.33	1.02	1.14
	After	0.93	1.16	1.02	0.8	0.91
			Reduction factor		**22**	**20**
1980 Mammoth Lake	Main	2.74	2.21	2.21	1.24	1.24
	After	1.07	1.09	1.01	0.98	1.06
			Reduction factor		**21**	**15**
1979 Imperial Valley	Main	1.56	1.32	1.26	1.18	1.24
	After	1.32	1.52	1.32	0.87	1
			Reduction factor		**26**	**19**
1983, Coalinga	Main	0.83	0.65	0.65	1.28	1.28
	After	2.01	1.85	1.69	1.09	1.19
			Reduction factor		**15**	**7**
2010 Christchurch	Main	0.61	0.52	0.48	1.17	1.27
	After	0.53	0.5	0.45	1.06	1.18
			Reduction factor		**9**	**7**
2010 Christchurch CCC 4-event	Main	0.61	0.52	0.48	1.17	1.27
	After-3	1.3	1.95	1.73	0.67	0.75
			Reduction factor		**43**	**41**

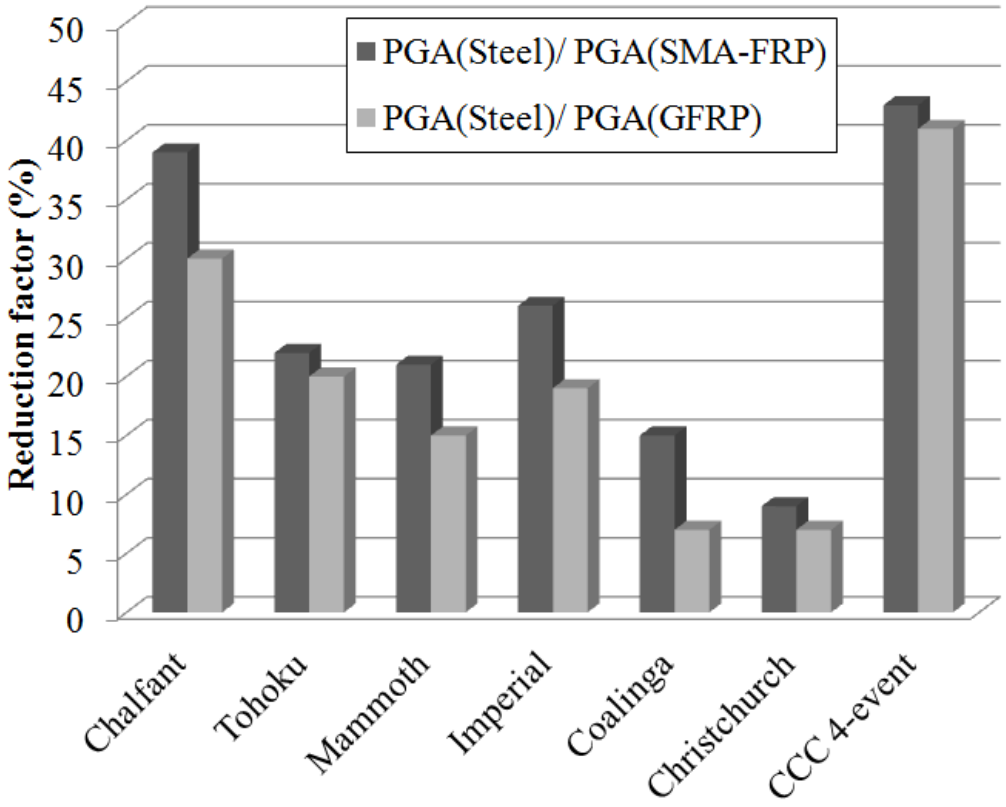

Figure 8-24**:** Reduction factors for MRF-3%

Reduction factors computed for all the seven considered cases causing 4% IDR in MRF-4% have been tabulated in table 8-6. For 2-event sequence the maximum reduction factor was exhibited by MRF-4% once subjected to Tohoku earthquake sequence. The reduction factors in this comes out to be 45%, 33% when subjected to Tohoku sequences for SMA-FRP and GFRP reinforced MRF, respectively. For 4-event sequence from Christchurch earthquake reduction factors to be 49% and 46% for SMA-FRP and GFRP reinforced MRF, respectively. Thus 4% IDR provides more severe case for reduction factor for steel MRF once compared to SMA-FRP and GFRP reinforcement. Although results show that MRF-4% reinforced with GFRP is exhibiting better behavior in comparison with steel, but it was noticed that the GFRP

reinforcement reached rupture strains in almost all the beams in all the sequential record cases. Thus, attainment of 4% IDR is at the cost of rupture of longitudinal reinforcement in the beam, leads to development of plastic hinge which would then trigger progressive collapse of the frame. Figure 8-25 shows the bar chart for reduction factors once MRF-3% is subjected to the various sequential inputs.

Table 8-6: PGA causing 4% IDR in steel, SMA-FRP and GFRP reinforced MRF

Earthquake	**Sequence**	**PGA (g) causing 4% IDR in MRF-4%**			**PGA Ratio**	
		Steel	**SMA-FRP**	**GFRP**	**PGA(Steel)/ PGA(SMA-FRP)**	**PGA(Steel)/ PGA(GFRP)**
1986, Chalfant Valley	Main	1.43	1.3	1.12	1.1	1.28
	After	0.96	1.54	1.16	0.62	0.83
			Reduction factor		**44**	**35**
2011 Tohoku	Main	2.27	1.55	1.4	1.46	1.62
	After	1.29	1.61	1.19	0.8	1.08
			Reduction factor		**45**	**33**
1980 Mammoth Lake	Main	2.78	1.85	1.81	1.5	1.54
	After	1.09	1.05	0.89	1.04	1.22
			Reduction factor		**31**	**21**
1979 Imperial Valley	Main	1.62	1.26	1.19	1.29	1.36
	After	2.12	2.44	2.28	0.87	0.93
			Reduction factor		**33**	**32**
1983, Coalinga	Main	0.96	0.92	0.86	1.04	1.12
	After	2.21	2.57	2.17	0.86	1.02
			Reduction factor		**17**	**9**
2010 Christchurch	Main	0.64	0.48	0.42	1.33	1.52
	After	0.58	0.53	0.48	1.09	1.21
			Reduction factor		**18**	**20**
2010 Christchurch CCC 4-event	Main	0.64	0.48	0.45	1.33	1.42
	After-3	1.37	2.02	1.8	0.68	0.76
			Reduction factor		**49**	**46**

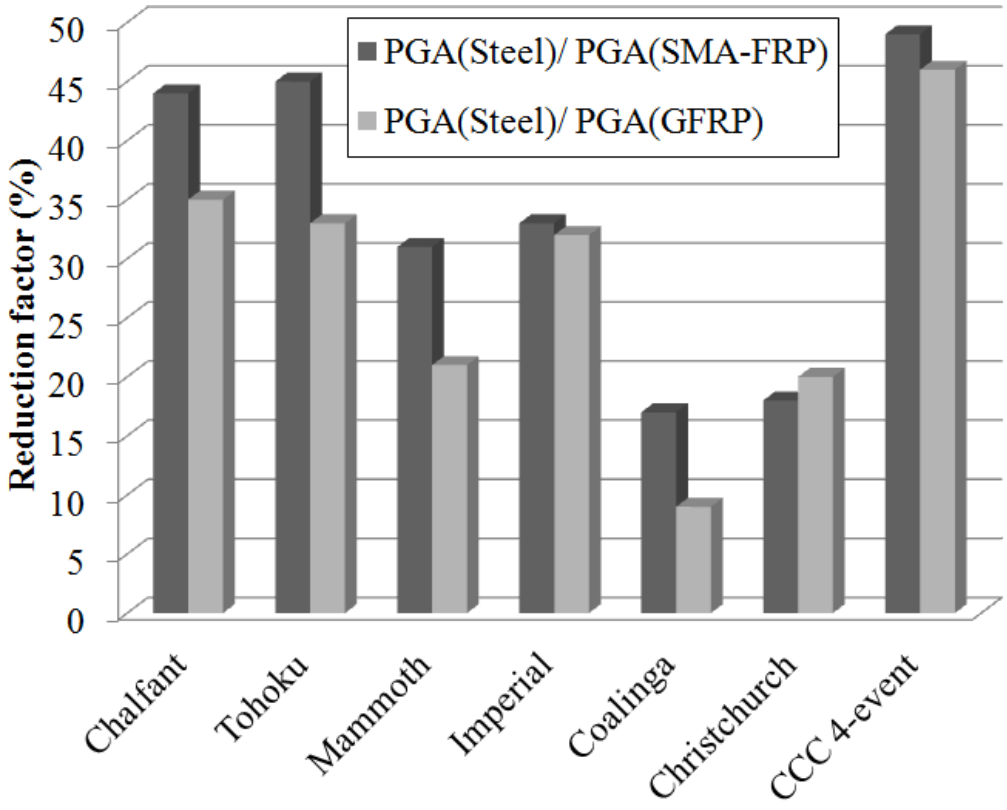

Figure 8-25**:** Reduction factors for MRF-4%

It is evident from the results that the seismic sequence leads to larger permanent IDR in comparison with the corresponding single main shock event. Due to multiplicity of earthquakes and accumulation of damage, there would be increased displacement demand on the structure for any aftershock case under consideration. Increased displacement demands then lead to higher values of permanent IDR. As mentioned earlier, the sustenance of drifts and magnitude of residual drift depends on the duration of shaking and number of cycles. A ratio between durations of main and aftershock records was computed for all the records as shown in table 8-3. This duration ratio of any sequential record less than one implies longer aftershock record and more number of cycles as compared to main shock, thus more potential to accumulate damage

after an initial main shock event. A correlation between the duration ratio and reduction factor was formulated for each sequence for both SMA-FRP and GFRP cases in comparison with steel reinforcement. Figure 8-26 shows the plot between the two unit-less values for both MRF-3% and MRF-4% scenarios.

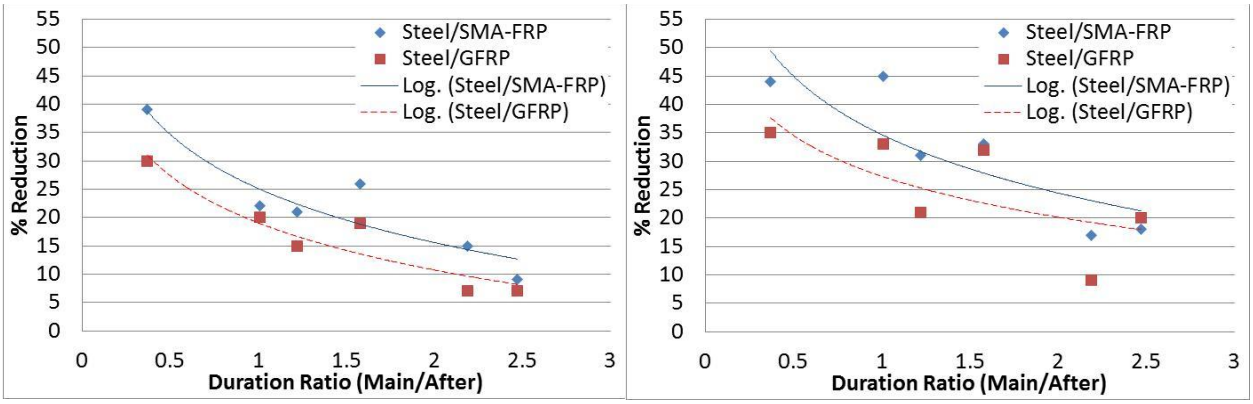

Figure 8-26**:** Relationship between reduction factor and duration ratio for SMA-FRP and GFRP frame (a) MRF-3% (b) MRF-4%

Results for 3%-MRF case shows that steel reinforced frame requires more reduction factor for an aftershock scenario for SMA-FRP reinforced frame as compared to GFRP reinforced frame. The results from Figure 8-26 satisfactorily point out that SMA-FRP reinforced frame exhibits superior performance in relation to steel frame once compared with GFRP reinforced frame. For every earthquake sequences considered, the reduction factor for steel/SMA-FRP was greater than steel/GFRP scenario. A logarithmic tread line was plotted for steel/SMA and steel/GFRP scenarios and for both MRF-3% and MRF-4% cases as seen in figure 8-25. From the plot it is evident that the reduction factor value tends to increase in 4% IDR case

as compared to 3% case for both steel/SMA-FRP and steel/GFRP scenarios. Figure 8-25 also points out the fact that as the duration ratio increases, the reduction factor decreases. This is true for both 3% and 4% IDR cases, however the slope and shape of the curve changes. So in other words, if the duration factor is less (meaning the aftershock is longer and has more cycles), more damage (quantified as reduction factor) would be exhibited by steel reinforced frame. This proves that the seismic damage for multiple earthquakes is higher than that of single ground motion. Thus traditional seismic design process, which essentially is based on isolated design ground motion, is inadequate to achieve dependable estimation of permanent residual drifts and damage. Results also show the capability of the proposed SMA-FRP composite rebars in accumulating minimal damage under sequential strong seismic events to enhance the performance of RC MRF structures.

CHAPTER 9

Testing of Small Scale RC Beam with SMA-FRP Composite Reinforcement

9.1 Introduction

The research work presented in the previous chapters has helped in proving the concept of using SMA-FRP composite as reinforcement with or without supplementary conventional fibers at a material level. The efficacy of proposed reinforcement has also been proven numerically under seismic loading. However, there is still lack in the knowledge related to its behavior once embedded in concrete member. Manufacturing of the proposed reinforcing material needs to be extended beyond the realm of dog bone coupon specimen to actual rebar. This entails designing of a concrete beam and reinforcing it with proposed composite rebars. Aim of this chapter is to seek the efficacy of the new proposed SMA-FRP rebar in concrete member and to exhibit ductility and crack closing after the damage. Ability of the proposed SMA-FRP composite rebars in accumulating minimal damage after repeated cyclic loading is sought in this chapter, to enhance the performance of RC elements. This chapter presents the experimental testing and application of the SMA-FRP composite rebar embedded in small scale concrete beam under quasi-static flexural loading. The beam was tested under 3 point bending to failure with displacement controlled cyclic regime, which allowed studying the hysteretic and re-centering property of proposed SMA-FRP composite.

9.2 Manufacturing of square SMA-FRP composite rebar

The length of SMA-FRP composite rebar had to be restricted to 280 mm due to the limitation of the dimensions of hot-press. This length of rebar in turn affects the length of concrete beam which will be reinforced with the manufactured SMA-FRP composite rebar. Keeping this in mind, a cutout of 280 mm in length, 3.2 mm in width was made in the silicone mould which was 3.2 mm in thickness. This cutout in silicone was used as dam for assembling the SMA and resin matrix layer by layer to manufacture square SMA-FRP rebar. All the SMA wires used in the manufacturing process were 280 mm in length and underwent training to stabilize their mechanical properties, as explained earlier in section 5.3. Resin M10 as described in section 4.4.2, was used as matrix for SMA composite rebar. 22 trained SMA wires of 500 μm in diameter were used in manufacturing of one composite rebar. In total two SMA composite rebars were manufactured for reinforcing concrete beam (discussed in section 9.3). Figure 9-1 shows the layout of the silicone mould dam with cutouts, ready for manufacturing process.

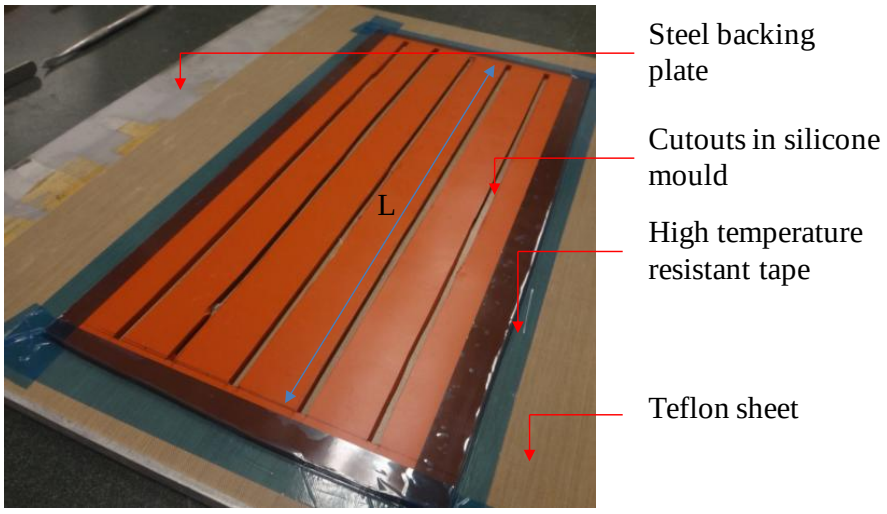

Figure 9-1: Layout of the silicone mould for manufacturing of square SMA-FRP rebar

The 22 trained SMA wires were distributed in four layers along the height of the cutout in silicone dam. All the layers were separated by segments of porous fabric cloth along the length of the composite rebar (L). The function of these porous fabric segments was to bifurcate each layer of SMA wires while at the same time, not hinder the flow of resin into the gaps between SMA wires. Figure 9-2 shows schematics of the layout of the SMA-FRP composite rebar.

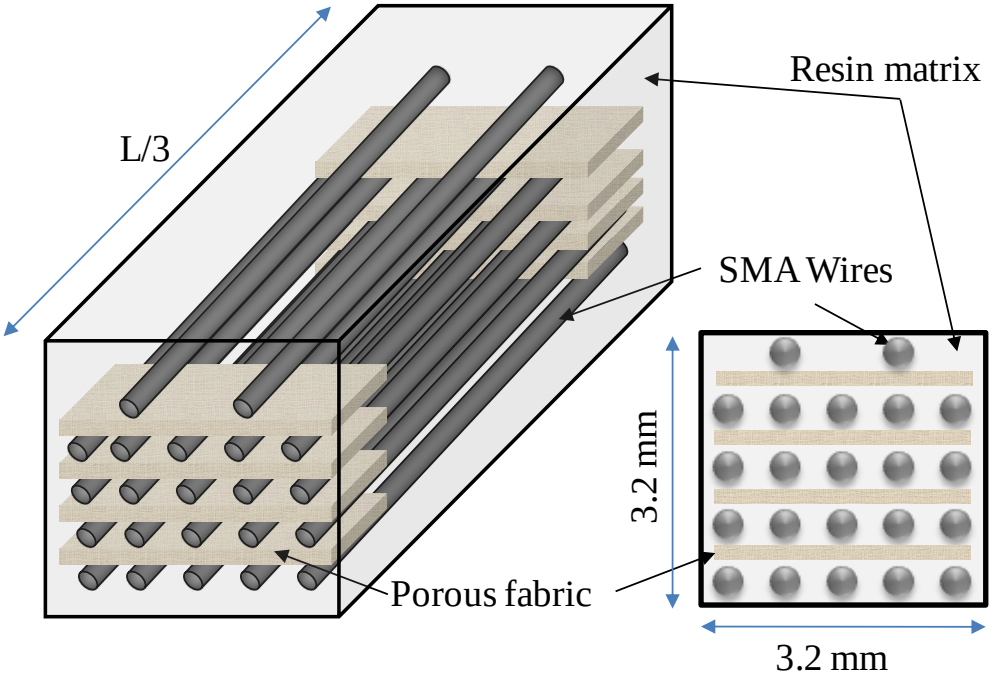

Figure 9-2: Schematics of layout of SMA-FRP composite rebars

Resin matrix was degassed for 30 minutes before pouring into the moulds, layer by layer. Figure 9-3 shows the embedding of one of the trained SMA wires inside the mould along with placing of porous fabric after each layer of SMA wires at L/3 distance along the length of rebar.

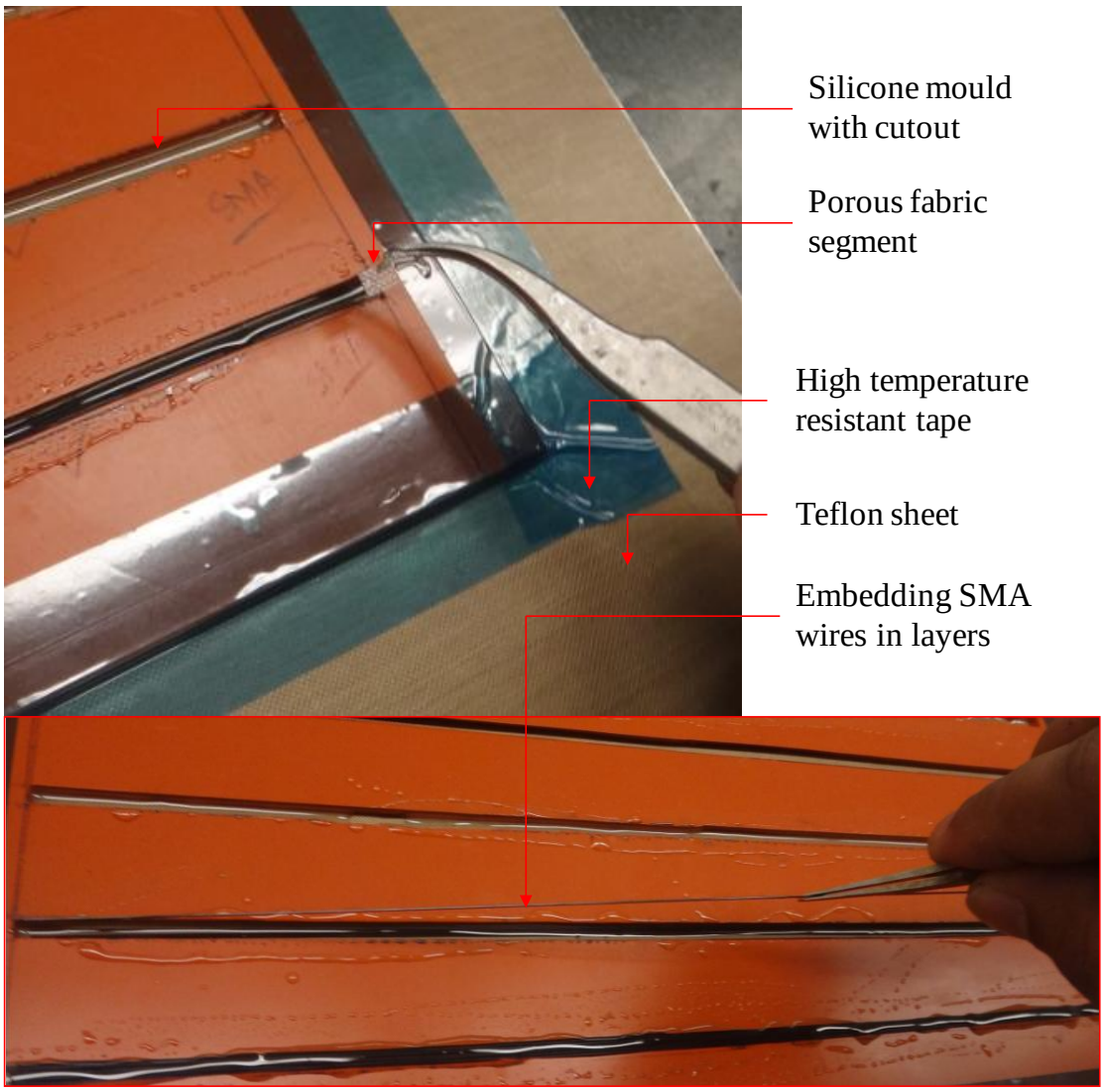

Figure 9-3: Embedding of trained SMA wires and placing of porous fabric

Once the laying of all 22 wires in each cutout was complete, the whole mould setup was covered by permeable nylon and bleeder cloth to capture any over flowing resin. The mould setup was then subjected to 172.3 kPa pressure and 35^{o}C curing temperature in the hot-press for

a period of 24 hours. The schematics of proposed configuration of the SMA-FRP hybrid composite is shown in figure 9-4.

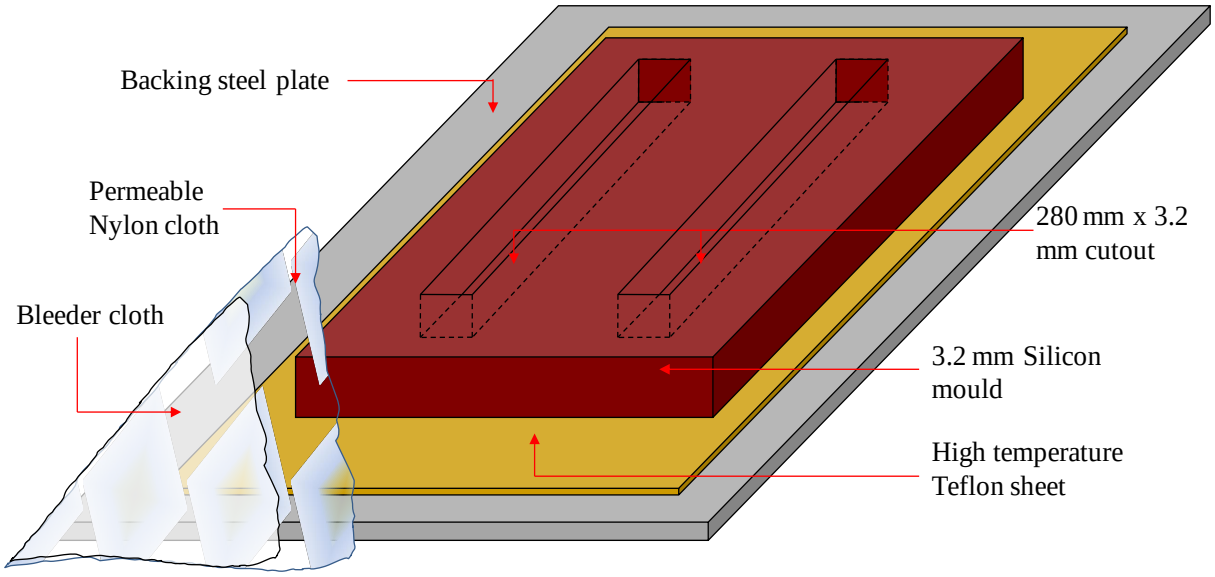

Figure 9-4: Schematic of manufacturing setup for SMA-FRP rebars

After the curing period, the SMA composite rebars were extracted from the mould and were ready for placing in concrete beam. Area of each composite rebar was measured and is shown in table 9-1. The first SMA composite rebar (SC-1) with 22 SMA wires and composite area of 10.24 mm^2 allowed achievement of 39.3% FVF. SC-2 achieved 40.6% FVF. The final dimension and FVF which was achieved in the SMA composite for each rebar is shown in table 9-1.

Table 9-1: FVF of manufactured SMA-FRP composite rebars

Specimen	Tag	Resin Matrix M10	Average Composite Area (mm^2)	Area of 22 SMA wires (mm^2)	Reinforcement FVF
SMA comp-1	SC-1	EPON-862, EPIKURE-3274, Heloxy-48	10.2	4.0	39.3%
SMA comp-2	SC-2		9.9	4.0	40. 6%

9.3 Concrete beam details

As mentioned earlier, because of limitation of hot-press which restricted the length of SMA-FRP composite rebars, the concrete beam was also required to be scaled down accordingly. The T-beam was 250 mm in length, 51 mm in depth with 64 mm and 25 mm in width for flange and web, respectively. Because of small scale of reinforcement, the concrete beam was designed without lateral reinforcement (stirrups). The reinforcement ratio was kept as 1.25% as a design parameter, which allowed calculation of beam cross sectional area required to achieve the target reinforcement ratio. The main aim of test was to investigate the ductility and re-centering capability of SMA composite reinforced concrete beam, which requires SMA composite rebar to sustain high straining. Since no stirrups were provided, the concrete was left un-confined. In order to delay the crushing of concrete at top of the beam, T-beam cross section was selected for design purpose. This will allow increase in the curvature capacity of the beam's section, hence force SMA composite rebars to experience high strains during testing. The T-beam cross sectional dimensions were optimized to allow embedment of the two manufactured SMA-FRP composite rebars as tension reinforcement with 6 mm cover from bottom. Schematics of the designed T-beam with dimensions of the cross section are shown in figure 9-5.

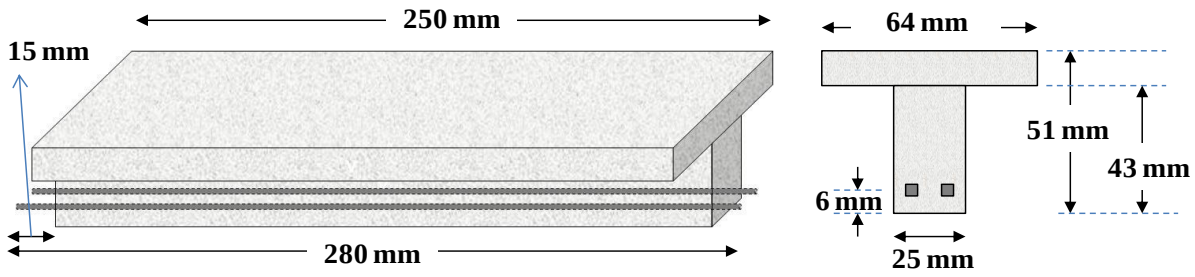

Figure 9-5: Schematics of designed T-beam with cross sectional dimensions

Figure 9-5 shows projection of composite rebars beyond the face of the beam. This projection on both ends is intended for anchoring the rebars at both ends using U-clamps to restrict slippage of the rebars along the beam length during testing. Since the manufactured rebars have smooth surface finish, in the likelihood of them de-bonding along the interface with concrete, the proposed U-clamp attachments will be beneficial in restraining this slippage. In order to achieve the desired reinforced concrete T-beam, wooden mould were prepared for casting of the desired cross section. A wooded mould with inner length, width and depth as shown in figure 9-5 was constructed with opening at each ends for the two projecting composite rebars. Manufactured wooden mould for T-beam with embedded SMA composite rebars is shown in figure 9-6.

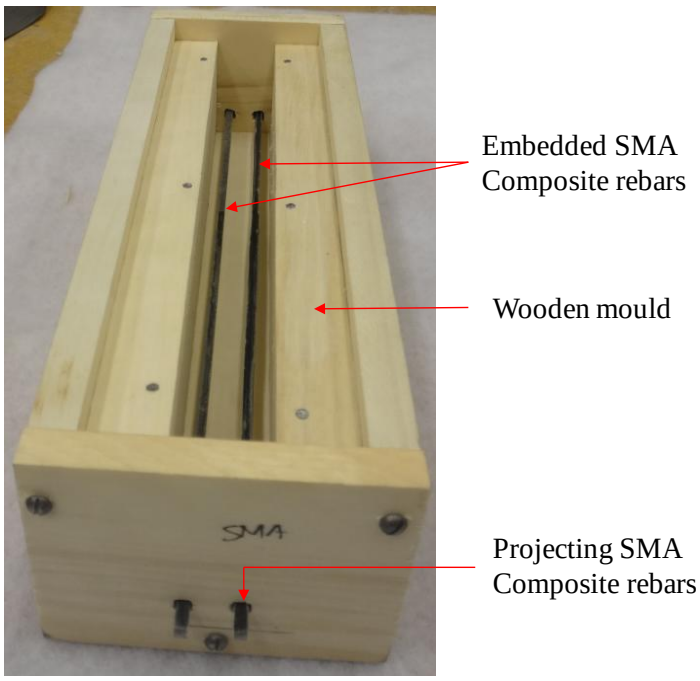

Figure 9-6: Wooden mould with embedded SMA composite rebars

Ordinary Portland cement (OPC) was used in casting the beam. Because of miniature nature of the SMA composite reinforcement and beam cross section, coarse aggregate were not used. Only fine aggregate (sand) was used to produce grout with adopted mix proportion shown in table 9-2. The concrete mix was designed to achieve strength of 42 MPa or more. Achievement of higher grout strength would help in further delaying crushing of concrete in compression at top of the beam. Plasticizer admixture was used to increase the workability and flow characteristics of the grout in and around the SMA composite reinforcement.

Table 9-2: Concrete mix design

Water cement ratio (w/c)	Contents by Weight (gm)			Plasticizer (1% by volume of OPC) (ml)
	Water	OPC	Fine aggregate (Sand)	
0.35	217.4*	557.6	1115.2	5.6
* Includes 2% absorption of water by sand				

American standard for testing materials (ASTM) C305 (ASTM C305, 2012) was followed for mixing the contents of the grout mix. Figure 9-7 shows the casting of T-beams with grout. Pouring of grout in the wooden mould was done on a vibrating table to allow better flow of grout between and around the rebars. The vibration was restricted to 5 seconds to avoid segregation and bleeding in the grout.

Figure 9-7: Casting of small scale T-beam

Same grout mix was used to prepare six 50 mm cubes which were tested after 14 days of curing to obtain compressive strength of the beams. These cubes were manufactured and tested in accordance with ASTM C109/ C109M (ASTM C109/C109M, 2013). Average compressive strength achieved from the six cubes was 55 MPa, which exceeded the target strength. This high strength grout will allow SMA composite rebar to sustain higher strains before failure of concrete in compression. As mentioned earlier, U-clamps were installed on the projected end of the SMA composite reinforcement to restrict slippage of composite rebar along the beam length. Figure 9-8 shows two installed U-clamps with 3.5mm opening on SMA composite reinforcement on one of the beam. These U-clamps exerts clamping force on the composite rebar against the face of the beam, thus restricting slippage during the test.

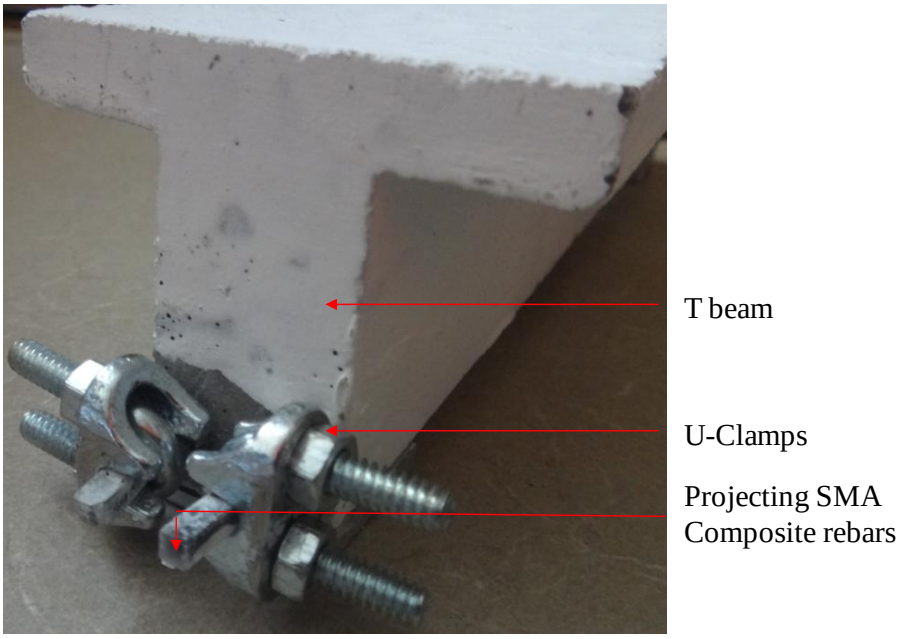

Figure 9-8: Installed U-clamps on SMA composite rebars at each end

9.4 Instrumentation and test setup

The small scale beam was investigated in flexural under three point bending test in a simply supported configuration. A notch was provided at the mid span on the bottom of the beam starting just below the reinforcement. Provision of notch will facilitate initiation of flexural crack at the specified location. Since maximum moment in simply supported beam occurs at mid span, so the notch was created so as to facilitate crack at pre-determined location. The beam was rested on a roller and a pin support at each end through support brackets, while the load will be applied in the middle of the beam through load cell. Linear variable displacement transducer (LVDT) was used to measure the vertical deflection of the beam under the load. Location of various gauges used for measurements during the testing has been shown in figure 9-9.

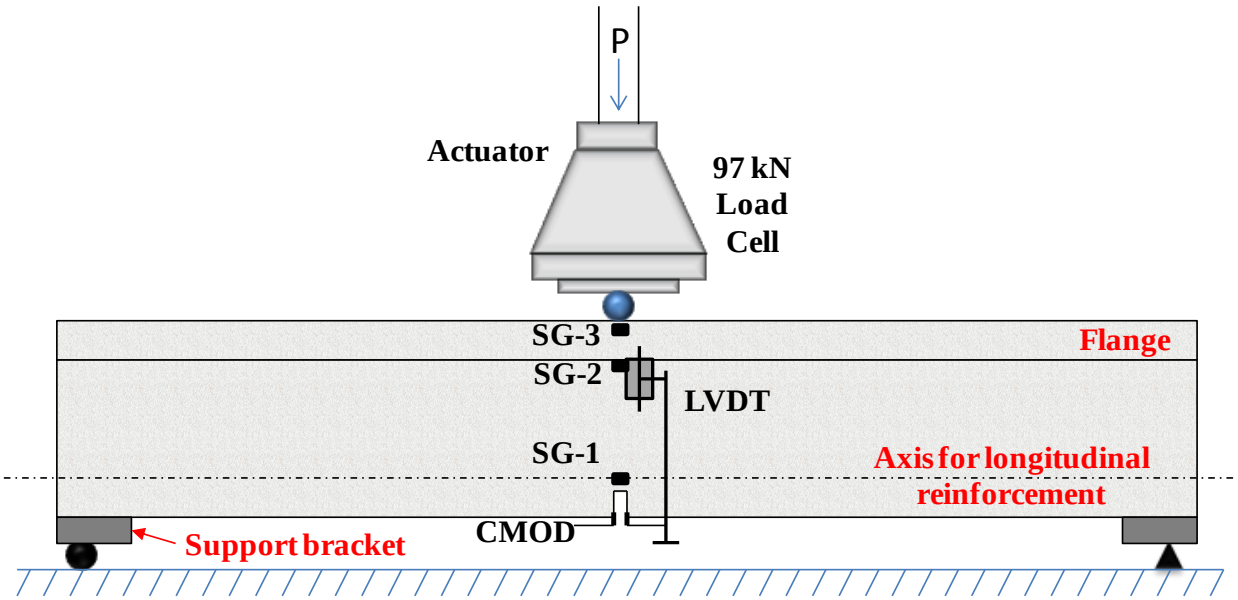

Figure 9-9: Location of measuring instruments on RC T-beam

Three strain gauges were used along the height of beam at mid span to measure strains in concrete. SG-1was provided right above the notch. Reading from this strain gauge will give indication of crack appearance and progression. SG-2 was provided at the top of the web, right under the flange. Reading from this strain gauge will give indication of progression of crack and shifting of neutral axis. SG-3 was provided at the T-beam flange. Reading from this strain gauge will give indication of crushing of concrete in compression. Crack mouth opening device (CMOD) was used to measure the opening of the provided notch after initiation of the crack. CMOD reading will also help in determining of crack closing thus indicating re-centering capability of SMA composite rebar. All the measuring instruments were connected to data acquisition system (DAQ) for recording of readings during the test. The test setup along with testing frame is shown in figure 9-10.

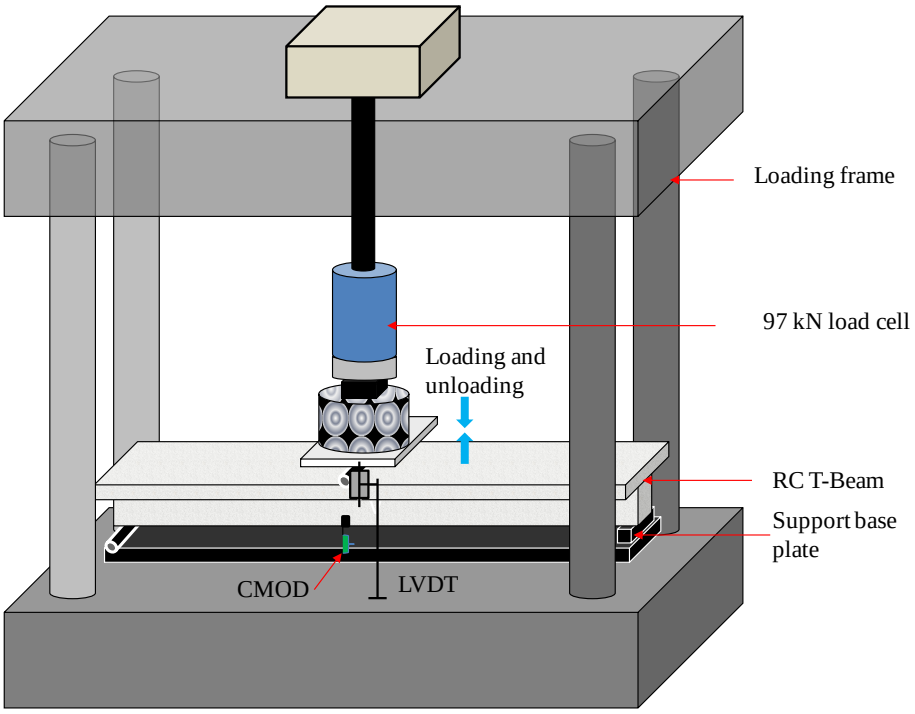

Figure 9-10: Details of test setup and loading frame

The 3-point bending test on RC T-beam reinforced with SMA composite reinforcement was controlled using displacement reading from actuator. Constant actuator displacement rate of 0.25 mm/min was used throughout the test. For loading segment of the cycle, limit detection was placed in loading protocol using reading from LVDT. This limit detection was user selected and allowed the loading segment of the cycle to stop. After this, the unloading cycle begins which is again controlled by displacement reading from actuator. However again limit detection from load cell (zero force) was placed to stop the unloading segment of the cycle. This procedure was repeated for all subsequent loading and unloading cycles. For each cycle the target displacement from LVDT was set at an absolute value of 1.15 mm. This absolute value was chosen in order to have an initial cycle before the phase transformation in SMA. The final test setup along with all the instrumentation used during the testing has been shown in figure 9-11.

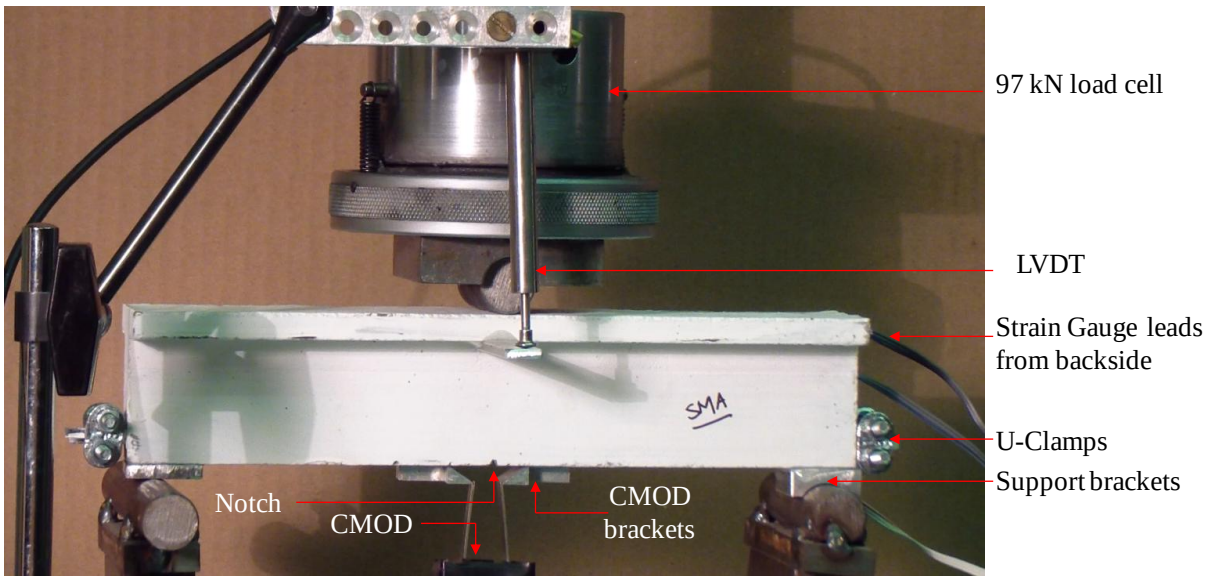

Figure 9-11: Actual test setup and instrumentation

9.5 Testing and Results

The test results from load cell, LVDT, CMOD and strain gauges were collected and were plotted to assess the behavior of the beam reinforced with composite. The results were able to offer insight about flexural behavior of proposed composite in addition to bondage with concrete. Plots were developed between LVDT vertical deflection at midspan, CMOD horizontal deflection and readings from strain gauges in relation to force to facilitate the understanding of the behavior of beam reinforced with proposed composite reinforcement.

9.5.1 Load-deflection and crack opening response

In order to facilitate examining and understanding the load-deflection curves of the beam, the response curve was segregated in terms of cycles and points. In total, 4 downward deflection cycles were conducted which included loading of the beam to target deflection and then unloading till the force is zero. All four cycles and the points (A to P) during the test are shown in force-deflection plot in figure 9-12. As the externally applied load increased beyond the initial cracking load of the beam, the crack depth and crack mouth opening displacement (CMOD) also increases. Figure 9-13 shows the CMOD readings of the tested beam in relation to loading. Since CMOD significantly influence the durability of structures and may accelerate corrosion of internal longitudinal steel reinforcement. Hence ability of reinforcement to close the cracks initiated due to nonlinear loading is also an important aspect for the sustenance of the structures.

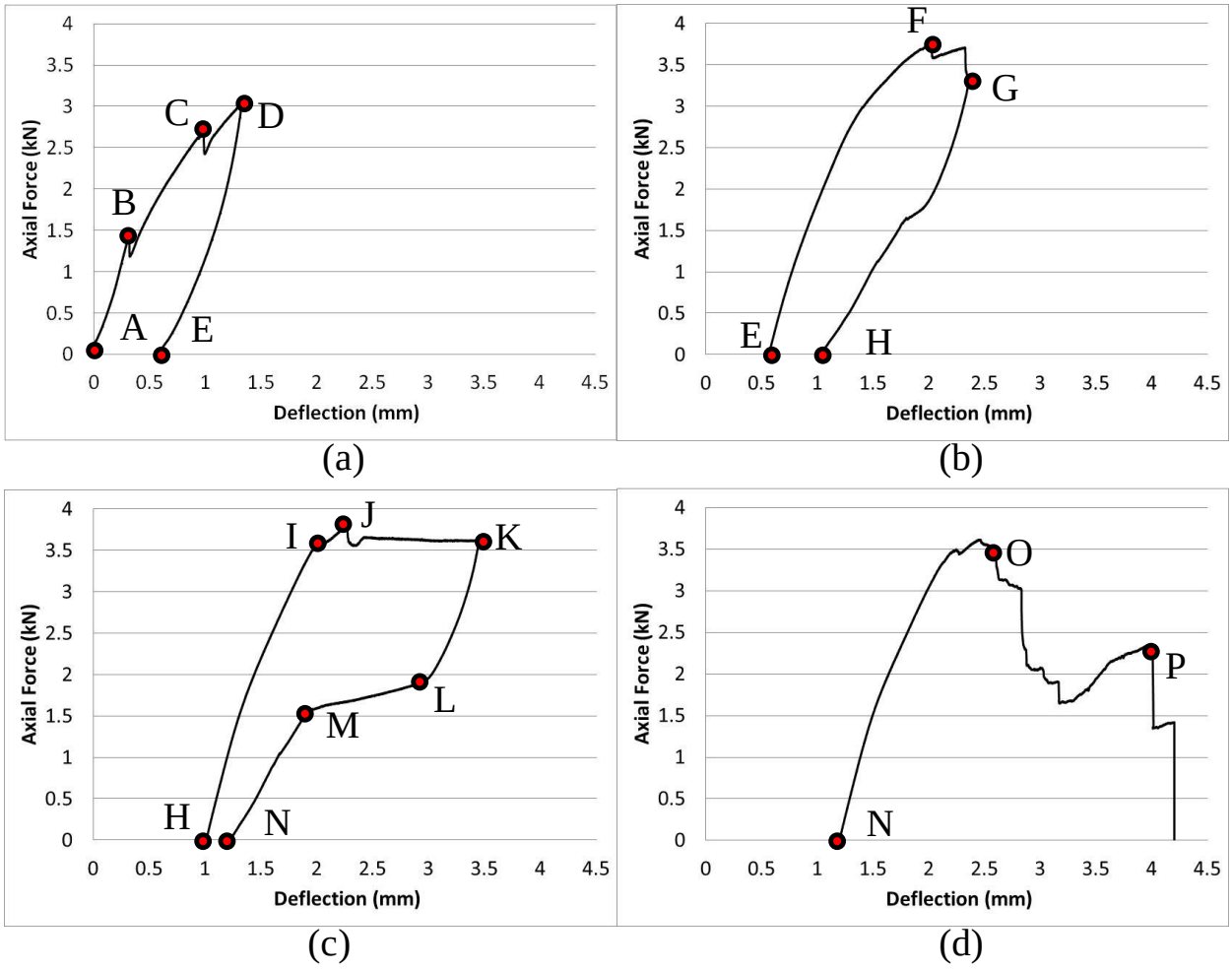

Figure 9-12: Load versus mid span deflection plots of T-beam (a) Cycle-1 (b) Cycle-2 (c) Cycle-3 (d) Cycle-4

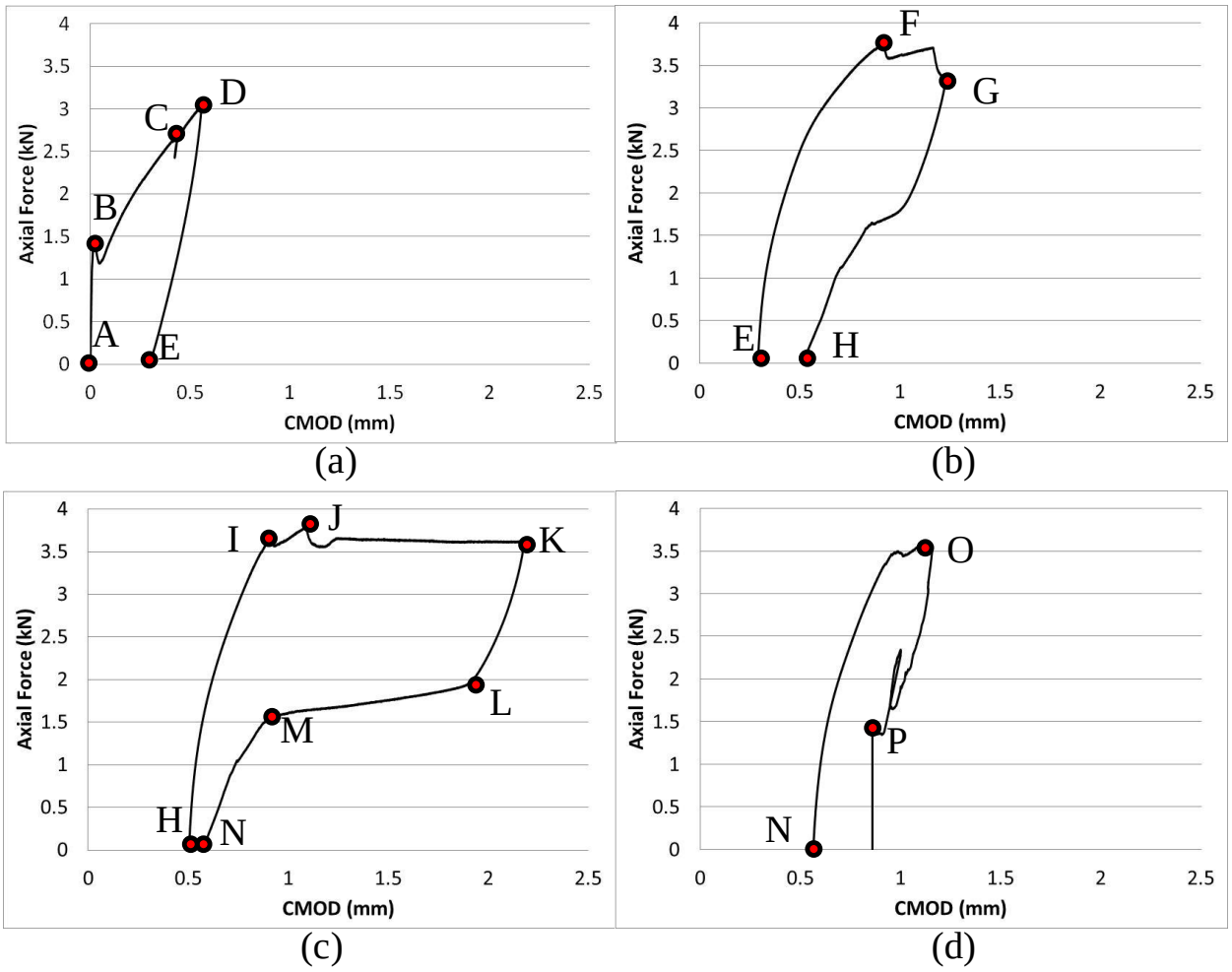

Figure 9-13: Crack mouth opening displacement plots of T-beam (a) Cycle-1 (b) Cycle-2 (c) Cycle-3 (d) Cycle-4

At point-A, the beam initially was in an unloaded position as shown in figure 9-11, from where the load started to increase till cracking load. At point-B, the flexural crack initiated from provided notch at cracking load of 1.31 kN with deflection of 0.29 mm. From point-A till point-B, the CMOD showed almost negligible increase in horizontal displacement because of notch being intact. Figure 9-14 shows the initiation of flexural crack at point-B. After point-B, the CMOD recorded jump in horizontal displacement because of initiation of crack. At point-C, web

shear crack initiated on the right side of the beam at 2.63 kN load with deflection of 0.93 mm at mid-span. Figure 9-15 shows the initiation of shear crack at point-C.

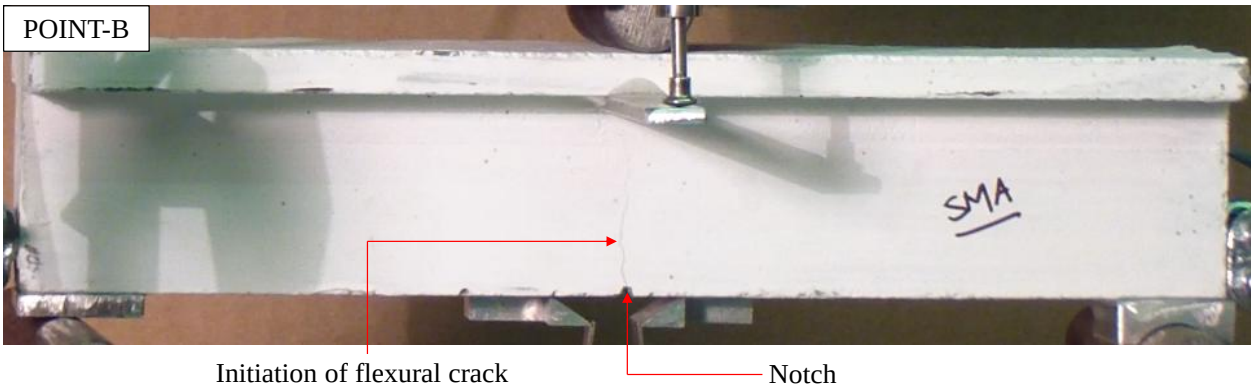

Figure 9-14: Point-B; Initiation of flexural crack from notch

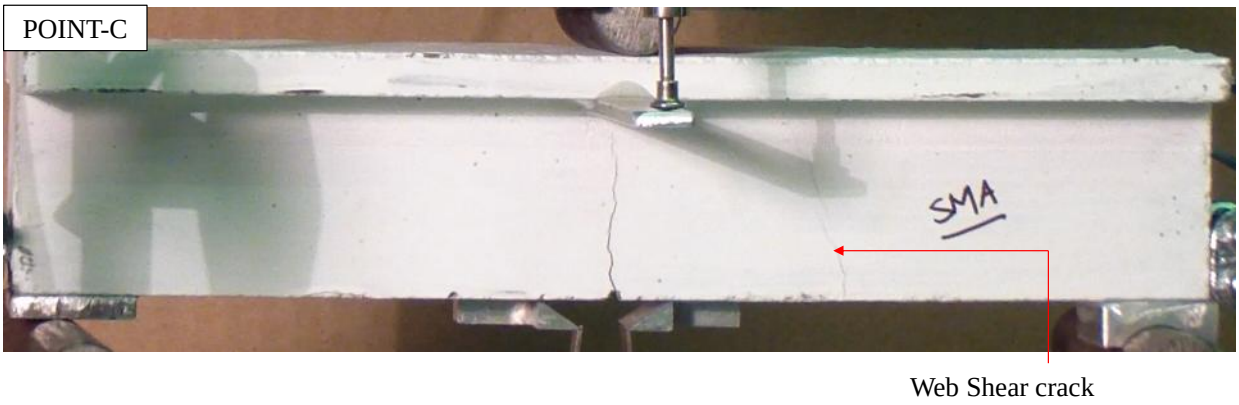

Figure 9-15: Point-C; Initiation of shear crack

It is known fact that concrete shear strength is the combination of resistance from compressive zone, aggregate interlocking, dowel action and shear reinforcement. This premature

appearance of shear crack could primarily be related to absence of shear reinforcement and aggregate interlocking (because of use of grout instead of regular concrete). Point-D is the completion of loading phase of the 1st cycle, as shown in force-deflection plot in figure 9-12a. The peak load and deflection at this point were 3.05 kN and 1.28 mm, respectively. Hereafter the load was reduced at control rate till the force in the load cell was zero (Point-E). At point E, the beam accumulated 0.57 mm residual deflection (should be close to zero because SMA should still be in the Austenite phase, elastic range) which suggest slight slippage of smooth SMA composite rebars only in the mid-span region. This slippage would also trigger nullifying of dowel action which would add to the explanation provided earlier for development of premature shear cracks. Figure 9-16 shows the complete closing of shear crack with residual crack opening at mid-span at point E.

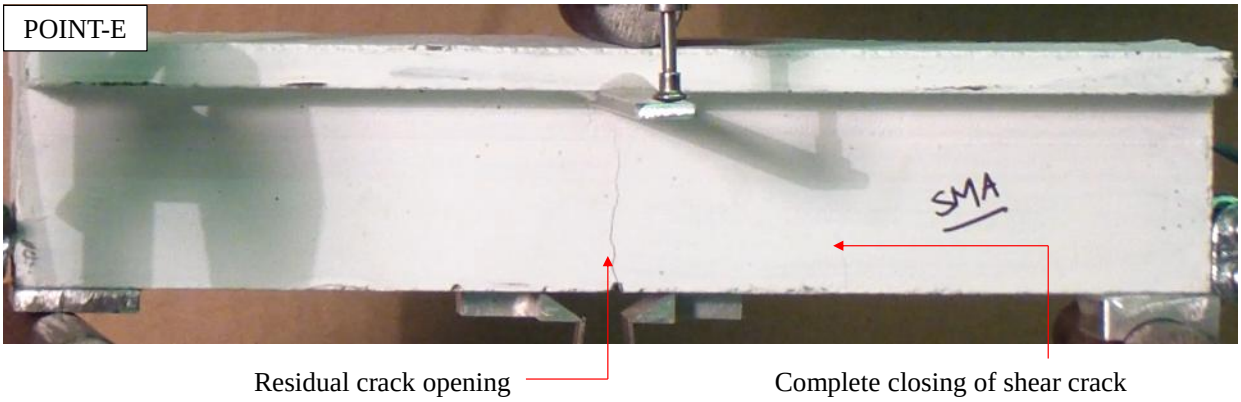

Figure 9-16: Point-E; End of 1st cycle

Point-F is the load where forward transformation in SMA (yielding), i.e. start of phase transformation from Austenite to Martensite is observed. This happened at 3.69 kN load with

corresponding deflection of 1.96 mm at mid-span. Hereafter the test was continued till the achievement of target deflection of 2.33 mm (Point-G). At this point, maximum flexural and shear crack opening was observed for the 2nd cycle. Figure 9-17 shows the picture of point-G.

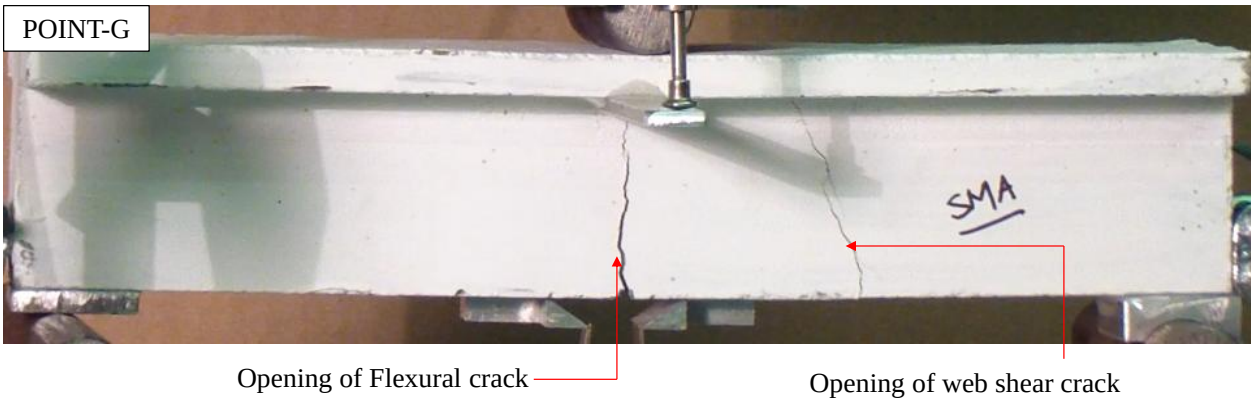

Figure 9-17: Point-G; End of loading phase of 2nd cycle

Point-H marks the completion of 2nd cycle. At this point the observed residual crack opening at mid-span was 1.01 mm. Even after the SMA wires experienced phase transformation within composite rebar, because of super-elastic property, SMA composite rebar was able to recover much of the residual deflection at mid-span. Although results suggest that SMA composite rebar experienced some slippage along interface with concrete, recovery of deflection by 75% shows re-centering capability. Figure 9-18 shows the completion of 2nd cycle and closing of cracks.

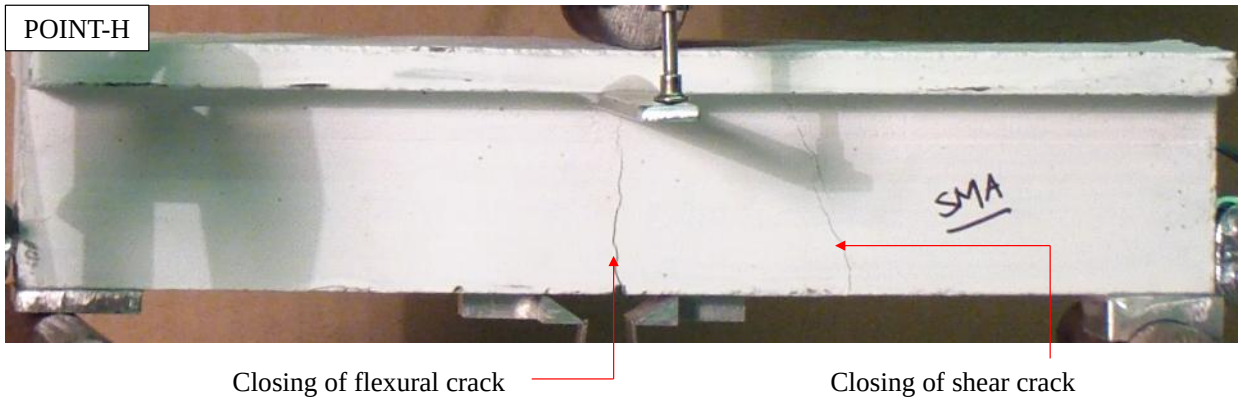

Figure 9-18: Point-H; Completion of 2nd cycle

Point-I again marks the forward transformation in SMA in the 3rd cycle. This happened at 3.55 kN load with corresponding deflection of 1.99 mm at mid-span. Hereafter the loading continued till reaching of point-J which is the peak load point for the test with 3.73 kN and corresponding deflection of 2.2 mm. Point-K is the maximum deflection of the beam in the 3rd cycle. The peak deflection measured at this point was 3.37 mm with corresponding load of 3.62 kN. Figure 9-19 shows beam configuration at this point with maximum flexural crack opening at mid-span.

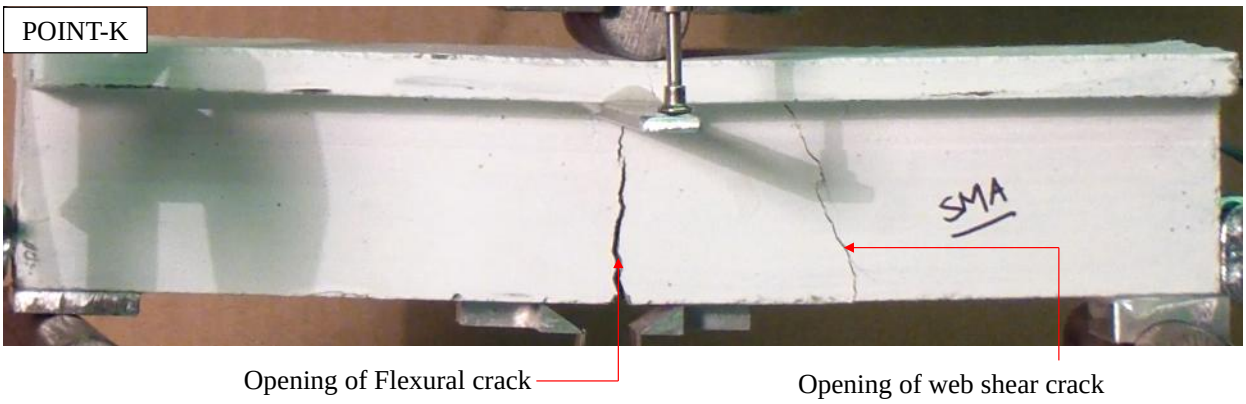

Figure 9-19: Point-K; End of loading phase of 3rd cycle

Point-L and M marks the Martensite to Austenite start and Austenite to Martensite finish phase transformation in SMA wires. Because of super-elastic property associated with SMA wires, SMA composite rebar is able to recover residual strains and displacements. Point-N, which is the completion of 3rd cycle, shows excellent re-centering of T-beam due to presence of SMA composite rebars. This crack closing and recovery would have not been possible in steel reinforced beam because of permanent damage and plasticity in steel material. Better engagement of SMA composite rebar in 3rd indicates drop in slippage at the interface between SMA composite rebar and concrete. This could be either because of engagement of SMA composite rebar with concrete due to presence of unintentional deformations along the length of rebar (From manufacturing process) or restraining of composite rebar by U-clamps at both ends. At this point the observed residual crack opening at mid-span was 1.21 mm. This is recovery of 92% of deflection, shows unique ability of re-centering of SMA composite rebar. At the end of 3rd cycle the beam experience addition of only 0.2 mm residual deflection. Picture of beam at point-N is shown in figure 9-20 with excellent crack closing and deflection recovery ability.

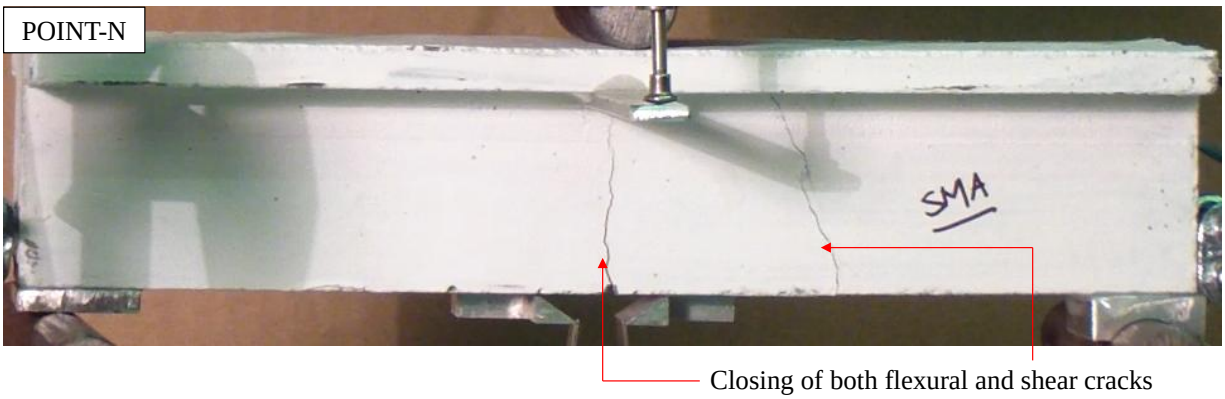

Figure 9-20: Point-N; Completion of 3rd cycle with excellent re-centering

At point-O shown in figure 9-12d, there was more progression of shear crack relative to flexure crack. The load and deflection at this point were 3.4 kN and 2.53 mm, respectively. Because of this progression of web shear crack, which extended along the horizontal plane of the reinforcement, complete shear failure was observed at point-P at deflection value of 3.94 mm. Both these points, O and P, have been shown in figure 9-21 and 9-22, respectively. In point-P the shear cracks expose the SMA composite rebar and even extended into T-beam flange. Point-P marked the culmination of the test. Summary of test data including mid span deflection, force, CMOD readings at different points during the tests is presented in table 9-3.

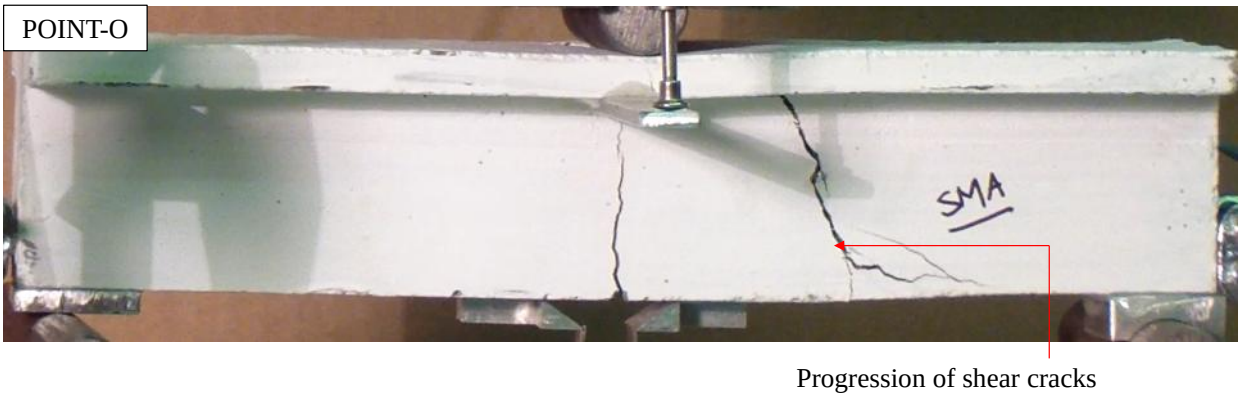

Figure 9-21: Point-O; Progression of shear cracks

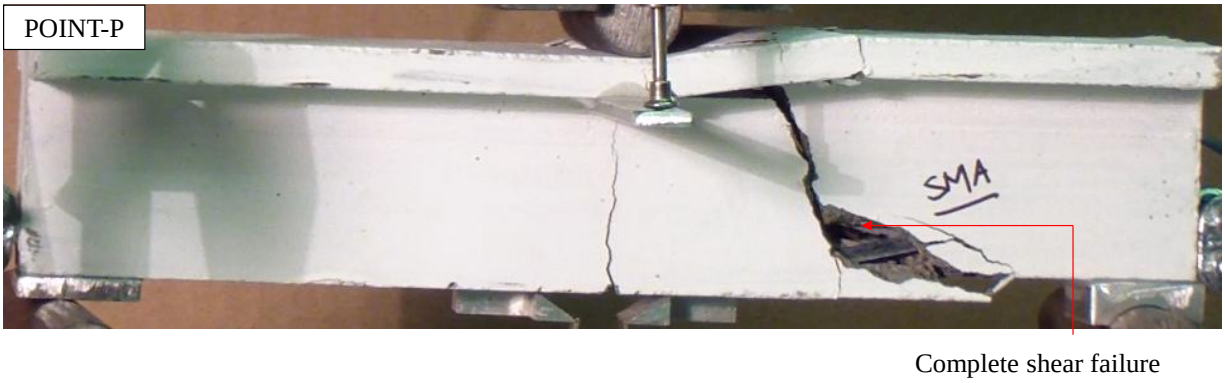

Figure 9-22: Point-P; Complete shear failure

Test results show excellent crack mouth closing of beam by SMA composite reinforcement even after yielding, especially in the 3rd cycle, once the composite rebar got fully engaged. In the 3rd cycle the SMA composite rebars were able to close the mouth opening by 96.4%, which provides insight to the re-centering and damage control ability of the SMA composite. Results show much superior performance of SMA composite rebars in terms of ductility, energy dissipation through hysteretic action, re-centering to recover residual

deflections, without permanent damage to the reinforcement. This is not possible for beams reinforced with steel or GFRP rebars.

Table 9-3: Test data at various points

Cycles	Phase	Point	Description	Vertical Deflection (mm)	Force (kN)	CMOD (mm)
1	Loading	A	Un-cracked (extending from zero load)	0	0	0
		B	Initiation of flexural crack	0.29	1.31	0.012
		C	Initiation of shear crack	0.93	2.63	0.4
		D	End of loading phase-Cycle 1	1.28	3.05	0.53
	Unloading	E	End of 1st Cycle	0.57	0	0.29
2	Loading	F	Forward transformation / yielding - Austenite to Martensite start	1.96	3.69	0.87
		G	End of loading phase-Cycle2	2.33	3.44	1.19
	Unloading	H	End of 2nd Cycle	1.01	0	0.5
3	Loading	I	Forward transformation / yielding	1.99	3.55	0.88
		J	Peak loading	2.2	3.73	1.05
		K	End of loading phase-Cycle 3	3.37	3.62	2.14
	Unloading	L	Reverse transformation - Martensite to Austenite start	2.92	1.89	1.84
		M	Phase transformation - Martensite to Austenite finish	1.98	1.58	0.93
		N	End of 3rd Cycle	1.21	0	0.56
4	Loading	O	Widening of shear cracks	2.53	3.5	1.13
		P	Complete shear failure	3.94	2.33	0.86

9.5.2 Ductility and hysteretic behavior

From figure 9-12, it is evident that the T-beam reinforced with SMA-FRP composite was able to dissipate energy through hysteretic action without accumulation of much residual deflection. This recovery of vertical deflection is because of re-centering capability while at the

same time dissipating energy using wide hysteresis. For 1st cycle, the energy dissipated (area under force-deflection curve) was 1.66 joules. For 2nd cycle, in which the SMA rebar showed forward and reverse stress transformation, was able to dissipate 2.9 joules energy. This is 74% increase in energy dissipation which was effected by yielding of SMA composite rebar. In the 3rd cycle the beam showed wide hysteresis and was able to dissipate 3.72 joules energy which is 124% increase from 1st cycle. The wider hysteretic behavior and re-centering capability exhibited by SMA composite reinforced concrete element is the hallmark of proposed composite rebar for use in seismic zones. T-beam exhibited yielding at a deflection value of 1.96 mm, thus it was able to achieve 1.2 and 1.8 ductility (μ) in 2nd and 3rd cycle. Beam reinforced with GFRP rebar would not be able to show any hysteresis and ductility if subjected to same loading protocol. Figure 9-23 shows energy dissipation of SMA-FRP composite reinforced concrete T-beam along with ductility values

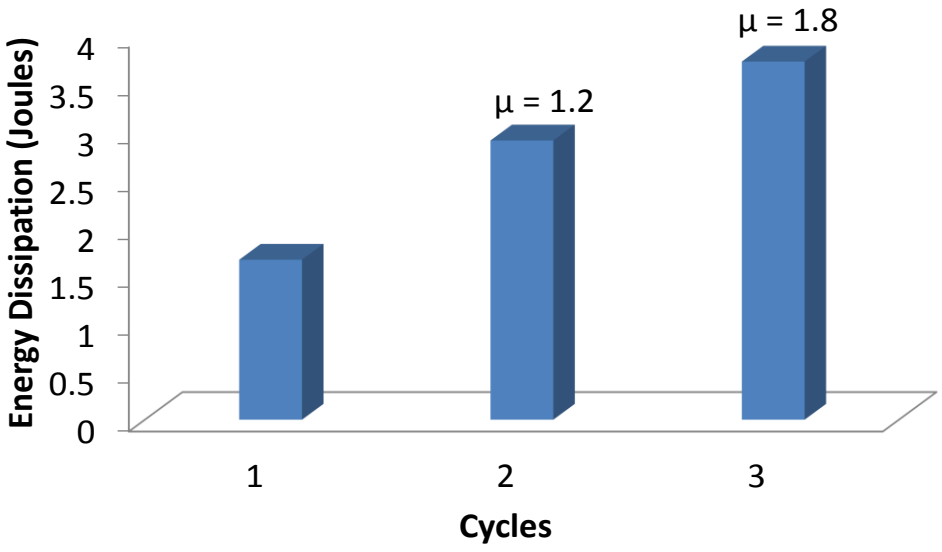

Figure 9-23: Energy dissipation of SMA-FRP composite reinforced concrete T-beam

9.5.3 Concrete strains

As shown in figure 9-9, three strain gauges were used along the height of beam at mid span to measure strains in concrete. SG-1 was provided right above the notch, while SG-2 was installed on the web, right under the flange. SG-3 was installed on the T-beam flange side face. Reading from this strain gauge will give indication of crushing of concrete in compression. Readings from all three strain gauges are presented in table 9-4. SG-1 was able to record initiation of crack but soon reached its capacity (7.46%) as the crack opened in the first cycle. SG-2 experienced compressive stresses initially before initiation of flexural crack. However right after the crack initiation and progression (Point-B), SG-2 started to experience tensile strains. Like SG-1, SG-2 also reached its capacity by Point-C. Data from SG-3 has been plotted in figure 9-24 in relation to loading for first 3 cycles. Figure 9-24 shows that in 1^{st} and 2^{nd} cycles, SG-3 experienced compressive strains and exhibited residual compressive strains of 0.019% and 0.21%, respectively. In the 3^{rd} cycle, SG-3 started to really stretch and reached its compressive capacity of 4%. During the compressive straining of SG-3 in 3^{rd} cycle, the gauge did not get damaged and was able to record data during the unloading phase starting at point-M. The residual compressive strain in SG-3 at end of the 3^{rd} cycle was 0.57%.

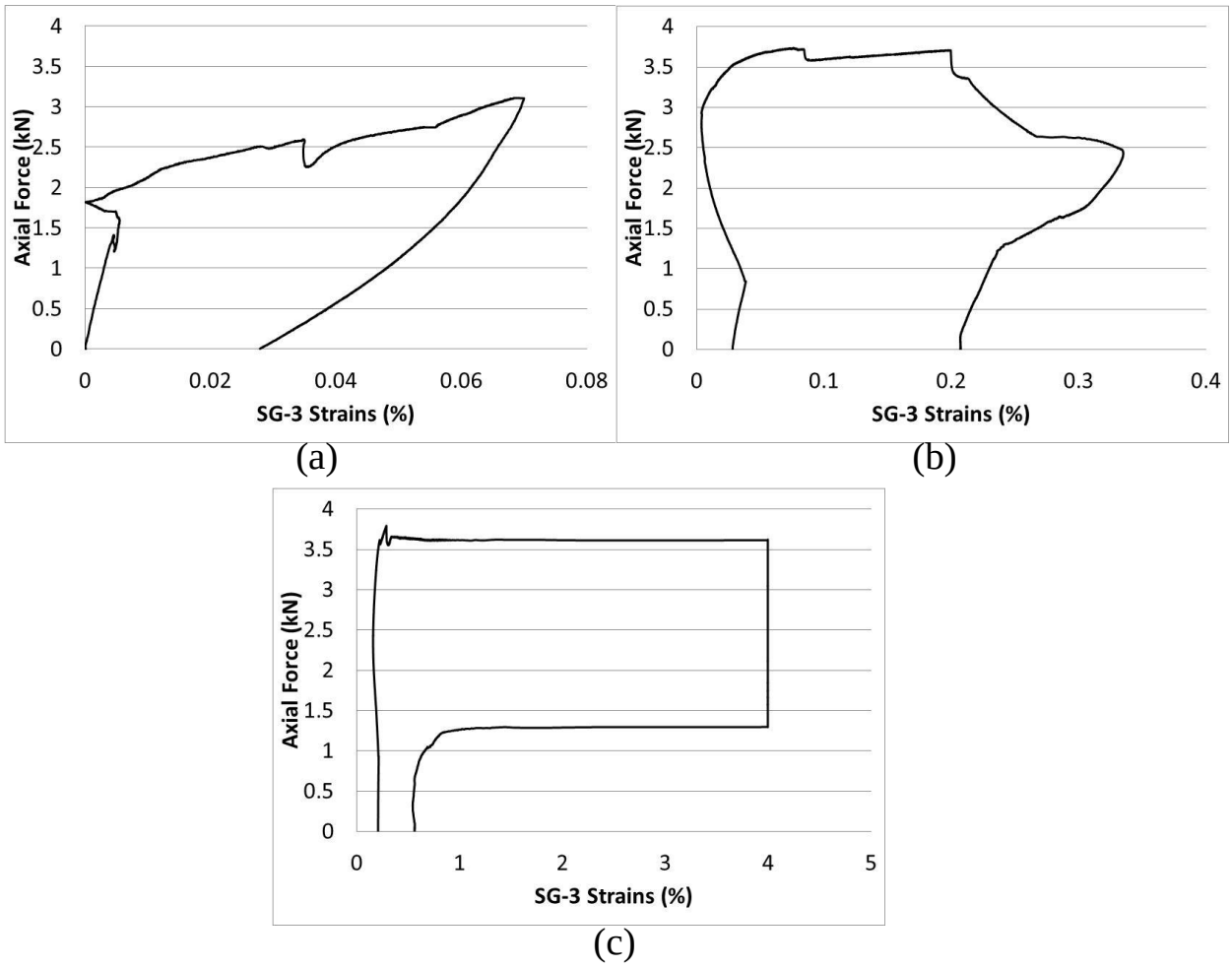

Figure 9-24: Compressive strain reading from SG-3 versus Load (a) Cycle-1 (b) Cycle-2 (c) Cycle-3

Table 9-4: Test data for strain gauges at various points

Cycles	Phase	Point	Description	Force (kN)	SG-1 (%)	SG-2 (%)	SG-3 (%)
1	Loading	A	Un-cracked extending from zero load	0	0	0	0
		B	Initiation of flexural crack	1.31	7.46	1.01	-0.008
		C	Initiation of shear crack	2.63		7.46	-0.024
		D	End of loading phase-Cycle 1	3.05			-0.036
	Unloading	E	End of 1st Cycle	0			-0.019
2	Loading	F	Forward transformation / yielding - Austenite to Martensite start	3.69			-0.087
		G	End of loading phase-Cycle2	3.44			-0.33
	Unloading	H	End of 2nd Cycle	0	Peaked out	Peaked out	-0.21
3	Loading	I	Forward transformation / yielding	3.55			-0.23
		J	Peak loading	3.73			-0.298
		K	End of loading phase-Cycle 3	3.62			-4
	Unloading	L	Reverse transformation - Martensite to Austenite start	1.89			-4
		M	Phase transformation - Martensite to Austenite finish	1.58			-1.44
		N	End of 3rd Cycle	0			-0.57

CHAPTER 10

Summary, Conclusions and Recommendations

10.1 Summary

This dissertation studied a new type of SMA based composite (SMA-FRP) reinforcement for concrete framed structures. The new composite has the capability of dissipating energy through hysteretic action and re-centering under seismic loading. The proposed SMA-FRP reinforcing bar comprise of polymeric resin reinforced with small diameter superelastic SMA fibers with or without supplementary reinforcing fibers. This reinforcement is sought as an alternative to conventional steel rebars which exhibit permanent damage due to its plasticity. The new SMA-FRP composite is also superior to conventional FRP rebars which have limited rupture strain and non-ductile behavior under excessive loading.

An experimental investigation involving material system development through exploration of constituents of the proposed SMA-FRP composite reinforcement was carried out. Small diameter (50 μm) diameter NiTi SMA wires were selected as primary reinforcing material for the composite. SMA wires which exhibit degradation in mechanical properties with continued cycling were mechanically trained to stabilize their properties like Young's modulus, austenite to martensite start stress (forward transformation stress) and residual strains. Selection of host resin matrix for the composite reinforcement was selected based on high elongation performance. Various resin mixtures ingredients were explored by manufacturing coupon

specimens which were tested under quasi-static tensile loading. Use of reinforcing fibers like S-glass, E-glass and Kevlar as supplementary reinforcement for the composite was investigated. Preliminary material selection and their rightful combination in manufacturing high elongation composites was one of the main focus areas of this study. Thereafter SMA-FRP composite specimens with varying FVF were tested and results were compared with composites reinforced with conventional fibers. Various percentages of SMA and glass fibers have been utilized as reinforcing material in composite and their efficacy in energy dissipation has been evaluated. Hybrid composite specimens reinforced with SMA wires and glass fiber strands were first designed and then manufactured. During the process, relationship between weight of fiber and FVF was developed, which formed basis for design. Guidelines for manufacturing of the SMA-FRP composite specimens were established and formulated for any combination of reinforcing material. Cyclic tensile tests on these composites have been performed to study stiffness, strength, residual strains and ultimate elongation properties. All the coupon specimens were tested under strain control loading protocol. SMA-FRP coupon specimens were also tested under cyclic loading and effect of compression and buckling on tensile behavior was explored. Efficacy of manufacturing technique was investigated using SEM with both back scatter electron and secondary electron images. Thorough surface preparation and polishing techniques were explored to make ready, damaged specimens after testing for microscopy.

The constitutive material properties of the proposed composite, explored during coupon testing were then utilized to develop numerical models which were utilized in prototype MRFs using FE software OpenSees. Numerical material models developed showed ability to depict the

hysteretic behavior of the composite with various reinforcement percentages. The ability of the proposed modeling method to capture the SMA-FRP composite behavior and their suitability for use in structural level models was explored. Numerical models for two prototype MRFs were developed in which newly proposed composite was restricted to plastic hinge zones where most of the inelasticity gets accumulated. Both force based and performance based design approaches were used to show efficacy of SMA-FRP composite reinforcement under both design approaches. Equivalent static force method and capacity spectrum method were explored for design process. MRF were designed with steel, proposed SMA-FRP composite and GFRP reinforcement was subjected to suit of ground motion using IDA technique. Comparison on their performance in terms of IDR, accumulations of residual drifts and energy dissipation was done. Energy dissipation accompanied by negligible residual drifts due to activation of pseudo-elastic behavior of the SMA-FRP composite was investigated using stress-strain relationship. IDA helped in understanding the response parameters of SMA-FRP composite reinforcement associated with seismic forces, in comparison with other reinforcements. The designed frames were also subjected to main shock-aftershock sequential seismic events. 2-event and 4-event sequences from various natural earthquake records were used to explore the accumulation of residual deformation of the structure which is critical to mitigate damage from aftershocks. Accumulation of these permanent drifts; damage and vulnerability to reach dangerous drift limits were quantified in terms of reduction factor. A correlation of this damage parameter with ground motion duration was developed for various performance objectives and target drifts.

Finally, an experimental investigation involving exploration of proposed composite as a square rebar was done. The proposed rebar was first fabricated and then embedded in small scale concrete T-beam. The SMA-FRP composite reinforced T-beam was tested under cyclic loading till failure. Crack mouth closing, ductility, and re-centering capability of the tested beam with the new composite were explored.

10.2 Conclusions

Results of this research indicated use of SMA-FRP composite in plastic hinge zones of RC MRF under single or multiple seismic hazards, as an effective strategy to provide ductility, dissipate energy through hysteresis while providing re-centering capability. These desired properties make SMA-FRP composite reinforcement an ideal replacement to steel and GFRP reinforcements in selected plastic hinge lengths / zones of MRF.

In the first part of this research, constituents for manufacturing of SMA-FRP composite were explored. Based on test observations, following conclusions can be drawn from this segment:

- Epoxy EPON-862, curing agent EPIKURE-3274 and diluents modifier Heloxy-48 were selected as ingredients for the resin matrix with 100:40:5 pbw proportion. The selected resin was able to show high elongation properties with ductility of 4.7 at a strain value of 8%.
- Reduction in accumulation of residual strains as exhibited by FRC-7 specimen, points out the re-centering capability of SMA composite reinforcement, which combined with wider

hysteresis (energy dissipation) is an important characteristic, especially in the high seismic zones.

- 7 μm diameter S-glass fibers were selected over E-glass and Kevlar fibers for use in manufacturing of hybrid SMA-FRP composite because of its high elongation capability with average rupture strain of 3.4%.
- Hybrid composite PRC-3 and PRC-5 specimens (manufactured with S-glass) showed better stiffness and strength as compared to the FRC-7 specimen., while the FRC-7 composite exhibited better ductility and energy dissipation capability. This shows that both types of composites have their own advantages; hence could be used for different applications.
- Technique employed to design the hybrid composite was verified by the computation of modulus of elasticity for PRC-3 and PRC-5. Thus the composite designing technique utilized in this research can be successfully employed for fabrication of composite with other target properties.
- SEM images did not show any anomalies like de-bonding/de-lamination between resin and SMA wires in the manufacturing process. Efficacy of resin in filling all air voids and cavities around glass fibers and SMA wires was proven.
- FRC-13 specimen, which experienced compressive cycles in addition to tensile cycles, was able to show ductility of 3.9 before exhibiting de-bonding between SMA wires and surrounding resin. Due to buckling of specimen during compression cycles, SMA wires de-bonded with resin after 6 % strain cycle with the resin crushing in compression by the

end of 7% strain cycle. Results show that compressive behavior does affect the tensile behavior of composite after 5% strains.

In the second part of this research, constitutive behavior was modeled numerically and was extended to frame analysis. These qualified results (slip between rebar and concrete was ignored) offer insight to structural performance of the moment resisting frames reinforced with SMA-FRP composite in comparison with steel and GFRP reinforcements. Following conclusions can be drawn from this segment:

- Results indicated that the numerical models developed in this study are capable of predicting closely, the initial stiffness, transformation stresses and strains, and the post-yield behavior of SMA-FRP composite. Technique of combining material in parallel with assignment of various FVF was effective in capturing the SMA-FRP composite behavior and thus is suitable for use in structural level models.
- Results from force based design approach involving seismic input showed that initially, steel reinforced frames experienced lesser IDR as compared to SMA-FRP reinforced frames due to higher initial modulus of elasticity of steel. However, as the seismic demand increases, steel reinforcement experiences yielding, plasticity and permanent damage, causing frame to exhibit higher IDR and residual IDR as compared to SMA-FRP reinforced frame.
- The average increase in maximum PGA for 3S1B MRF reinforced with steel and SMA-FRP was 42% and 20% respectively, as compared to GFRP reinforced MRF. However

for 6S2B frame, this difference was 23% and 14% for steel and SMA-FRP reinforced frames, respectively. This can be attributed to more redundancy in the 6S2B MRF as compared to 3S1B MRF.

- Results showed that the SMA-FRP-reinforcement had much better performance in ways to curb damage by recovering the applied strains. It was observed by comparing the residual ID values that, SMA-FRP-reinforced frame exhibited on average 84% and 82% less residual ID compared to 3S1B and 6S2B steel reinforced frame. This can be attributed to the undamaged state of SMA-FRP composite reinforcement as compared to steel reinforcement which is prone to permanent damage due to plasticity. This tendency and property of SMA-FRP to re-center itself after experiencing inelasticity is the hallmark of SMA material and is that which distinguishes it from GFRP and steel as reinforcing material.
- Results from multi-event seismic hazard analysis using performance based design indicated that the sequential record causes the MRF to experience more IDR as compared to any single seismic event (main shock) as it is subjected to more displacement demands. Increased displacement demand leads to higher values of IDR and residual drifts, indicating more damage.
- Results from seismic sequential analyses showed accumulation of residual IDR in case of steel reinforced frames due to damage and plasticity effects. Accumulation of damage from main shock makes steel reinforced MRF much more susceptible to collapse as compared to SMA-FRP composite reinforced frames because of their re-centering capability. As a sample, steel reinforced MRF-4% accumulated 0.78% and 1.21%

residual IDR from main shock and aftershock sequence of Chalfant valley earthquake, respectively. This net residual IDR increase by 55% is due to sequential earthquake influence. Once compared with results from MRF-3% subjected to same earthquake sequence, the difference increase net residual IDR is by 31%. Thus MRF-4% exerts more demand on steel reinforcement as compared to MRF-3%, exhibiting more accumulation of residual IDR.

- Accumulation of IDR from main shock and vulnerability to aftershock was quantified in terms of 'reduction factor'. From sample analysis results, these reduction factors come out to be 43% and 41% once PGA required by steel MRF to reach performance levels is compared to SMA-FRP and GFRP reinforcement, respectively once subjected to Christchurch 4-event sequence for MRF-3% case. For MRF-4% case, subjected to same 4-event sequence exhibit 49% and 46% reduction factor for SMA-FRP and GFRP reinforcement, respectively. From the results it is evident that the reduction factor value tends to increase in 4% IDR case as compared to 3% IDR demand for both steel/SMA-FRP and steel/GFRP scenarios.
- A correlation between this reduction factor associated with steel reinforced frame and ground motion parameters such as duration ratio was developed. Results point out the fact that as the duration ratio increases, the reduction factor decreases. This proves that the seismic damage for multiple earthquakes is higher than that of single ground motion, thus need for more robust and re-centering reinforcement type, as proposed in this study.

In the last segment of this research, efficacy of proposed composite was explored experimentally by manufacturing square rebars which were embedded in small scale concrete T-beam and tested under 3-point bending. Following conclusions can be drawn from this segment:

- Results from testing showed that SMA-FRP composite rebars are able to close the tensile cracks (measured using CMOD) due to its re-centering capability. In the 3rd cycle, the SMA composite rebars were able to close the mouth opening by 96.4% with negligible residual deflection.
- SMA-FRP reinforced beam showed excellent hysteresis in the 3rd cycle. The hysteretic energy dissipated in the 3rd cycle was 124% more as compared to 1st cycle. The beam initially experienced flexural crack from the provided notch, but later developed shear crack because of absence of lateral reinforcement and aggregate interlock. The ultimate failure of the beam in 4th cycle was due to shear.

10.3 Recommendations for future work

The following research related topics are still in need of further investigations:

- Use of SMA ribbons instead of wires, could have potential for use as reinforcing material in composite. Ribbons will offer more stiffness in desired orientation and thus can provide better stiffness and resistance against deflections.

- Use of SMA-FRP composite has potential to provide solution to corrosion issues associate with steel reinforcement. This inherent advantage of SMA-FRP reinforcement can further be studied for use in structures exposed to harsh environmental conditions.
- Other cost-effective types of SMA need to be explored as replacement for NiTi SMA for use in composite rebars. They could provide better stiffness and will bring the manufacturing cost down, associated with expensive NiTi material.
- Variability in material properties can be utilized to perform sensitivity analysis to assess effect of each constituent on overall properties of the designed composite.
- During manufacturing of rebars, a scheme to develop deformation and corrugations along the length of rebar should be developed. This will minimize the slippage and de-bonding between SMA composite rebar and concrete.
- Autoclave involving vacuum assisted resin transfer molding (VARTM) should be explored for manufacturing life size rebars for embedding in full scale concrete members.
- De-bonding and slip relationship for proposed composite rebar needs to be developed and modeled numerically.
- Experimental study of a scaled beam-column joint reinforced with proposed composite reinforcement should be conducted under cyclic loading regime, to fully investigate the hysteretic dissipation capability, slippage, re-centering, effects of axial loads and shear effects etc. Results from these experiments can also be utilized to verify developed material models when incorporated in element and system level models.
- Experimental study for developing mechanical couplers for proposed SMA-FRP composite rebars and conventional GFRP rebars for exploring their practical application.

- More numerical seismic analysis, involving sequential seismic hazard need to be conducted to develop better correlations between various damage levels in concrete structures and sequential ground motion input.
- Code provisions for the seismic design of steel reinforced concrete structures needs to be re-visited for SMA-FRP composite reinforced structures considering its large deformation capability, negligible residual strain, and re-centering capability.

CHAPTER 11

References

American Concrete Institute (ACI) 318. Building Code requirements for Structural Concrete (ACI 318-11). *ACI Committee 318,* Farmington Hills, MI, USA, 443 pp. 2011.

Ahsan M. Sheikh, Saif M. Hussain. Pakistan earthquake reconstruction and recovery program. *Structural Magazine.* November 2008. pp 28-31.

Amadio C.., Fragiacomo M, Rajgelj S. The effects of repeated earthquake ground motions on the non-linear response of SDOF systems. *Earthquake Eng. Struct. Dyn.* 2003. 32:291–308.

Arias, A. *A measure of earthquake intensity. Seismic Design for Nuclear Power Plants,* Hansen, R. Editor, MIT Press, Massachusetts, 438-483. 1970.

Ashby, M.F. *Materials selection in mechanical design*. 4th edition. Pergamon Press, Oxford, 2011.

American standards for testing materials (ASTM), ASTM C109: *Standard test method for compressive strength of hydraulic cement mortars*. ASTM, West Conshohohoken, PA, 2013.

American standards for testing materials (ASTM), ASTM C305: *Standard practice for mechanical mixing of hydraulic cement pastes and mortars of plastic consistency*, ASTM, West Conshohohoken, PA, 2012.

ATC-40. Seismic evaluation and retrofit of concrete buildings, vol. 1. *Applied Technology Council*, Redwood City (California), 1996.

Bank L.C. Composites for Construction: Structural Design with FRP Materials, 1st edition, Wiley, NewYork, 2006.

Benmokrane B., Chaallal O. and Masmoudi R. Flexural response of concrete beams reinforced with FRP reinforcing Bars. *ACI Materials Journal*. 1995. Vol **91**, No2.

Beskos D.E., Hatzigeorgiou G.D. Inelastic displacement ratios for SDOF structures subjected to repeated earthquakes. Engg. Struct. 2009. 31:2744–55.

Bradberry, T.E. Concrete bridge decks reinforced with fiber reinforced polymer bars. *Transportation Research Record 1770*, Transportation Research Board, Washington, D.C., 94–104. 2001.

Brinson L.C. One-Dimensional Constitutive Behavior of Shape Memory Alloys: Thermomechanical derivation with non-constant material functions and redefined martensite internal variable. *Jour. of Intell. Mat. Sys. and Struc*. 1993. **4**, (229 – 242).

Callister, W.D. *Materials Science and Engineering: An introduction*, **6th** edition, Wiley, NewYork, 2003.

Chai, Y. M.J.N. Priestley and F. Seible. Seismic retrofit of circular bridge columns for enhanced flexural performance. *ACI Structural Journal.* 1991. 88(**5**): 572-584.

Chopra, K.A., *Dynamics of structures, theory and application to earthquake engineering*, **3rd** edition, Prentice Hall, New Jersey. 2006.

DesRoches R., McCormick J. and Delemont M. Cyclic properties of superelastic shape memory alloy wires and bars *J. Struct. Eng*. 2004. ASCE **130** 38–46.

Dolce, M. and Cardone, D. Mechanical behaviour of shape memory alloys for seismic applications. Martensite and austenite Ni-Ti bars subjected to torsion. *International Journal of Mechanical Sciences.* 2001. **43**: 2631-2656.

Elnashai A.S. and Luigi D.S. *Fundamentals of Earthquake Engineering*. Wiley New York, 2008.

Enright M. P., Frangopol D. M. Reliability-based condition assessment of deteriorating concrete bridges considering load redistribution. *Journal of Structural Safety*. 1999. 21 159-195.

Federal emergency management agency. NEHRP guidelines for the seismic rehabilitation of buildings. *Report FEMA 273*. Washington (DC). 1997.

Federal emergency management agency. Next generation Performance based seismic design guidelines *Report FEMA 445*. Washington (DC). 2006.

Fragiacomo, M., Amadio, C., and Macorini, L. Seismic response of steel frames under repeated earthquake ground motions. *Engineering Structures.* 2004. **26**, p.2021–2035.

Freeman S.A. Development and use of capacity spectrum method. *Proceedings of the 6th US National Conference on Earthquake Engineering*. 1998. Seattle, EERI, Oakland, California,

Gong, J. M., Tobushi, H., Takata, K., Okumura, K., and Endo, M. Cyclic superelastic deformation of TiNi shape-memory alloy. *Materials Science Forum.* 2002. 394-395.

Garcia J.R., Moreno J.Y., Maldonado I.A. Evaluation of existing Mexican highway bridges under mainshock–aftershock seismic sequences. *Proceedings of the 14th world conference on earthquake engineering.* 2008. China. Paper 05-02-0090.

Garcia J.R., Manriquez J.C.N. Evaluation of drift demands in existing steel frames under as-recorded far-field and near-fault main shock–aftershock seismic sequences. *Engineering Structures.* 2011. 33 621–634.

Harris H. G., Somboonsong W. and Ko F. K. New ductile hybrid FRP reinforcing bar for concrete structures *J. Compos. Constr*. 1998. **2** 28–37.

Hatzigeorgiou G.D., Liolios A.A. Nonlinear behaviour of RC frames under repeated strong ground motions. *Soil Dyn. Earthq. Engg.* 2010. 30:1010–25.

Hebda D. A. and White S. R. Effect of training conditions and extended thermal cycling on nitinol two-way shape memory behavior *Smart Materials and Structures.* 1995. **4**, 298-304.

http://www.geolocation.ws/v/P/23097314/after-the-quake/en.

http://www.rta.nsw.gov.au/publicationsstatisticsforms/reports/index.html

Husid, L.R. Characteristicas de terremotos. Analis general. *Revista del IDIEM*. 1969. Santiago, 8, 21-42.

Janke L., Czaderski C., Motavalli M. and Ruth J. Applications of shape memory alloys in civil engineering structures-overview, limits and new ideas. *Mater. Struct*. 2005. **38** 578–92.

Jeong, G.D., and Iwan, W.D. The effect of earthquake duration on the damage of structures. *Earthquake Engineering and Structural Dynamics*. 1988. 16, 1201–1211.

Jonnalagadda K., Sottos N., Qidwai M., Lagoudas D. Transformation of Embedded Shape. *J. of Intell. Mat. Sys. and Struc*. 1998. **9.**

Katz, A. Bond mechanism of FRP rebars to concrete. *Materials and Structures.* 1999. **32**, 761-768.

Keesler, R.J. and Power, R.G. Corrosion of epoxy coated rebar's keys segmental bridge Monroe County. Report No. **88-8A**, *Florida dept. of Transportation, Materials office, corrosion research Laboratories, Florida, USA.* 1998.

Lagoudas, D. C. *Shape Memory Alloys: Modeling and Engineering Applications*, New York, NY: Springer Science and Business Media, LLC. 2008.

Lee D. H., Kim D., Lee K. Analytical approach for the earthquake performance evaluation of repaired/retrofitted RC bridge piers using time-dependent element. *Nonlinear Dyn* 2009. 56: 463–482.

Li Q., Ellingwood B.R. Performance evaluation and damage assessment of steel frame buildings under main shock–aftershock sequences. *Earthq Engg. Struct. Dyn.* 2007. 36:405–27.

Lim, T. J., and McDowell, D.L. Mechanical behaviour of an Ni-Ti shape memory alloy under axial-torsional proportional and non proportional loading. *Journal of Engineering Materials and Technology, Transactions of the ASME.* 1999. **121** 9-18.

Liu, Y., Xie, Z., Humbeeck, J.V. and Delaey, L. Asymmetry of stress-strain curves under tension and compression for NiTi shape memory alloys. *Acta Materialia*. 1998. **46**: 4325-4338.

Luco, N., Bazzurro, P. and Cornell, C.A. Dynamic versus static computation of the residual capacity of a main shock-damaged building to withstand an aftershock. *13th World Conference on Earthquake Engineering.* Aug. 2004. Vancouver, B.C., Canada,

Mander J. B., Priestley J. N. and Park R. Theoretical stress strain model for confined concrete *J. Struct. Eng*. 1988. **114** No. 8.

Mazzoni S. Open System for Earthquake Engineering Simulation (OpesSees). *OpenSees Command Language Manual* (Berkeley, CA: Pacific Earthquake Engineering Research Center, University of California). 2009.

Melton, K. N. Ni-Ti based shape memory alloys. *Engineering aspects of shape memory alloys*, T. W. Duerig, K. N. Melton, D. Stckel, and C. M. Wayman, eds. Butterworth-Heinemann, Boston, MA, 21–33. 1990.

Menegotto M. and Pinto. Method of analysis for cyclically loaded RC plane frame including changes in geometry. *Preliminary Report IABSE* vol **13**, pp 15–22. 1973.

Michaud, Véronique and Schrooten. Shape Memory Alloy Wires turn Composites into Smart Structures. Part II: Manufacturing anti Properties. *Smart Structures and Materials* 2002*: Industrial and Commercial Applications of Smart Structures Technologies Proceedings of SPIE*. 4698 (1), 406-415.

Miyazaki, S., Imai, T., Igo, Y., and Otsuka, K. Effect of cyclic deformation on the pseudoelasticity characteristics of Ti-Ni. *Metallurgical Transactions A.* 1986. **17A**, 115–120.

Momentive : http://www.momentive.com/

Naito H., Sato J., Funami K., Matsuzaki Y. and Ikeda T. Analytical study on training effects of pseudoelastic transformation of shape memory alloys in cyclic loading *J. Intell. Mater. Syst. Struct*. 2001. **12** 295–300.

Nehdi M., M. S. Alam, M. A. Youssef. Development of corrosion-free concrete beam column joint with adequate seismic energy dissipation. *Engineering Structures.* 2009. ***32** 2518_2528*.

Otsuka, K. and Wayman, C. M. *Shape memory materials*. Cambridge University Press, New York. 1998.

Otsuka, K. and Shimizu, K. Pseudoelasticity and shape memory effects in alloys. *International Metals Reviews*, 1986. **31(3),** 93–114.

Otsuka K., Xu Y., Toyama N., Yoshida H., K. Jang B., Nagai H., Oishi R. and Kishi T. Fabrication of TiNi/CFRP smart composite using cold drawn TiNi wires. *Smart Structures and Materials* 2002: Active Materials: Behavior and Mechanics, Proceedings of SPIE Vol. 4699.

Paine, Jeffrey S. N. and Rogers, Craig A. Shape memory alloys for damage resistant composite structures. *Active Materials and Smart Structures*. 1995. **2427 (1),** 358-371.

Pappada S.; Rametta, R.; Toia, L.; Coda, A.; Fumagalli, L.; and Maffezzoli, A. Embedding of Superelastic SMA Wires into Composite Structures Evaluation of Impact Properties, *Journal of Materials Engineering and Performance.* 2008. **18**, 522-530.

Pastore, Christopher M. and Ko, Frank K. Braided Hybrid Composites for Bridge Repair. *National Textile Center Annual Report*: November 1999, F98-P01, USA.

Paulay T. and Priestley M. J. N. *Seismic Design of Reinforced Concrete and Masonry Buildings*, New York, Wiley, 1992.

Penar B.W. Recentering beam column connections using shape memory alloys. *MS thesis* Georgia Institute of Technology, Atlanta, USA. 2005.

Perkins, J. Ti-Ni and Ti-Ni-X shape memory alloys. *Metals Forum.* 1981. **4(3**), 153– 163.

Priestley, M.J.N., Seible, F., Xiao, Y., and Verma, R. Steel Jacket Retrofitting of Reinforced Concrete Bridge Columns for Enhanced Shear Strength—Part 1: Theoretical Considerations and Test Design. *ACI Structural Journal.* 1994. 91(**4**), p.394-405.

Rizkalla S., Hassan T. and Hassan N. Design recommendations for the use of FRP for reinforcement and strengthening of concrete structures. *Prog. Struct. Engg. Mater*. 2003. **5**:16–28.

Rogers C. Active vibration and structural acoustic control of shape memory alloy hybrid composites experimental results, *J. Acoust. Soc. Am*. 1990. **88 (6),** 2803-2811.

Rogers C. Liang, C. and Jia, J. Structural modification of simply-supported laminated plates using embedded shape memory alloy fibers. *Computers and Structures*. 1991. **38**, 569-580.

Rosenblueth E, Meli R. The 1985 Mexico earthquake: causes and effects in Mexico City. *Conc. Int. (ACI).* 1986. 8(5):23–34.

Rubinsky I.A. and Rubinsky A. An Investigation into the use of the fiber-glass for the prestressed concrete. *Magazine of concrete research*, pp 23-31. 1954.

Said A. M. and Nehdi M. L. Use of FRP for RC frames in seismic zones: part II. Performance of steel-free GFRP reinforced beam-column joint. *Appl. Compos. Mater.* 2004. **11** 227–45.

Saiidi M., Zadeh M., Ayoub C. and Itani A. A pilot study of behavior of concrete beams reinforced with shape memory alloys *J. Smart Mater. Civ. Eng*. 2007. ASCE **19** 454–61.

Sittner P. and Stalmans R. Developing hybrid polymer composites with embedded shape-memory alloy wires. *Journal of the Minerals, Metals and Materials Society*. 2000. 52(10), 15-20.

Scott B., Park R., Preistley M.J.N. Stress strain behavior of concrete confined by overlapping hoops at low and high strain rates. *Journal of American concrete institute*. 1982. 79(1): 13-27.

Shin M. and Andrawes B. Experimental investigation of actively confined concrete using shape memory alloys *J. Engg. Struct*. 2010. **32** 656–64.

Somboonsong Ko, Frank K., and Harris, Harry G. Ductile hybrid fiber reinforced plastic reinforcing bar for concrete structures: design methodology. *ACI Materials Journal.* 1998. **95 (6)**, 655-666.

Sozen MA. Review of Earthquake response of reinforced concrete buildings with a view to drift control. State-of-the-Art in Earthquake Engineering, *Turkish National Committee on Earthquake Engineering*, Istanbul, Turkey, 383–418. 1981.

Sterzla, T. and Winzek, B. Bistable shape memory thin film actuators. *Smart Structures and Materials 2003: Active Materials: Behavior and Mechanics, Proceedings of SPIE* 2003. 5053 (1), 101-109.

Strnadel, B., Ohashi, S., Ishihara, T., Ohtsuka, H., and Miyazaki, S. Cyclic stress-strain characteristics of Ti-Ni and Ti-Ni-Cu shape memory alloys. *Materials Science and Engineering*: A. 1995. **202:** 148-156.

Tadaki, T., Otsuka, K., and Shimizu, K. Shape memory alloys. *Ann. Rev. Mater. Sci.* 1988. **18**, 25–45.

Tobushi, H., Shimeno, Y., Hachisuka, T., and Tanaka, K. Influence of strain rate on superelastic properties of TiNi shape memory alloy. *Mechanics of Materials*. 1998. **30**, 141–150.

Tsoi, K.; Stalmans, R.; Schrooten, J.; Wevers, M.; and Mai, Y. Impact damage behaviour of shape memory alloy composites. *Materials Science and Engineering*. 2003. **A342,** 207-215.

Vamvatslos, D. & Cornell,A.C. Incremental dynamic analysis. *Earthquake Spectra.* 2001. **20(2)**, pp. 523-553.

Wayman, C. M. and Duerig, T. W. An introduction to martensite and shape memory. *Engineering aspects of shape memory alloys*, T. W. Duerig, K. N. Melton, D. Stckel, and C. M. Wayman, eds., Butterworth-Heinemann, Boston, MA, 3–20. 1990.

Wang H. and Belarabi A. Static and fatigue bond characteristics of FRP rebars embedded in fiber reinforced concrete *J Compos Mat.* 2010. Vol. **44**, No. 13.

Weber, André; Schweinfurth, Jörg; and Jütte, Ben. Newly developed GFRP rebar in diaphragm walls of large tunneling projects. *Tunneling and Underground Space Technology*. 2006. **21**(3-4), 437.

Wei Z. G.; Sandstrom, R.; and Miyazaki, S. Shape memory materials and hybrid composites for smart systems Part II Shape-memory hybrid composites Part II Shape memory hybrid composites. *Journal of Material Science.* 1998. **33**, 3763-3783.

Wierschem N. and Andrawes B. Superelastic SMA–FRP composite reinforcement for concrete structures *J. Smart Mater. Struct*. 2010. **19** 13.

Wines J.C. and Hoff G.C. *Laboratory investigation of plastic-glass fiber reinforcement for reinforced and prestressed concrete*. Vicksburg MS: US corps of Engineers, WES. 1966.

Xu Y., Toyama N., Yoshida H., and Kishi T. A novel technique for fabricating SMACFRP adaptive composites using ultrathin TiNi wires. *Smart Materials and Structures.* 2002. **12**, 196-202.

Zafar A. and Andrawes B. Incremental dynamic analysis of concrete moment resisting frames reinforced with shape memory composite bars. *Journal of Smart Materials & Structures*. 2012. **21** 025013-14pp.

Zafar, A. and Andrawes, B. Fabrication and cyclic behavior of highly ductile superelastic shape memory composites. *ASCE J. Mater. Civ. Eng*. 2013. doi: 10.1061/(ASCE) MT.1943-5533.0000797.

Zhang, Run-xin and Ni, Qing-Qing. Mechanical properties of composites filled with SMA particles and short fibers. *Composite Structures*. 2007. **79 (1),** 90-96.